**warwick.ac.uk/lib-publications**

# Tailor-braiding for efficient composite structures

by

## Anubhav Singh

A thesis submitted in fulfilment of the requirements for the degree of
**Doctor of Philosophy in Engineering**

## WMG, University of Warwick

December 2020

*Dedicated to the unfortunate citizens of the world who lost their livelihood and lives during the COVID-19 pandemic*

# Contents

# List of figures

# List of tables

x

# Acknowledgement

# Declaration

This thesis is submitted in partial fulfilment of the requirements for the degree of Doctor of Philosophy. The presented research was carried out from October 2017 to November 2020. The research described is my own and not the product of collaboration.

The contents of this thesis have been used to produce the following journal publications:

Singh A, Reynolds N, Carnegie CR, Micallef C, Keating EM, Winnett J, Barnett A, Barbour S, Hughes DJ. A novel route for volume manufacturing of hollow braided composite beam structures. Advanced Manufacturing: Polymer & Composites Science. 2019:1–6.

Singh A, Reynolds N, Keating EM, Barnett A, Barbour S, Hughes DJ. The effect of braid angle on the flexural performance of structural braided thermoplastic composite beams. Composite Structures. Accepted for publication.

Singh A, Reynolds N, Keating EM, Barnett A, Barbour S, Hughes DJ. Three-point flexural performance of tailor-braided thermoplastic composite beam structures. Composite Structures. Accepted for publication.

*Anubhav Singh*
01/12/2020

Signed and dated

# Abstract

Braided composites find several applications in the aerospace and automotive industry. The flexibility of the braiding process combined with their superior damage resistance have firmly established them in the composites industry. The properties of braided composites are directly related with the fibre interlacement angle, i.e. braid angle. These include mechanical behaviour of the material as well as physical characteristics such as thickness, fibre volume fraction etc. Moreover, the weight of a braided composite component is also dependent on the braid angle. This dependence of braided composites' properties on braid angle presents an intuitive opportunity to optimise their structural performance by locally varying the braid angle. As such, this thesis presents an experimental investigation aimed at establishing the potential benefits of this novel concept of local braid angle variations, termed here as *tailor-braiding*.

Based on the dependence of multiple characteristics of braided composites on braid angle, three-point flexure was selected as the appropriate test scenario to evaluate the mechanical performance of the tailor-braided composites at a structural level. A novel bladder moulding process called rapid variothermal moulding was developed to manufacture braided beams using commingled glass fibre-polyamide 6 tows, ensuring consistent part quality for the subsequent mechanical test program. Beams with uniform braid angles of 30°, 45° and 60° were manufactured and tested in three-point flexure to establish a benchmark for the assessment of the tailor-braided beams. Based on these results, a tailor-braiding strategy was adopted to manufacture and test tailor-braided beams with axial as well as radial braid angle variations.

Comparison of the observed mechanical performance and detailed deformation analysis indicated a potential of 24% reduction in weight for axially tailor-braided beams while maintaining performance compared to the benchmark. Therefore, the proposed tailor-braiding concept is shown to enhance the structural efficiency of composite components.

# Abbreviations and terminologies

| | |
|---|---|
| A | Cross-sectional area of braided beam |
| AE | Acoustic Emission |
| ANOVA | Analysis Of Variance |
| BIM | Bladder Inflation Moulding |
| BIW | Body In white |
| BP | Braiding Plane during a braiding operation |
| $CO_2$ | Carbon dioxide |
| CAD | Computer Aided Design |
| CFRP | Carbon Fibre Reinforced Polymer |
| CMF | Composite Multispar Flap (Airbus project) |
| CMOS | Complementary Metal Oxide Semiconductor |
| CNC | Computer Numerical Control |
| CT | Computed Tomography |
| D | Beam outer diameter |
| d, x | Test machine crosshead displacement |
| DIC | Digital Image Correlation |
| $D_m$ | Braiding mandrel diameter |
| DP | Dual Phase (steel) |
| DSC | Differential Scanning Calorimetry |
| dx | x-displacement computed from DIC |
| dy | y-displacement computed from DIC |
| E | Young's modulus of beam material |

| | |
|---|---|
| e | Shear-driven deviation from pure flexure |
| $E_{abs}$ | Energy absorption during three-point flexure |
| $E'_{abs}$ | Mass-normalised energy absorption |
| FE | Finite Element (modelling) |
| $F_{mf}$ | Fibre mass fraction |
| FP | Fall Plane during a braiding operation |
| FPP | Fibre Patch Placement |
| $F_{vf}$ | Fibre volume fraction |
| G | Shear modulus of beam material |
| I | Moment of area of beam cross-section |
| IQR | Inter-Quartile Range |
| k | Cross-section shape dependent factor |
| L | Length of the beam |
| $L_s$ | Span length of a beam specimen |
| M | Beam weight |
| m | Weight of specimen in air |
| $m_c$ | Initial mass of test specimen and crucible |
| $m_{dw}$ | Weight of specimen in distilled water |
| $m_r$ | Mass of specimen residue and crucible after burn off |
| $MS_W$ | Mean square error within samples |
| n | Number of points on a particular section in DIC |
| $n_A$ | Sample size of a random sample A |
| $N_c$ | Number of carriers used in the braiding process |

| | |
|---|---|
| NCF | Non-Crimp Fabric |
| NEDC | New European Driving Cycle |
| $N_h$ | Number of horn gears on a braiding machine |
| $N_L$ | Number of braided layers |
| OEM | Original Equipment Manufacturer |
| P | Applied load |
| p | Braiding pitch |
| $P_{max}$ | Peak load |
| $P'_{max}$ | Mass-normalised peak load during three-point flexure |
| PA12 | Polyamide 12 |
| PA6 | Polyamide 6 |
| PEEK | Polyether ether ketone |
| PEKK | Polyether ketone ketone |
| PPS | Polyphenylene sulphide |
| PtFS | Production to Functional Specification |
| $q_{AB}$ | q-statistic for a random pair of samples A and B |
| R | Radius of braiding mandrel |
| $RMS_{23}$ | Root Mean Square error between y2 and y3 |
| RoI | Region of Interest |
| $R_{vf}$ | Resin volume fraction |
| RVM | Rapid Variothermal Moulding |
| S | Stiffness |
| S' | Mass-normalised stiffness |
| T | Linear mass of commingled tows |

| | |
|---|---|
| $TBr_A$ | Tailor-braided beam with axial braid angle variation |
| $TBr_R$ | Tailor-braided beam with radial braid angle variation |
| TFP | Tailored Fibre Placement |
| $T_g$ | Glass transition temperature of the polymer |
| $T_m$ | Melt temperature of the polymer |
| $UBr_{45}$ | Uni-braided beam with a braid angle of 45° |
| $UBr_{60}$ | Uni-braided beam with a braid angle of 60° |
| UD | Unidirectional (reinforcement fibres in a composite laminate) |
| v | Test machine cross head-speed |
| $v_m$ | Mandrel pull-off velocity during a braiding operation |
| $V_{vf}$ | Void volume fraction |
| w | Displacement at mid-point of a beam during three-point flexure |
| $w_t$ | Braided tow width |
| y1 | y-displacement at top section computed from DIC |
| y2 | y-displacement at middle section computed from DIC |
| y3 | y-displacement at bottom section computed from DIC |
| $\delta$ | Deflection at load point during three-point flexure |
| $\alpha, \theta$ | Braid angle |
| $\varepsilon_x$ | x-strain computed from DIC |
| $\dot{\epsilon}$ | Strain rate during three-point flexure |
| $\mu_A$ | Mean for a random sample A |
| $\rho$ | Specimen density |
| $\rho_0$ | Temperature dependent density of distilled water |

| | |
|---|---|
| $\rho_f$ | Fibre density |
| $\rho_L$ | Density of air |
| $\rho_r$ | Resin density |
| $\omega_h$ | Horn gear angular velocity |

**Terminologies**

In this thesis:

- **Composite** refers to a polymer matrix composite.
- **Component-level testing** refers to one scale above coupon testing, generally referred to as element-level testing in traditional design terminology.
- **Tow** refers to a bundle of filaments of glass or polyamide.
- **Fabric** refers to a processed textile with interlacements (predominantly braided in this work).

# 1 Introduction

## 1.1 Polymer matrix composites in the automotive industry

The transport industry is a major contributor to the global rise in carbon emissions. As of 2018, it accounts for 24% of the total $CO_2$ emissions [1–4]. This has brought the transport sector under considerable pressure to curb its carbon footprint. In particular, the automotive industry, which accounts for 72% of the transport sector's $CO_2$ emissions [3], has been under constant scrutiny over the last few decades. Several countries around the globe have formulated temporal emission targets to curb the environmental impact of road vehicles. For instance, in Europe, automotive original equipment manufacturers (OEMs) manufacturing passenger vehicles should limit their fleet-wide average $CO_2$ emissions to 95 g per kilometre from 2021 onwards [5]. As shown in Figure 1.1, these targets are constantly revised and aim at minimising the carbon footprint of road vehicles [6].
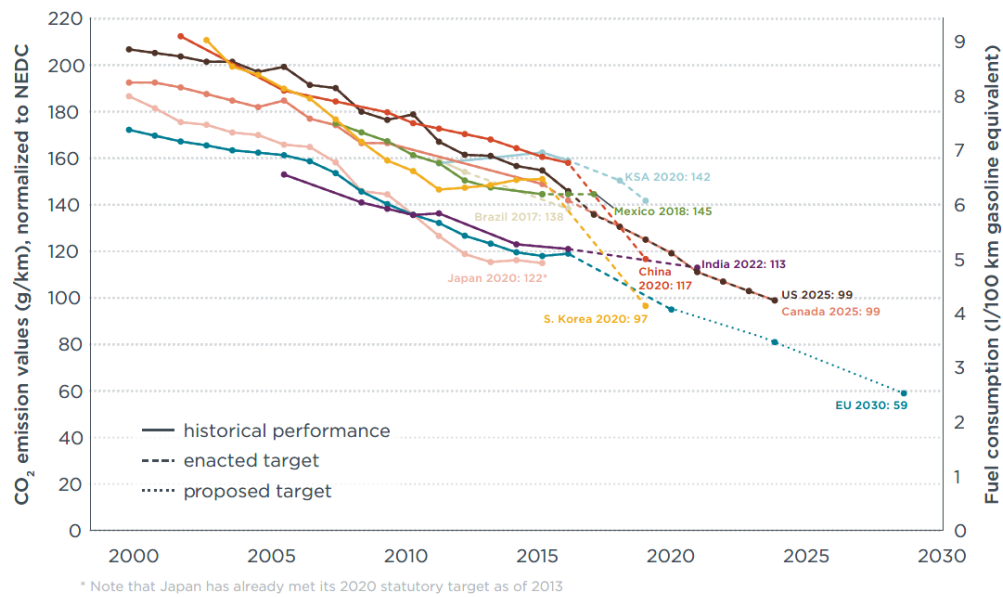


Figure 1.1 Average historic fleet emission data, implemented and proposed emission targets across the globe (Taken from [6]). Note: Data normalised to New European Driving Cycle (NEDC).

In order to meet the emission targets, lightweighting and powertrain electrification have been identified as two key strategies [7,8]. Since the vehicle weight affects energy efficiency, lightweighting has always been a priority for the manufacturers. Moreover,

powertrain electrification also relies on lightweighting to counterbalance the weight added by the additional components of the electric powertrain system [9]. In order to lightweight, the industry is considering various material substitutes with greater mass-specific properties, i.e. properties normalised with respect to mass. For instance, aluminium was used to replace several steel components in the 2012 Range Rover and the 2015 Ford F-150. Consequently, the masses of both these vehicles were at least 300 kg less than their respective predecessors [10]. In the pursuit of lightweight materials, polymer matrix composites (referred to as composites henceforth in this work), particularly those reinforced with carbon fibres, have fared as strong candidates. As shown in Figure 1.2, composites possess comparable modulus and strength while having lower density compared to conventionally used steel and aluminium [11].
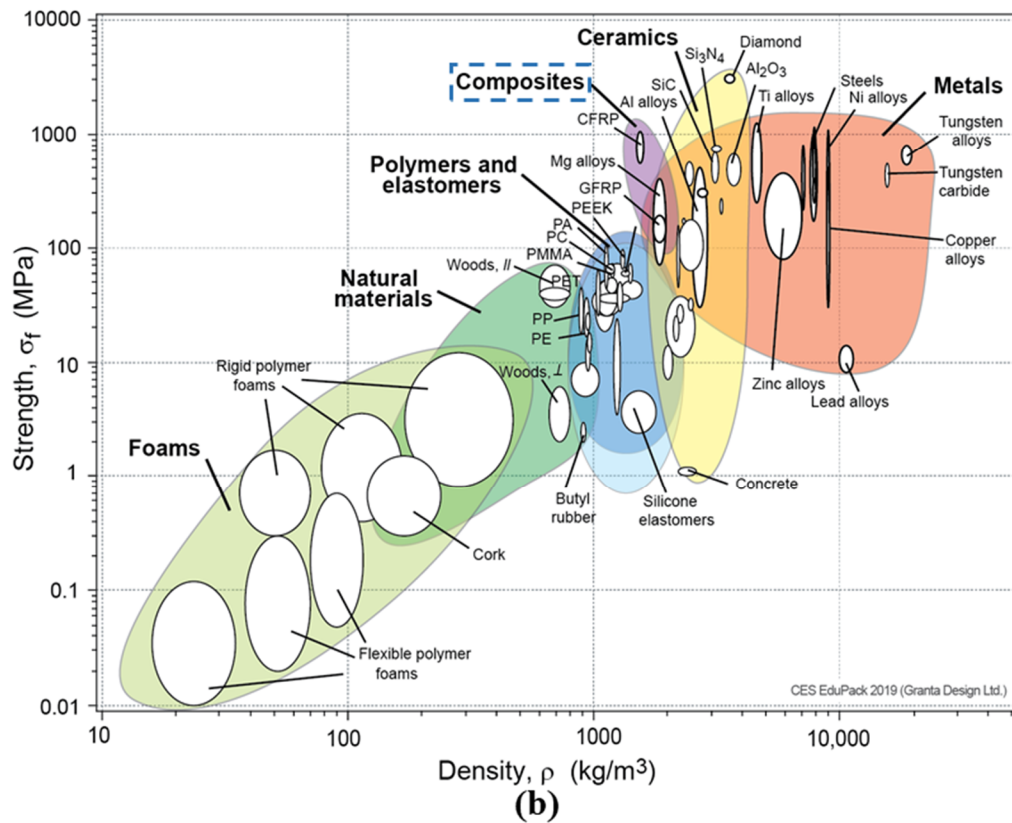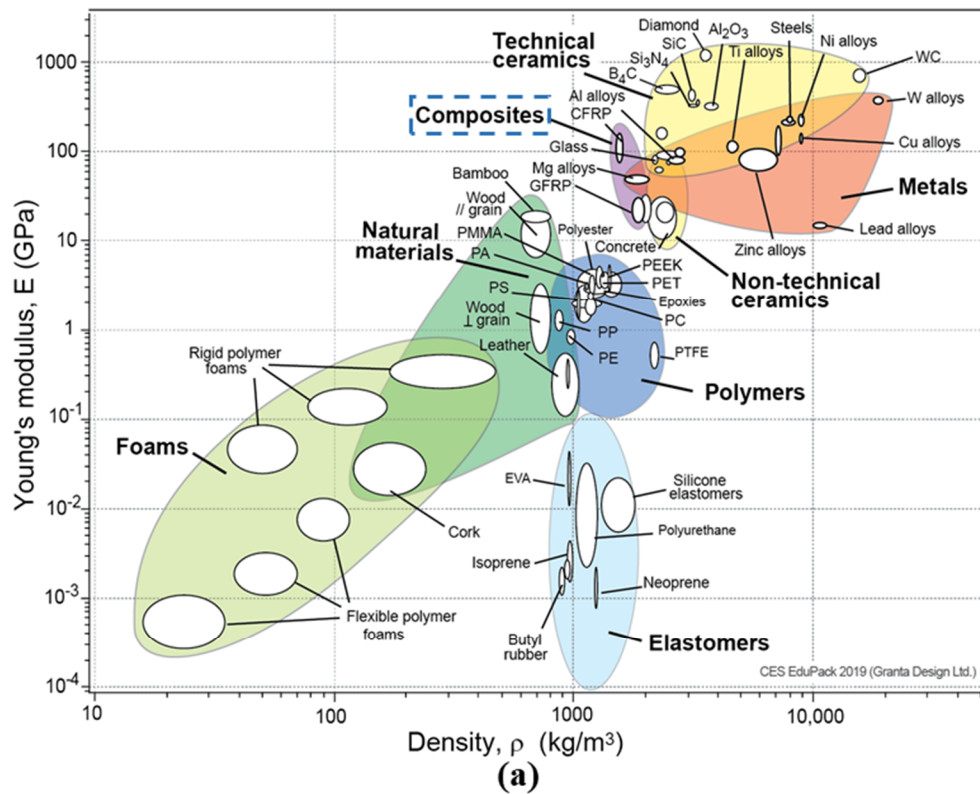
Figure 1.2 (a) Modulus and (b) Strength versus density curves showing the lightweighting potential of composites (Taken from [11]).

For a fundamental introduction and further information on composite materials, as well as their advantages and disadvantages, the readers are referred to references [12–14]. In the automotive industry, composite usage can be traced back to the use of fibreglass composite body panels in the 1953 Corvette [15], shown in Figure 1.3(a). Similarly, the motorsports industry has relied on composites for decades, with the first ever carbon fibre chassis introduced in 1980 by McLaren [16], shown in Figure 1.3(b). However, despite these early applications, high material costs and long processing times limited their application to low-volume and/or premium vehicles.



**(a)**　　　　　　　　　　　　　　**(b)**
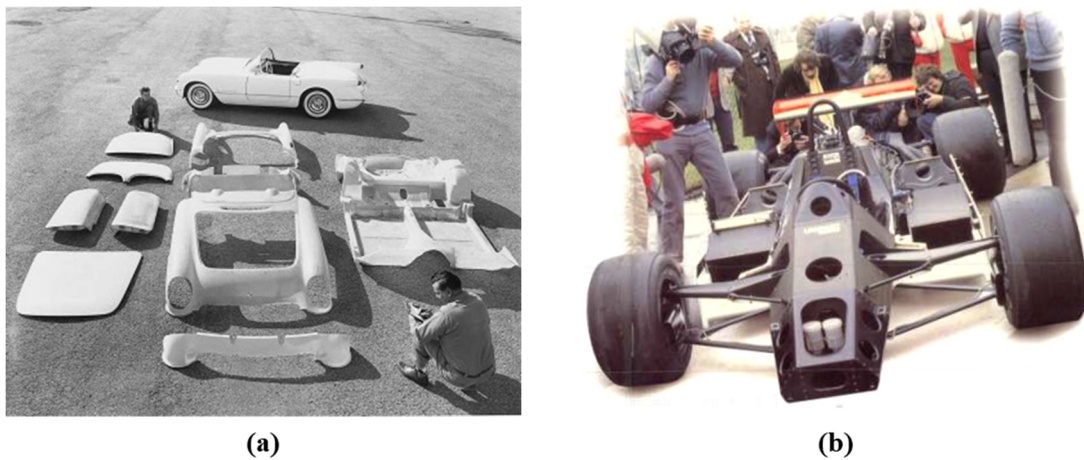
Figure 1.3 (a) Fibreglass body panels of 1953 Corvette (Taken from [15]) and (b) McLaren MP4/1 with the first ever carbon fibre chassis (Taken from [16]).

Owing to the potential benefits of composites, rapid advances have been recently made in efforts aimed at reducing their costs and processing times. Increasing market demand [17] has driven the development of cost-effective carbon fibre precursors [18,19] which is expected to reduce the cost of composite components. In addition, recently developed fast cure resins have demonstrated manufacturing cycles lower than two minutes [20,21] and should play an important role in bringing the part cycle time towards the targeted "part-per-minute" standard of the automotive industry. The use of such fast curing resin systems enabled the production of the first ever mass-produced composite intensive car, the BMW i3, with a production volume of 70 vehicles per day [22,23]. Parallel to the improvement in composite constituents, investment is being actively directed in research activities aimed at conception and development of novel manufacturing technologies. The recent establishment of dedicated research centres such as the Institute for Advanced Composite Manufacturing Institute (USA) [24] and

the Future Composites Manufacturing Research Hub (UK) [25] indicate the focus towards composite manufacturing. Composite manufacturing also forms a significant part of research conducted at other renowned research institutes [26–28].

## 1.2   Braided composites

A key composite manufacturing technology to have emerged over the last few decades is composite braiding. As a process, braiding has existed for centuries, but the realisation of its potential in composite manufacturing has been recent. It involves the use of multi-scale braiding machines to interlace continuous bundles of reinforcement fibres at a predefined angle with respect to the axis of production, as shown in Figure 1.4(a) [29]. This results in the production of generally hollow tubular dry fibre preforms, which can then be impregnated with resin. The automated control of the process supported by CNC controlled industrial braiding machines enables the production of complex-shaped parts at high production rates while reducing wastes as compared to other processes [30]. Figure 1.4(b) shows the braiding of a bus rear axle with variable cross-section [31], highlighting the capability of the braiding process to produce preforms of complex shapes. The vast investments in composite braiding by industry [32–34] and academia [35,36] are a testament of the interest in the technology's development and application.
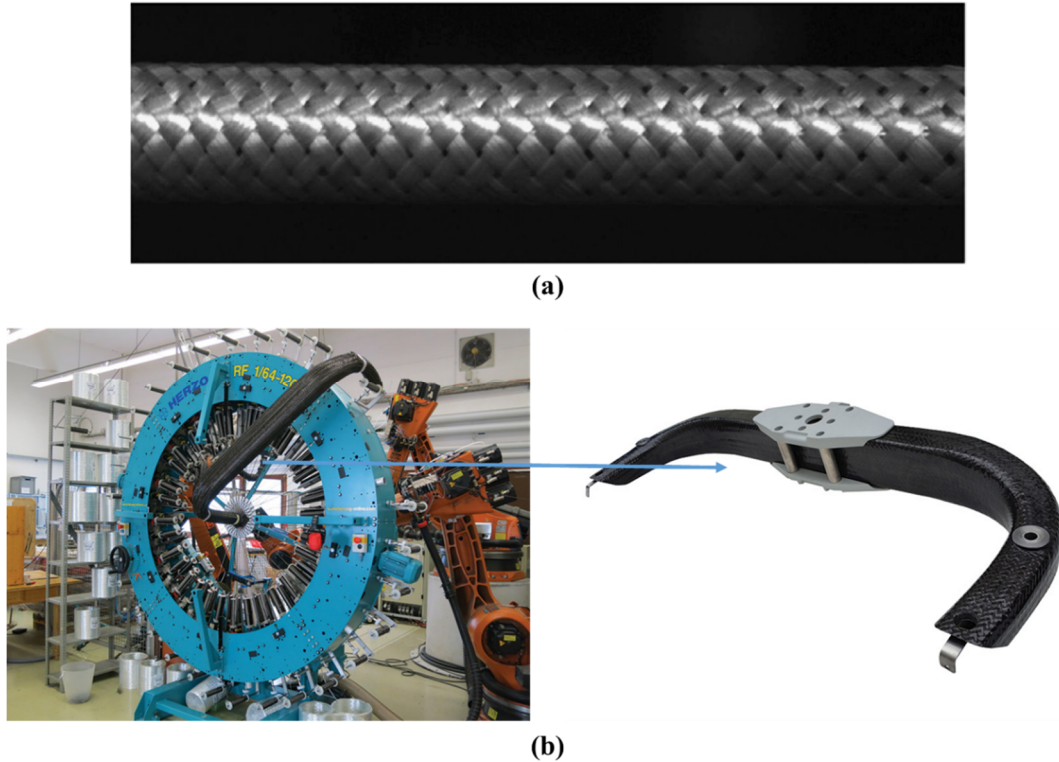
Figure 1.4 (a) Braided composite with fibres interlaced at an angle (Taken from [29]) and (b) Braiding of complex shaped bus rear axle (Adapted from [31]).

Braiding finds several applications in a wide range of industries. A&P Technology, one of the world-leading producers of braided textile, has developed a series of braided components for aerospace applications. These include the fan case of the GEnx engine [37] (for the Boeing 787 and 747-8), stator vanes for Honeywell jet engine [38], braided reinforcements for Bombardier wing flaps [39] etc. Moreover, braided composite frames were also developed for the Airbus A350-1000 [40].

In the automotive industry, braided composites have been used in simple components such as air ducts, overbraided fuel lines, fan blades etc. [29]. Braided composites have also been used in structural automotive components. For instance, Lexus utilised a braided carbon fibre composite with a foam core to produce lightweight A-pillars for the LFA Supercar [34]. Similarly, the BMW 7 series vehicle has a braided profile with a supporting core in its roof bows [41]. Owing to the interlaced network of reinforcement fibres, braided composites display unique phenomena of fibre bridging and tow scissoring. These phenomena, discussed in detail in Chapter 2, impart superior energy absorption characteristics to braided composites. Therefore, braided composites have been used in structures responsible for absorbing loads in the event of a high speed

6

crash. Mercedes-Benz have used braided cones in the frontal crash structure of the SLR McLaren series [42]. During a head-on collision, the cones absorb the crash energy and mitigate severe injuries to the passengers. The front sills (rocker panels) of the Lamborghini Aventador [43] are also made using carbon fibre braided composite. Figure 1.5 shows these crash-critical braided structures, which are supplied to the OEMs by the company Eurocarbon [44]. Recently, Porsche [45] revealed a braided carbon fibre composite wheel for the 911 Turbo S model. While being 20% lighter than the preceding aluminium alloy wheel, Porsche claims the braided wheels are also 20% stronger. Braided composites also find applications in the production of bicycle frames [42] as well as sports equipment such as tennis racquets [46] and fishing outriggers [47]. Moreover, braided composites are also used for manufacturing biomedical catheters [48]. The variety in the scale and end usage of braided composite products demonstrates the flexibility of the technology.



(a)  (b)
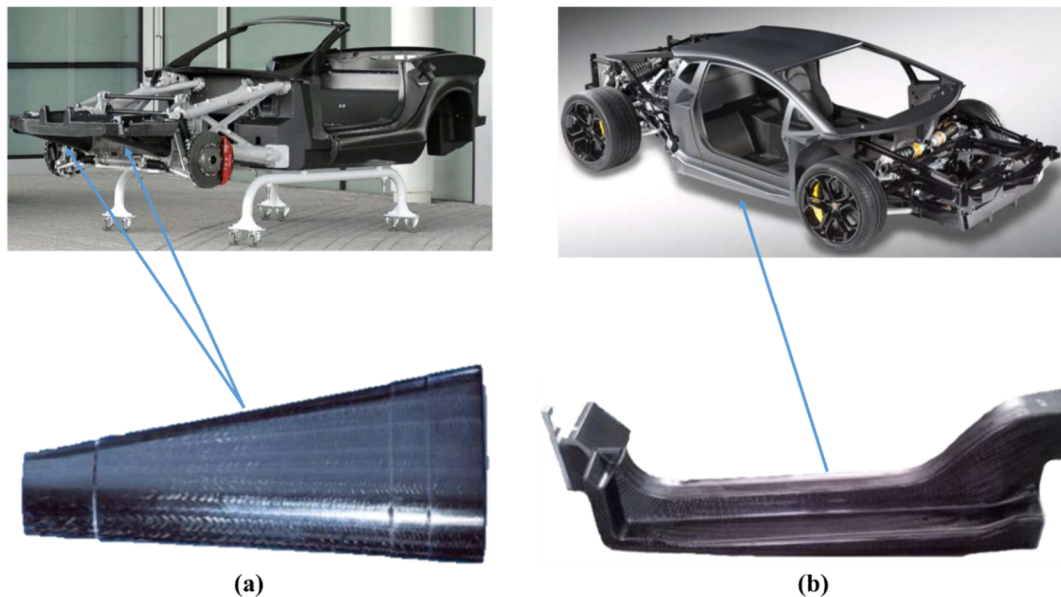
Figure 1.5 Braided composite application in (a) crash cones of Mercedes SLR and (b) side sill of Lamborghini Aventador (Taken from [44]).

Another advantage of the braiding process is the several available avenues to manufacture components to the user's specifications. The process can combine different types of reinforcements without adding significant time or cost to the process. A good example is the braiding of carbon and Kevlar (aramid) tows for achieving enhanced mechanical stiffness as well as energy absorption [49], as shown in Figure 1.6(a). In addition, the mechanical properties can be enhanced by selective introduction

of axial tows [50], as depicted in Figure 1.6(b).



**Axial tows in web**      **Axial tows in flange**

**(a)**      **(b)**
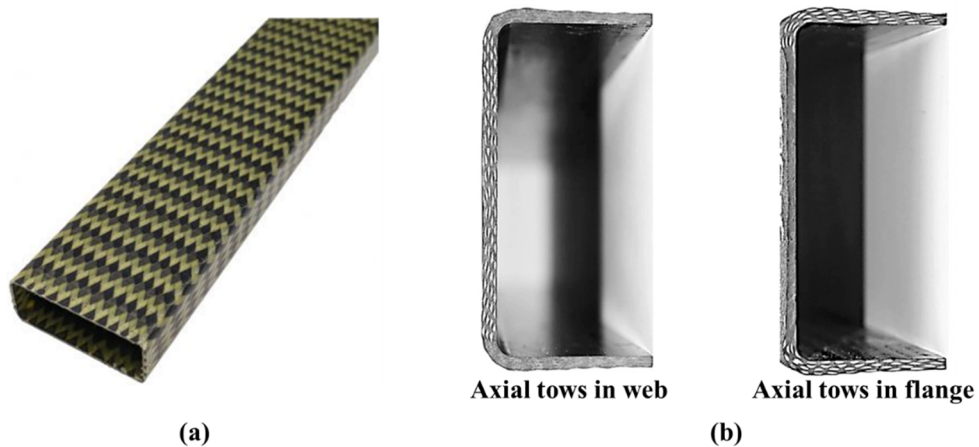
Figure 1.6 (a) Carbon and Kevlar fibres braided together for combined performance benefits (Taken from [49]) and (b) selective introduction of axial tows for improved mechanical properties (Taken from [50]).

Another technique of modifying the properties of braided composites is through variation of fibre angles in different regions of the composite. As shown in Figure 1.7, a transition in fibre orientation is achievable during the braiding process. Such a variation does not add significant cost and time to the process but possesses the potential to produce efficient structures. Currently, there exist only a handful of academic studies [51–55] investigating fibre angle variations during the braiding process, with no published evidence of industrial application.
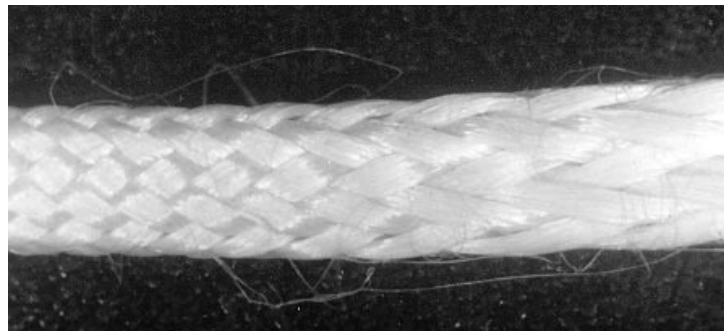


Figure 1.7 A glass fibre braid with continuous fibre angle transition (Taken from [52]).

## 1.3   Efficient utilisation of composite materials

A high degree of manufacturing control is a key advantage of composites and is largely apparent in the form of variations in fibre orientation, fibre type and part thickness. As demonstrated by the wing spar in Figure 1.8, this flexibility may be exploited to

optimise material usage without compromising the mechanical performance [56]. In the example shown, the load experienced during operation reduces from the fuselage to the wing tip, thus resulting in a spatially variable stiffness requirement. Therefore, the spar has been designed with region-dependent fibre orientations as well as thickness.
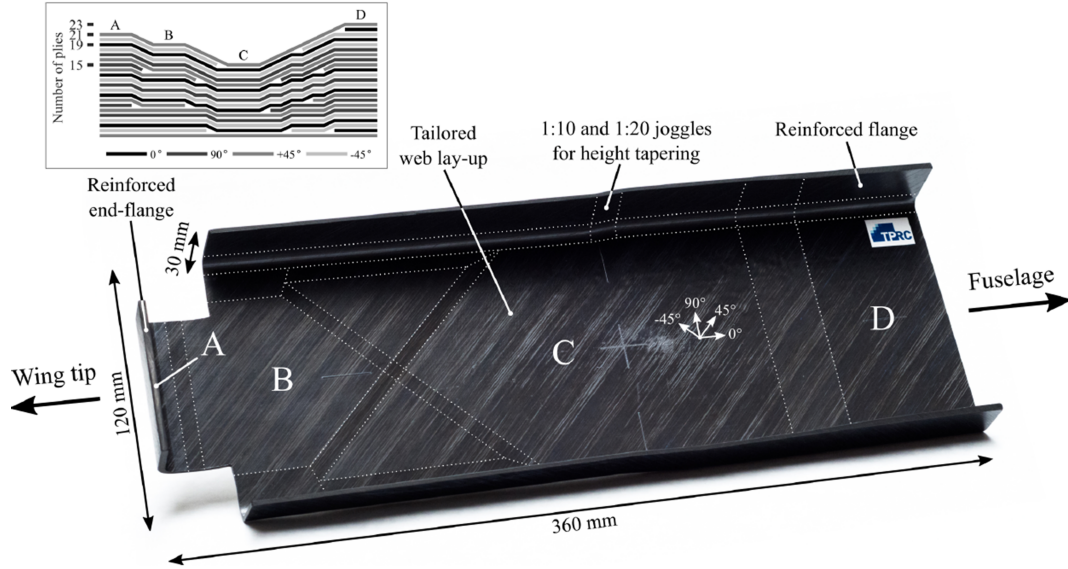


Figure 1.8 Wing spar with variable thickness and lay-up (Taken from [56]).

A similar selective material utilisation based on the part functionality is presented in Figure 1.9 for a composite automotive B-pillar [57]. The outer face uses 0° laminates, i.e. fibres running along the length of the B-pillar, to provide stiffness and prevent intrusion, while the inner hat section consists of off-axis fibres for maximum energy absorption. Moreover, 0° fibres are also used in the upper part of the hat section for strengthening the joint with the remaining body.

9
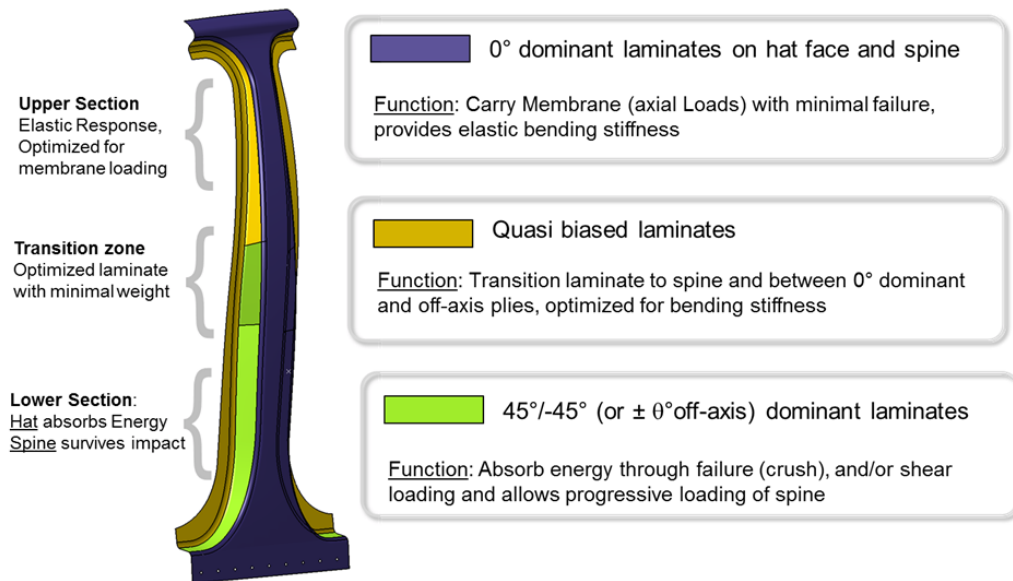
Figure 1.9 Composite B-pillar demonstrator design for optimal exploitation of material properties (Taken from [57]).

Besides fibre lay-up and thickness, efficient composite utilisation also includes choosing the right process to manufacture each component. The Body-In-White (BIW) of the sixth generation BMW 7-series (2015) shows the intelligent use of multiple manufacturing technologies. As shown in Figure 1.10, the BIW of the luxury-sedan consists of 16 composite components produced using 4 different technologies [58].
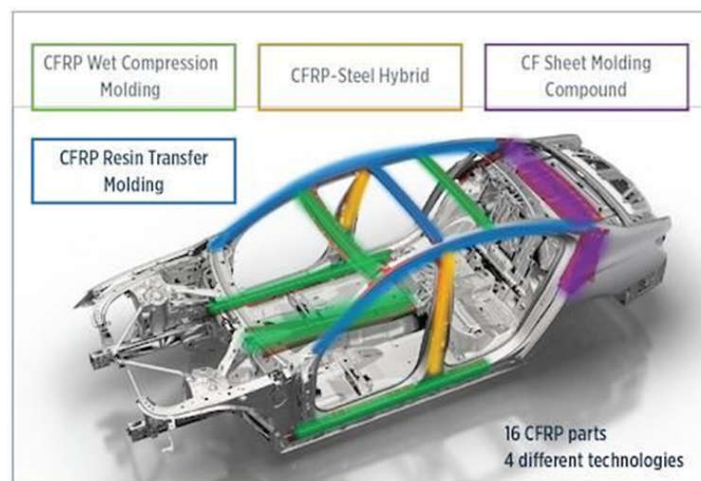


Figure 1.10 CFRP part distribution in the BMW 7 series based on manufacturing technique (Taken from [58]).

Several composite manufacturing technologies are exclusively based on exploiting the manoeuvrability of reinforcing fibres thus resulting in optimal material utilisation. The Fibre Patch Placement (FPP) technology by the company Cevotec uses fibre patches to

create high performance composite laminates with bespoke fibre orientation as well as thickness [59]. Similarly, Hightex has demonstrated the use of Tailored Fibre Placement (TFP) technology to optimise material usage by placing fibres in multiple orientations and selectively stitching them [60]. Therefore, the ability to define the material properties based on local structural requirements is advantageous for judicious material deployment. While satisfying the performance criteria, it also saves material, therefore reducing per part cost.

## 1.4  Scope of the project

This chapter introduced the drivers for lightweighting in the automotive industry and the role that composite materials can play in realising the lightweighting targets. The ongoing research towards achieving wide scale application of composites are aimed at overcoming the barriers of high material costs and long processing times of composites.

Among the rapid advances in composite technology, braiding was highlighted as an emerging manufacturing process with applications ranging from large scale aerospace structures to micro-scale applications such as medical catheters. The process offers various options to modify and vary the resulting structure by controlling the braided fibres, fibre orientation and the addition of axial reinforcements. Therefore, the process inherently allows for optimising braided structures as per any given performance requirements without incurring significant penalties.

The ability to *locally* vary fibre angles in braided structures appears to possess tantalising potential for the creation of structurally efficient components. In the context of this thesis, such an approach in the manufacturing of braided composites will be termed as *tailor-braiding*. The thesis presents a body of research targeting both the development of a production strategy for such tailor-braided components and a systematic experimental approach for assessing their prospective benefits in terms of mechanical performance and lightweighting. The following chapter identifies the current state-of-the-art relating to braided composite material properties and manufacturing methodologies thereof. Furthermore, Chapter 2 establishes the strategies used for material choice, composite processing and mechanical testing in this work.

# 2 Background and literature review

This chapter provides a review of the previously conducted research in the fields relevant to this thesis. The chapter begins with a detailed description of the braiding process and an overview of the manufacturing of braided composite components. Following this, the material properties of braided composites are discussed and the correlations between the properties and angle of the braided fibres, i.e. braid angle, are provided. Thereafter, the advantages of three-point flexural tests for evaluation of structural performance are described and the effect of braid angle on flexural behaviour of braided composite structures is discussed. This is followed by a review of intelligent hybridisation techniques that have shown an improvement in three-point flexure behaviour. The chapter concludes with an assessment of the identified research gaps in the literature and a statement of the research objectives for the research work presented in this thesis.

## 2.1  Braiding technology in composites

The braiding process relies on the coordinated motion of various components of a braiding machine to generate continuous interlacements of fibre tows. Figure 2.1(a) shows a typical horizontal maypole braiding machine with its major components [29]. The machine has a circular array of horn gears with dedicated slots for bobbin carriers. The fibre tows to be braided are wound over bobbins, which are then mounted on the bobbin carriers. These carriers are placed in the slots on the braiding machine's horn gears. During the braiding operation, alternate horn gears rotate in opposite directions, i.e. clockwise and counter-clockwise. Such rotation of the horn gears makes the carriers revolve at a constant angular speed. On arriving at the interface between two horn gears, the carriers are transferred to the adjacent horn gear. The resulting motion of the carriers traces a serpentine path in the plane of the horn gears, as shown in Figure 2.1(b). The free ends of the fibre tows from all the carriers are attached to the surface of a mandrel. The mandrel is simultaneously pulled along a linear path, away from or towards the rotating horn gears at a controlled rate, thus producing the diagonal interlacement of

the tows as they get deposited over the surface of the mandrel. Tension is maintained in the tows during the braiding operation by a spring-loaded mechanism attached to the carriers.
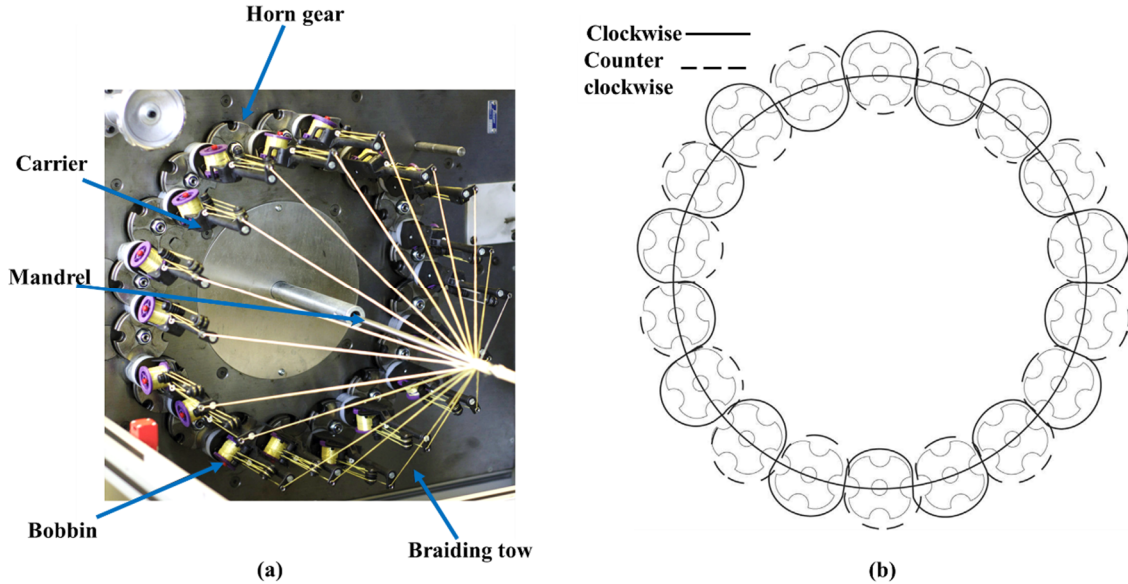


Figure 2.1 (a) Components of a braiding machine and (b) carrier motion along the braiding path (Taken from [29]).

Different arrangements of carriers on the horn gears produce different fibre architectures. The most common architectures, Diamond braid (1×1), Regular braid (2×2) and Hercules braid (3×3), are shown in Figure 2.2.
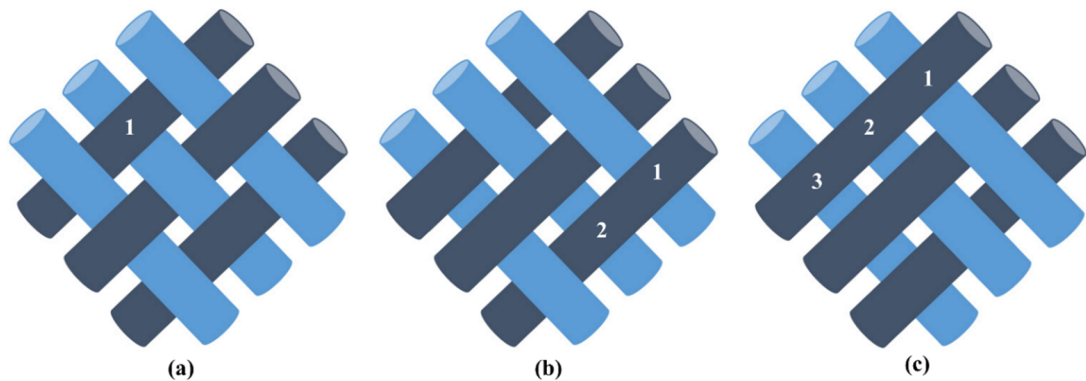


Figure 2.2 (a) Diamond braid, (b) Regular braid and (c) Hercules braid (Adapted from [61]). Note: 1, 2 and 3 indicate the number of tow intersections between two inter-layer cross-overs.

The tows in these different architectures undergo different numbers of intersections with tows having the opposite orientation before undergoing an inter-layer cross-over. The inter-tow friction at the cross-over points provides stability to the fabric and also

governs the drapability or conformability of the yarn over 3-D surfaces [62]. However, the cross-overs induce undulations in the tows, thus repeatedly offsetting them from a perfectly planar orientation.

The automated control of the entire process ensures rapid production rates with repeatable preform characteristics. By controlling the shape of the mandrel and size of the fibre tows, near-net shape preforms can be produced and directly carried to the next processing step without extensive trimming operations, thus reducing the waste generated in these intermediate steps [63]. However, in spite of the low-waste rapid preform production capability of the braiding process, industrial applications remain limited to high-end products. The principal barrier lies in the matrix injection and fibre impregnation stage, which is common across the majority of composite manufacturing processes. Therefore, in order to meet the industrial target volumes and become cost-competitive against metallic counterparts such as steel and aluminium, the rapid preform production achievable through braiding must be complemented with rapid matrix infiltration and curing methods.

## 2.2 Manufacturing of braided composites

Automotive and aerospace composites have been traditionally dominated by thermoset resins. Thermosets are characterised by cross-linking bonds that bind multiple polymer chains and impart strength and stiffness to the material. These cross-links are formed in an irreversible chemical reaction called curing. The curing is performed after wetting the reinforcement fibres with the thermoset precursors, which are generally in a liquid state at room temperature. However, achieving uniform cure in large scale components is a time consuming step and generally renders long part cycle times [64]. In addition, the irreversible nature of the curing process can lead to large quantities of waste during production and limits the recyclability and reusability of products. Owing to these limitations, there is substantial interest in thermoplastic matrices. Thermoplastics are readily available in the polymerised state as long-chain molecules and generally do not have cross-links. Therefore, they do not rely on a cure (polymerisation) reaction during processing. Unlike thermosets, they are melt-processable, i.e. they become a liquid upon heating beyond their melting point and can be reshaped. This process is repeatable

14

and hence provides ease of recycling and reuse [65] and opportunities for advanced joining [66–68]. Some of the general advantages and disadvantages of thermoplastics are listed in Table 2.1. The use of thermoplastic matrices has shown significant differences in mechanical behaviour compared to thermosets [69]. Moreover, previous studies provide conflicting results regarding the difference in effect of the presence of voids between thermoplastics and thermosets: some studies claim that both are equally affected [70], while others suggest that thermoplastics are more resilient to defects such as voids because of their greater ductility [71].

Table 2.1 Advantages and disadvantages of thermoplastic matrices.

| Advantages | Disadvantages |
|---|---|
| <ul><li>Rapid processing</li><li>Long shelf life</li><li>Toughness</li><li>Recyclability</li><li>Weldability</li><li>Environmental resistance</li></ul> | <ul><li>High viscosity</li><li>High processing temperature</li><li>Mechanical properties generally lower than thermosets</li></ul> |

Currently, the majority of the braided composites used in structural components in the automotive and aerospace industries are based on thermoset resins. Similarly, academic studies have primarily used thermosets in investigations of various characteristics of braided composites. Therefore, the availability of mechanical test data for braided thermoplastic composites is relatively low.

The emergence of high performance thermoplastic resins such as polyphenylene sulphide (PPS), polyether ether ketone (PEEK) and polyether ketone ketone (PEKK) has led to some noteworthy applications of thermoplastics in the aerospace industry [72–76]. In the automotive industry, thermoplastics have been traditionally used for semi-structural/non-structural applications with randomly oriented short fibre reinforcements [77]. However, legislations enforcing recyclability targets [5] have led to notable investments and research towards employing thermoplastics for structural applications [78–82]. Whilst semi-structural/non-structural applications are able to utilise short fibre manufacturing solutions, mechanical performance requirements of

structural parts necessitate the use of continuous fibre composites. Thus efforts have focussed towards achieving sub one-minute part cycle times for continuous fibre thermoplastic composite processes to meet the high volume automotive industry's part-per-minute cycle time standard [83].

A major barrier to the realisation of such targets is the high melt viscosity of thermoplastics, which hinders rapid infiltration and impregnation of fibre preforms. Therefore, the fibre impregnation and multi-layer consolidation are often conducted under high temperature and pressure in a discrete process to produce semi-finished pre-impregnated (prepreg) sheets. However, thermoplastic prepregs are often expensive, especially for high performance thermoplastics like PEEK [84,85], and could undergo deconsolidation during preheating, which leads to defects in the final component [86]. A suitable alternative is the use of hybrid fibre-thermoplastic matrix material systems. Hybrid systems are a blend of thermoplastic filaments with reinforcement fibres, which are available in several forms such as commingled, core-spun, co-knit, co-wrapped etc. [87]. Figure 2.3(a) depicts the various forms of hybrid systems. Such combinations of the thermoplastic polymer and reinforcement fibres result in short impregnation paths, i.e. flow distances of the molten thermoplastic required to achieve full fibre impregnation. This accelerates multi-layer consolidation and fibre wet-out stages, thus making hybrid fibre-thermoplastic systems directly processable without the need of a dedicated impregnation/consolidation operation [88,89]. Consequently, the manufacturing process is potentially faster and more economical as the time and equipment (plant/tooling requirement) required for the preconsolidation stage are eliminated. Among the available hybrid material systems, commingled tows are the most suitable option for braiding because of easy handleability [90,91]. Commingled tows also possess relatively superior drapability among other hybrid systems and can readily conform to different shapes [92]. Previous literature shows several instances of incorporation of commingled thermoplastic tows in a braiding process [93–96]. The consolidation of a commingled yarn during processing is shown in Figure 2.3(b). The fibre and matrix filaments are non-homogenously distributed in the cross-section [97]. Therefore, heating the tows above the thermoplastic melt temperature results in dry bundles of reinforcement fibres surrounded by the molten matrix. Externally applied

pressure leads to coalescence of the molten matrix around the fibre bundles. Finally, the pressure causes the matrix to infiltrate the agglomerated fibres and eventually bond with the fibres as the thermoplastic matrix solidifies with a reduction in temperature. The development of strong fibre-matrix interface is crucial for transferring the externally applied loads to reinforcing fibres [92,98]. To assist the fibre-matrix bonding, the surface of reinforcing fibres is often coated or sized with appropriate coupling agents [99].
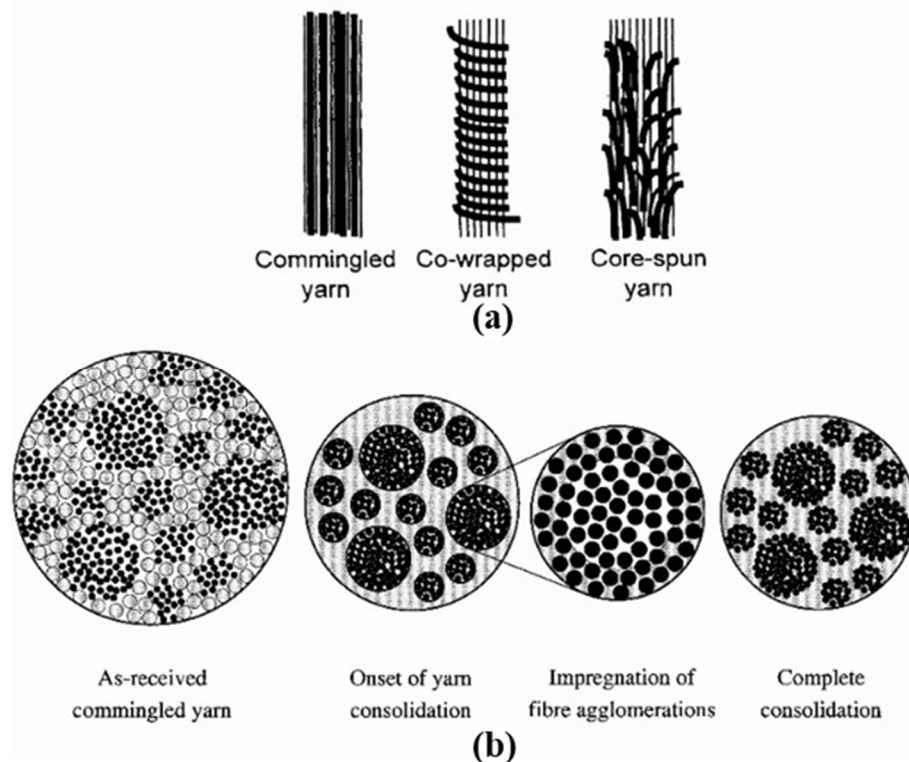


Figure 2.3 (a) Different types of hybrid thermoplastic systems (Taken from [87]) and (b) Steps during consolidation of a commingled system (Taken from [97]).

As discussed in Section 1.1, braiding inherently produces hollow fibre preforms, which are well-suited for the production of hollow composite parts. From the processing viewpoint, Bladder Inflation Moulding (BIM) has been found as a feasible route for hollow composite components [100]. A schematic of the BIM process is shown in Figure 2.4. It uses a two-part tool with a cavity in the shape of the required part. A bladder is inserted into the braided thermoplastic composite material to be moulded. This bladder-preform assembly is then placed into the cavity and the tool is closed. The tool is heated in an oven beyond the melting point of the thermoplastic with

17

simultaneous application of internal pressure through the bladder. The applied pressure supports the material in the required shape as well as presses the fibre layers closer, thus facilitating interlayer consolidation and fibre impregnation. The tool is then cooled below the melting point prior to demoulding.
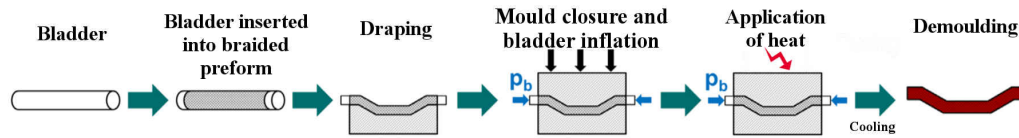


Figure 2.4 Steps involved in a conventional BIM process.

Being a simple and effective technique for consolidation of thermoplastic composites, BIM has found application in the fabrication of hollow lightweight parts in the sports industry [101,102]. The internally applied bladder pressure helps maintain tension in the fibres, which is essential to avoid fibre waviness and therefore achieve desired mechanical properties. This approach was investigated by Bernet *et al.* [103] for the production of braided bicycle handlebars using a commingled carbon fibre-polyamide 12 (PA12) material system. A consolidation time of one minute was claimed (dwell time above the melting point of PA12), although this does not include a likely extensive heating phase before bladder inflation. A hypothetical cost model was also presented in the same work, which showed the high volume potential of the manufacturing process. However, a suitable technique to achieve the fast heating and cooling rates, which is important for realising an acceptable cycle time, was not presented. In a similar piece of work by Bernet *et al.* [104], the mould was immersed in a large volume of water for rapid but uncontrolled cooling. However, this is impractical in a mass production environment where both cycle time and part consistency are critical. Therefore, there exists a need to develop manufacturing techniques that enable rapid processing of hollow braided preforms as well as precise process control. This would improve the suitability of thermoplastic braided composites for high volume manufacturing and support the exploitation of the advantageous mechanical properties of braided composites, which are discussed in the following section.

## 2.3  Mechanical properties of braided composites

Braided composites are known to have lower in-plane mechanical properties (strength

and modulus) as compared to unidirectional (UD) laminates. The out of plane undulations of the fibre tows observed in braided composites as well as fibre damage during the braiding process are responsible for the reported reduction [105]. These undulations are schematically depicted in the side view of a braided fabric shown in Figure 2.5. Moreover, the fibre crimping at interlacement points result in early initiation of damage in braided composites [106].



Figure 2.5 Side view of braided yarns in a diamond braid.

As an example, Figure 2.6(a) shows a comparison of in-plane tensile and shear moduli of braided composite against angle-ply laminates, while a comparison of the strains corresponding to damage onset is depicted in Figure 2.6(b). However, the planar properties can be improved by introducing axial tows during the braiding operation. This is termed as triaxial braiding.
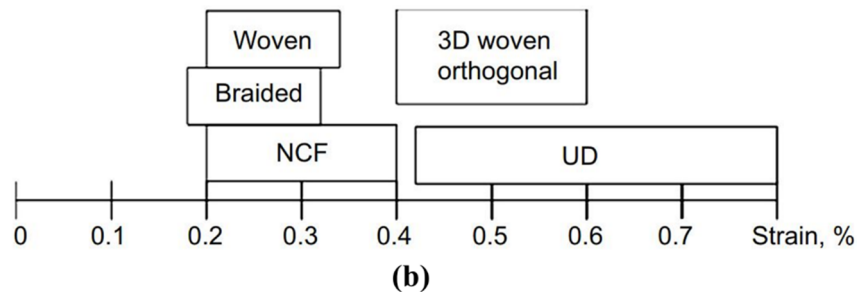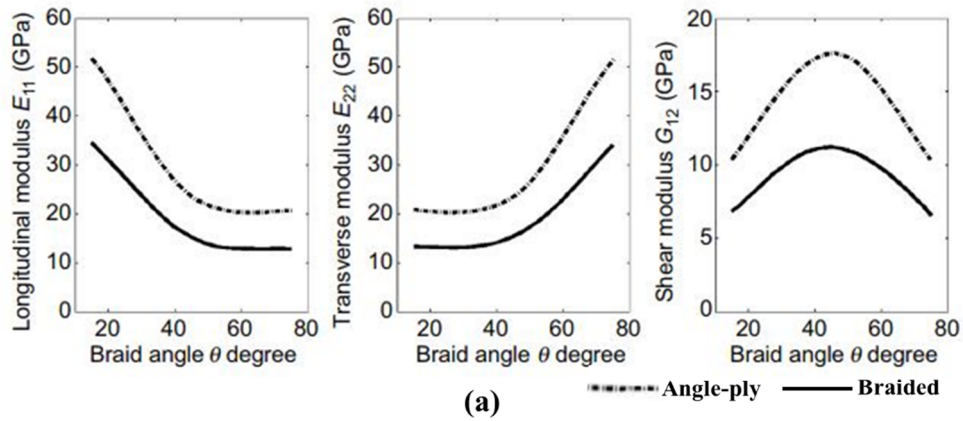


Figure 2.6 (a) Comparison of elastic moduli between braided and equivalent angle-ply laminates (Taken from [29]) and (b) Strain for onset of damage for different types of carbon fibre-epoxy composite materials (Adapted from [106]). Note: NCF is Non-Crimp Fabric, and UD is unidirectional.

19

Despite the inferior in-plane properties, the interlacement of fibres in braided composites acts as an inhibitor to the propagation of cracks, resulting in impact resistance and residual strength in the post-damage regime [30]. The observations of Sturm *et al.* [50], shown in Figure 2.7, are a good example of the enhanced damage resistance of braided composites at a structural level. As shown in the figure, the braided structures showed greater post-damage integrity as compared to the benchmark NCF (Non-Crimp Fabric) structure. This resulted in an improvement of approximately 18% in energy absorption for the braided structure. Also, the trans-layer pattern of braided tows provides greater delamination resistance. This is termed as "fibre bridging" [107] and increases the energy required for a delamination failure, which is easily induced upon low velocity impacts in unidirectional composites without any through-the-thickness reinforcements.
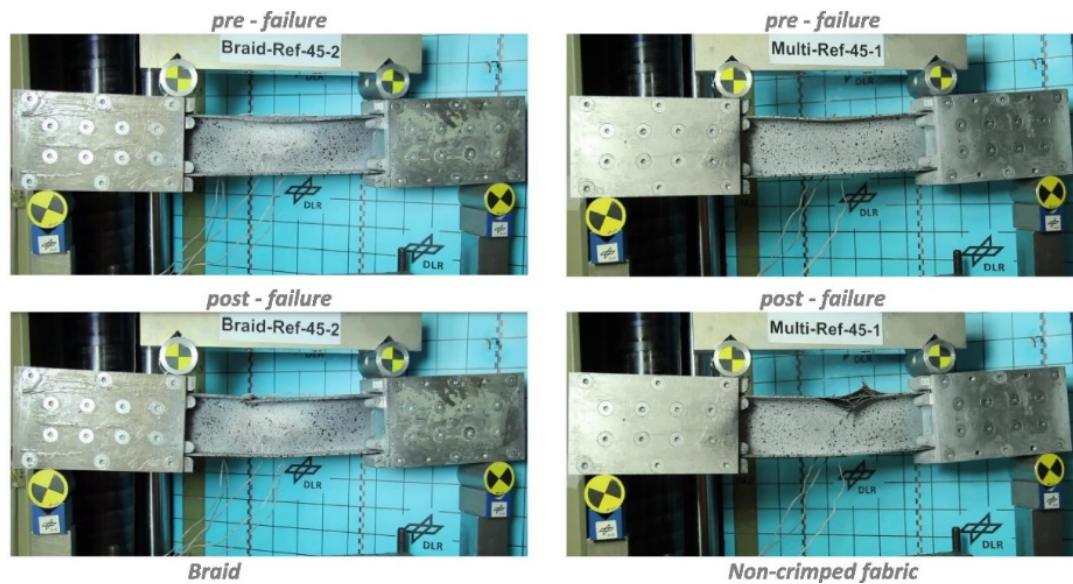


Figure 2.7 Comparison of damage during a four-point flexure experiment on braided (left) and NCF (right) composite beam structures (Taken from [50]).

Figure 2.8 shows the cross-section of a braided composite normal to the braid axis. A non-homogeneous material distribution is observable with resin-rich pockets between the fibre tows [93]. A similar microstructure is found for woven composites. Between woven and braided composites, the latter has been reported to possess relatively larger resin pockets [108]. Owing to the non-homogenous material distribution, the application of external loading results in non-uniform stress development that leads to complex damage mechanisms. These include matrix shear cracks and intra-tow

transverse cracks, which propagate along the fibre-matrix interface of braided tows as the load progresses. These are well documented in previous literature for biaxial as well as triaxial braided composites [108–115].
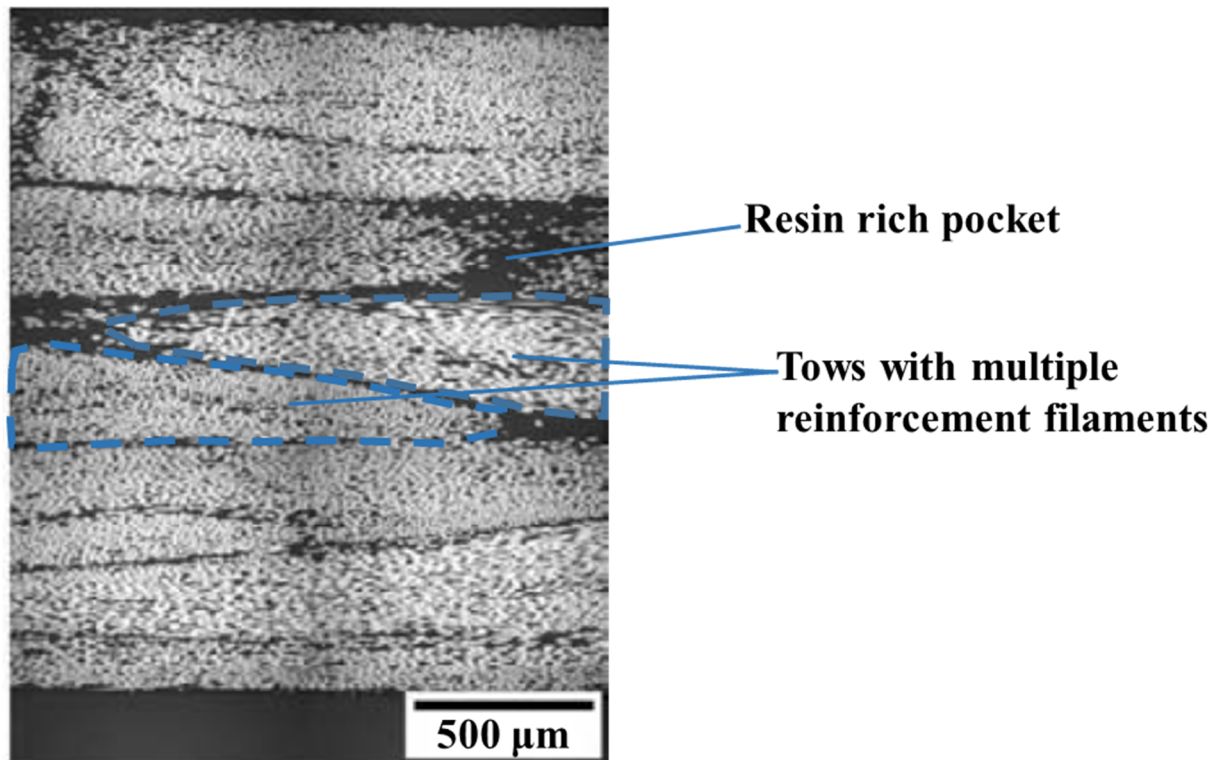


Figure 2.8 Microstructure of a multi-layer braided composite viewed normal to the braiding axis (Adapted from [93]).

A noteworthy phenomenon observed in braided composites when loaded in tension is 'tow scissoring'. It occurs following local fibre tow-matrix debonding and involves the rotation of fibre tows in the damaged region about the interlacement points. This fibre reorientation towards the loading direction occurs until a state of jamming or interlocking is attained by the fibres. Beyond this, no further rotation is possible and fibre failure occurs. Scissoring is schematically depicted in Figure 2.9.
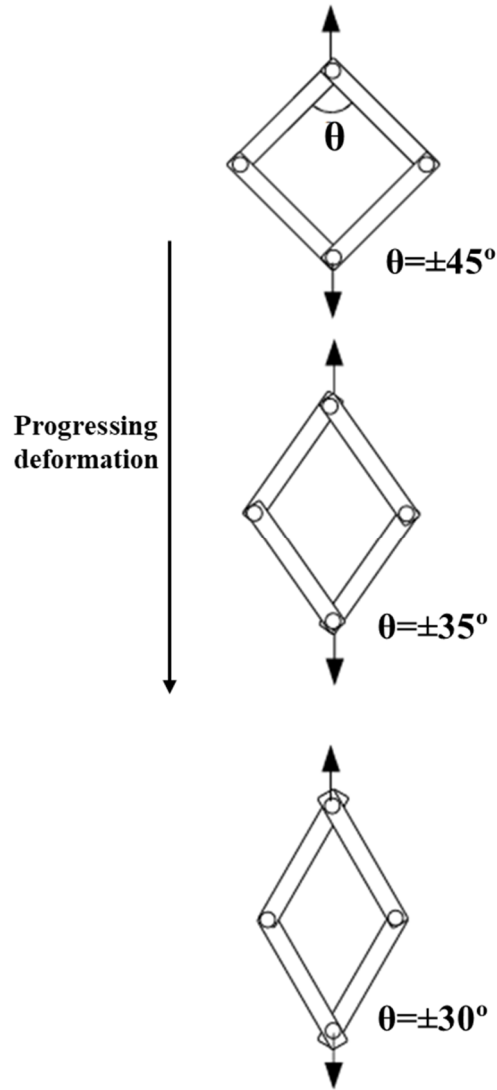
Figure 2.9 Scissoring mechanism of braided fibres. Note: θ represents the varying braid angle as the deformation advances (Adapted from [108]).

Particularly for biaxial braids, the scissoring was reported to delay the ultimate failure of the braided structures and sustain the externally applied load up to higher deformation levels. Extensive necking was reported before failure for tubular as well as flattened braided composite coupons under tensile loads, as shown in Figure 2.10. In triaxial braids, the tensile response is however dominated by the axial fibres [112]. Therefore, the reorientation of off-axis braided fibres is less pronounced as compared to biaxial braids.
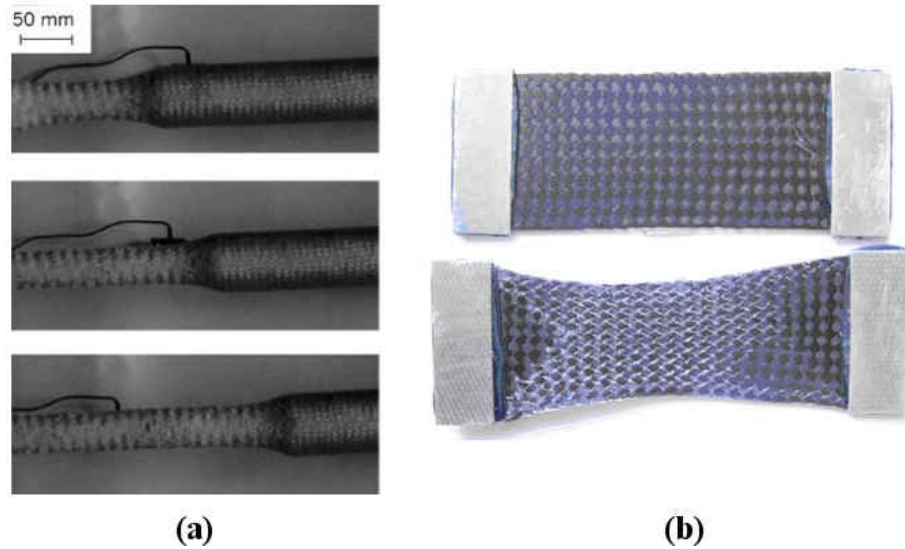
Figure 2.10 (a) Progressive necking resulting from scissoring of tubular braided composite (Taken from [111]) and (b) Flattened rectangular braided composite showing extensive necking after testing (Taken from [108]).

The properties and the physical phenomena during mechanical testing of braided composites discussed above show a significant dependence on braid angle. This is important from a design perspective as the braid angle can be directly controlled during the braiding process, thus dictating the resulting structural properties. The following section discusses these correlations.

## 2.4 Effect of braid angle on physical properties

The braid angle is defined as the angle between braided fibre tows and the axis of the braiding mandrel (longitudinal axis) as depicted in Figure 2.11.
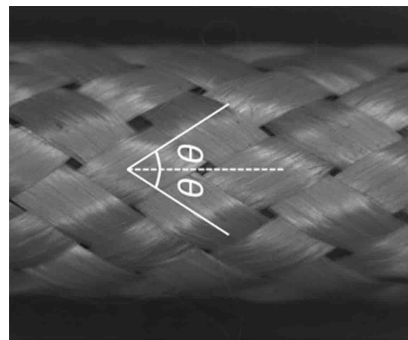


Figure 2.11 Braided fibres aligned at an angle ($\theta$) to the longitudinal axis (Taken from [29]).

The braid angle can be controlled and varied during the braiding of a preform and it is related to the braiding parameters through Equation 2.1. In this equation, $\alpha$ is braid

angle (degree), $\omega_h$ is horn gear angular velocity (rotations per minute), $N_h$ is number of horn gears, R is radius of mandrel (mm) and $v_m$ is mandrel pull-off velocity (mm/s). The relation shown in Equation 2.1 pertains to braiding onto circular mandrels. Equations for different cross-sections were developed by Du *et al.* [116].

$$\alpha = \tan^{-1}\left(\frac{2\omega_h R}{N_h v_m}\right) \hspace{2cm} \text{Equation (2.1)}$$

The braid angle has been reported to have a significant effect on the properties of braided composites. Figure 2.12 shows the variation in longitudinal modulus, transverse modulus and shear modulus with braid angle, as reported by Melenka *et al.* [117]. It is noteworthy that the results shown in the figure indicate a higher shear modulus for diamond braid compared to a regular braid. This contradicts the inverse correlation between mechanical properties and fibre crimp discussed in Section 2.3. However, the properties shown in the figure were evaluated using an analytical model with a simplified description of fibre crimp. Moreover, these properties were not experimentally verified. The expected trend of shear modulus with respect to braid pattern was confirmed through the experimental results reported by Chai *et al.* [118] who tested both diamond and regular braided beams under torsion. As anticipated, the regular braid showed greater shear modulus compared to the diamond braid.
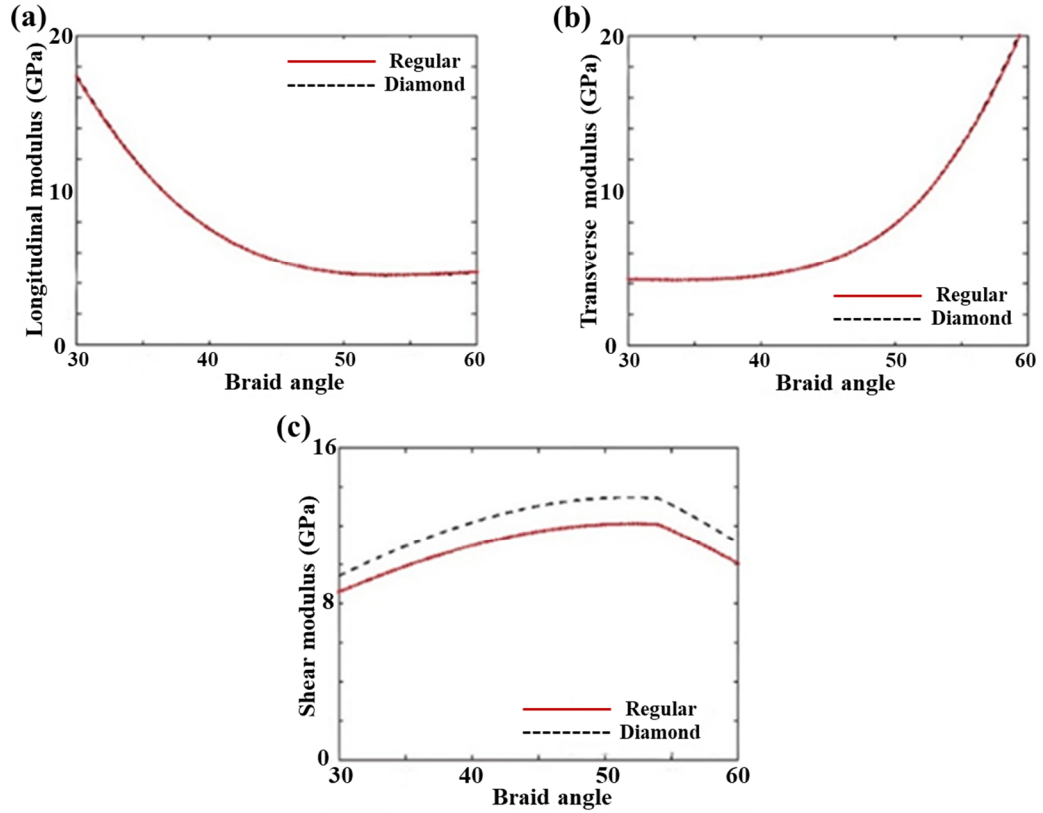
Figure 2.12 Effect of braid angle on (a) Longitudinal modulus, (b) Transverse modulus and (c) Shear modulus (Adapted from [117]).

Damage progression during tensile loading was also reported to depend on the braid angle. Harte *et al.* [111] observed a drastic change in damage behaviour while testing small scale biaxial braided tubes under tension. This is evident in the stress-strain curves shown in Figure 2.13. A near-linear response was observed for the specimen with a braid angle of 23° before a brittle failure occurred. On the other hand, the 55° specimens demonstrated a ductile or elastic-plastic response up to a much higher strain level. This was accompanied by extensive scissoring and visible necking during deformation. Conversely, the stress-strain curves corresponding to triaxial braids reported by Wehrkamp-Richter *et al.* [112] showed an approximately linear response for 30° and 45° braid angles, while the 60° curve showed a drastic change in slope upon reaching a critical strain value. Studies investigating the quasi-static compression of braided tubes with different braid angles for energy absorption applications also reported a significant dependence of the damage modes on braid angle [119–121].
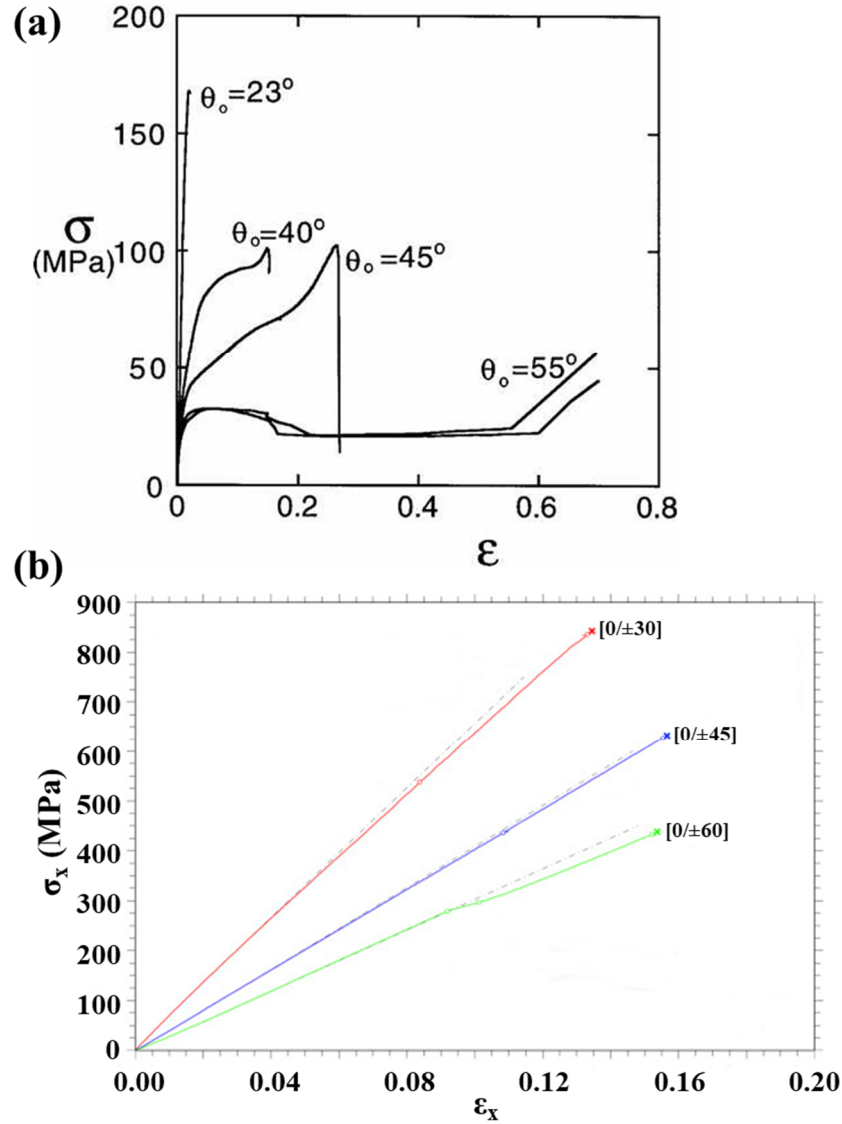
Figure 2.13 Stress-strain curve for (a) biaxial (Taken from [111]) and (b) triaxial (Adapted from [112]) braided specimens with different braid angles.

Apart from the mechanical properties, the braid angle also affects the geometry of the braided tows. With increasing braid angle, the thickness of braided tows increases, which translates into a thickness increase of the braided composite structure [93,122–124]. This is represented schematically in Figure 2.14. The thickness of multi-layered braided composites exhibits another interesting phenomenon. Theoretically, a multi-layered composite's thickness should be the sum of the individual thickness values of the stacked layers. However, in a braided structure, the tows travel across layers and occupy the spaces between the tows of the braided layer underneath. This is termed as nesting and is responsible for a relative reduction in the thickness of the overall

26

composite. It was reported that nesting is almost negligible at small braid angles, but becomes more prominent as the braid angle increases [124].
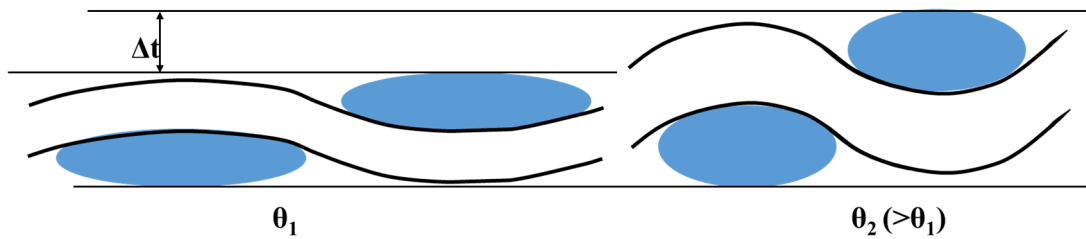


Figure 2.14 Schematic representing an increase in tow thickness with braid angle.

These observations indicate that braid angle not only affects the material properties but also the geometry of a braided composite. Importantly, both of these entities govern the mechanical response of a structural component. Therefore, in order to systematically understand the effect of braid angle on structural performance, mechanical testing should be expanded to component-scale specimens, where the effect of all the properties dependent on braid angle can be studied.

## 2.5 Assessment of mechanical performance: three-point flexural behaviour

Flexure tests are often used to assess the mechanical performance of structures. This could be attributed to the simplicity of specimen preparation and the testing procedures. Unlike fundamental characterisation tests such as pure tension or compression, flexure tests suffer less from issues linked to gripping of the specimen, end tabs, lateral support etc. [125]. Moreover, coupon level tensile or compressive tests induce idealised stress states, which are not representative of structural load cases. On the other hand, flexure tests introduce a complex stress state in the specimen that is a combination of tension, compression and shear. A simplified schematic of a beam undergoing pure flexure is shown in Figure 2.15. As shown in the figure, the beam experiences compression in the region above the neutral axis, while the region below is under tension.
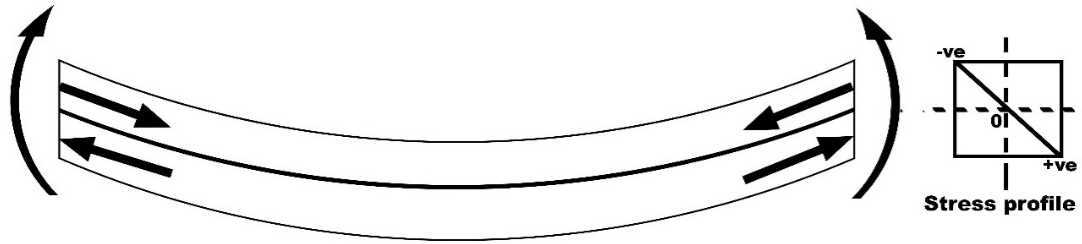
Figure 2.15 Stress profile developed during flexure.

Three-point and four-point flexural loading scenarios are schematically depicted in Figure 2.16. As evident from the shear force diagrams, a four-point flexure test induces pure flexure in a specimen. In contrast, a linear non-uniform shear stress profile is observed in addition to flexural stress in a three-point flexure test. The effect of the induced shear stress can be minimised by testing specimens of appropriate span to depth ratio [126]. Nevertheless, three-point flexure is considered to be more relevant for structural applications as it is comparable to real-life load cases, for instance, side impact on an automotive structure [77]. Indeed, several studies have used three-point flexure for assessing automotive side impact beam performance [127–131].
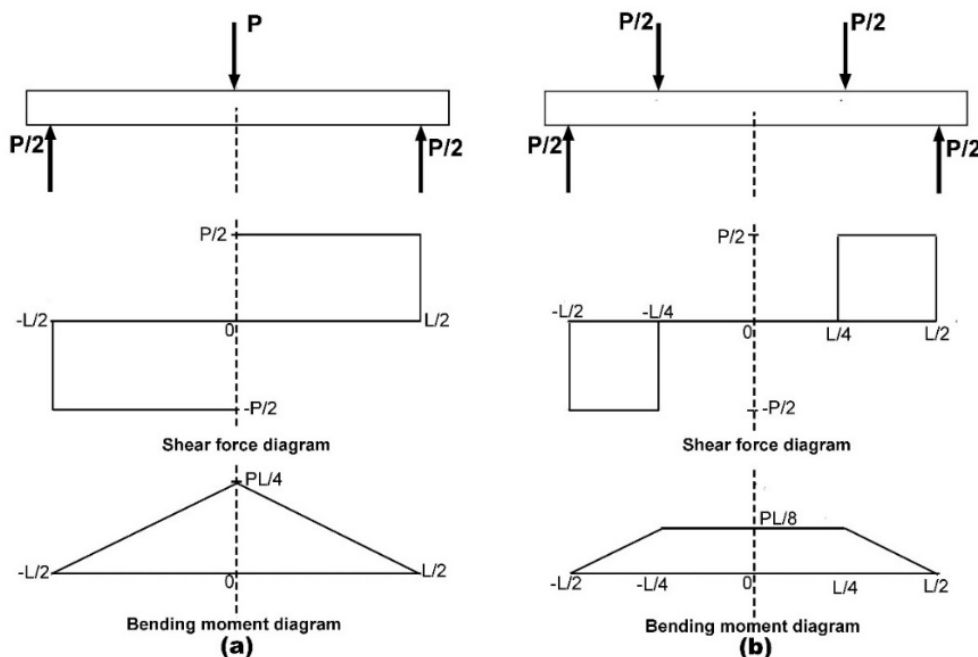


Figure 2.16 Schematics of (a) three-point and (b) four-point flexure tests with the corresponding shear force and bending moment diagrams.

Moreover, the point load at the centre of the specimen in a three-point flexure test also tends to induce localised damage underneath the loading roller. Therefore, two evident

deformation mechanisms are observed, i.e. global beam flexure and localised crush. These are depicted in Figure 2.17.



Figure 2.17 (a) Flexure and (b) localised crush during three-point flexure.
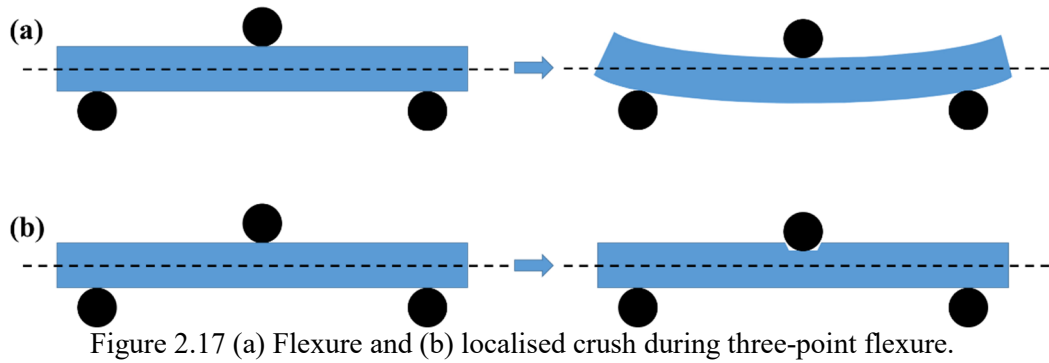
Thus, a suitably designed three-point flexure test can be used to assess a structure's resistance to both these deformation mechanisms. The localised crush in the loaded region manifests in different forms depending on the material and geometry of the specimens [132–136]. Localised crushing becomes more important in hollow beam structures as the load is concentrated in small regions that bear the impact, as shown in Figure 2.18. Previous studies reported metallic beams to develop "hinges" about which the entire structure bends at constant load [137,138]. On the other hand, composites were reported to develop cracks that grow with load progression and ultimately lead to a loss of stiffness and cause failure [139,140].



(a)                                                    (b)
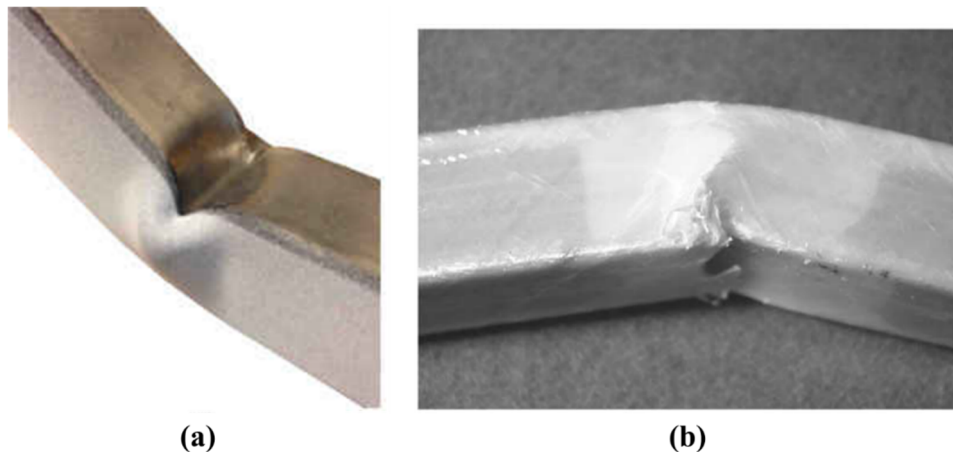
Figure 2.18 Localised deformation for (a) metallic and (b) composite hollow beams during three-point flexure (Taken from [140]).

Based on Euler-Bernoulli theory, the flexural stiffness of a specimen can be related to its properties through Equation 2.2. In this equation, P is the applied load (N), δ is the

deflection at load point (mm), I is the moment of area ($mm^4$), E is Young's modulus of the material (GPa) and $L_s$ is the span length of the beam specimen (mm).

$$\frac{P}{\delta} = \frac{48EI}{L_s^3}$$
<div align="right">Equation (2.2)</div>

This simplified relation, which neglects localised deformation, shows that the global flexural stiffness is a combination of the material's Young's modulus as well as the geometry dependent section modulus.

On the other hand, the localised deformation was reported in several investigations to depend on the specimen thickness for metallic [141–143] as well as composite beam specimens [144]. Additionally, in hollow beams subjected to three-point flexure, the area under the impactor develops biaxial stress states. Therefore, material properties in the transverse direction also play a role, particularly for composites because of their anisotropic material behaviour.

Previously reported three-point flexure tests of hollow composite beams showed that the dominant deformation mode between global flexure and localised crush depends on the characteristics of the material and geometry of the structure. For instance, owing to their higher resistance to localised crush, thicker beams were observed to undergo relatively greater global flexure [141,143,144]. This is depicted through the results of Liu *et al.* [144] for composite beams, shown in Figure 2.19. As evident from the figure, beams with three layers remained intact after the test, while the beams with nine layers underwent complete breakage into two separate parts. This was due to the localised failure of the top wall being delayed in the 9-layer beam as compared to the 3-layer beam. Consequently, global flexure dominated in the 9-layer beam and resulted in the development of tensile stresses in the bottom wall. As the deformation progressed, the tensile strength limit was reached in the bottom wall and rupture was observed. In contrast, the severe localised crush in the top wall of the 3-layer beam led to negligible straining of the bottom wall and the damage remained limited to the top wall.
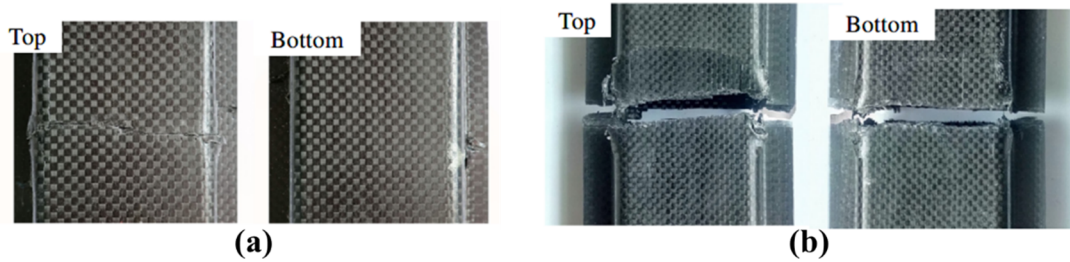
Figure 2.19 Top and bottom views of composite beams with (a) three layers and (b) nine layers after flexure experiments (Adapted from [144]).

As mechanical behaviour of the material as well as geometry are both directly related with braid angle, it is intuitive to expect braid angle to correlate with localised crushing during three-point flexure, however, such a correlation has not been reported in the past. Studies on three-point flexure test response of braided rectangular coupons showed a decrease in flexural modulus and strength with increasing braid angle [93,145,146]. Moreover, increasing the braid angle was observed to delay the failure. Potluri *et al.* [124] conducted three-point flexure tests of tubular braided composites and reported similar trends of flexural modulus and strength as observed for rectangular coupons in previous studies. These coupon-level studies showed a strong correlation between the flexural performance and braid angle. However, none of these studies reported localised deformation during three-point flexure. This was likely due to the flat geometry or the small scale of the tubular braided coupons used in the tests. On the other hand, Sturm *et al.* [50] performed four-point flexure tests on open section braided beams. The beams with greater braid angles showed postponed web buckling as compared with specimens having smaller braid angles. This was attributed to greater transverse stiffness and thickness. As a result, the specific energy absorption was greater in beams with greater braid angles. Although the results were from a four-point test configuration, they were representative of the potential effect of braid angle on the deformation mode under flexural loading. In a recently published study [147], severe localised crushing was reported during three-point flexure tests. However, the size of the loading roller and span to diameter ratio of the tested specimens were both inclined to induce localised crush over global flexure irrespective of braid angle. Moreover, the fibre volume fractions of the specimens were below 35%, which is not typical of structural composites. Thus, there is a shortage of available literature investigating the potential correlations between braid angle and multiple deformation modes in three-point

31

flexure. Establishing the influence of braid angle on deformation at a structural level would enable further optimisation of braided composite beam structures through efficient manufacturing strategies including braid angle variations.

## 2.6 Tailoring and hybridisation of beams

The dependence of localised deformation on material and geometry has encouraged studies on beams with so-called *tailored* configurations i.e. beams with variable properties. Duan *et al.* [142] tested top-hat shaped metallic structures with greater thickness in the loading zone that were produced via a tailor-rolling process. Similarly, Sun *et al.* [143] used functionally graded metallic beams under flexure. Both of these approaches were reported to achieve significant weight saving without compromising mechanical performance. In addition to tailored metallic beams, the flexure behaviour of metal-composite hybrid beams has also been investigated. Kim *et al.* [148] described the flexure performance of aluminium-composite hybrid beams. The mechanical performance showed significant dependence on the ply orientation of the laminate. The UD 0° laminate could bear a lower load as compared to the UD 90° laminate because of lower reinforcement in the transverse direction. Keating [149] tested dual-phase (DP) steel beams that were locally reinforced with glass-polyamide patches in three-point flexure. The additional stiffness provided by the local composite reinforcement allowed for downgauging of the steel without compromising the mechanical performance. This resulted in a 30% reduction in the mass compared to virgin DP steel beams. Similarly, Sun *et al.* [150] showed that an improvement in the three-point flexure performance was achievable through the use of local CFRP patches on circular Aluminium beams.

The braiding process inherently allows controlling of braid angle during the production of beam structures [151]. This capability of the braiding process has been utilised in the past to produce structures with variable braid angle. Carey *et al.* [51] varied the braid angle for achieving variable stiffness along the length of composite catheter shafts with different combinations of fibres and matrices. Similarly, variable stiffness was achieved by Fujihara *et al.* [55] in dental posts by braiding the fibres with a graded variation in braid angle. Boss *et al.* [52] fabricated braided rods with a gradual braid angle variation. A hybrid of Kevlar and carbon fibres in an epoxy resin system was utilised with the

target application of dental posts. The flexural and tensile moduli of these variable braid angle specimens were found to be an average of the properties corresponding to specimens with uniform braid angles. On the other hand, the tensile strength depended on the braid angle that had the lowest strength. Ganesh *et al.* [152] used braided preforms with graded braiding angles in single-bond lap joints. Braid angle was varied to gradually reduce the longitudinal modulus from the loaded end to the joint overlap region. The results showed a more uniform stress distribution in the overlap area as compared to joints without a modulus variation. Stanier *et al.* [53,153] performed open-hole tensile tests on specimens with a controlled braid angle variation and reported an improvement in strength compared to specimens with a constant braid angle. Similar improvement in tensile strength of braided tubes with graded braid angle profiles was reported by Huang *et al.* [54].

The abovementioned studies showed that braid angle variations are achievable and can result in improved performance. However, the available studies are limited to uniaxial loads. In order to establish the viability of braided composites with variable braid angle, it is important to analyse their performance in structural load cases. As discussed previously, three-point flexure is a simple and effective loading scenario for general assessment of structural performance. The localised loading in three-point flexure subjects the test specimen to variable stress states, thus making it ideal for testing of beam structures where trade-offs between different characteristics that depend on braid angle can be studied. Moreover, the weight of braided structures is also directly related to the braid angle [50,147]. Thus, lightweighting is identified as a potential benefit of utilising braid angle variations. The three-point flexural response of braided beams with a braid angle variation has not been reported before and will be the major focus of this thesis. Within this thesis, the length-wise variation of braid angle will be referred to as *tailor-braidi*ng.

## 2.7   Summary and gaps in literature

The sections covered in this chapter span across multiple topics. Each section provides fundamental knowledge as well as the current status of relevant research. There are specific gaps in literature that have been identified as listed below:

- There exists a shortage of studies investigating the properties of braided thermoplastic composites. Among thermoplastic material systems, the use of commingled thermoplastic tows was identified as a potential method for high volume manufacturing of braided thermoplastic composite parts. However, the current state-of-the-art lacks the required high volume readiness in terms of part cycle time as well as process control.

- The few published studies on three-point flexure behaviour of braided composite beams show a significant dependence on braid angle. In all these investigations, the specimen geometry and test parameters produced only one deformation mode between global flexure and localised crushing for all braid angles. Therefore, the studies did not explore the potential correlations between braid angle and multiple deformation modes, which occur during three-point flexure and dictate the subsequent structural performance.

- Braided composite parts with a braid angle variation were shown to result in enhanced mechanical performance in previous studies. However, these studies were limited to idealised uniform loads that did not subject the specimens to structural load cases. Moreover, the studies did not exploit the dependence of mass on braid angle, i.e. lightweighting potential of varying braid angle was not investigated. Several properties that dictate the mechanical performance in three-point flexure depend on braid angle for braided composites. Therefore, three-point flexure test is ideal for the structural assessment of braided structures with a braid angle variation. To the best of author's knowledge, there does not exist any open literature addressing this prospect.

## 2.8   Research objectives

Based on the identified gaps in literature, it is proposed that there is exciting potential to investigate a tailor-braiding approach to produce beams with inherently improved structural efficiency i.e. improved mass-specific performance. The use of thermoplastic matrix materials offers added benefits in terms of recycling and reuse. If a viable volume-ready manufacturing solution could be developed, efficient tailor-braided structures could provide lightweighting benefits within important manufacturing sectors, such as the automotive industry. Thus this thesis reports an investigation of the

performance of tailor-braided beams with a length-wise (axial) braid angle variation in three-point flexure.

The objectives of this thesis are:

- To develop a manufacturing method with precise process control for the production of thermoplastic braided beams with consistent part quality.
- To evaluate the effect of braid angle on deformation modes in three-point flexure tests of component-scale braided beams having uniform braid angles.
- To evaluate the lightweighting and mechanical performance benefits of the proposed *tailor-braiding* concept using three-point flexure tests.

The research is pictorially summarised in Figure 2.20.
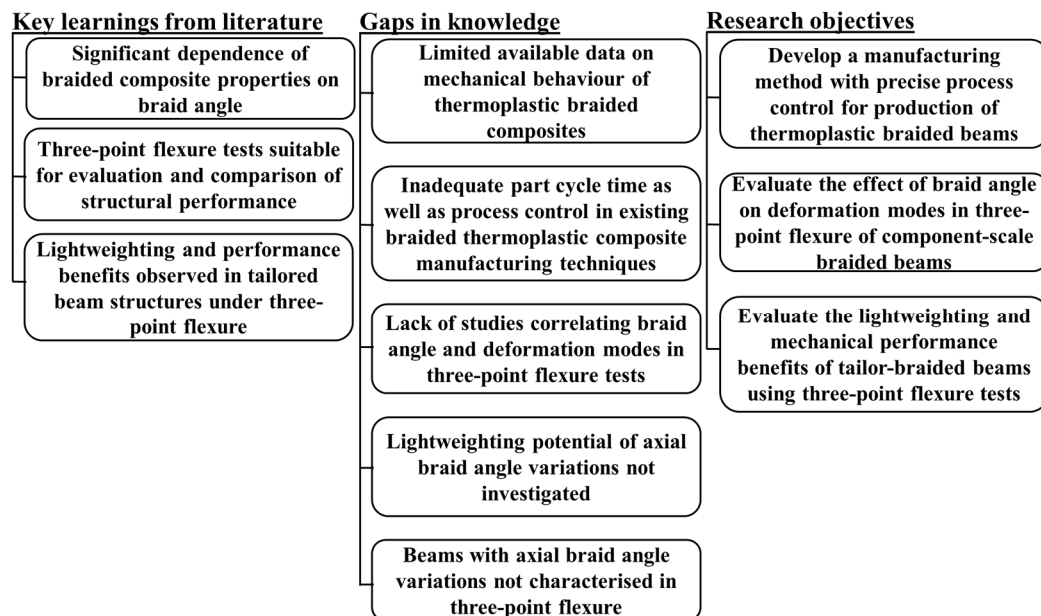


Figure 2.20 Conception of the research work presented in the thesis.

## 2.9 Structure of thesis

Chapter 1 provided a broad scope of the thesis and established the context through brief descriptions of the multiple topics that justify the undertaken work.

Chapter 2 presented a review of the scientific literature corresponding to manufacturing, material behaviour and testing of braided composites, which underlined

the specific research objectives of this thesis.

Chapter 3 will describe the materials and methodologies used in the research work. This will include characteristics of the commingled tows as well as the details of the braiding process. The chapter will also discuss the techniques used for evaluating the quality of braided composite beams as well as details of the test setup utilised for three-point flexure tests with justifications and error metrics as and when required.

Chapter 4 describes the development of a novel manufacturing process for consistent production of hollow thermoplastic braided composite beams, which is an essential precursory step to performing the planned mechanical assessment of the proposed tailor-braided beam structures. An existing bladder moulding process was also developed to serve as a benchmark for assessment of the new process. Following the initial development, the chapter also describes a set of iterative modifications introduced to improve the process and subsequently manufacture braided beams for the three-point flexural test program.

Chapter 5 presents the three-point flexure test results of braided composites beams with three different braid angles. The results include analyses of load-displacement evolution, deformation modes as well as surface strains obtained using digital image correlation. The results establish the correlation between braid angle and three-point flexural performance of the hollow braided beams tested in this work and will serve as a benchmark for assessing the performance of tailor-braided beams.

Chapter 6 describes the development of a tailor-braiding strategy for manufacturing of braided composite beams with axial as well as radial braid angle variation based on the results of Chapter 5. This is followed by descriptions of tailor-braiding, quality evaluation and three-point flexural testing of the tailor-braided beams. The chapter concludes with a comparison of the mechanical performance of the tailor-braided beams against the benchmark established in Chapter 5 and highlights the effect of tailor-braiding, thus addressing the research question of the thesis.

Chapter 7 summarises the results obtained in Chapters 4-6 and lists the limitations of

the conducted research as well as recommendations for future research work on this topic. The chapter also discusses the wider implications of the work with examples from the industry where the concept of tailor-braiding can be applied effectively.

# 3 Experimental materials and methods

This chapter presents the materials and the experimental methodologies employed in this work. Firstly, the commingled material system utilised for manufacturing braided beams is introduced and its characteristics are explained. This is followed by a detailed description of the braiding process used to produce braided preforms from commingled tows. Furthermore, the techniques employed to evaluate the quality of the manufactured braided beams are detailed. Finally, the equipment and methods utilised for mechanical testing of the braided beams with the use of contact as well as non-contact deformation measurement techniques are presented. The novel beam manufacturing process that was developed in this work is presented in Chapter 4.

## 3.1    Commingled thermoplastic material

A commingled E-glass/polyamide 6 (PA6) yarn from Coats Performance Materials plc. [154] was used for braiding. PA6 was selected because of its favourable characteristics for high volume applications in the automotive industry [77]. The PA6 was in a natural condition i.e. uncoloured. The linear mass of the commingled material is 1650 Tex (g/km) with a fibre mass fraction of 73%. This theoretically corresponds to a fibre volume fraction of 54%. A Mettler Toledo DSC 1 was used to perform Differential Scanning Calorimetry (DSC) to record the thermal transitions in PA6 in a temperature range between 25 °C and 250 °C. A steady rate of 10 °C/min was used during heat-up and cool-down. Figure 3.1 shows the obtained DSC curves. For clarity, only the temperature range between 120 °C and 250 °C is shown. As evident from the figure, the melting and recrystallisation peaks were obtained at approximately 221 °C and 185 °C respectively. The obtained temperature data corresponding to the melting and recrystallisation will be used for developing an optimal thermal process profile to be implemented during the moulding of the braided beams. This is explained in detail in Chapter 4. The glass transition temperature of the material is 60 °C as per the manufacturer's specifications [155].
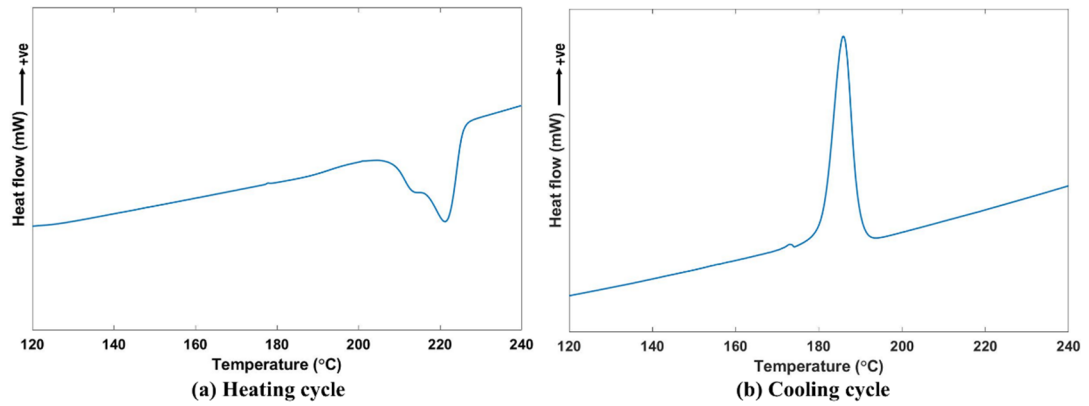
Figure 3.1 DSC curve showing (a) melting peak and (b) recrystallisation peak of PA6 from the commingled material. Note: Positive y-axis represents heat flow out of the DSC crucible.

## 3.2 Braiding

The commingled tows were braided using a 64-carrier braiding machine at Composite Braiding Limited, Derby, UK. Figure 3.2 shows the braiding setup.
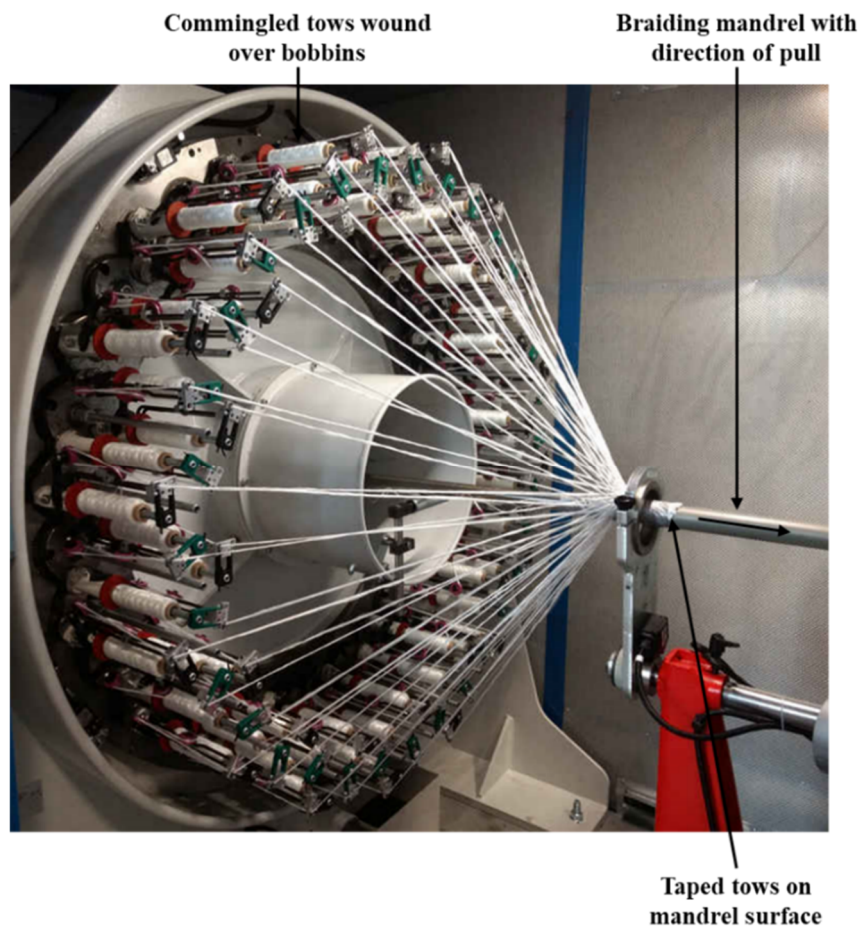


Figure 3.2 Braiding of commingled tows using 64-carrier braider.

39

The architecture of the braided yarn depends on the number of carriers used in the braiding process. Using all 64 carriers results in a 2×2 regular braid, while half capacity, i.e. 32 carriers, produces a 1×1 diamond braid. Flattened pieces of these two yarn architectures are shown in Figure 3.3.
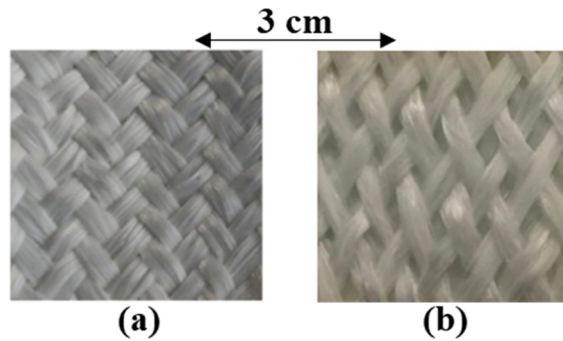


Figure 3.3 (a) 2×2 regular and (b) 1×1 diamond braided preform after flattening.

Diamond braids with braid angles of 30°, 45° and 60° were selected for the mechanical test program. Ideally, a 2×2 regular braid pattern is preferred for structural applications because of reduced crimp. However, for the material system used in this work, using a 2×2 regular braid pattern resulted in a lack of control over the braid angle, and hence a 1×1 diamond braid was selected. This is discussed in detail in Chapter 4. For each braid angle, three layers of the commingled tows were overbraided in the same direction of travel, by resetting the mandrel position between the braiding of adjacent layers.

During the braiding process, braiding pitch was used as the input variable to the braiding machine. It is defined as the axial length of a braided fabric required for a particular braided tow to return to its initial radial position. Figure 3.4 schematically depicts the braiding pitch (p).
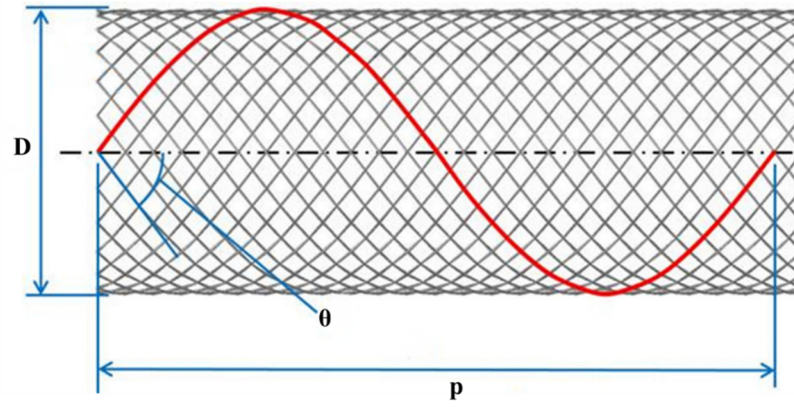
Figure 3.4 Schematic representation of braiding pitch (Taken from [156]).

For a given mandrel diameter, the pitch is related with the braid angle as per Equation 3.1. In this equation, $\alpha$ is the braid angle, $D_m$ is mandrel outer diameter (mm) and p is braiding pitch (mm). Increasing the pitch results in a reduction in braid angle.

$$\alpha = \tan^{-1}\left(\frac{\pi D_m}{p}\right)$$  Equation (3.1)

In Chapter 2, bladder moulding was identified and selected for manufacturing the braided beams. During the bladder moulding process, bladder inflation causes the braid to expand and hence changes the braid angle, as shown in Figure 3.5. The expansion also causes a length-wise contraction of the braid.
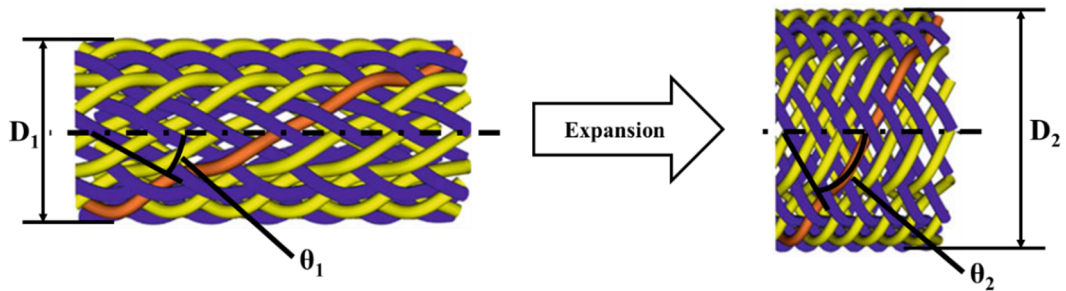


Figure 3.5 Change in braid angle upon expansion of a braid (Adapted from [157]).

For a particular braid, the braid angles at different diameters are related as per Equation 3.2. In this equation, $D_1$ is initial diameter (mm), $\theta_1$ is initial braid angle, $D_2$ is final diameter (mm) and $\theta_2$ is final braid angle.

$$\frac{D_1}{\sin \theta_1} = \frac{D_2}{\sin \theta_2}$$  Equation (3.2)

41

Therefore, for known values of the target braid angle, the outer diameter of the mandrel and the final part diameter, the braiding pitch was estimated for each layer by Composite Braiding Limited. Table 3.1 depicts the braiding parameters used for each layer for the three different braid angles.

Table 3.1 Braiding parameters for different layers.

|  | 30° | 45° | 60° |
|---|---|---|---|
| **Layer1 pitch (mm)** | 192.3 | 121.2 | 75.5 |
| **Layer2 pitch (mm)** | 193.8 | 120.9 | 74.2 |
| **Layer3 pitch (mm)** | 195.7 | 120.9 | 70.9 |

After braiding three layers over the length of the mandrel, the mandrel was carefully removed from the braiding machine. In order to maintain tension in the braided tows, masking tape was applied to constrain the ends of the braided fabric on the mandrel. Figure 3.6 shows an overbraided mandrel before extraction from the rear end of the braiding machine.
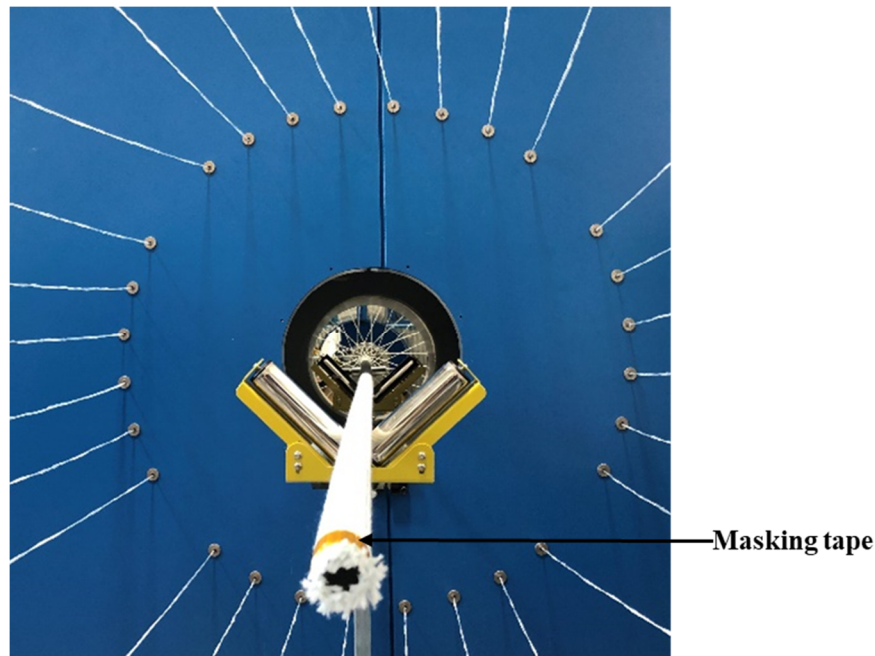


Figure 3.6 Overbraided mandrel with masking tape before extraction from the braiding machine.

The overbraided mandrels were wrapped in cushioned plastic wrap during transport and storage to prevent contamination and damage. For moulding of braided beams, the

braided material was cut and then carefully removed from the mandrel to obtain a preform of the required length. At least five preforms could be extracted from the braided fabric on a single mandrel. Figure 3.7 shows an extracted preform before the moulding process. The moulding process is discussed in detail in Chapter 4.



Figure 3.7 Preform of specific length after removal from mandrel.

## 3.3 Comparison of braided beams using destructive evaluation

Following the bladder moulding of the braided beams, the physical characteristics of the manufactured braided beams were analysed and compared by performing sectioning on one beam of each braid angle. The focus was on features such as thickness and fibre content, which were previously reported to show a dependence on braid angle and also affect mechanical performance. Moreover, voidage resulting from variability in the material as well as the manufacturing process is known to affect the mechanical properties of composite specimens [158]. Therefore, a qualitative and quantitative comparison of voidage was conducted.

The fractional composition of the beams was determined using resin burn-off tests and the specimens were analysed under an optical microscope to measure the thickness of the beams. The methodologies and equipment used for these two evaluation techniques are discussed in this section.

### 3.3.1 Evaluation of beam composition: Resin burn-off

Resin burn-off tests were conducted to determine the fibre volume fractions ($F_{vf}$) and void volume fractions ($V_{vf}$) of the braided beams. Six 20 mm long semi-circular specimens were cut from the manufactured braided beams. All the extracted specimens had a mass of > 500 mg. Prior to resin burn off, the specimens were weighed in two different media, i.e. air and distilled water to determine their densities using the Archimedes principle. The procedure recommended as per BS EN ISO 1183-1 [159] was followed. A Mettler Toledo New Classic ME105DU balance with the MS-DNY-

54 density apparatus was used for performing density measurements. The balance had a precision of 0.01 mg. While weighing the specimens in distilled water, the surface porosity of the specimens could lead to fluid absorption. This would cause a density overestimation and falsify the results. Therefore, the lowest reading on the balance was noted after the measurement stabilised. The temperature of distilled water was measured using a thermometer clipped onto the beaker and the density of distilled water at the noted temperature was used.

The densities were evaluated from the measured masses as per Equation 3.3. In this equation, $\rho$ is specimen density (g/cm$^3$), m is the mass of the specimen in air (g), $m_{dw}$ is the mass of the specimen in distilled water (g), $\rho_0$ is temperature dependent density of distilled water (g/cm$^3$) and $\rho_L$ is density of air (.00012 g/cm$^3$).

$$\rho = \frac{m}{(m-m_{dw})}(\rho_0 - \rho_L) + \rho_L \qquad \text{Equation (3.3)}$$

Following the density measurement, the thermal degradation of the resin was performed using the method introduced by Gupta *et al.* [160]. An 1800 Watt Milestone ETHOS UP High Performance Microwave heating system was used. This is shown in Figure 3.8(a).
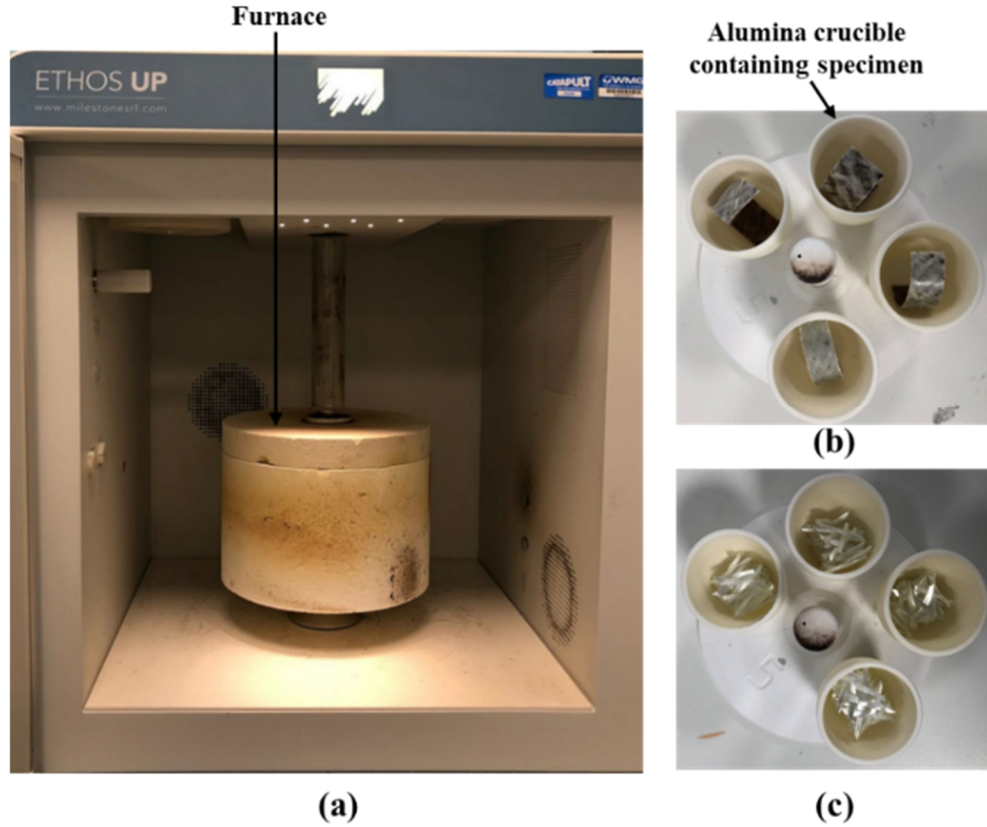
Figure 3.8 (a) SiC furnace placed inside the microwave chamber; braided specimens in alumina crucibles (b) before and (c) after the burn-off.

The specimens were held in alumina crucibles and positioned on a 5-slot crucible holder, as shown in Figure 3.8(b). The crucible holder was placed in a PYRO ultrafast cylindrical furnace, following which the furnace was put inside the microwave chamber. The chamber was closed and the temperature was increased to 500 °C and maintained for 30 minutes. After cooling the chamber to room temperature, the furnace was retrieved. The mass of the residual dry fibres was determined by weighing the retrieved crucibles, shown in Figure 3.8(c), and deducting the predetermined mass of empty crucibles. Before every burn-off experiment, the crucibles were cleaned by heating them to 600 °C and maintaining the temperature for 1 hour. Finally, the $F_{vf}$ and $V_{vf}$ were subsequently evaluated as per Equations 3.4-3.7, listed in BS ISO 14127 [161]. In these equations, $F_{mf}$ is fibre mass fraction, m is initial mass of test specimen (g), $m_c$ is initial mass of test specimen and crucible (g), $m_r$ is mass of specimen residue and crucible after burn-off (g), $F_{vf}$ is fibre volume fraction, $R_{vf}$ is resin volume fraction, $V_{vf}$ is void volume fraction, $\rho_f$ is fibre (E-glass) density (2.54 g/cm$^3$) and $\rho_r$ is resin (PA6) density (1.15 g/cm$^3$). The densities of E-glass fibre and PA6 were provided by the

45

supplier [162].

$$F_{mf} = \frac{m - m_c + m_r}{m} \times 100 \qquad \text{Equation (3.4)}$$

$$F_{vf} = F_{mf} \times \frac{\rho}{\rho_f} \qquad \text{Equation (3.5)}$$

$$R_{vf} = (100 - F_{mf}) \times \frac{\rho}{\rho_r} \qquad \text{Equation (3.6)}$$

$$V_{vf} = 100 - (F_{vf} + R_{vf}) \qquad \text{Equation (3.7)}$$

### 3.3.2  Microstructural analysis

The cross-section of the beams perpendicular to the beam axis was selected for performing microstructural analysis. Two cylindrical specimens, approximately 10 mm long, were extracted by slicing the beams perpendicular to the beam axis using an abrasive cutter. During the slicing operation, the specimens were inserted in a rigid steel cylinder, which was clamped between the rigid jaws, as shown in Figure 3.9(a). This prevented possible damage in the samples that could have resulted upon clamping the specimens directly, as shown in Figure 3.9(b). After slicing, the specimens were mounted in room temperature curing epoxy resin.
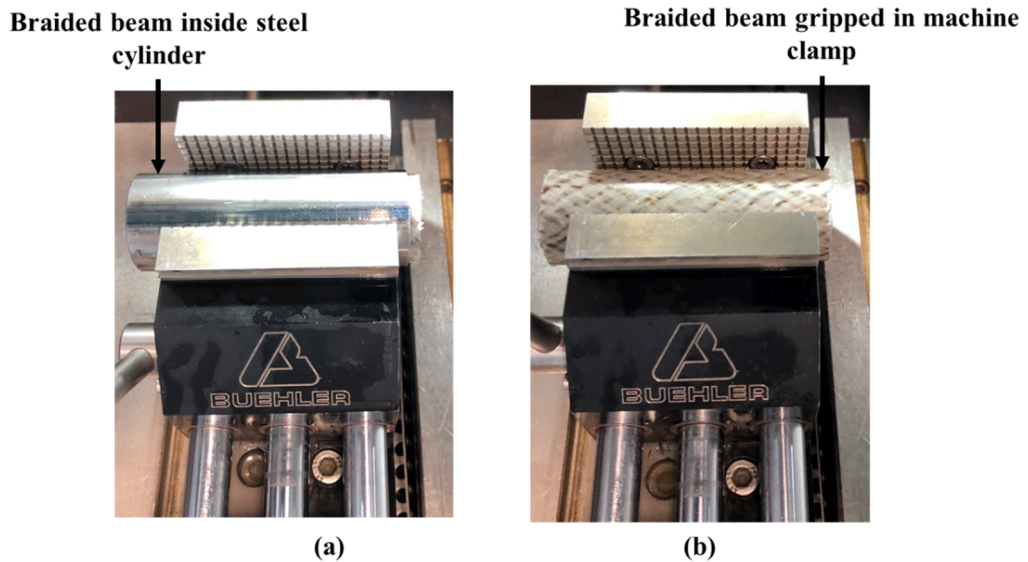


Figure 3.9 Braided beam clamped during the slicing process (a) with and (b) without protective steel cover.

Following the cure of the mounting resin, the surfaces of the specimens were polished using a Buehler EcoMet™ 300 automatic grinder-polisher. A 3 μm polish was found suitable. The different steps involved in the polishing operation are listed in Table 3.2 with the parameters and abrasive accessories used during every stage.

Table 3.2 Steps and parameters employed during the polishing of mounted samples.

| S. No. | Surface | Abrasive | Load (N) | Base speed (RPM), direction | Time (min:sec) |
|--------|---------|----------|----------|------------------------------|----------------|
| 1 | Carbimet abrasive paper | P400 grit SiC water cooled | 30 | 300 complementary | 3×2:00 |
| 2 | Texmet P | 6 μm MetaDi Supreme diamond suspension | 30 | 150 contra | 5:00 |
| 3 | VerduTex | 3 μm MetaDi Supreme diamond suspension | 30 | 150 complementary | 5:00 |

After polishing, the specimens were imaged using an automated stage ZEISS Axio Imager 2 microscope fitted with a 5 megapixel Axiocam 305 digital camera. A magnification of 5x was used. ZEISS ZEN 2 Core imaging software was used to perform stitching and generate images covering a wide area of the specimen cross-section. A typical stitched image captured using the optical microscope is shown in Figure 3.10. For measuring the specimen thickness, the specimens were imaged using a macro zoom camera at a magnification of 1x. The thickness was measured using the Omnimet image analysis software. For each braid angle, the thickness was measured at a minimum of 350 locations between the two polished specimens. The results of the quantitative as well as qualitative analyses are detailed in Chapter 5. Their implications on the mechanical performance of the braided beam structures are also discussed.
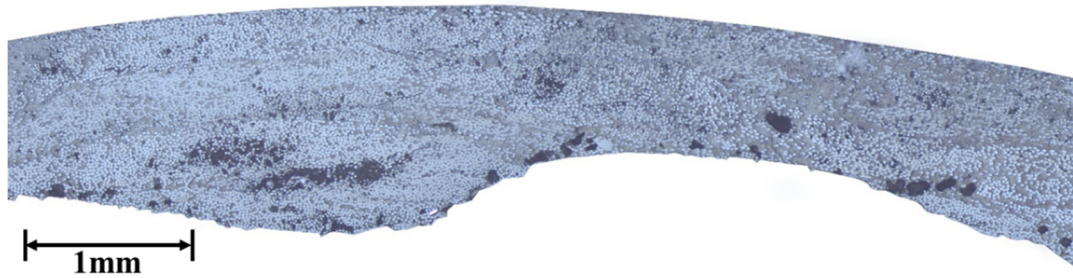
Figure 3.10 Stitched micrograph of a braided beam section obtained using optical microscopy.

## 3.4 Quasi-static three-point flexure

Three-point flexure tests were used to establish a correlation between the mechanical performance and braid angle of the manufactured braided beams. As discussed in Chapter 2, three-point flexure subjects a specimen to complex stress states and allows for combined assessment of two deformation mechanisms: global flexure and localised crush. The test setup used in this work is shown in Figure 3.11(a). An Instron 5800R test machine equipped with a 100 kN load cell was used. Test control and data collection were performed using the Instron material testing software Bluehill version 2. Manufactured beams were cut to a length of 420 mm using a dry chop saw. During the test, the beams were supported over a test span of 350 mm on rollers having a diameter of 40 mm. A central loading roller of 100 mm diameter was used. In order to measure the vertical displacement of the lower outer surface of the beams, an Instron 2630-112 extensometer was used in deflectometer mode. The extensometer was attached to a spring-loaded plunger, as shown in Figure 3.11(b). The plunger had machined notches on its base as well as the movable tip. The forks of the extensometer were inserted into these notches and tightly held using elastic bands, thus making a linear deflectometer. The deflectometer assembly was rigidly fixed onto the test fixture such that the tip of the plunger was in close contact with the lower surface of the beam (directly below the central roller) throughout the flexural deformation.
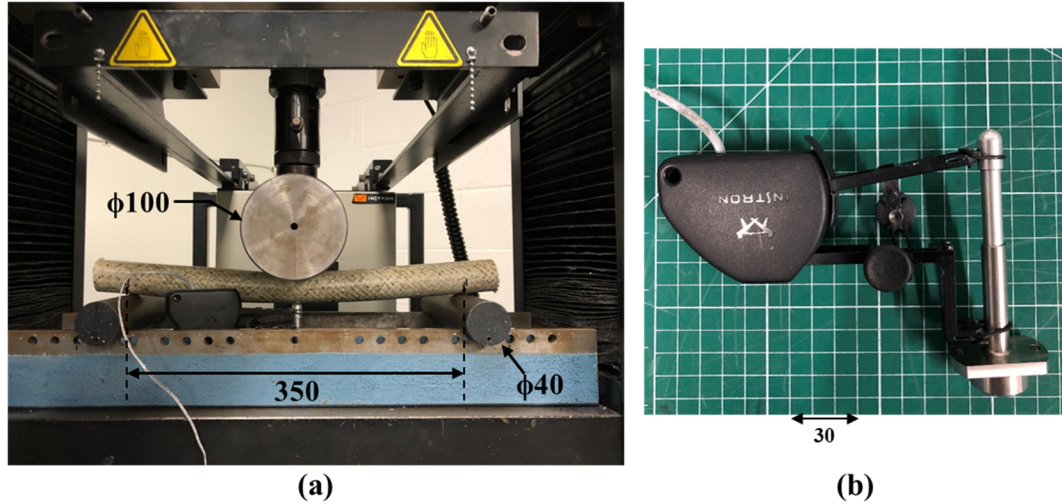
Figure 3.11 (a) Three-point flexure setup on the test machine frame and (b) deflectometer assembly. Note: Dimensions are in mm.

The difference between the bottom surface displacement and the crosshead displacement was used to evaluate the localised crushing on the top surface of the beam. For each beam type, six repeats were tested in three-point flexure, however, the bottom surface displacement was recorded for only three of these repeats. In order to maintain consistency across the different test specimens, all the braided beams were tested one day after moulding them using the braided preforms. After moulding, the beams were stored in sealed plastic boxes until the testing. Before each test, the beam was preloaded to 10 N to ensure full engagement of the upper loading roller with the beam before starting the test. The test was carried out at a constant crosshead displacement rate of 10 mm/min, which corresponds to a flexural strain rate of less than 2 %/min as per Equation 3.8. In the equation, $\dot{\epsilon}$ is strain rate (/min), D is beam outer diameter (mm), v is cross head-speed (mm/min) and $L_s$ is length of test span (mm). The test data was recorded at a rate of 10 Hz.

$$\dot{\epsilon} = \frac{6Dv}{L_S^2} \qquad\qquad \text{Equation (3.8)}$$

As described in Chapter 2, three-point flexure also introduces beam shear in the test specimen. Beam shear is a deviation from flexural loading and could severely modify the results of a three-point flexure test. Therefore, the test parameters should be selected such that the results represent the desired flexure properties instead of the shear characteristics of the beams. The effect of the inter-laminar shear during three-point

flexure was quantified by Tolf *et al.* [126] as per Equations 3.9 and 3.10. In these equations, w is displacement at mid-point of the beam (mm), P is the applied load (N), $L_s$ is span length (mm), E is Young's modulus of beam material (GPa), G is shear modulus of beam material (GPa), I is moment of area of beam cross-section (mm$^4$), k is cross-section shape dependent factor and A is cross-sectional area (mm$^2$).

$$w = \frac{PL_s^3}{48EI} + \frac{PL_s}{4kGA}$$  Equation (3.9)

$$w = \frac{PL_s^3}{48EI}[1 + e]$$  Equation (3.10)

The term e depicts the shear-driven deviation from pure flexure. It is a geometry dependent term and increases with the depth to span ratio of the specimen. The recommended specimen geometries in existing ASTM [163] and ISO [164] standards for flexure testing of rectangular coupons are aimed at minimising this error term. For hollow circular beams tested in this work, the error term was estimated to be less than 10% as per Equation 3.11.

$$e = 3\frac{E}{G}\left(\frac{D}{L_s}\right)^2$$  Equation (3.11)

Dedicated experiments were performed to evaluate the compliance of the test setup and the precision of the load cell in the load range observed during the flexural testing of the beams. Results of these experiments indicated that a maximum displacement of 0.03 mm was induced due to the system compliance while the maximum error in the load cell measurements was less than 2%. These experiments as well as calibration certificates for the equipment utilised in this work are detailed in Appendices A-D.

## 3.5 Digital image correlation

With the purpose of recording and comparing the surface strains and displacements induced during the three-point flexure tests, three-dimensional Digital Image Correlation (DIC) was used. As demonstrated in literature, DIC is a powerful tool for accurately capturing the multiaxial strains as well as out-of-plane deformations

observed in three-point flexure tests [165,166]. A schematic of the three-point flexure setup for testing the manufactured beams with the DIC measurement system is shown in Figure 3.12. The DIC measurements were performed using a matched pair of GOM 12M digital cameras equipped with Complementary Metal Oxide Semiconductor (CMOS) sensors. The lenses attached to the cameras had a focal length of 100 mm. DIC software GOM ARAMIS [167] version 6.1 was used to acquire the DIC images. During preliminary experiments, the majority of deformation was observed to occur in the contact region of the beams directly under the loading roller. Therefore, the central segment of the beams was selected as the Region of Interest (RoI).
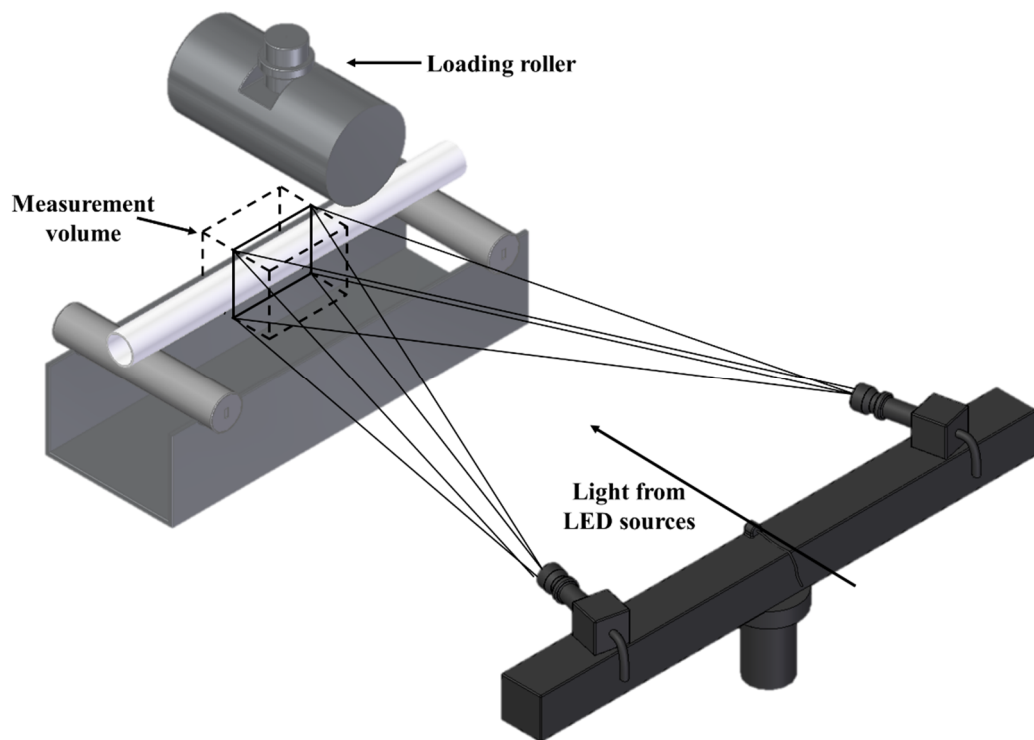


Figure 3.12 Schematic of 3D DIC measurement during three-point flexure testing of the manufactured beams.

It should be noted that the surface strain measurements were made on the region of the beam surface visible to the cameras. The area undergoing crush damage was beneath the central loading roller and therefore could not be captured within the view of the cameras. A measurement window of 150 mm × 100 mm was found suitable to capture the RoI. The DIC measurement system consisting of the two cameras was set up parallel to the test frame. The recommended values of inter-camera distance and frame distance specified in the GOM ARAMIS manual were used [168]. The cameras were focused in

a plane coinciding with the surface of the circular beam closest to the cameras. A sharp focus was achieved by performing the focusing operation with completely open lens apertures. Based on the diameter of the beams, a depth of field of 39 mm was used to account for the out of plane deformation during flexure. This was achieved at an f-stop number of f/16 in both the cameras as per the GOM recommendations. The beams were illuminated using LED lights during the three-point flexure experiments. A false colour projection on a white surface was utilised to evaluate the quality of illumination and ensure that both the cameras showed similar patterns. The measurement system was calibrated using a CP20 90 × 72 calibration plate provided by GOM. In order to ensure consistency, the calibration and the experiments were performed under the same conditions. Before performing three-dimensional calibration of the optical apparatus, the cameras were turned on and allowed to warm up and equilibrate for 30 minutes. For a calibration to be deemed successful, the calibration deviation must lie between 0.01 and 0.04 pixels.

A stochastic white speckle pattern on a matt black background was applied in the RoI for every beam. Firstly, the beam surfaces were cleaned and coated with a black coloured base using a Plastikote Black Primer. A white emulsion paint diluted to approximately 50% by volume was used to create the speckle pattern. The black base was allowed to dry, following which, the white speckle pattern was sprayed using a Badger airbrush. For the GOM 12 M, a speckle distribution with approximately 9 pixels per dot is recommended [169]. A trial and error approach was undertaken to achieve the required fineness of the pattern. This was aided by the nozzle on the airbrush, which could be adjusted to produce dots of the required size. An example of the speckle pattern created on the beam surface is shown in Figure 3.13. During the analysis of the acquired images, the software divides each image into an array of quadrangular facets. The size of the facets can influence the strain resolution as well as noise patterns. Therefore, the default GOM ARAMIS facet size of 19 pixels with an 80% step was employed. For each beam, the maximum possible exposure time without over-exposing any pixel in the image was selected.
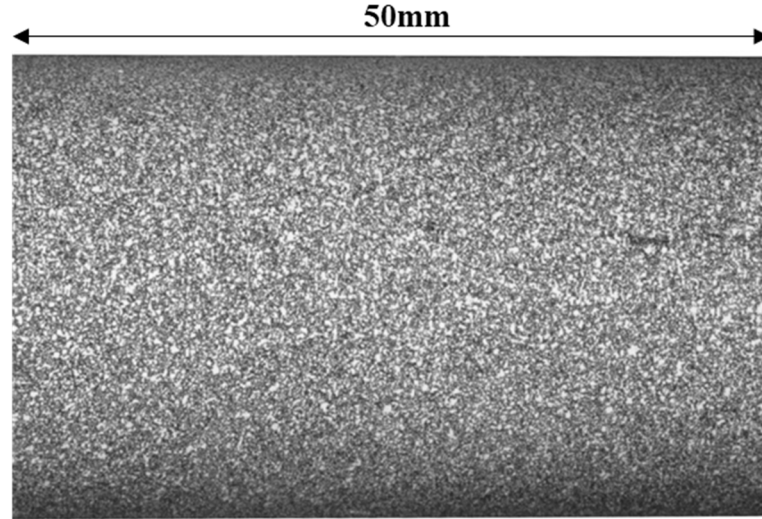
Figure 3.13 Speckle pattern created on the outer surface of braided beam.

The image acquisition during the experiments was performed at a rate of 2 Hz. The DIC system and software parameters are listed in Table 3.3.

Table 3.3 DIC system parameters employed during acquisition and analysis.

| Parameter | |
| --- | --- |
| Sensor/camera | GOM 12M |
| Lens | Titanar 100 mm |
| Camera angle | 25° |
| Image window | 4000 pixel × 3000 pixel |
| Measurement area | 150 mm × 100 mm |
| Calibration plate used | CP20 90 × 72 |
| Facet size | 19 pixels (16 pixels step size) |
| Lens Aperture | f-stop f/16 |
| Depth of field | 39 mm |
| Exposure time | 55 to 60 ms (depending on speckle pattern) |
| Frame rate | 2 Hz |

The post-processing of the DIC data was conducted using GOM Correlate Professional [170]. For every beam, the software creates a surface component using the recognised facets. In order to ensure that the measured displacements are aligned correctly with respect to the beam, a modified alignment was created and applied to the surface component. The alignment procedure is shown in Figure 3.14. A CAD geometry of a cylinder with the same outer diameter as the braided beams was imported into the GOM CORRELATE interface. This CAD geometry served as the reference for aligning the surface component. The initial alignment was performed using the *3-point alignment*

feature. This involved selection of three points on the nominal CAD surface, followed by selection of the corresponding points on the actual surface component. The alignment was further improved by using the *Local Best-fit* alignment feature of the software.
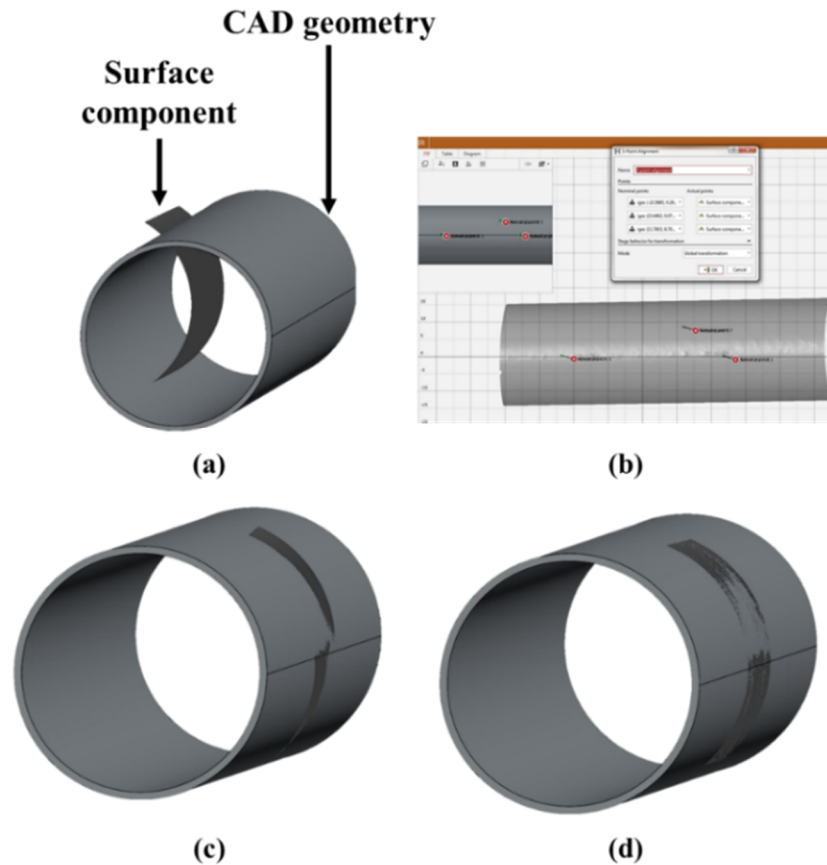


Figure 3.14 (a) Misaligned surface component and CAD; (b) 3-point alignment procedure; improved alignment after employing (c) 3-point alignment and (d) local-best fit.

For every beam, six static images were captured after preloading. These images were analysed to estimate the measurement accuracy as well as evaluate the fitness of the pattern and calibration for successful acquisition of DIC data. Figure 3.15 shows the strain distribution in a static image. The 'false' strain values shown in the figure appear due to random noise. The 'false' strain is randomly distributed across the entire image without any localised anomalies, as shown in the figure, indicating that the measurement system is correctly set up.
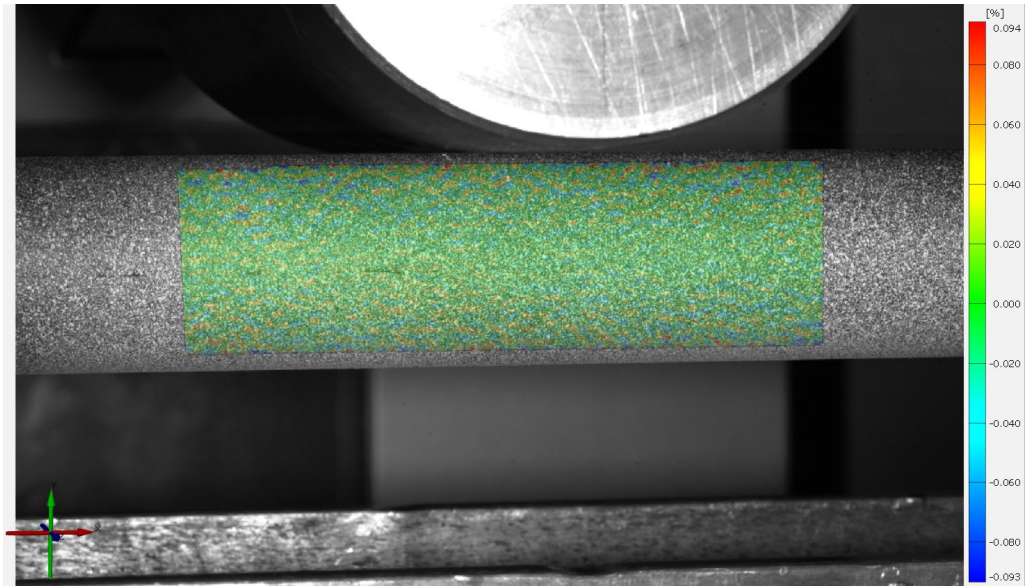
Figure 3.15 Static image with a distribution of false strain values.

Assuming that the strain measurements in static images are normally distributed, the mean of these falsely induced strains and displacements represent the bias of the measurement, while the standard deviations represent the resolution of the measuring system [169]. These bias and precision values are detailed in Chapters 5 and 6 with the corresponding analyses of the measured strains and displacements.

## 3.6    Summary

This chapter has described the methodologies and equipment employed in the experiments performed in this work. These include the braiding process, destructive part quality evaluation and three-point flexure testing. Detailed descriptions of each technique with respective sources of error and their implications on the results of this work were provided. The results obtained using the experimental methods detailed in this chapter are discussed and analysed in Chapters 5 and 6. The next chapter describes the development of a novel manufacturing process with favourable part cycle time as well as precise process control, which is essential to produce braided beams with consistent part quality.

# 4 Development of high volume manufacturing route

The potential of commingled thermoplastic material systems for rapid manufacturing of hollow braided composite components was discussed in Chapter 2. The lack of high volume readiness in the previously investigated Bladder Inflation Moulding (BIM) approaches was highlighted and a need for enhanced process control capabilities was identified. In order to test and compare braided composite beams with different braid angle profiles (uniform and tailored), it is crucial to manufacture beams with consistent quality and prevent uncontrolled manufacturing variabilities from affecting the mechanical performance of the produced beams. Therefore, given the inadequacy of conventional BIM approaches, a novel process named as Rapid Variothermal Moulding (RVM) was developed by the author. This chapter presents the development of the RVM process. The process utilises a locally controllable, responsive tooling, which complements the high rate of preform production of the braiding process, thus improving the overall viability of the process for high volume part production. Initial manufacturing trials and process streamlining were performed using a 25° 2×2 braided fabric. In order to assess the RVM process, a conventional BIM process was used as a benchmark. The RVM process was iteratively improved and subsequently used to manufacture braided beams for mechanical testing and comparison.

## 4.1 Initial development of Rapid Variothermal Moulding (RVM)

In this section, the manufacturing of hollow braided beams using the benchmark BIM process and the novel RVM process are explained. The characteristics of the RVM process are discussed and a cycle time-process control comparison with the BIM process is shown. All the trials and comparisons were performed using a 25° 2×2 regular braided fabric.

### 4.1.1 Conventional Bladder Inflation Moulding (BIM)

In this work, a BIM process in commercial use at Composite Braiding Limited for

prototype manufacturing of components served as a benchmark. The characteristics of the BIM process were described in section 2.2. A dedicated metallic moulding tool was designed by the author and fabricated for the BIM process. A mild steel grade S275JR was used for the tool. Figure 4.1(a) shows one half of the tool. In order to ensure that the tool design was adequate for the process conditions, static FE simulations were carried out using the package solidThinking Inspire$^{TM}$ [171]. A temperature of 240 °C and internal bladder pressure of 20 bar was used during the simulations, as per the recommendations of Composite Braiding Limited. The corresponding results are shown in Figure 4.1(b). The stresses and deflections were found to be within acceptable limits and hence, the design was approved for fabrication. The tool has a 560 mm long channel running across its length with a circular cross-section of 35 mm diameter for moulding parts of appropriate size for mechanical testing. The choice of the mould cavity diameter, i.e. beam outer diameter, of 35 mm was based on the results of Micallef [172], who tested 35 mm outer diameter braided beams with a braid angle of 25°. During these tests, both localised crushing and global flexure were observed simultaneously, which was appropriate for investigating the correlation between braid angle and deformation modes, as proposed in Chapter 2. The grooves at each end of the tooling, visible in Figure 4.1(a), are meant to house custom-made metallic end fittings, which connect the bladder to an external pressure line. The design for the groove, as well as the end fittings, were provided by Composite Braiding Limited.
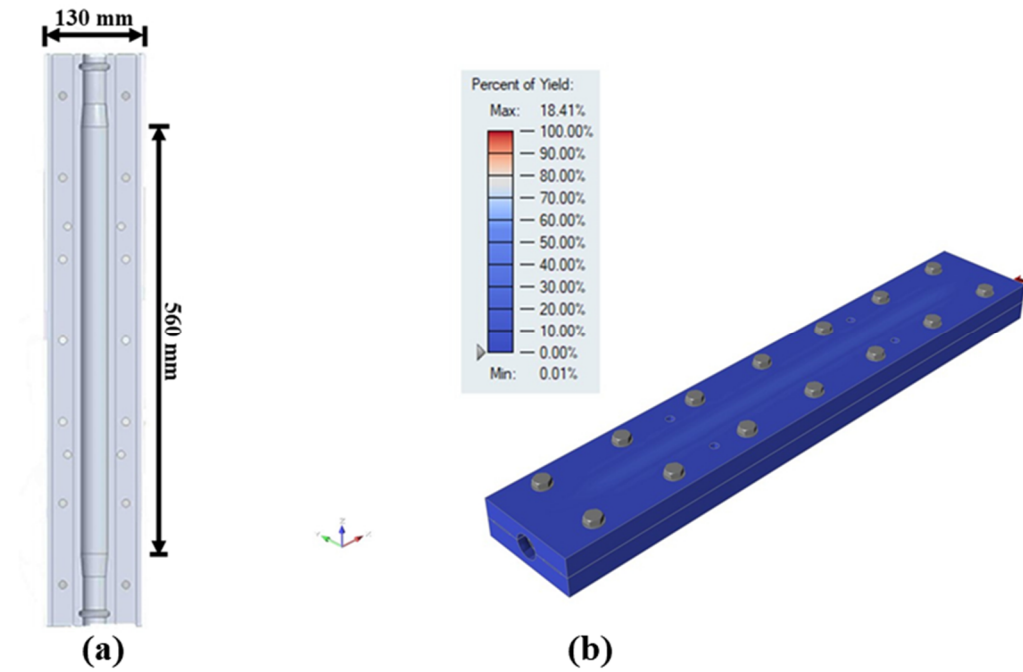
Figure 4.1 (a) CAD model showing half tool with mould cavity for producing hollow tubular parts using BIM and (b) Stresses predicted by static thermo-mechanical simulation of the tool subjected to 250 °C with 20 bar internal pressure.

After removing the braided preform from the mandrel, it was pulled over a silicone rubber bladder. The end fittings were attached to both ends of the bladder and the entire bladder-preform assembly was placed into the circular tool cavity. The two-part tool is shown in Figure 4.2 with the bladder-preform assembly. The two parts of the mould were fixed together by bolts and the mould was placed in the oven at Composite Braiding Limited. The mould was heated up to a temperature of 240 °C, approximately 20 °C above the melt temperature of PA6, following which the bladder was internally pressurised to 2 MPa (20 bar) using a compressor. The pressure and temperature were maintained for 10 minutes allowing for consolidation. Following this, the internal pressure was withdrawn. The oven was switched off and the tool was allowed to cool naturally inside the oven.

Figure 4.2 Top and bottom halves of the BIM tool with bladder-preform assembly in the mould cavity.

Mould extraction and unfastening were commenced at a temperature of 90 °C, significantly below the recrystallisation temperature of PA6. The final demoulding temperature was approximately 70 °C. Figure 4.3(a) shows a glass fibre braided composite beam manufactured using the conventional BIM process. There was a small amount of polymer matrix bleed at the tool parting line. These solidified matrix fragments were found to weigh less than 0.3% of the total beam. The beams had smooth outer surfaces due to contact with the tool, while the inner surfaces had the undulating texture of the braided fabric due to contact with the flexible silicone rubber bladder. A closer view of the produced part, shown in Figure 4.3(b), revealed brownish discolouration and some fibre waviness on the outer surface. Similar discolouration was also observed on the internal surface. However, there was negligible fibre waviness on the inner surface. The discolouration phenomenon is discussed in detail in section 4.2.3.
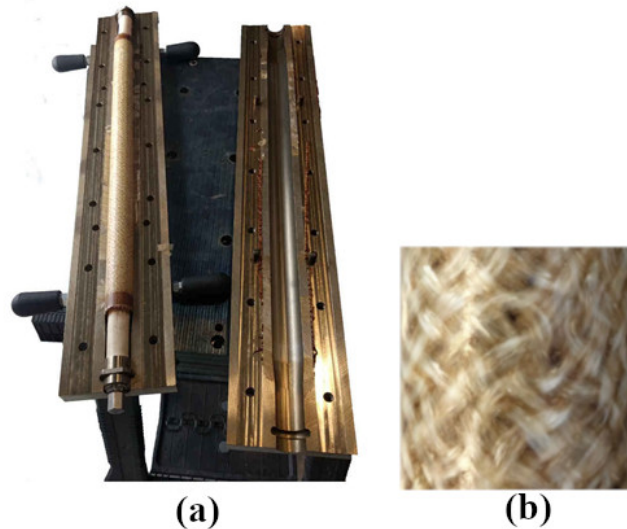
Figure 4.3 (a) Braided beam after tool separation following the BIM process and (b) close view of the braided beam surface showing fibre waviness and discolouration.

The entire process cycle including demoulding and tool separation took 4 hours. Such a long process cycle is not feasible considering the typical targets in high-volume manufacturing environments such as the automotive industry. Moreover, given the crude nature of thermal control particularly in the cooling phase of the process, it is reasonable to expect significant inconsistency in the thermal profiles, not only between different parts but also between different regions of the same part. As highlighted in Chapter 2 for previous BIM approaches, processing inconsistency can affect the in-service performance of components due to thermal distortions, uncontrolled crystallinity etc. Importantly, from the viewpoint of the mechanical testing to be undertaken in this work, inconsistent manufacturing can introduce unknown variability to the mechanical performance of the beams and reduce the confidence in the obtained results. Hence, it was necessary to develop a suitable manufacturing process for consistent production of test specimens.

### 4.1.2 Rapid variothermal moulding

The proposed novel RVM setup is an integration of three key components:

(i) Elements of the conventional BIM process: The elements and steps involved in a conventional BIM process were discussed in the previous section. The mould surface design, end fittings and bladders used in the BIM process were directly carried over to

the new process. The mould cavity dimensions of the BIM tool were replicated in the RVM tool for producing beams with an outer diameter of 35 mm. As discussed in the previous section, the selected beam cross-sectional dimensions were suitable for conducting the proposed research on correlations between braid angle and deformation modes.

(ii) A patented Production to Functional Specification (PtFS) concept by Surface Generation Limited [173]: The PtFS technology enables rapid heating and cooling of customised moulding tools. Figure 4.4 shows an overview of the PtFS setup with each component.
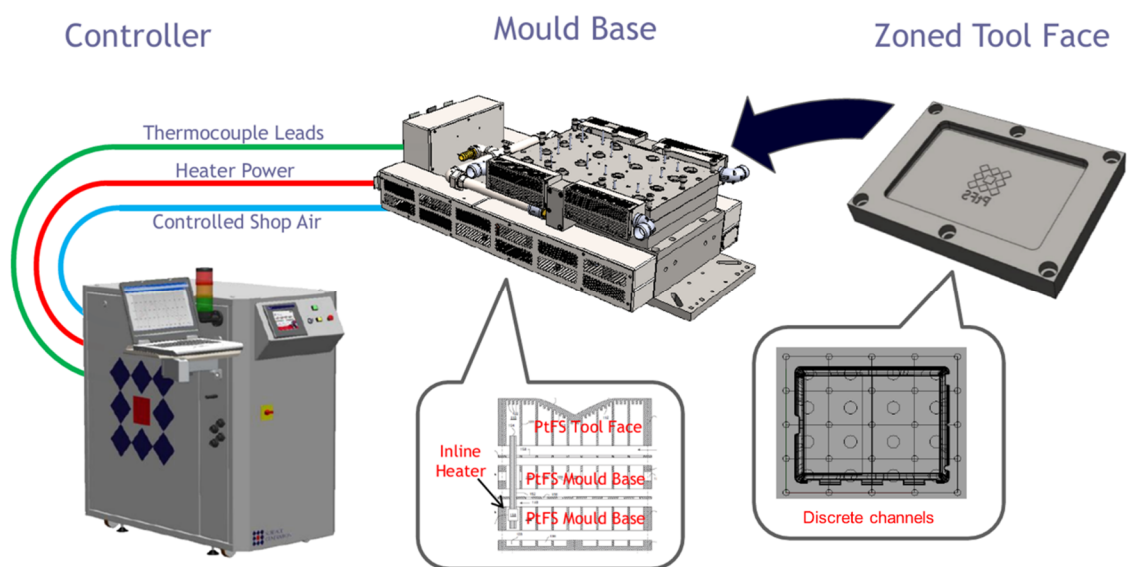


Figure 4.4 Overview of PtFS technology (Taken from [173]).

The reverse faces of the tools are machined into an array of thin-walled channels. The design of the channels is performed via advanced simulations by Surface Generation. The objective of this design exercise is to minimise the thermal mass, for rapid heating and cooling, while ensuring that the tool is able to withstand the mechanical loads of the manufacturing process. The fabricated tool faces are mounted over the mould bases, connected to the system controller. The schematic presented in Figure 4.5 shows a sectional view of the tool face mounted on the mould base. Each channel has a dedicated heater (represented by A in figure) and a thermocouple (B in figure) located in the base below the tool face. A supply of compressed air (E in figure) and electrical power (D

in figure) is directed to every channel. Controlling the heater and compressed air supply to each channel separately allows for rapid heat up and cool down as well as precise local control over the temperature in each zone of the part being moulded. The controller facilitates the development of bespoke thermal profiles, for individual channels or a group of channels, through a user interface in a dedicated software called Orchestrator. During a process, real-time temperature data corresponding to each tool face feeds into the controller via the respective thermocouples. Using this real-time temperature as feedback, the controller adjusts the electrical power as well as the airflow rate to achieve the local target temperature.
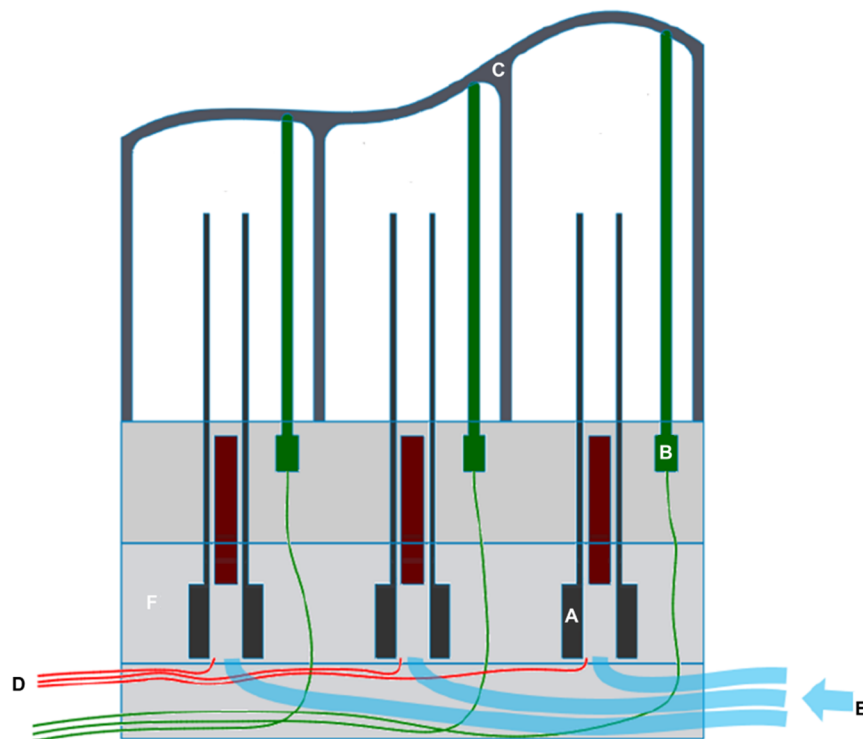


Figure 4.5 Sectional schematic of PtFS tool setup (Adapted from [173]). Note: A represents heater, B represents thermocouple, C represents mould surface, D represents electrical power, E represents compressed air flow and F represents the tool base.

In this work, an existing PtFS base setup [89,174] at WMG with a total of 32 channels (16 on each tool half) was used. A set of tool faces was designed by the author to allow the production of beams identical in dimension to those made using the BIM process. A three dimensional schematic of the tool with the segregated channels is shown in Figure 4.6(a). The tool has two adjacent mould cavities out of which only one was used

in this work. The figure shows the uniform distribution of the channels across the RVM tool, with each channel representing a point of individually controllable heat input into the tool face. This indicates the superior spatial precision of the RVM process compared to conventional BIM, where the heat input cannot be controlled locally. Figure 4.6(b) shows the top view of the tool with marked thermocouple locations. The end channels of the tool are also highlighted in the figure. Monitoring the temperature of these end channels is critical as they are expected to incur relatively greater heat loss to the ambient atmosphere compared to the other channels. As discussed later in the section, such a disparity can be eliminated by varying the input thermal power locally across the tool, however, the same would not be possible in conventional BIM.



(a)                                                    (b)
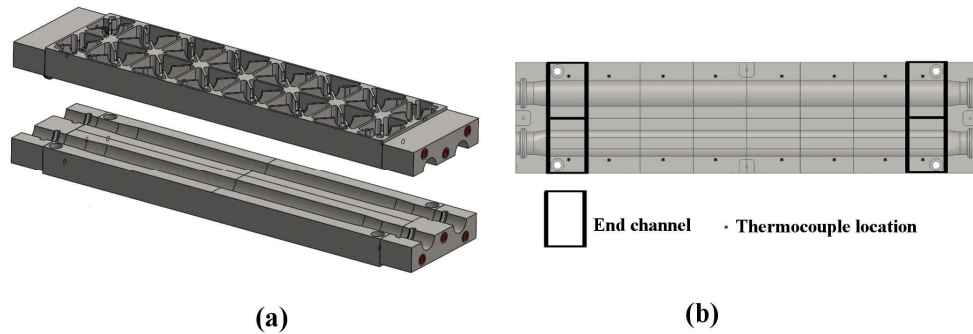
Figure 4.6 (a) Three-dimensional schematic of the RVM tool faces showing segregated channels and (b) top view of the tool face with marked thermocouple locations and end channels.

(iii) Hydraulic press: The application of a press enables rapid opening and closure of the tools, thus reducing the time between cycles. A 100 ton Dassett hydraulic press was used in this work. The customised tool faces were mounted with the PtFS setup on the press as shown in Figure 4.7.

Figure 4.7 Customised tool faces with the PtFS setup mounted onto the press.

Based on trials performed on the BIM tool, a consolidation time, i.e. time at consolidation temperature, of 6 minutes and consolidation temperature of 250 °C were initially chosen. A water-based release agent was applied on both the moulding surfaces. A pre-programmed heating cycle was implemented, created using the Orchestrator software interface. The first segment of the cycle involved preheating of the tool to 50 °C, i.e. heating each channel to a temperature of 50 °C. Following the preheat, a bladder-preform assembly prepared similarly as described for the BIM process was placed into the tool cavity. The press was then closed and the temperature was increased to 240 °C at a rate of 40 °C/min. The temperature was held at 240 °C for 6 minutes with simultaneous pressure application. After cooling down to 180 °C, the part was demoulded. The temperature was further reduced to 50 °C and the tooling was prepared for the next cycle. An internal bladder pressure of 0.4 MPa (4 bar) was applied from the point of tool closure until the press was opened. At the time of the trials, this was the maximum available pressure due to limitations of the manufacturing environment. A typical part produced using the RVM process is shown in Figure 4.8. Similar to the BIM process, there was visible fibre waviness on the outer surface of the RVM part. However, the discolouration was absent, which indicated a positive correlation between the time above melting temperature and part discolouration.

64

Figure 4.8 Braided beam in lower RVM tool half after opening the press. Note: The cavity on the right-hand side was unfilled.

With a 6-minute consolidation time, a press cycle time of 17 minutes was achieved. The channel-wise temperature-time data, extracted using the software interface, is shown in Figure 4.9. The average temperature of all the channels in each tool half, i.e. top and bottom tool halves, as well as the average temperature of the end channels on each tool half are plotted in the figure.
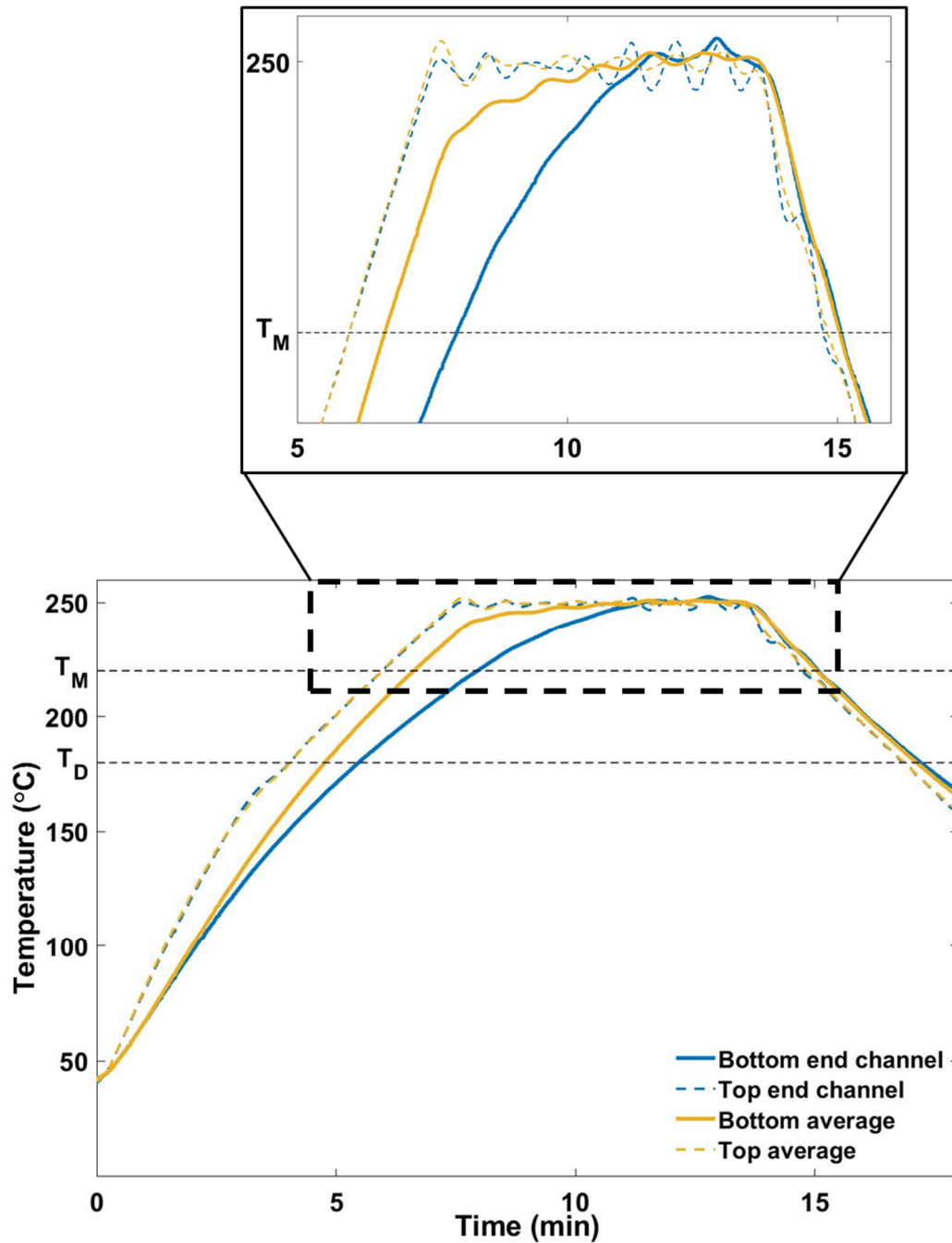
Figure 4.9 Average and end-channel temperature profiles of the top and bottom tool halves.

The observable difference in the profiles of the top and the bottom tool halves was due to a difference in thermal mass, the lower tooling half being heavier due to physical requirements of the press system. The figure also shows that the channels on the bottom tool, especially the ones located at the tool ends (marked in Figure 4.6(b)) were heating up at a slower rate. Additionally, during the consolidation phase the temperature data showed an undulating trend around the target consolidation temperature. Therefore, a detailed package of work was undertaken to ensure uniform and constant temperature

across all the channels of the tool. A modified exhaust system was installed by Surface Generation to recirculate the high temperature exhaust air through the tool ends. Moreover, various control features of the PtFS system were employed. These have been detailed below:

- **Preheat temperature:** Before loading the bladder-fabric assembly, the central channels of the tool were preheated to 150 °C, while the end channels were preheated to 165 °C to achieve uniformity during the consolidation phase. This also allowed to reduce the time between adjacent part cycles, as the next preform could be placed into the cavity soon after demoulding of the previous consolidated part. The modified exhaust system facilitated in maintaining the applied preheat temperature in each zone of the tool.
- **Variable thermal power control:** Each channel of the PtFS tool has a dedicated electrical heater. Using the software, variable power was made available for different channels during each stage of the process. The optimal values of power were obtained through a trial and error approach.
- **Process transition:** The software was used to apply logical rules to ensure simultaneous process transitions between different stages of the process for all channels. This was particularly critical during the beginning and the end of the consolidation/dwell phase.
- **Uniform cooling rate:** During the cooling stage, at any given instant, the channel with the slowest response i.e. highest temperature was designated as the "rate-governing channel" for the entire tool. Consequently, the PtFS system dynamically controlled the electrical power and compressed air flow to each channel, resulting in a uniform cooling rate of approximately 13 °C/min.

The finally obtained temperature profile is shown in Figure 4.10.
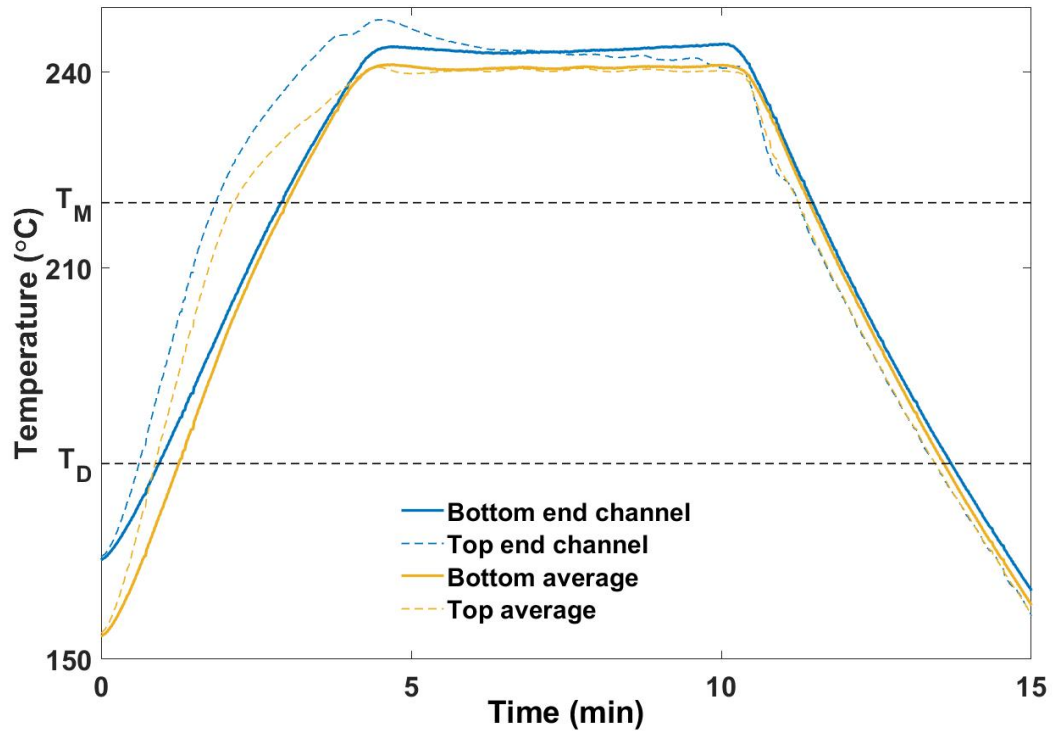
Figure 4.10 Average and end-channel temperature profiles of the top and bottom tool halves after employing PtFS control features.

As evident in the figure, the implementation of these features resulted in a significant improvement in uniformity across the component, particularly during the consolidation and cooling phases. The end channels were provided with greater power, thus allowing them to reach the consolidation temperature and maintain it for the stipulated time. Using the control features, the total press cycle lasted for approximately 14 minutes.

It can be noted from Figure 4.10 that the tool surface temperature during the consolidation phase in the modified profile was 240 °C. This is because tool surface temperature measurements conducted using externally applied thermocouples revealed that there was a variable difference between the thermocouple reading and the mould surface temperature. This was a consequence of the positional offset between the thermocouples embedded in the tool bases and the electric heaters (located at the centre of each channel, shown in Figure 4.6(b)). The comparison is shown in Figure 4.11 for the consolidation and cool down phases of the process for a 15 minute consolidation cycle. During the consolidation phase, the actual mould surface temperature was approximately 10 °C above the thermocouple reading. Therefore, although the embedded thermocouples in the tool measured a temperature of 240 °C, the actual part

68

consolidation temperature was 250 °C. As the temperature reduced, the offset shrunk and both readings were approximately the same at glass transition temperature of the PA6, i.e. 60 °C. This offset was considered during the development of the modified thermal profiles.
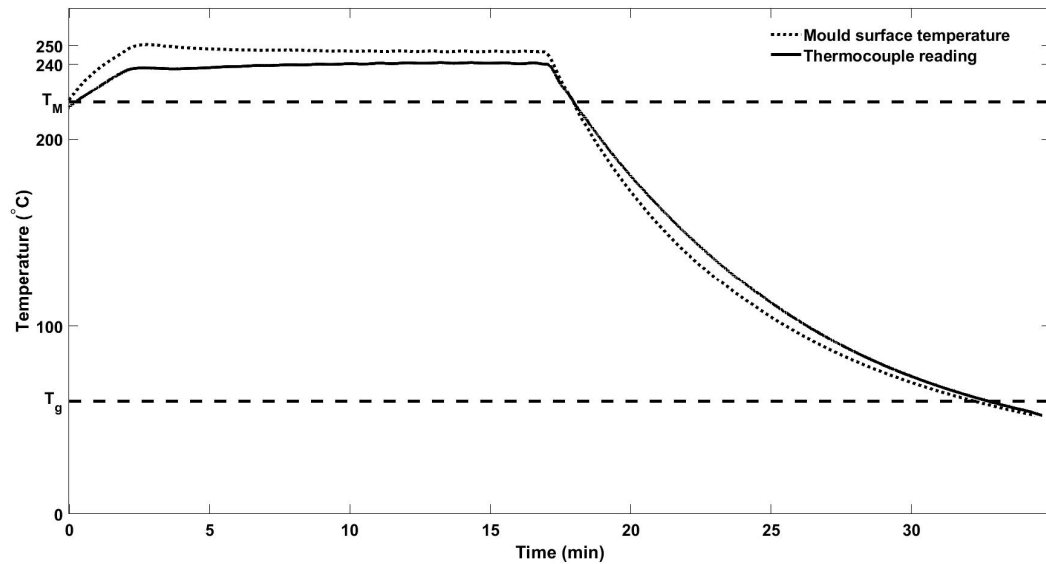


Figure 4.11 Comparison between mould surface temperature and PtFS thermocouple readings during the RVM process.

Figure 4.12 shows the conventional BIM and proposed RVM processes represented in the form of flowcharts. The route utilised for heating/cooling the tooling and the use of a press in the RVM route resulted in a 97% reduction in the time taken during the temperature ramp-up and cool-down phases of the process. Moreover, the features of the PtFS technology ensured a uniform temperature profile across the entire length of the part. Such uniformity across the tool is difficult to achieve using conventionally heated systems.
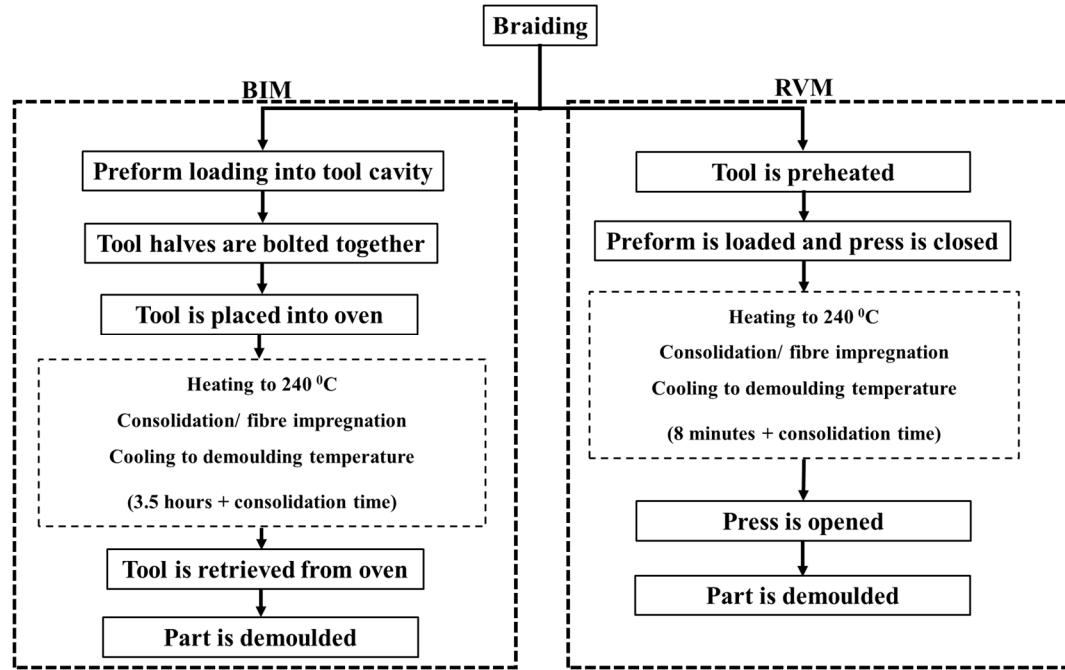
Figure 4.12 Flowchart with step-wise description of conventional BIM and proposed RVM processes.

## 4.2   Improvements in overall beam manufacturing

Following the successful development of the RVM process, the manufactured braided beams were evaluated to assess their suitability for performing the planned mechanical testing exercise. This section details the defects identified and the corrective actions taken to improve the quality of the manufactured beams.

### 4.2.1   Inconsistency in regular braid

The RVM process was used to manufacture beams using 2×2 regular braided preforms. Braid angles of 25°, 45° and 60° were chosen and three beams were manufactured for each braid angle. For each manufactured beam, the braid angle was measured at a minimum of 20 locations on the outer surface. A significant error between the measured and target braid angles was observed, as shown in Figure 4.13.
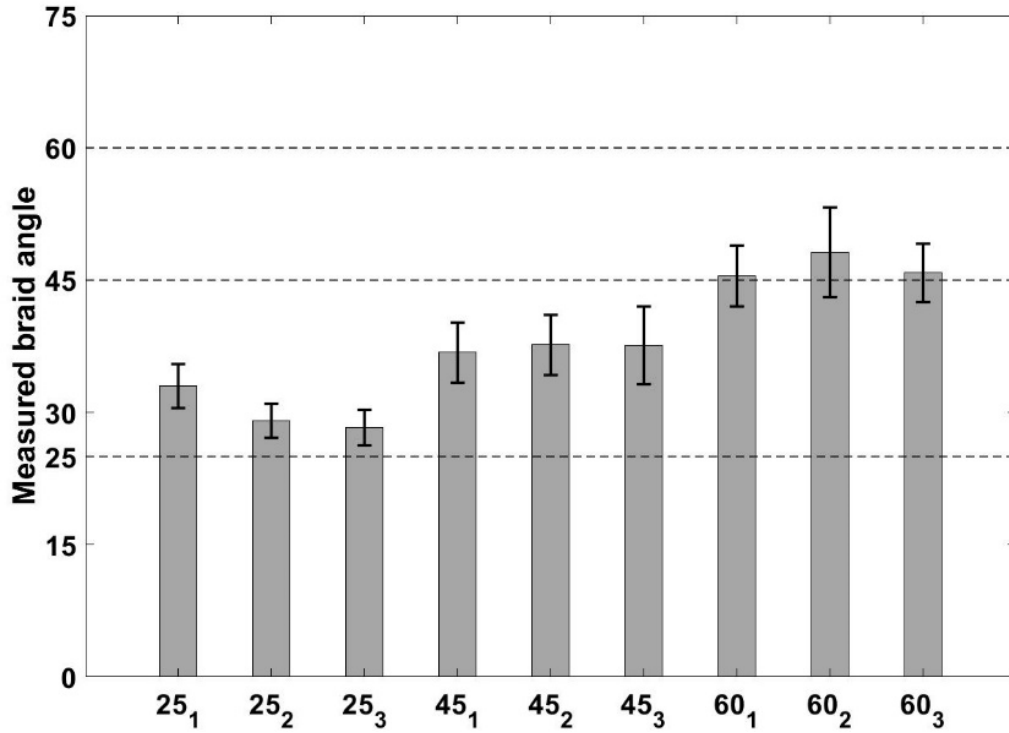
Figure 4.13 Measured braid angle values for braided beams produced using 2×2 fabric. Note: bars represent mean values and errors represent one standard deviation.

To investigate the discrepancy between measured and expected braid angle, the mass of the braided beams were predicted using a volume-based analytical approach, as per Equation 4.1. In this equation, M is the beam mass (g), $N_L$ is the number of braided layers, $N_c$ is the number of carriers used during the braiding operation, T is the linear mass of commingled tows (g/km), L is the length of the beam (mm) and $\theta$ is braid angle. The mass calculated using this equation gives the total ideal mass of commingled material required to braid a particular length at the given braid angle. Therefore, comparing the measured mass values with theoretical prediction indicates any bias in the braiding parameters used, while the randomly measured braid angle values give an estimate of the variability in fibre orientation introduced during various stages of the process.

$$M = \frac{N_L N_c TL}{\cos \theta} \qquad \text{Equation (4.1)}$$

The comparison of measured beam mass against the theoretically predicted values, shown in Figure 4.14, confirms that the braiding process was unable to achieve the target braid angles.

71
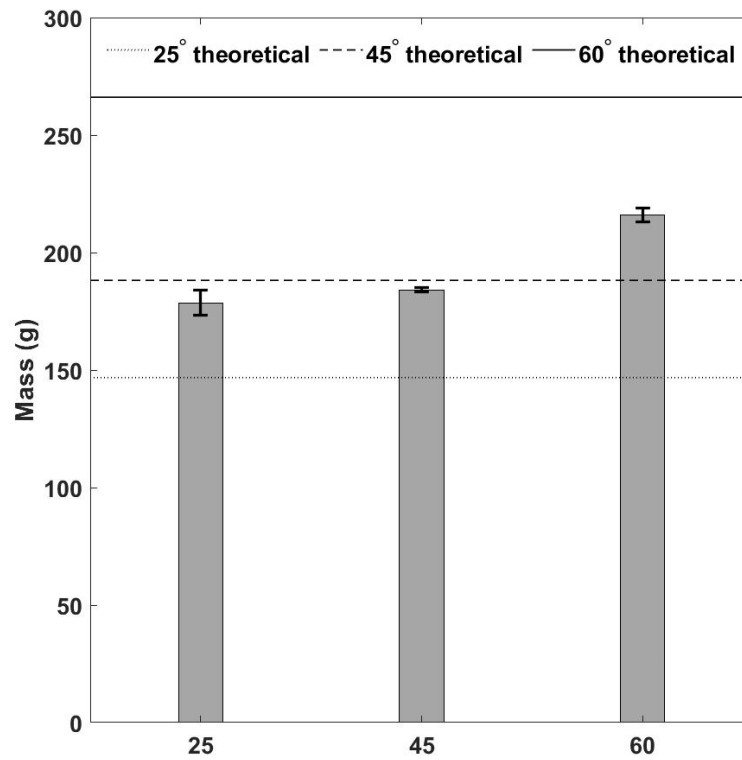
Figure 4.14 Measured mass of braided beams produced using 2×2 fabric.

In addition, there was significant overlap in the braid angle and beam mass data of the 25° and 45° beams, which would render the comparative mechanical tests inconclusive. Therefore, it was concluded that the 2×2 braid was not suitable for investigating the effect of braid angle on the mechanical performance of braided beams and a 1×1 diamond braid was considered for the manufacturing of beams. For the diamond braid, the braid angles of 30°, 45° and 60° were considered and shown to deliver consistent results. These three braid angles were selected to maximise the disparity in the resulting physical characteristics of the beams while respecting the bounds of applicable braid angles in industrial applications. Similar range and values of braid angle were also used in previous literature to investigate the mechanical behaviour of braided composites [50,124].

### 4.2.2   Reduction in fibre waviness

The fibre waviness observed on the outer layer of the 2×2 beams produced during the manufacturing trials indicated that there was a lack of tension in the fibre tows during the mould cycle. Similar waviness was also observed for 1×1 diamond braid. During bladder inflation, the expansion of the braid is expected to induce tension in the fibres.

72

Therefore, it was hypothesised that reducing the diameter of the commingled braided performs would result in greater expansion and induce greater tension in the tows in the outer layer, thus reducing fibre waviness. In order to confirm this hypothesis, the size of the mandrel used in the braiding process was reduced from 30 mm to 25 mm, and beams were produced using the same process parameters. The resulting beams showed a significant reduction in fibre waviness on the outer surfaces, as shown in Figure 4.15. This confirmed the hypothesis regarding preform size, and hence all the following braiding operations were performed using 25 mm mandrels.
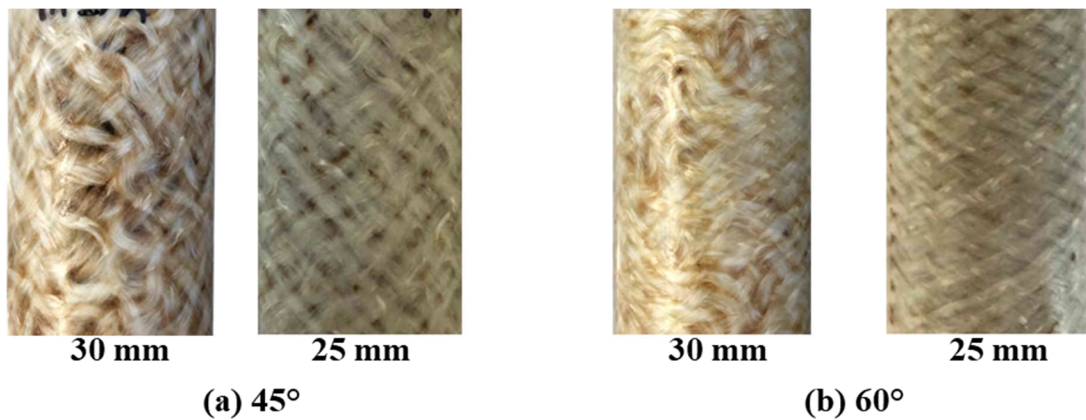


Figure 4.15 Reduction in fibre waviness in 1×1 braid through a reduction in mandrel diameter for (a) 45° and (b) 60° braided beams.

The increase in expansion during bladder inflation caused a greater contraction in the preform length. Among the three braid angles of 30°, 45° and 60°, this contraction was highest for 60° braid, with the longest possible preform, i.e. 530 mm long, being reduced to 430 mm in the final part. This contraction is shown in Figure 4.16. For this reason, a beam length of 420 mm was selected for the three-point flexure. As described in Chapter 3, for a beam diameter of 35 mm, a beam length of 420 mm with a test span of 350 mm limited the shear-induced deviation from global flexure to less than 10% and hence was appropriate for three-point flexure tests.



Figure 4.16 Contraction in length of 60° braided beam compared to an unprocessed preform.

### 4.2.3 Optimisation of process parameters for 1×1 braid

The 1×1 diamond braid had the same diameter as the 2×2 regular braid but was produced using half the carriers. Therefore, the braided tows covered relatively less surface area, leaving large visible gaps in between as compared to the regular braid. This is depicted in Figure 4.17. Consequently, achieving adequate consolidation would likely require longer impregnation distances as compared to the 2×2 braid.



| (a) | (b) | (c) | (d) |
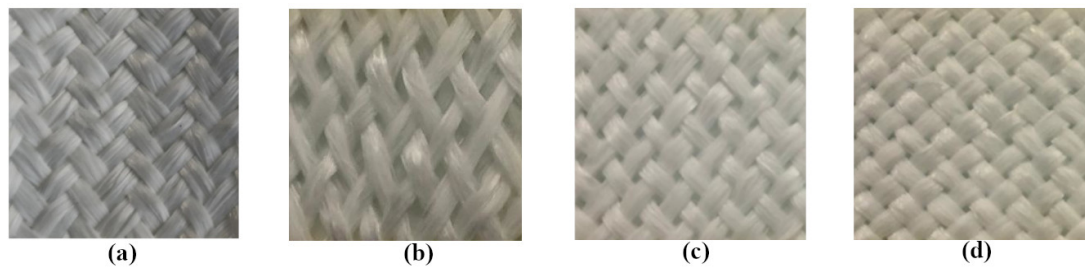
Figure 4.17 (a) 2×2 regular 45° preform; 1×1 diamond preforms with braid angles of (b) 30°, (c) 45° and (d) 60°.

Thus, a different set of the processing parameters: consolidation time, temperature and pressure, was required for the 1×1 braid. Among these three parameters, the consolidation pressure and temperature were limited to 20 bar and 250 °C respectively because of the limited high temperature durability of the silicone rubber bladders, as observed in preliminary trials on the RVM tool. Processing beyond both these limits had resulted in bladder bursts during trials. Therefore, experimental trials were performed to optimise the remaining parameter, i.e. consolidation time. Three levels of consolidation time were selected: 8 minutes, 15 minutes and 20 minutes. One 1×1 diamond braid with a 45° braid angle was manufactured using each consolidation time. The outer surfaces of the three manufactured beams are shown in Figure 4.18.

**(a)**           **(b)**           **(c)**
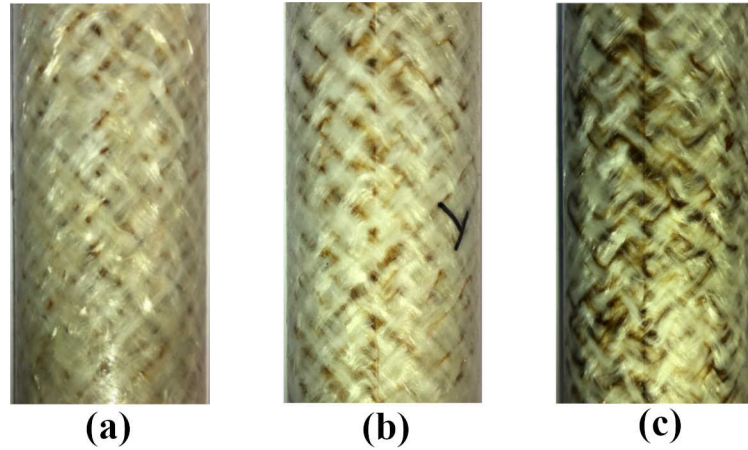
Figure 4.18 Braided beams processed using consolidation times of (a) 8 min, (b) 15 min and (c) 20 min.

An improvement in consolidation with increasing consolidation time was visible from 8 to 15 minutes through a reduction in the content of dry fibres on the outer surface. However, beams consolidated for 15 and 20 minutes did not have a significant difference in outer surface dryness. Moreover, discolouration similar to the BIM beams was observed on the outer surface, which increased with consolidation time. It is noteworthy that the discolouration in diamond braids was greater than the regular braids, which indicated a possible correlation between discolouration and the surface area coverage of the fabric. Previous literature has linked this discolouration with thermo-oxidative degradation of the PA6 [175,176]. Moreover, a review paper by Levchik *et al.* [177] reported links between the discolouration of PA6 and the surrounding environment and also showed that heating the polymer for longer durations aggravated the effect. In order to confirm the hypothesis, 5 cm long commingled tows extracted from the braided fabric were heated in an ambient atmosphere and argon separately. The fabric heated in the presence of argon displayed no discolouration, which confirmed that the interaction of ambient air with the PA6 at high temperature was responsible for the discolouration. This is depicted in Figure 4.19. Therefore, the larger gaps between braided tows in the diamond braid as compared to regular braid resulted in greater interaction with air, which in turn led to greater discolouration in the finally produced beam.
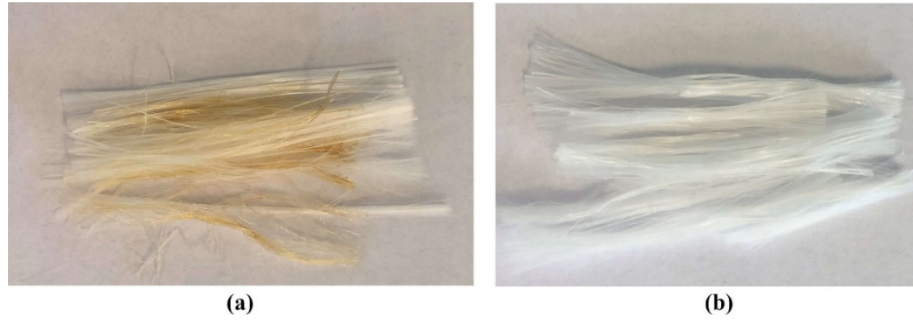
Figure 4.19 Retrieved commingled fabric after heating to 250 °C: (a) visible brownish discolouration upon heating in an ambient atmosphere with exposure to air and (b) no discolouration upon heating in an inert argon atmosphere.

The beam consolidated for 15 minutes was a reasonable compromise between surface dryness, i.e. consolidation quality, and discolouration. Therefore, a consolidation time of 15 minutes was used in the manufacturing of all braided beams in this work.

## 4.3    Moulding of braided beams for mechanical testing

This section details the final established procedure for consistent manufacturing of beams. As the braided beams were manufactured with the purpose of testing and comparing their performance in three-point flexure, it was essential to minimise the effect of uncontrolled factors on the mechanical performance of the beams, thus ensuring that the univariate comparative analysis based on braid angle is valid. Therefore, certain modifications were introduced at different stages of the manufacturing process. These modifications are described below:

**(i)    Drying of fabric before moulding**

As PA6 is hygroscopic, the material could absorb moisture. This is detrimental for final part quality as the moisture can expand during the moulding process and result in voidage. Therefore, as discussed in Chapter 3, the braided preforms were always wrapped in cushioned plastic during transport and storage. Moreover, prior to the moulding process, the braided preforms were dried in an industrial dryer at 70 °C for 24 hours to remove absorbed moisture from the fabric. A 1% drop in preform mass was observed after the drying process.

76

## (ii) Bladder pressure in heating phase

After loading the preform assembly into the mould and closing the press, an internal bladder pressure of 4 bar was applied during the heating phase. This ensured that the braided fabric was in contact with the tool surface and also removed excess air from the mould cavity. Upon reaching the consolidation temperature of 240 °C, the pressure was increased to 20 bar. Following the consolidation phase of 15 minutes, the bladder pressure of 20 bar was maintained as the part cooled down to the demoulding temperature.

## (iii) Demoulding temperature

Demoulding temperature is critical to avoid the formation of residual stresses in the part [178]. While pursuing shorter cycle times, usual industrial practice is to demould semi-crystalline thermoplastics when the temperature drops below the recrystallisation temperature and allow the part to cool down to the room temperature in ambient conditions. However, this uncontrolled cooling could result in a mismatch in the cooling rates in different parts of the thermoplastic component, giving rise to residual stresses. As the braided composite beams manufactured in this work were for the sole purpose of mechanical testing, part quality was prioritised over cycle time. Therefore, demoulding was carried out at a temperature of 50 °C, which is below the glass transition temperature of PA6, thus limiting the residual stresses in the parts.

The modifications discussed above resulted in a total press cycle time of 37 minutes. Figure 4.20 shows the finally developed process profile for the parts manufactured for testing.
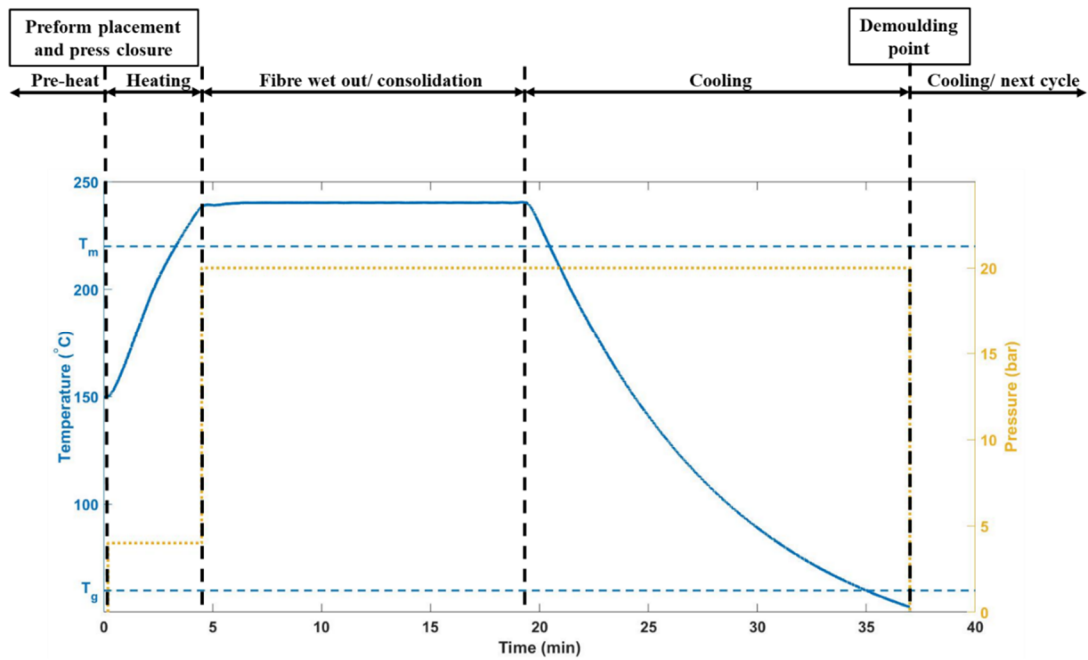
Figure 4.20 RVM process profile showing pressure and temperature during the process cycle.
Note: melt temperature and glass transition temperature of PA6 are shown for reference;
temperature represents average measurements of the internally embedded thermocouples.

## 4.4    Quality assessment of manufactured beams

Using the RVM process established in the previous section, seven beams of each braid
angle were manufactured. The outer and inner surfaces of the consolidated 30°, 45° and
60° braided beams are shown in Figure 4.21(a), (b) and (c).



(a)                          (b)                          (c)
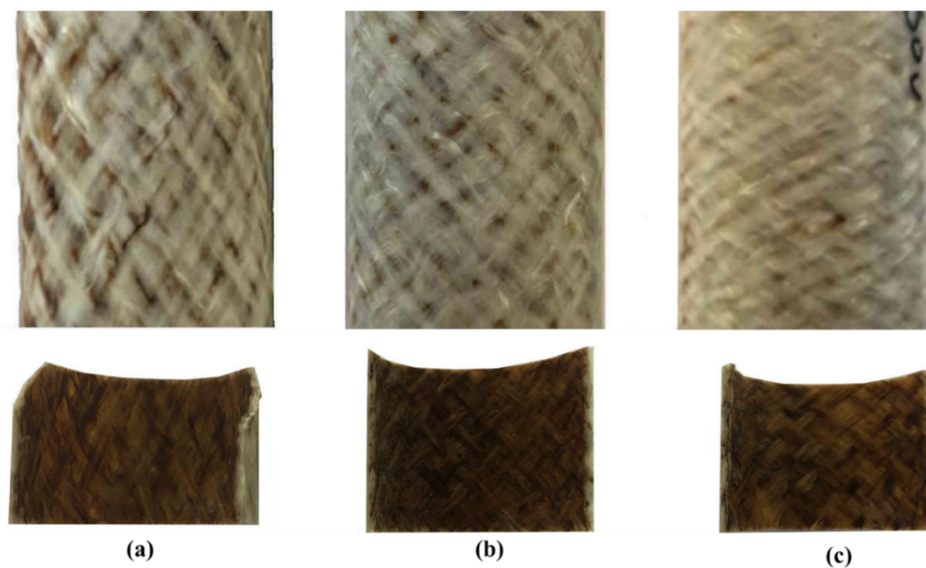
Figure 4.21 Outer and inner surfaces of (a) 30°, (b) 45° and (c) 60° braided beams produced
using RVM.

78

Similar to the flattened braids shown in Figure 4.17, an increase in the surface area covered by the fibres was observed with increasing braid angle. This was in agreement with previous studies [179]. Brownish discolouration was observed on the outer surfaces of the beams. On the outer surface, the degree of discolouration appeared to decrease with increasing braid angle, however, all the beams showed similar levels of discolouration on the inner surfaces. Patches of dry fibres and intermittent fibre waviness were also observed on the outer surfaces of the consolidated beams. This suggested that there remained scope for further improvement in the consolidation parameters. The abovementioned defects were characterised using suitable techniques and their effect on the mechanical performance are detailed in Chapter 5. Similar to the 2×2 braided beams, the braid angle was measured at 20 random locations on the outer surfaces of six beams for each braid angle. These measurements are shown in Figure 4.22.
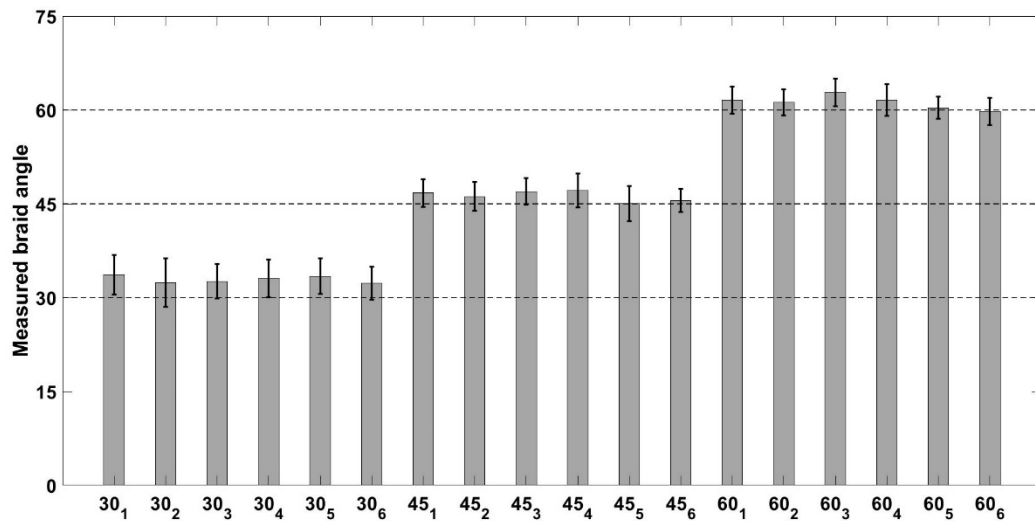


Figure 4.22 Measured braid angle values for braided beams produced using 1×1 fabric.

Relative to the 2×2 braided beams, there was a significant improvement in the mismatch between the measured and expected braid angle values. Figure 4.23 depicts the masses of the beams, which increased with braid angle and were in good agreement with the analytically predicted values.
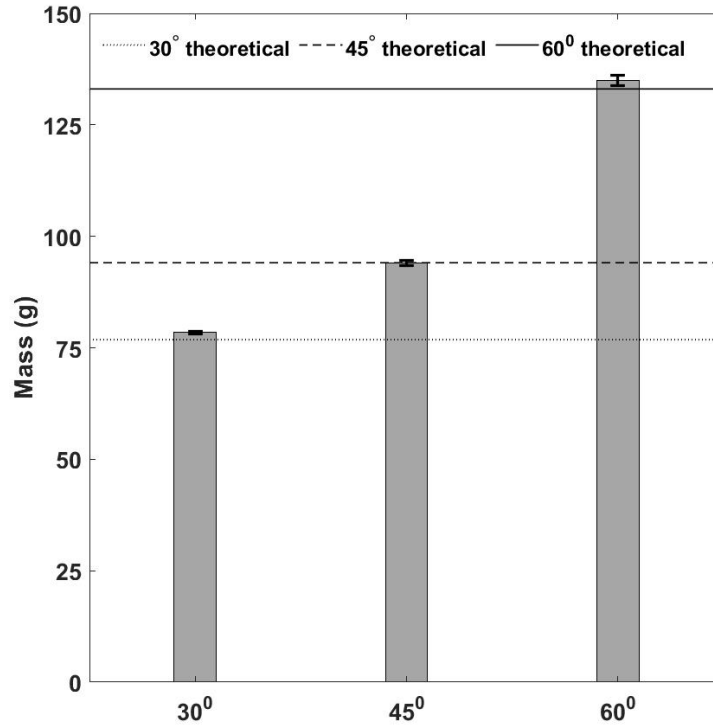
Figure 4.23 Measured mass of braided beams produced using 1×1 fabric.

The braid angle measurements on the 30° beams showed the maximum offset with respect to the target angle, however as shown in Figure 4.22, the offset was consistent across all 30° beams. Additionally, unlike the 2×2 braided beams, neither the braid angle measurements nor the mass values showed any overlap between the beams with different angles. Therefore, the manufactured 1×1 diamond braided beams were found suitable to conduct mechanical testing.

## 4.5   Summary

This chapter described the development and improvement of the novel RVM process.

The ability to monitor and control the discrete channels of the tool individually was found to result in a uniform temperature profile throughout the part. The achieved repeatability and precision in thermal control, which is not possible in conventional BIM, eradicated the influence of uncontrolled variabilities during the manufacturing process, thus producing braided beams suitable for mechanical testing.

The responsive nature of the tooling also resulted in a significant reduction in part cycle

time compared to the conventional BIM process, thus improving the readiness for high volume manufacturing. The cycle time of the RVM process could be further optimised, but falls out of scope as the focus of the process development here was to produce beams with consistent quality for the subsequent mechanical testing.

The 2×2 regular braided beams manufactured during initial manufacturing trials were found unsuitable for the mechanical test program due to inconsistency in braid angle. This was likely due to specific considerations at the time of manufacture that could be addressed with further work. It was shown through a comparison of measured beam masses with analytically calculated values that the braid angle could not be controlled during the braiding process for the 2×2 braid architecture. Therefore, a 1×1 diamond braid architecture was chosen for manufacturing the beams.

Fibre waviness observed on the outer surface of the beams during the trails was significantly reduced by reducing the mandrel diameter to 25 mm. Also, a different set of manufacturing parameters were developed to optimise part quality for the 1×1 braided beams. The resultant part cycle time was 37 minutes. The finally established RVM process profile was used to manufacture beams with different braid angles. The mass and braid angle measurements of the manufactured beams were found to be consistent across all repeats, which confirmed their fitness for mechanical testing. The next chapter details the results of the three-point flexure tests of the manufactured beams and provides further quality evaluation results as well as their implications on the comparative mechanical performance analysis.

# 5 Effect of braid angle on the flexural performance of braided thermoplastic composite beams

This chapter presents the three-point flexural test results of braided beams with different braid angles. The chapter commences with a quality evaluation of the braided beams manufactured using the RVM process. This includes a detailed analysis of beam composition and thickness. This is followed by a comparison of the load-displacement data obtained from three-point flexural tests. Using visual observations of the deformed beams as well as the recorded localised crushing data, the dominant modes of deformation and their dependence on braid angle are evaluated. Finally, surface strain and displacement data available from the optical strain measurements are presented and further insights into the beam deformation are provided. The observed mechanical performance will guide the subsequent tailor-braiding strategy and also serve as a benchmark for assessing the performance of the manufactured tailor-braided beams.

## 5.1   Evaluation of part quality

### 5.1.1   Resin burn-off results

The $F_{vf}$ and $V_{vf}$ values of the braided beams determined from resin burn-off experiments (described in section 3.3.1) are listed in Table 5.1.

Table 5.1 $F_{vf}$ and $V_{vf}$ estimated from resin burn-off. Note: values represent mean ± std. dev.

|  | $F_{vf}$ (%) | $V_{vf}$ (%) |
|---|---|---|
| **30°** | 48.8 ± 1.1 | 7.8 ± 1.2 |
| **45°** | 49.9 ± 1.1 | 8.5 ± 1.2 |
| **60°** | 49.6 ± 1.1 | 10.5 ± 0.8 |

Single-factor Analysis of Variance (ANOVA) was performed to statistically compare the $F_{vf}$ and $V_{vf}$ obtained for the three braid angles. A 95% confidence level was used. The corresponding p-values for the $F_{vf}$ and $V_{vf}$ comparisons are listed in Table 5.2.

Table 5.2 p-values corresponding to $V_{vf}$ and $F_{vf}$ comparisons obtained from ANOVA.

| | p-value |
|---|---|
| $V_{vf}$ | 0.002 |
| $F_{vf}$ | 0.236 |

The p-value corresponding to $F_{vf}$ is greater than 0.05. Therefore, the ANOVA results indicate that the $F_{vf}$ values did not differ significantly between the braided beams with different braid angles. The lack of correlation between $F_{vf}$ and braid angle was due to the predetermined composition of the commingled preforms used to manufacture the braided beams. Similar observation was reported by Laberge-Lebel [93] for rectangular braided coupons manufactured using a commingled carbon fibre-PA12 system. However, the p-value for $V_{vf}$ is less than 0.05, which indicates that the void content was significantly different between the three beams. In order to analyse the difference in the $V_{vf}$ values, a post hoc analysis was performed using the Tukey-Kramer method [180]. As per the method, the Studentised range statistic q was evaluated for each pair using Equation 5.1. In this equation, $q_{AB}$ is q-statistic for the pair A-B, $\mu_A$ is mean for sample A, $\mu_B$ is mean for sample B, $n_A$ is sample size of A, $n_B$ is sample size of B and $MS_W$ is mean square error within samples.

$$q_{AB} = \frac{|\mu_A - \mu_B|}{\sqrt{\frac{MS_W}{2}\left(\frac{1}{n_A} + \frac{1}{n_B}\right)}} \hspace{3cm} \text{Equation (5.1)}$$

If the evaluated q value is greater than the critical value of q, determined from the q-table, it implies that the difference between the means corresponding to the respective pair of samples is statistically significant. The obtained q-values corresponding to every comparison are listed in Table 5.3.

Table 5.3 q-values obtained from Tukey-Kramer post-hoc analysis performed for $V_{vf}$. Note: values indicating a statistically significant difference are underlined.

| Pair | q ($V_{vf}$) | $q_{critical}$ |
|---|---|---|
| 30°- 45° | 1.70 | 3.67 |
| 45°- 60° | <u>4.22</u> | 3.67 |
| 30°- 60° | <u>5.92</u> | 3.67 |

The results indicate that the $V_{vf}$ of the 30° and 45° beams are similar, while the voidage is greater for the 60° beams. As higher void content typically results in reduced mechanical properties of composite structures [158], the three-point flexural response of the 60° beams would be expected to be more severely affected as compared to the 30° and 45° beams.

## 5.1.2    Braid geometry measurements

As discussed in Chapter 3, an image analysis software was used to measure beam thickness from the cross-section image generated using a macro zoom camera. The measured thickness values were distributed in increasing bands of 0.05 mm between the maximum and minimum values for each braid angle. The resulting distributions are shown in Figure 5.1 in the form of frequency line plots.
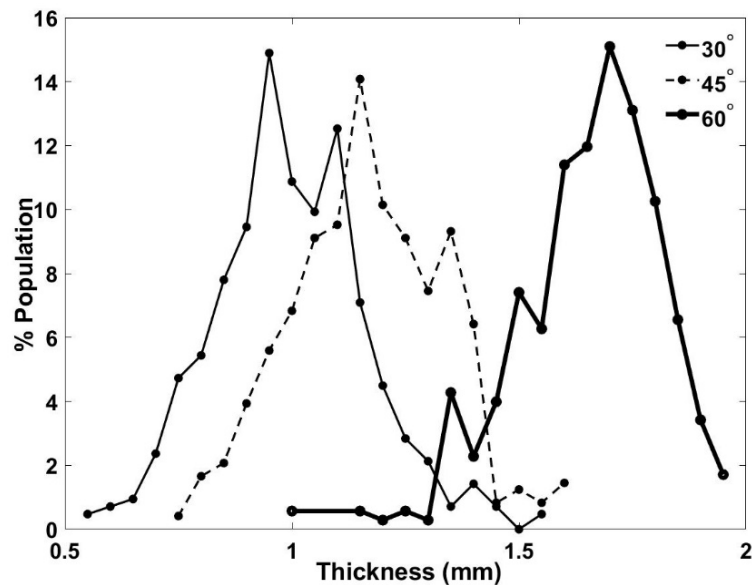


Figure 5.1 Measured thickness for braided beams with different braid angles. Note: Thickness values are grouped in bands of 0.05 mm.

For each braid angle, the thickness distribution showed a significant spread. This observed variation could be explained as follows. As discussed in Chapter 2, a dry braided preform inherently has an undulating texture because of the interlacement of reinforcement fibres. Upon braiding multiple layers, the fibre tows are positioned either directly over the tows or in the inter-fibre gaps in the braided layer underneath. This random stacking in a multi-layered braided preform increases the thickness variation.

During the RVM process used in this work, the braided preforms with such randomly stacked tows were in contact with non-rigid silicone rubber bladders on the inner surface. Therefore, the conformable nature of the bladders resulted in a retention of the undulating texture of the braid. These undulations manifested in the form of the thickness variations observed in the consolidated braided beams. Moreover, during the consolidation phase of the process, the lateral flow of the molten polymer could also have caused an agglomeration of the fibre tows, leaving gaps in the surrounding regions, thus contributing to the thickness variation.

The mean, maximum and minimum thickness for each braid angle are listed in Table 5.4. The histograms show that the thickness increased with braid angle. The mean thickness increased by 18% from the 30° to 45° beam, while the increase from 45° to 60° was 42%.

Table 5.4 Mean, maximum and minimum thickness values measured for different braided beams. Note: All values are in mm.

| Thickness | 30° | 45° | 60° |
|---|---|---|---|
| Mean | 0.972 | 1.145 | 1.630 |
| Maximum | 1.503 | 1.596 | 1.934 |
| Minimum | 0.526 | 0.747 | 1.118 |

Besides thickness, braided tow width was measured on the outer surface of the untested braided beam for each braid angle at 25 randomly located points. The measured tow width was used to analytically determine the cover factor, i.e. surface area of the braided composite covered by the braided fibres, as per Equation 5.2. Further details of the analytical calculations can be found in references [181,182]. In the equation, $w_t$ is tow width (mm) and $N_c$ is the number of carriers used in braiding.

$$\text{Cover factor} = 1 - \left(1 - \frac{w_t N_c}{2\pi D \cos \alpha}\right)^2 \qquad \text{Equation (5.2)}$$

Table 5.5 shows the measured tow width and the analytically estimated cover factor for beams with different braid angles. The width of the tows decreased with increasing

braid angle, while the cover factor increased, which is in agreement with previously reported results.

Table 5.5 Tow geometry parameters corresponding to different braided beams. Note: tow width values represent mean ± std. dev.

|  | 30° | 45° | 60° |
|---|---|---|---|
| **Tow width (mm)** | 3.18 ± 0.18 | 2.69 ± 0.16 | 2.23 ± 0.14 |
| **Estimated cover factor** | 78.3% | 80.2% | 87.7% |

### 5.1.3 Microstructural analysis

Figure 5.2 shows selected micrographs of the three beams (30°, 45° and 60°).
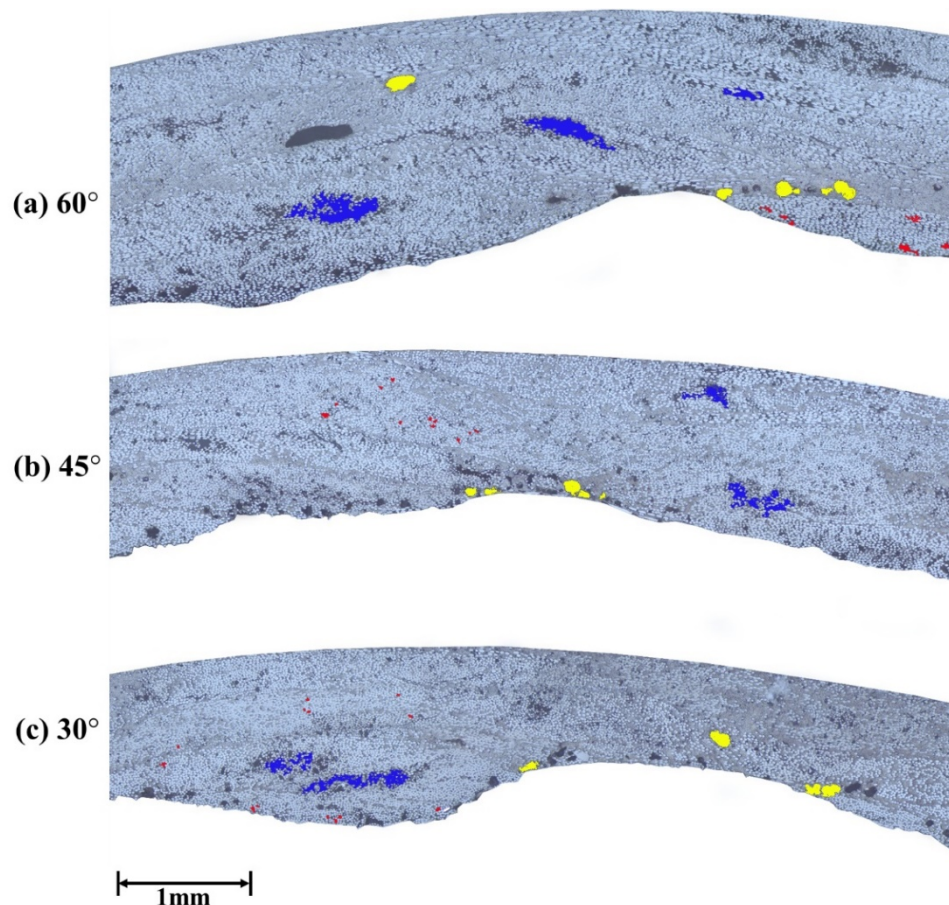


Figure 5.2 Micrographs of braided beam sections with braid angles of (a) 60°, (b) 45° and (c) 30°. Note: Coloured regions highlight a representative selection (non-exhaustive) of intra-tow micro (Red), intra-tow macro (Blue) and inter-tow voids (Yellow).

The observed material distribution displaying resin rich pockets between fibre tows is characteristic of braided composites. Three types of voids were identified from the micrographs:

(a) Intra-tow micro voids: Circular voids visible as dark spots between fibre filaments.

(b) Intra-tow macro voids: An agglomeration of multiple micro-voids that lead to the formation of larger voids, often elliptical in shape.

(c) Inter-tow voids: Voids in the resin-rich pockets between fibre-tows.

The effect of the difference in void content on the comparison of mechanical performance between the three different beam variants is discussed in the next section. In addition to void fraction, void characteristics such as location, morphology and distribution also individually influence mechanical performance [183,184]. Moreover, previously conducted investigations have shown that the effects of the void characteristics on mechanical performance are specific to material as well as load cases [70]. Therefore, a discrete work package would be required to establish the absolute effect of voidage on the performance of the beams tested in this work, which was considered out of scope of this study.

## 5.2 Static three-point flexure performance

Figure 5.3 shows the load-crosshead displacement curves obtained from the three-point flexure tests. The crosshead displacement was limited to 18 mm for all the beams, as further applied displacements led to visible lateral movement at the beam-support roller interface.
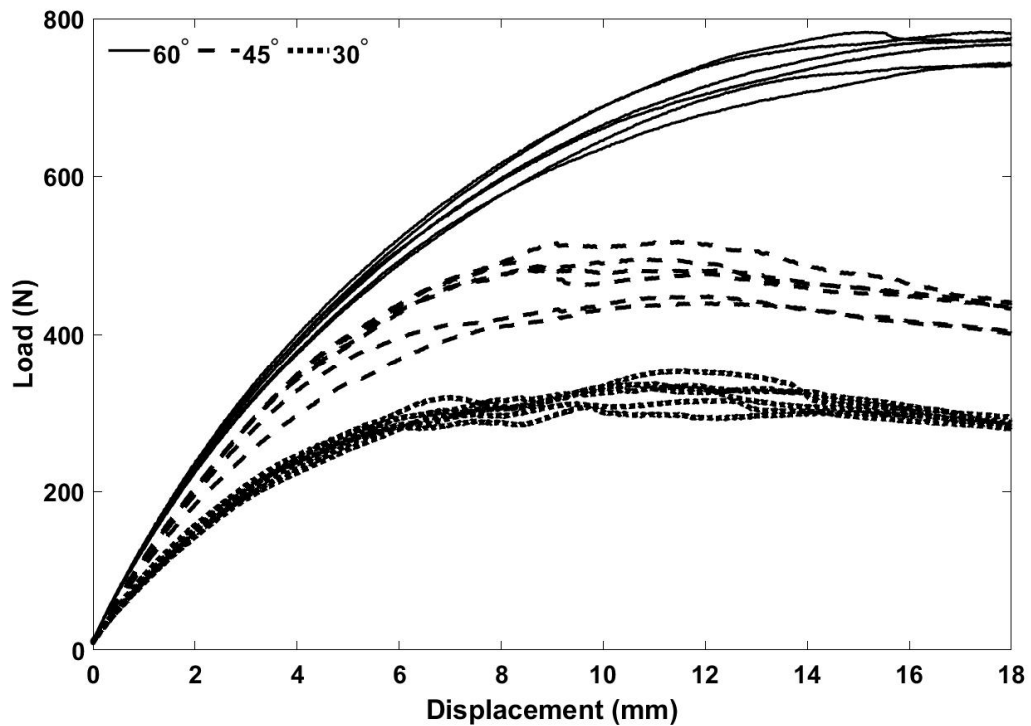
Figure 5.3 Load-crosshead displacement data from three-point flexure experiments for 6 repeats of each 30°, 45° and 60° beam sets.

The load-displacement curves corresponding to different braid angles form three discrete populations. This indicates a significant dependence of the mechanical response on braid angle, which directly influences both material properties and beam thickness. Each response showed an initial increase in load. During this load rise, audible cracking was noted for all the beams. For the 60° beams, the load generally increased throughout the deformation, with a visible plateauing within the last one millimetre of crosshead displacement. On the other hand, for the 45° and 30° beams, the load increased to a local maximum followed by undulating load profiles with multiple peaks and troughs, ending with an ultimate steady decline.

Figure 5.4 shows one deformed beam for each braid angle in the test setup before unloading. The visible differences in the cross-sectional depth and bottom surface curvatures between the three beams indicate the correlation between the deformation modes and braid angle. Cracks were observed ex-situ in the loading area for every beam. These cracks originated in the region in direct contact with the loading roller and propagated along the braided fibres. None of the beams had visible damage in the region of the beam opposite the central loading point.
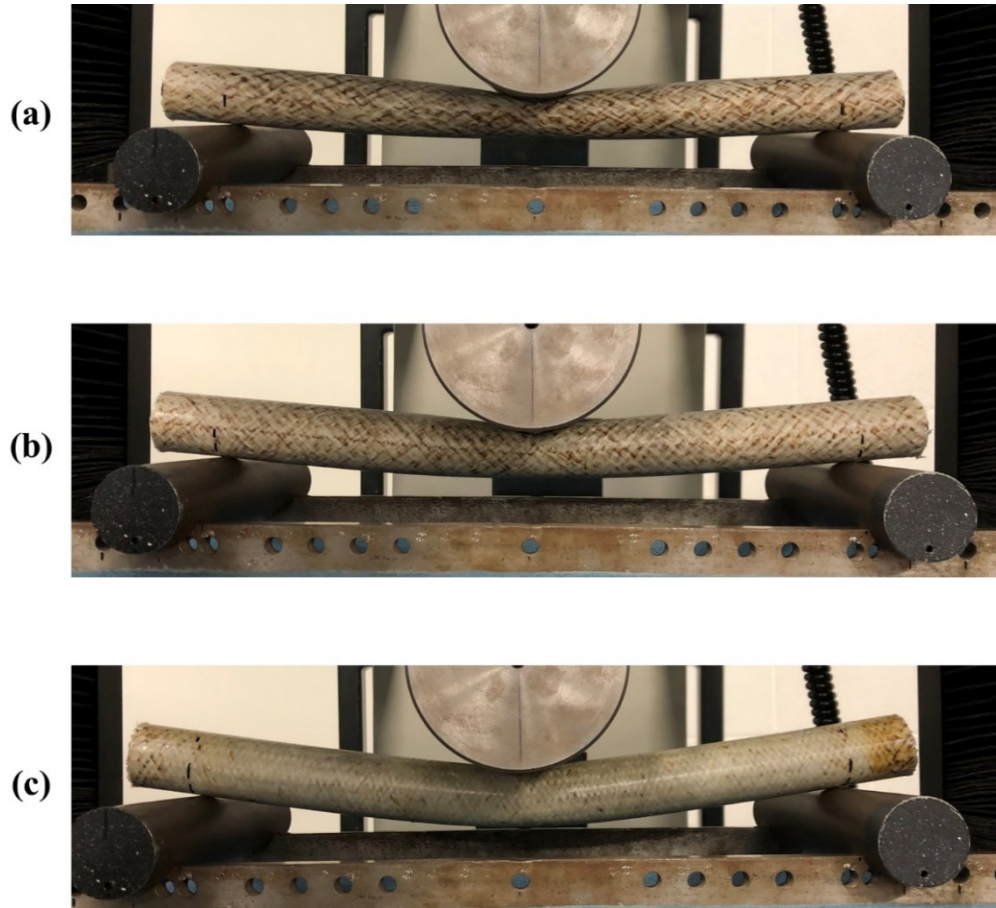
Figure 5.4 Beams with braid angles of (a) 30°, (b) 45° and (c) 60° in the test fixture after 18 mm of crosshead deflection.

A closer view of the unloaded deformed beams revealed that there was a transition from a single-region contact at the start of the test to a double-region contact at the loading roller-beam interface. The contact transitions were more noticeable for the 30° and 45° beams as compared to the 60° beams. Therefore, it is reasonable to assume that the localised contact-dependent damage propagation was responsible for the variable trends observed in the load-displacement curves. After unloading the beams, the 30° and 45° beams returned to their original shape, while the 60° beams had a noticeable permanent curvature.

The extent of localised crushing, estimated using the difference between the crosshead position and the deflectometer position, is plotted against crosshead displacement in Figure 5.5. The curves show that the localised crushing initiated with the onset of flexural deflection and progressed with an approximately linear trend. For a crosshead displacement of 18 mm, the localised crushing accounted for approximately 63%, 45%

and 19% of the applied crosshead deflection for 30°, 45° and 60° beams respectively. Therefore, localised crush was the dominant deformation mode for the 30° beams, while global flexure was observed to dominate for the 60° beams. The response of the 45° beams was intermediate between the 30° and 60° beams.
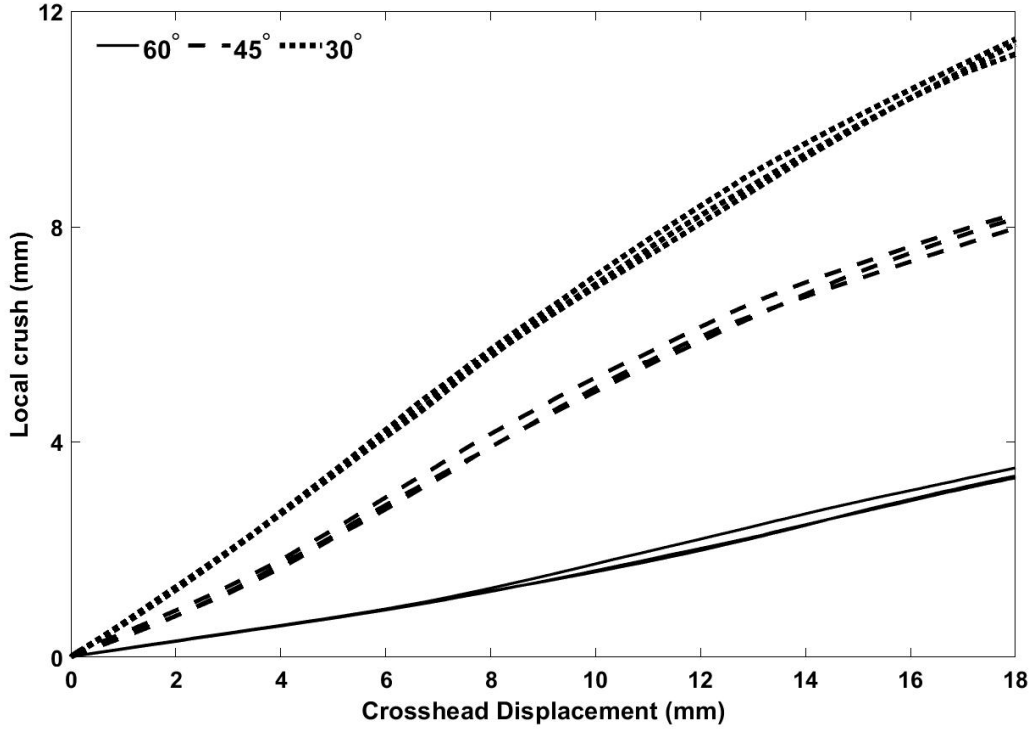


Figure 5.5 Progression of localised crushing (from the difference between crosshead displacement and the deflectometer displacement) during three-point flexure.

The stiffness of the braided beams during the three-point flexure tests was determined using a chord definition represented in Equation 5.3. In this equation, S is stiffness (N/mm), P is load (N) and d is crosshead displacement (mm).

$$S = \frac{\Delta P}{\Delta d}$$
<div align="right">Equation (5.3)</div>

The displacement range between 0.2 mm and 1 mm was considered for the stiffness calculations. In this range, the per cent localised crushing was 62%, 38% and 15% for the 30°, 45° and 60° beams respectively. The 60° beams showed the highest stiffness and peak load values, which are shown for the three braid angles in Figure 5.6.
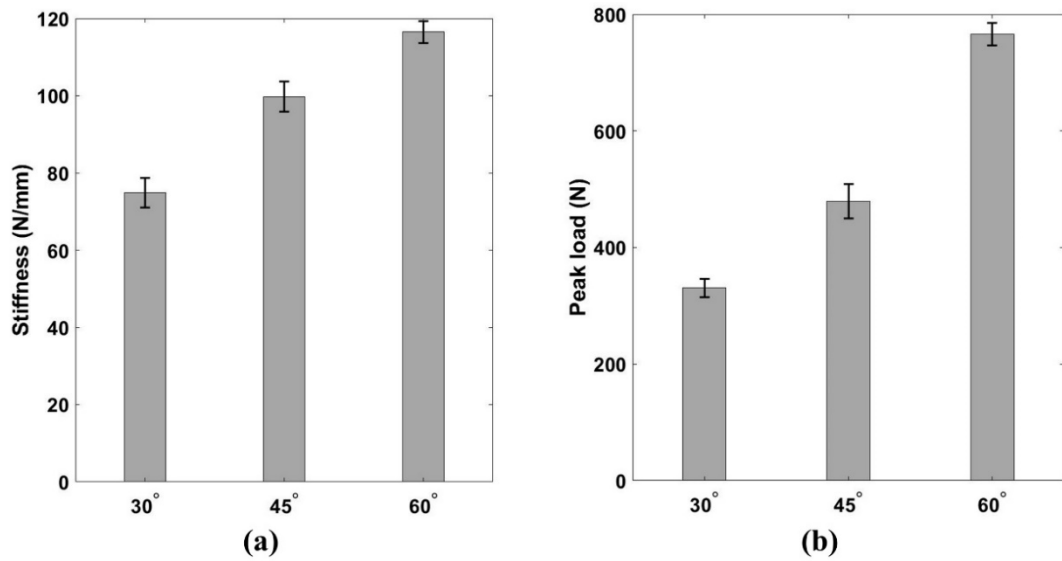
Figure 5.6 (a) Stiffness and (b) peak load data for different beams. Note: bars represent mean values from 6 repeats and errors represent one standard deviation.

It is important to note that stiffness and peak load here are indicators of structural mechanical response, which is a combination of the material characteristics of the beam as well as the beam section geometric properties. The average stiffness of the 45° and 30° beams were 14% and 36% lower relative to the 60° beams respectively. Similarly, the average peak load values were 37% and 57% lower respectively. This suggests that the effect of the aforementioned observed small disparity in void content is not a dominant factor upon the flexural response and the analysis based on the braid angle of beams remains meaningful.

The observed trends of stiffness and peak load are in disagreement with the results reported by Potluri *et al.* [124] using coupon scale beams. This disagreement was likely due to the localised crushing observed in the present work, which was not observed previously. However, the work by Potluri *et al.* studied thermoset matrix-based composites and did not report the number of test repeats, which made it difficult to perform a conclusive comparison.

### 5.2.1 DIC analysis

As discussed in Chapter 3, 3D DIC was used to record the surface deformation characteristics for one specimen of each beam type. The bias and precision of displacements and strains from a series of static images were calculated to estimate the

accuracy of the DIC setup. The corresponding mean values recorded during the testing of the 30°, 45° and 60° beams are shown in Table 5.6.

Table 5.6 Mean bias and precision of DIC measurements estimated from static images.

| Mean bias [$\varepsilon_x$ (%)] | Mean precision [$\varepsilon_x$ (%)] | Mean bias [dx (mm)] | Mean precision [dx (mm)] | Mean bias [dy (mm)] | Mean precision [dy (mm)] |
|---|---|---|---|---|---|
| 0.0001 | 0.0162 | 0.0029 | 0.0003 | -0.0007 | 0.0004 |

The evolution of axial strain ($\varepsilon_x$), i.e. surface strain along the beam axis, is shown for the three braid angles in Figure 5.7(a). The load-crosshead displacement response of the beams tested with the DIC measurements are also shown in Figure 5.7(b) for reference. A non-uniform distribution was observed in all the strain profiles.
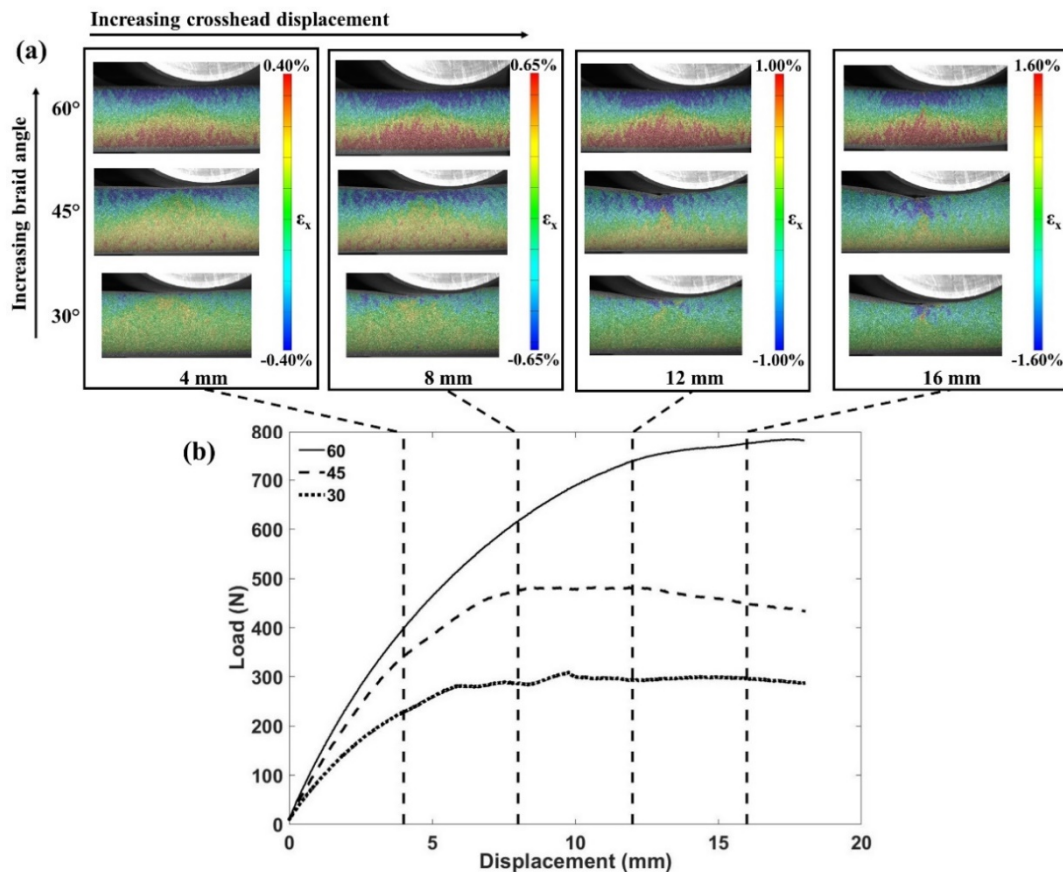


Figure 5.7 (a) $\varepsilon_x$ progression with crosshead displacement during three-point flexure and (b) load-displacement curves corresponding to the beams tested with DIC measurement.

92

The strain profile corresponding to the 60° beam approximates to pure flexure with distinguishable bands of compressive and tensile strains of similar magnitude in the top and bottom regions of the beam. These strain bands were symmetric about the central load introduction point and maintained their trends with increasing deflection. The effect of localised crushing appeared towards the end of the deformation in the form of minimal observable strain localisation in the upper loading region. Contrary to the 60° beam, the severe localised crushing in the 30° beam resulted in concentrated zones of compressive strain in the top region (around the central roller), while negligible strain was observed in the bottom region. With increasing crosshead displacement, the cracks propagated from the central loading point and appeared in the RoI. This was accompanied by further strain concentration in this loading region. The 45° beam showed emerging compressive and tensile strain bands similar to the 60° beam during the initial phase. However, the magnitude of the bottom region tensile strain was significantly lower. As the localised damage progressed into the RoI, strains became concentrated in the upper loading region similar to the 30° beam.

The minimal strain in the bottom region for the 30° and 45° beams was a consequence of severe localisation of the deformation in the loading region. Similarly, although greater tensile strain was recorded in the bottom region of the 60° beams, there was an observable localised strain in the loading region during the later stages of the crosshead movement. For all the beams, the observed localisation of the deformation likely occurred before the bottom region strain exceeded the critical (tensile) failure strains of the braided composite beams being tested. Hence, no visible cracks/damage in this part of the beams was observed.

In order to further explore the differences in strain distribution that arose during loading of the beams, three parallel horizontal sections were constructed on the beam surface using the GOM software, from which the flexural strain was computed, as shown in Figure 5.8. The figure also shows that the three computed sections flex with the increasing deformation. Along each section, the GOM Correlate interface was used to evaluate flexural strain, computed as the average of the axial strains calculated at all integration points along the chosen line section.

93
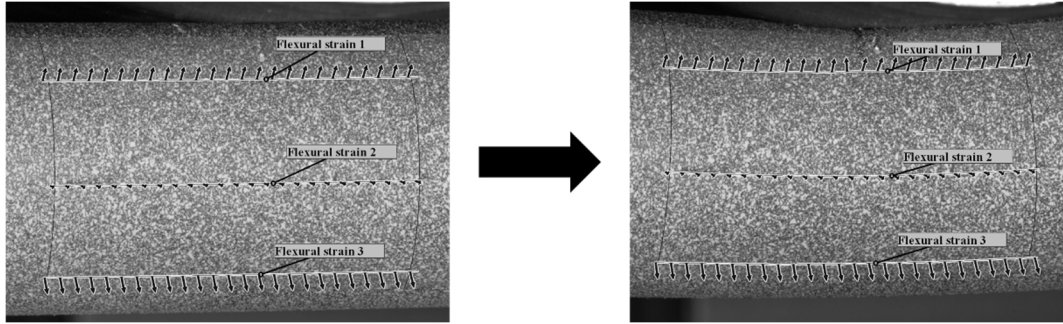
Figure 5.8  Horizontal sections (strain 1-3) constructed on the surface of a beam showing the initial (preloaded) condition and the condition at increased crosshead displacement.

The evolution of the flexural strains 1, 2 and 3, corresponding to the top, middle and bottom regions respectively, are plotted against crosshead displacement for different braid angles in Figures 5.9(a), (b) and (c).



(a) 30°



(b) 45°



(c) 60°
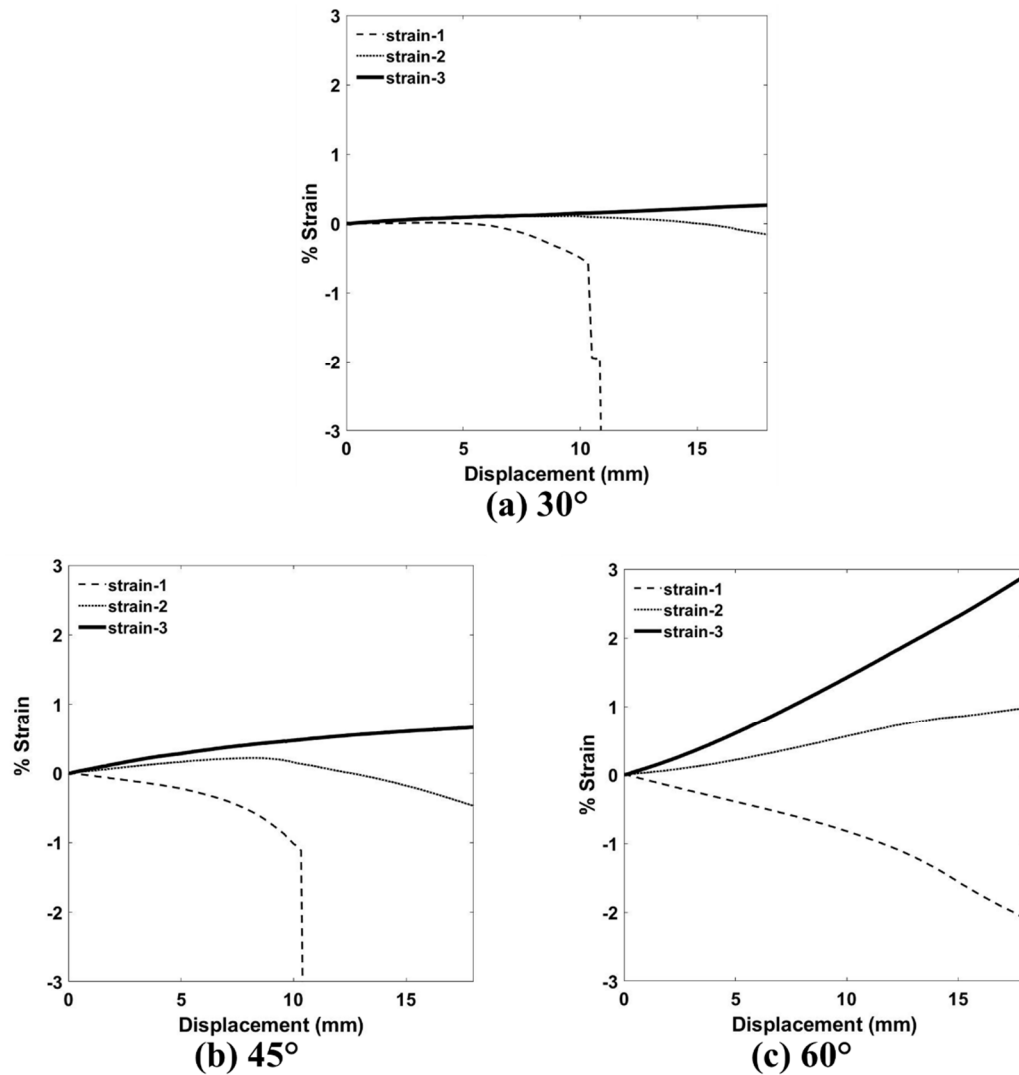
Figure 5.9 Evolution of flexural strain at 3 locations (strain 1-3) for braided beams during three-point flexure with braid angle of (a) 30°, (b) 45° and (c) 60°.

Irrespective of braid angle, the top and bottom region strains (strain 1 and 3) showed increasing compressive and tensile trends respectively throughout the deformation. Owing to the localised deformation, the top region strain measurements (strain 1) became invalid for the 30° and 45° beams once damage propagated into the uppermost section. Until that point, the top region strains showed comparable magnitudes for all braid angles. On the contrary, the strains in the bottom region (strain 3) calculated for the 30° and 45° beams were low in magnitude in comparison to the 60° beam. Quantitatively, the bottom region strains at test completion (a crosshead displacement of 18 mm) were 77% and 91% lower for 45° and 30° beams respectively as compared to the 60° beam. In the middle region (strain 2), the flexural strains were initially tensile for all the braid angles. However, as the deformation advanced and the 30° and 45° beams collapsed under the loading roller, the recorded strains transitioned into compressive domain, while the obtained strain in the corresponding middle region in the 60° beam remained tensile.

The observed disparity in the bottom region strains explains the difference in the final shape of the beams. For the 30° and 45° beams, the bottom region underwent negligible tensile straining, which was likely within the elastic limits of the material and therefore did not produce a permanent change in shape during the three-point flexure test. On the other hand, the greater tensile straining in the 60° beams appeared to have exceeded the elastic limit of the material under tension, thus resulting in a permanent deformation that was visible in the form of a shape change. A dedicated tensile test program would provide a quantitative comparison of the elastic limits of the braided composite beams with the observed strains, thus confirming the proposed explanations. Such a test program should be considered as a part of future research work.

In addition to these flexural strain analyses, three further parallel sections were constructed on the beam surface using the GOM software, as shown in Figure 5.10(a). The downward (y-) displacements were recorded on all the points lying on these sections with respect to the crosshead. Figure 5.10(b) shows the progression of section-wise y-displacements y1, y2 and y3 with increasing crosshead displacement. The increase in disparity between the three section-wise displacements with decreasing braid angle is a representation of the departure from pure global flexure and into

localised crush. Moreover, the increasing curvature of y3 with increasing braid angle further indicates the escalation of tensile deformation in the bottom region.



(a)



(b)
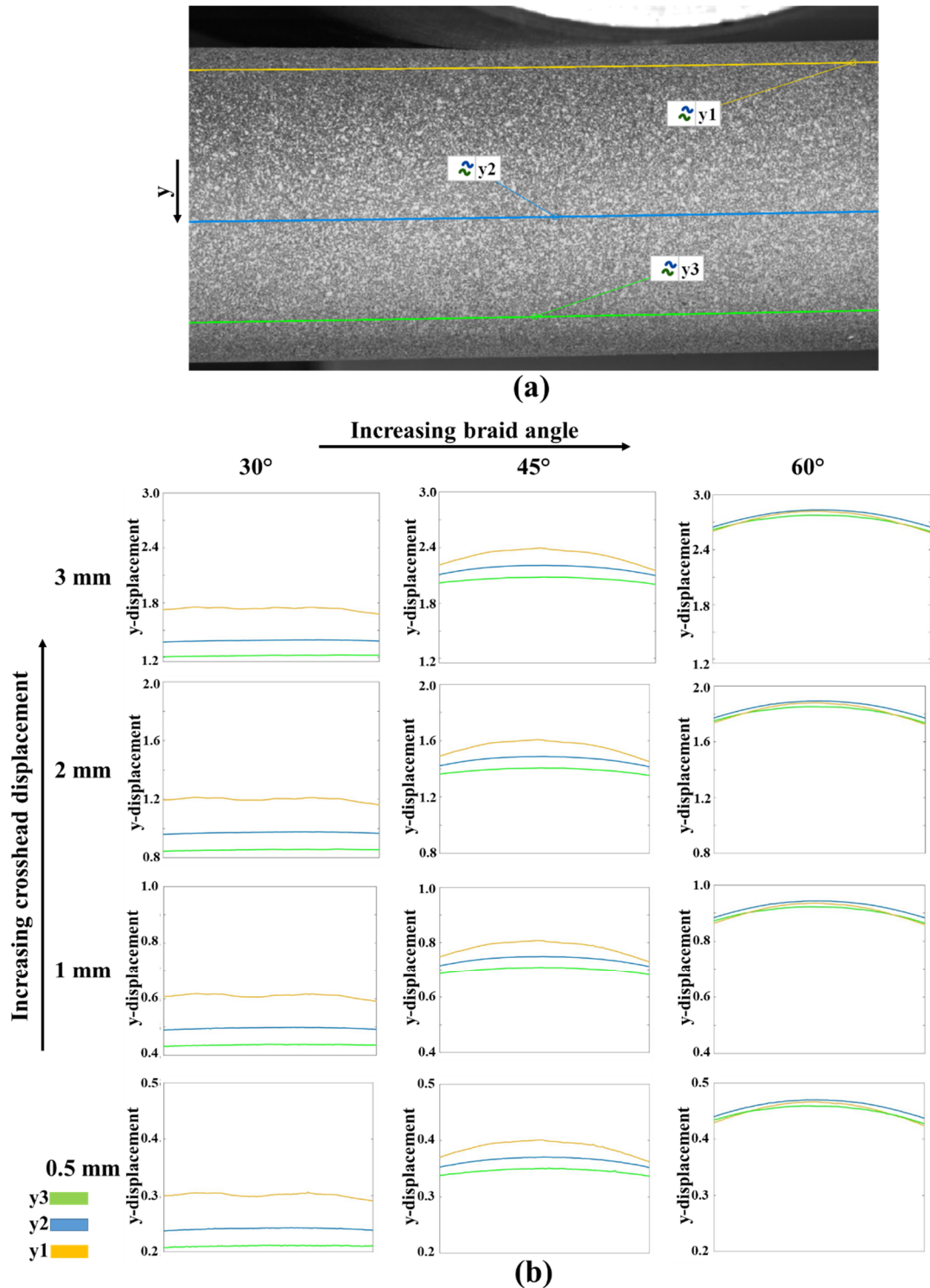
Figure 5.10 (a) Parallel sections y1-3 for comparing flexural displacements (y-, downward in the figure) on the surface of a beam and (b) evolution of downward y-displacement y1, y2 and y3 for beams with different braid angles during three-point flexure (increasing crosshead displacement).

The results are interesting in that the DIC measurements show that with decreasing braid angle, the bottom halves of the braided beams showed a decreasing tendency, i.e. away from flexural deformation. This was due to the localised crushing in the upper half of the beam accommodating most of the applied crosshead displacement. Moreover, the higher tensile strain measured in the bottom half of the 60° beam explains the plastic deformation (permanent curvature) observed after unloading.

The observed braid-angle dependence of the overall mechanical response is attributed to three braid angle dependent factors:

(i) **Thickness:** As per classical beam flexure theory, increasing the section thickness improves the resistance of a structure to flexural deformation. Furthermore, the proclivity of a hollow section for localised crushing decreases with increasing wall thickness. Therefore, an increase in wall thickness makes the beam more resistant against both deformation modes and is expected to render an improvement in mechanical response. As observed in previous studies as well as discussed here, the thickness of braided beams increases with braid angle.

(ii) **Material moduli:** Theoretically, axial modulus of a material is positively correlated to the resistance to flexural deformation in a structure. On the other hand, transverse modulus, directed along the hoop direction for a circular beam, would strengthen a beam structure against local crushing. For a braided composite, axial modulus decreases with braid angle, while transverse modulus increases.

(iii) **Surface Coverage:** The resin rich pockets present on the surface - as well as in the internal structure - often act as damage initiation sites for braided composites [107,108]. As discussed earlier, the surface fibre coverage of the braided beams increased with increasing braid angle. Therefore, the 30° beams, having the least fibre coverage, had relatively larger resin rich pockets on the outer surface, followed sequentially by the 45° and 60° beams. Thus, it is proposed that the interaction of the central loading roller with the increased level of resin rich regions in the 30° beams contributed to early initiation and propagation of localised damage.

The flexure test results show that increasing the braid angle resulted in enhanced mechanical performance. Moreover, the poorer mechanical performance of the lower braid angles coincided with greater local crushing. Considering the observed trends of the three discussed braid-angle dependent features as well as their expected influence upon deformation behaviour, the flexure test results indicate that resistance to localised crush was the critical performance factor for the beams characterised in this work. It is proposed that localised crush is an important consideration for thermoplastic composites in this particular loading configuration because of the lower stiffness and higher ductility of the matrix compared to thermosetting matrices, and thus explains any disagreement of the results obtained in this work with previously reported results from studies on the latter material type.

## 5.3   Summary

In this chapter, the static three-point flexure test results of braided composite beams with braid angles of 30°, 45° and 60° were presented. An evaluation of the beam quality was performed using resin burn-off experiments and optical microscopy, followed by a detailed analysis and comparison of voidage in the braided beams. The analysis revealed that the beams with different braid angles showed a statistically significant difference in the void content. However, a detailed understanding of the effects of voids on three-point flexural performance in such braided thermoplastic composite beam structures is out of the scope of this thesis. Results of the three-point flexural tests showed that the stiffness and peak load were positively correlated with braid angle, decreasing by 36% and 57% for the 30° beams compared to 60° beams respectively. The superior performance of the 60° beams despite their greater voidage indicated that the effect of braid angle on flexural performance dominated over the knockdown resulting from voidage. Hence, the performed single-factor analysis based on braid angle is valid.

During the three-point flexure tests, the applied flexural deflection manifested through two principal deformation modes: localised crushing and global flexure. Localised crushing was observed to account for 63%, 45% and 19% of the total deflection for the 30°, 45° and 60° beams respectively at the point of maximum experimental deflection.

Surface strain profiles obtained using 3D DIC showed significant variation between the beams with different braid angles, particularly on the lower face furthest away from the loading point. Analysis of the flexural strains as well as the transverse displacements showed significant tensile deformation in the bottom region for the 60° beam. On the other hand, the localised crush-dominant deformation led to minimal applied strains in bottom regions of the 30° and 45° beams.

The results indicated that resistance to localised crushing is a critical factor dictating the mechanical response of the braided beams tested in this work. It was speculated that the observed differences in the mechanical performance, as well as deformation modes, was a combined effect of three braid angle dependent factors: thickness, material moduli and surface fibre coverage. The observed trends of flexural performance disagreed with previously reported flexural results of coupon scale braided beams, which could be attributed to the effect of scale and test geometry of the beams as well as the use of relatively ductile lower stiffness thermoplastic matrix as opposed to thermoset matrices as studied previously. The obtained results were used to devise a strategy to manufacture tailor-braided beams and investigate their mechanical response, which is detailed in the next chapter.

# 6 Three-point flexural performance of tailor-braided thermoplastic composite beam structures

In this chapter, the three-point flexural test results of tailor-braided beams are presented and the effect of tailor-braiding on mechanical performance is established. It should be noted that to assist the clarity for the reader a specific nomenclature is adopted for this chapter as described next in this section. The chapter begins with the conception of a suitable strategy for length-wise tailoring of braid angle, i.e. axial tailor-braiding (TBr$_A$). This is achieved through a mass-normalised assessment of the flexural response of uni-braided beams, i.e. beams with uniform braid angles, which was presented in Chapter 5. Additionally, a layer-wise braid angle variation, i.e. radial tailor-braiding (TBr$_R$) is also considered for comparison. This is followed by a description of the adopted modifications in the braiding process to produce the tailor-braided preforms. The evaluation of quality of the manufactured tailor-braided beams is described next, followed by the comparison of their mechanical performance with the benchmark uni-braided beams. The chapter concludes with an analysis of the implications of the proposed tailor-braiding strategy with respect to weight-saving as well as the deformation behaviour of the braided beams.

## 6.1 Tailor-braiding strategy

The three-point flexure test results of uni-braided beams with braid angles of 30°, 45° and 60° were presented in Chapter 5. Due to time constraints, the tailor-braiding investigation was limited to two braid angles: 45° and 60°. As reported in Chapter 5, the applied crosshead displacement resulted in two principal deformation modes: global beam flexure and localised crushing. Quantitatively, 45% and 19% of the total deflection in the uni-braided 45° beams (UBr$_{45}$) and 60° beams (UBr$_{60}$) respectively was through local crushing. Beam deformation analyses indicated that for the tested uni-braided beams, resistance to localised crush was the critical governing factor in

overall mechanical performance. In addition to the two performance indices used in Chapter 5, i.e. stiffness (S) and peak load ($P_{max}$), energy absorption ($E_{abs}$) was evaluated for the $UBr_{45}$ and $UBr_{60}$ beams, as per Equation 6.1. In this equation, $E_{abs}$ is energy absorption (Nmm), P is load (N) and x is crosshead displacement (mm), which was limited to 18 mm during the tests.

$$E_{abs} = \int_0^{18} P \, dx$$                                                    Equation (6.1)

Compared to the $UBr_{45}$ beams, S, $P_{max}$ and $E_{abs}$ were 17%, 60% and 43% greater respectively for the $UBr_{60}$ beams, clearly demonstrating overall superior mechanical performance. However, comparing the average masses, presented in Chapter 4, showed that the relative improvement in the mechanical performance of the $UBr_{60}$ beams was accompanied with a 44% increase in mass compared to the $UBr_{45}$ beams. This data was used to calculate mass-normalised performance indices (S', $P'_{max}$, $E'_{abs}$), and these are shown in Figure 6.1 with the respective absolute performance indices (S, $P_{max}$ and $E_{abs}$) for both of the uni-braided beams.

Figure 6.1 Measured values of (a) S and S', (b) $P_{max}$ and $P'_{max}$ and (c) $E_{abs}$ and $E'_{abs}$ of the $UBr_{45}$ and $UBr_{60}$ beams. Note: bars represent mean values from six repeats and errors represent one standard deviation.

In order to compare the mass-specific properties, i.e. S', $P'_{max}$ and $E'_{abs}$, a single factor ANOVA was performed. A significance level of 0.05 was selected and the resulting p-values are listed in Table 6.1.

Table 6.1 p-values obtained from ANOVA performed for comparing the mass-normalised performance indices of $UBr_{45}$ and $UBr_{60}$ beams.

| Property | p-value |
|---|---|
| Specific Stiffness | 8.99E-07 |
| Specific Peak load | 0.002 |
| Specific Energy Absorption | 0.962 |

As the p-value for the mass-specific energy absorption ($E'_{abs}$) was greater than 0.05, it could be stated with 95% confidence that the difference in $E'_{abs}$ between the $UBr_{45}$ and $UBr_{60}$ beams was not statistically significant, however, differences between beams in specific stiffness (S') and specific peak load ($P'_{max}$) were statistically significant. Specifically, S' was 23% greater for $UBr_{45}$ beams, while $P'_{max}$ was 11% greater for $UBr_{60}$ beams. Therefore, despite the superior absolute performance of the $UBr_{60}$ beams, they did not offer a clear advantage from a structural lightweighting perspective over the $UBr_{45}$ beams under flexural loading.

These mechanical test results as obtained from the uni-braided beams were used as a baseline for devising a tailor-braiding strategy for the current study. Given the greater resistance of the $UBr_{60}$ beams to localised crush and the greater specific (flexural) stiffness of the $UBr_{45}$ beams, it was hypothesised that tailor-braided beams with a braid angle of 60° in the central loading region with adjacent regions of 45° located symmetrically on either side would result in overall improved mechanical performance compared to 45° beams, whilst being significantly lighter than $UBr_{60}$ beams. Therefore, as shown in Figure 6.2(a), a 45°/60°/45° configuration was selected for the $TBr_A$ beams. Moreover, recently reported results presented by Wu *et al.* [147] suggested that a radial variation can also modify the flexural response. Therefore, beams with a layer-wise braid angle variation, i.e. radial tailor-braiding ($TBr_R$), were also manufactured and tested for comparison. For the $TBr_R$ beams, as the outer layer directly interacts with the

loading roller, beams with two inner layers of 45° and an outer layer of 60°, i.e. a $[\pm 60°/\pm 45°/\pm 45°]$ braid angle profile, were manufactured for comparison with the TBr$_A$ beams as shown in Figure 6.2(b).
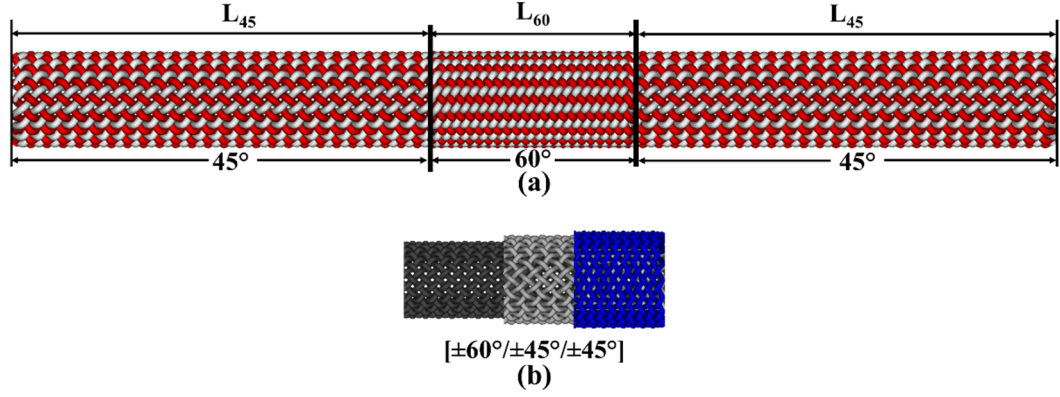


Figure 6.2 Schematic of (a) axial (TBr$_A$) and (b) radial (TBr$_R$) braid angle variation. Note: L$_{45}$ and L$_{60}$ represent the lengths of 45° and 60° regions respectively.

## 6.2    Braiding of the tailor-braided preforms

During the braiding process, the fibre tows originate from the bobbins on the braiding machine. The bobbins are in a constant circular motion in a fixed plane adjacent to the braiding machine, called the braiding plane (BP). All the fibre tows converge on the braiding mandrel in a plane known as fall plane (FP). Because of the location of the FP relative to the BP, the angle subtended between a fibre tow and the mandrel is equal to the braid angle. This is schematically depicted in Figure 6.3.
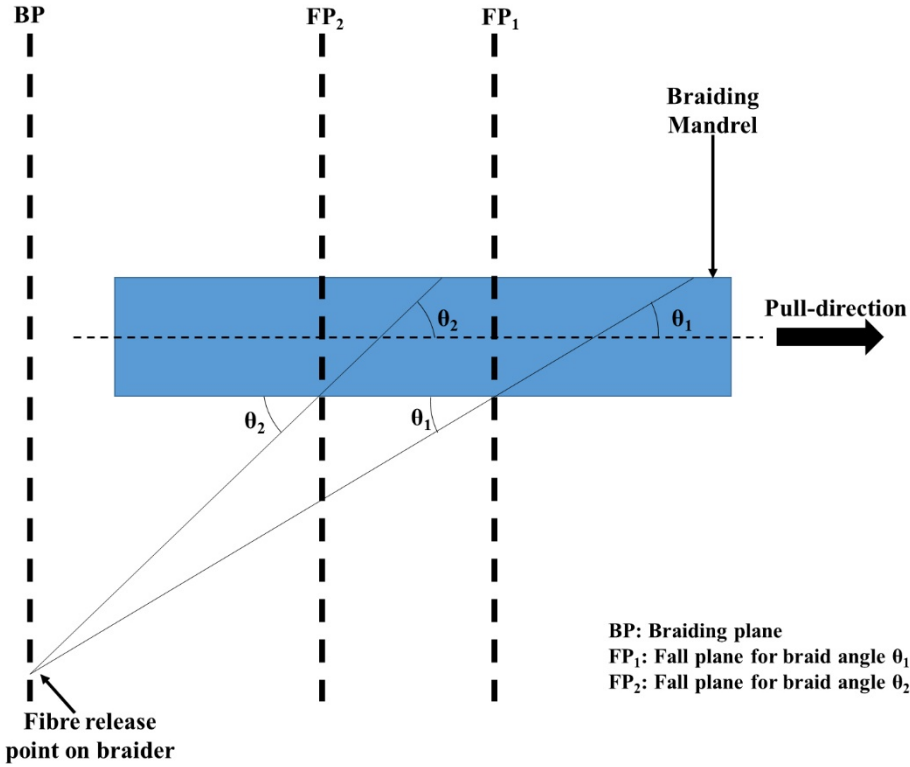
Figure 6.3 Schematic of the braiding process showing the location of fall planes $FP_1$ and $FP_2$ corresponding to different braid angles $\theta_1$ and $\theta_2$.

As shown by Nishimoto *et al.* [151], an axial braid angle variation necessitates a shift of the FP. Therefore, implementing a braid angle variation during continuous braiding creates a transition region on the resulting braided beam between the FPs of the two target braid angles. This transition region has a continuously varying braid angle. However, during the initial braiding trials of the $TBr_A$ preforms, the transition regions were found to be extremely long with respect to the length of the beams produced and tested in this work. Therefore, a step transition was adopted. This was achieved by braiding the tows in a start-stop mode, as depicted in Figure 6.4(a). After braiding the required length at the FP corresponding to 45°, the process was stopped, the mandrel was moved linearly to align the tow convergence point with the FP of 60° and the braiding process was restarted with the corresponding braiding parameters. This adjustment process was repeated to achieve the required length of the tailored braid. The FPs for braid angles of 45° and 60° are shown in Figure 6.4(b). The adjustment process was repeated for each layer of these multi-layer braided preforms. On the other hand, the braiding of $TBr_R$ preforms was conducted by braiding the two inner layers at 45° and the outermost layer with a braid angle of 60°.

105
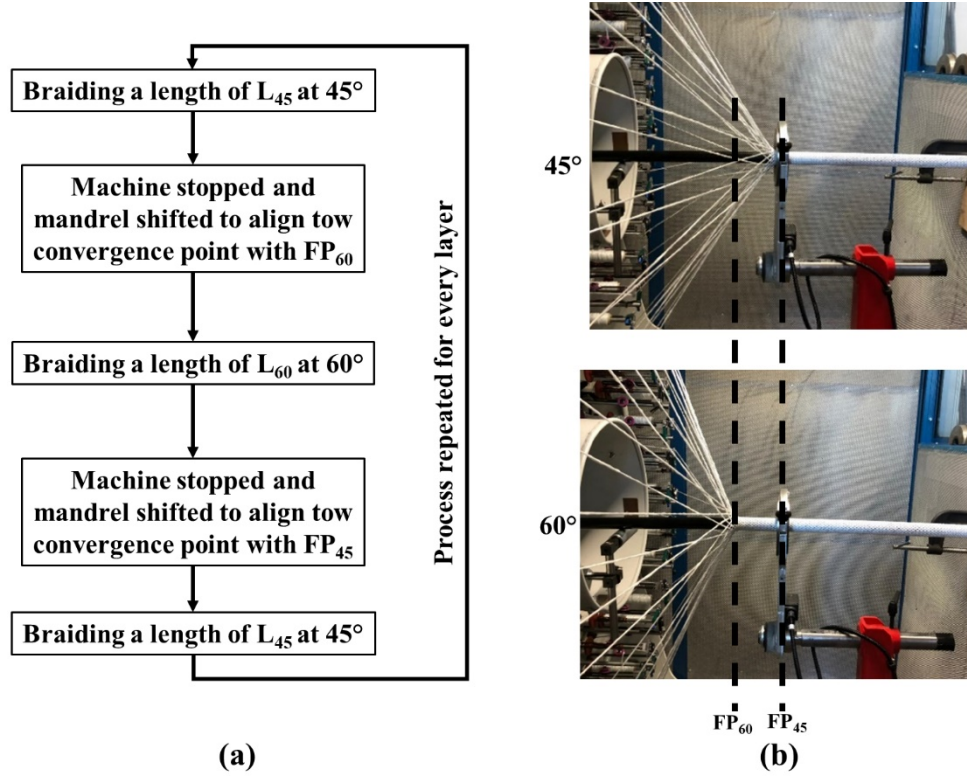
Figure 6.4 Start-stop braiding: (a) Steps for adjustment in braid angle and (b) Fall planes for 45° and 60° on the braiding mandrel.

The start-stop nature of the braiding process used in this work would add significant manufacturing time to the braiding process. Moreover, as discussed subsequently, a step change in braid angle could affect the stability of the preform and result in defects, particularly during the bladder inflation stage of the moulding process. It is possible to replace this with a continuous process via independent computer control of the pull-away mechanism [63]. This could be further improved through preliminary braiding simulations, which are available in commercial design software [185]. However, the braiding machine utilised in the present study did not have the required capabilities to incorporate these process control strategies. Nevertheless, their implementation must be considered in the future to improve the quality of the obtained preforms.

Following the braiding process, the preforms having three layers of braided fabric were used to produce tubular braided beams with an outer diameter of 35 mm via the Rapid Variothermal Moulding (RVM) process in a similar way to that described in Chapters 4 and 5 for the uni-braided beams.

## 6.3 Quality evaluation of tailor-braided beams

The produced TBr$_A$ beams had an approximately 80 mm-long region of braid angle of 60° in the centre, with equal-length regions of 45° located at both ends. The outer surfaces of the TBr$_A$ and TBr$_R$ braided beams produced using the RVM process are shown in Figure 6.5. For comparison, surfaces of UBr$_{45}$ and UBr$_{60}$ beams are also shown.
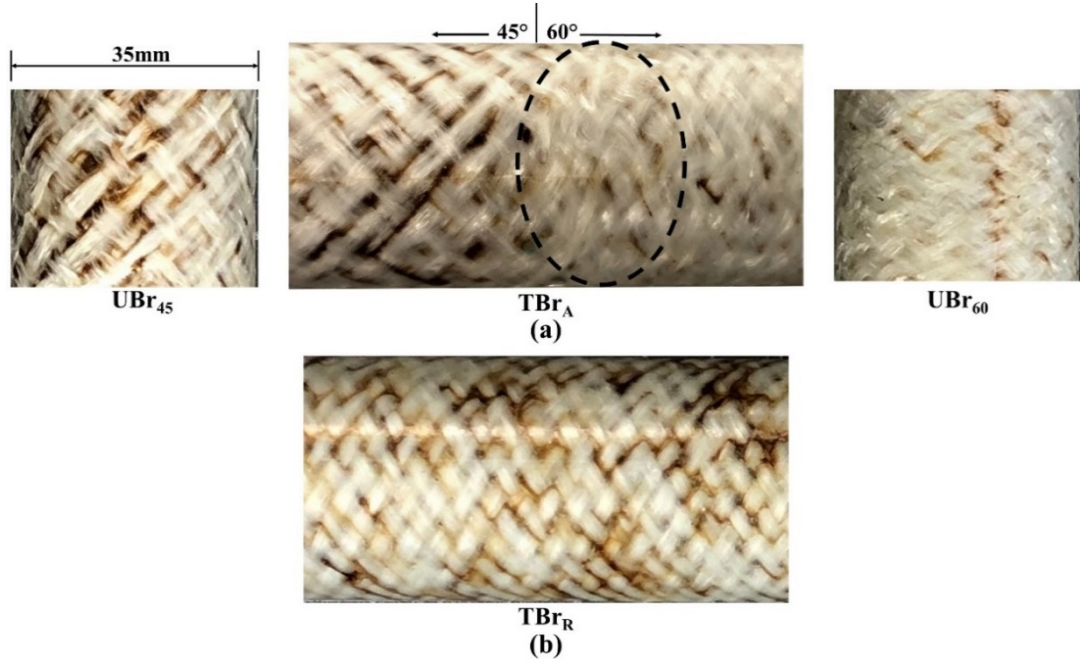


Figure 6.5 Outer surfaces of (a) TBr$_A$ and uni-braided beams; (b) TBr$_R$. Note: encircled region shows fibre waviness in TBr$_A$ beams.

As explained in Chapter 4, the visible discolouration on beam surfaces was due to exposure of the molten PA6 polymer to ambient air during the moulding process. Also as described in Chapter 4, there was an observable difference in the brownish discolouration on the outer surfaces of the UBr$_{45}$ and UBr$_{60}$ beams, which was likely due to larger air gaps between tows in the UBr$_{45}$ beams. For the TBr$_A$ beams, this difference in discolouration between regions with braid angles of 45° and 60° created an identifiable transition zone between the two regions. As shown in the figure, the fibres in both regions resemble the outer surface characteristics of the corresponding uni-braided beams. Fibre waviness was observed at angle transition points as well as the adjacent 60° region in all of the beams. This was likely due to the discrete step-change in braid angle during manufacturing (as opposed to a continuous variation), and

107

thus could be eliminated via computer-controlled braiding as discussed in the previous section. On the other hand, the discolouration on the surface of the $TBr_R$ beams was an intermediate between the $UBr_{45}$ and $UBr_{60}$ beams. Unlike the uni-braided and $TBr_A$ beams, the $TBr_R$ beams did not show any dry fibres on the outer surface. This is discussed later in this section.

The mass of all the beams was measured after cutting them to a length of 420 mm (Figure 6.6). The mean mass of the $TBr_A$ beams was 3% lower than the $TBr_R$ beams. The tailor-braided beams were approximately 10% heavier than the $UBr_{45}$ beams, but 24% lighter than $UBr_{60}$ beams.
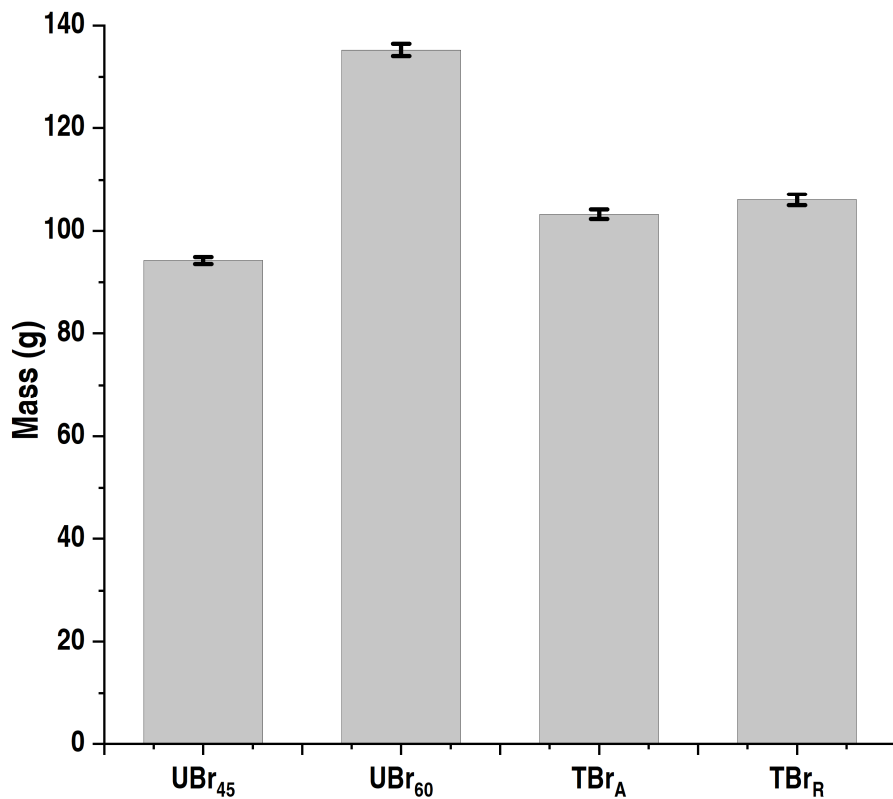


Figure 6.6 Measured mass of the uni-braided and tailor-braided beams. Note: bars represent mean values from all repeats and errors represent one standard deviation.

Braid angle was physically measured at randomly located points on the outer surface for four repeats for both types of tailor-braided beams and are shown in Figure 6.7. Due to the fibre waviness at the transition points and shorter span of the 60° region in the $TBr_A$ beams, limited measurements (minimum 6) were possible. The deviation in the measured braid angles was similar to the values previously recorded for the uni-braided
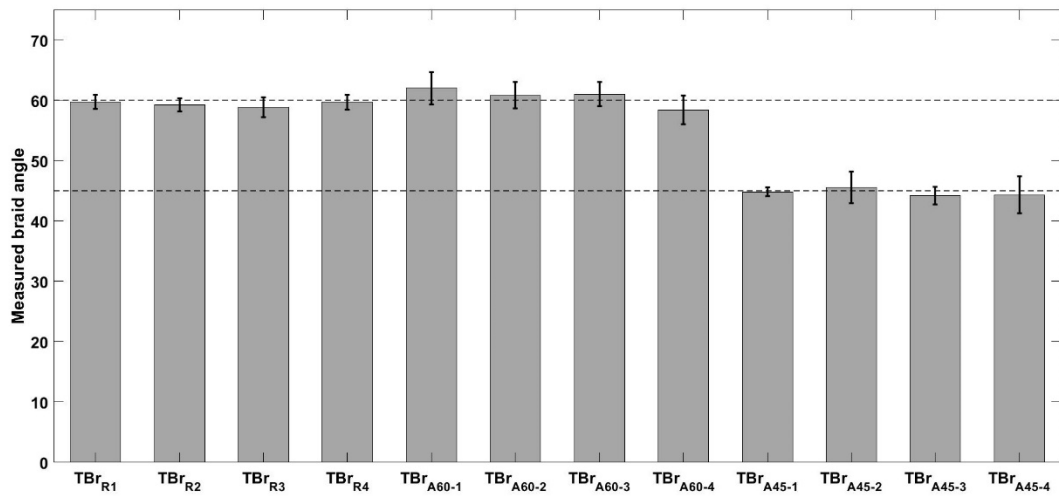
beams.



Figure 6.7 Measured braid angle for beams 1-4 of each type of tailor-braided beams. Note: bars represent mean values from all repeats and errors represent one standard deviation.

The measured thickness distributions are represented through box plots shown in Figure 6.8.
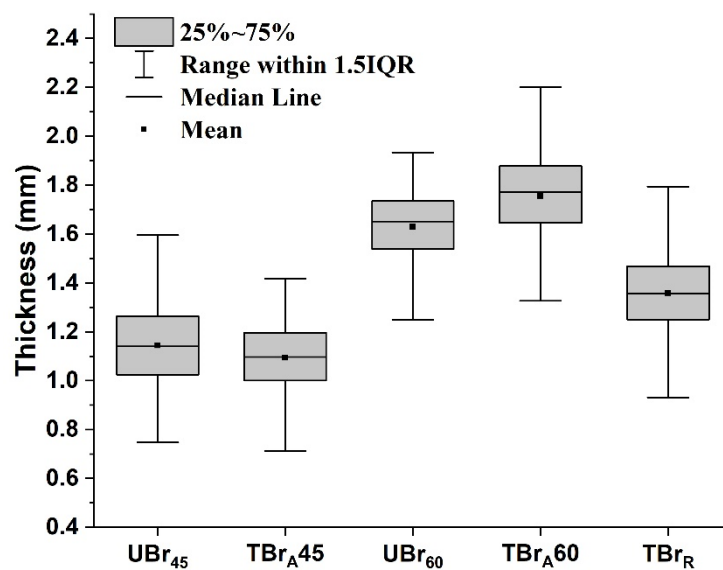


Figure 6.8 Box plots representing thickness distributions corresponding to tailor-braided beams. Note: thickness distributions of uni-braided beams are shown for comparison; IQR represents Inter Quartile Range.

The thickness of the $UBr_{45}$ and $UBr_{60}$ beams, reported in Chapter 5 are also shown for comparison. The thickness measurements of the two regions of $TBr_A$ beam are in reasonable agreement with the corresponding uni-braided beams. However, the $60°$

109

region showed greater variance against its uni-braided counterpart as compared to the 45° region, which could be a result of increased braid angle distortions, observable as fibre waviness on the outer surface. As expected, the thickness distribution of the $TBr_R$ beams resided between the measured values corresponding to the two uni-braided beams, with the mean thickness being approximately 19% greater than $UBr_{45}$ but 17% less than $UBr_{60}$.

Figure 6.9 (a) and (b) shows selected micrographs of the 60° and 45° regions of $TBr_A$ beams respectively. For reference, micrographs of $UBr_{45}$ and $UBr_{60}$ beams are also shown. The $TBr_A$ and corresponding uni-braided micrographs showed comparable characteristics, with fibre tows separated by resin rich regions. Regions with extensive tow distortion/fibre waviness are highlighted in the micrograph pertaining to the 60° region of $TBr_A$ beams. The waviness could affect the mechanical performance of the beams and highlights the scope for improving process control during the tailor-braiding. A micrograph of a $TBr_R$ beam is also shown in Figure 6.9(c). Notably, a resin-rich region was visible in the outermost layer (60° layer) above the fibre tows, explaining the absence of dry regions on the outer surface. The micrographs of both the tailor-braided beams showed intra-tow and inter-tow voids similar to the uni-braided beam sections. However, based on the prior detailed analysis of void content in addition to the mechanical test results of the uni-braided beams (Chapter 5), it is proposed that the presence of voids does not prejudice the comparative analysis of mechanical performance as performed here.
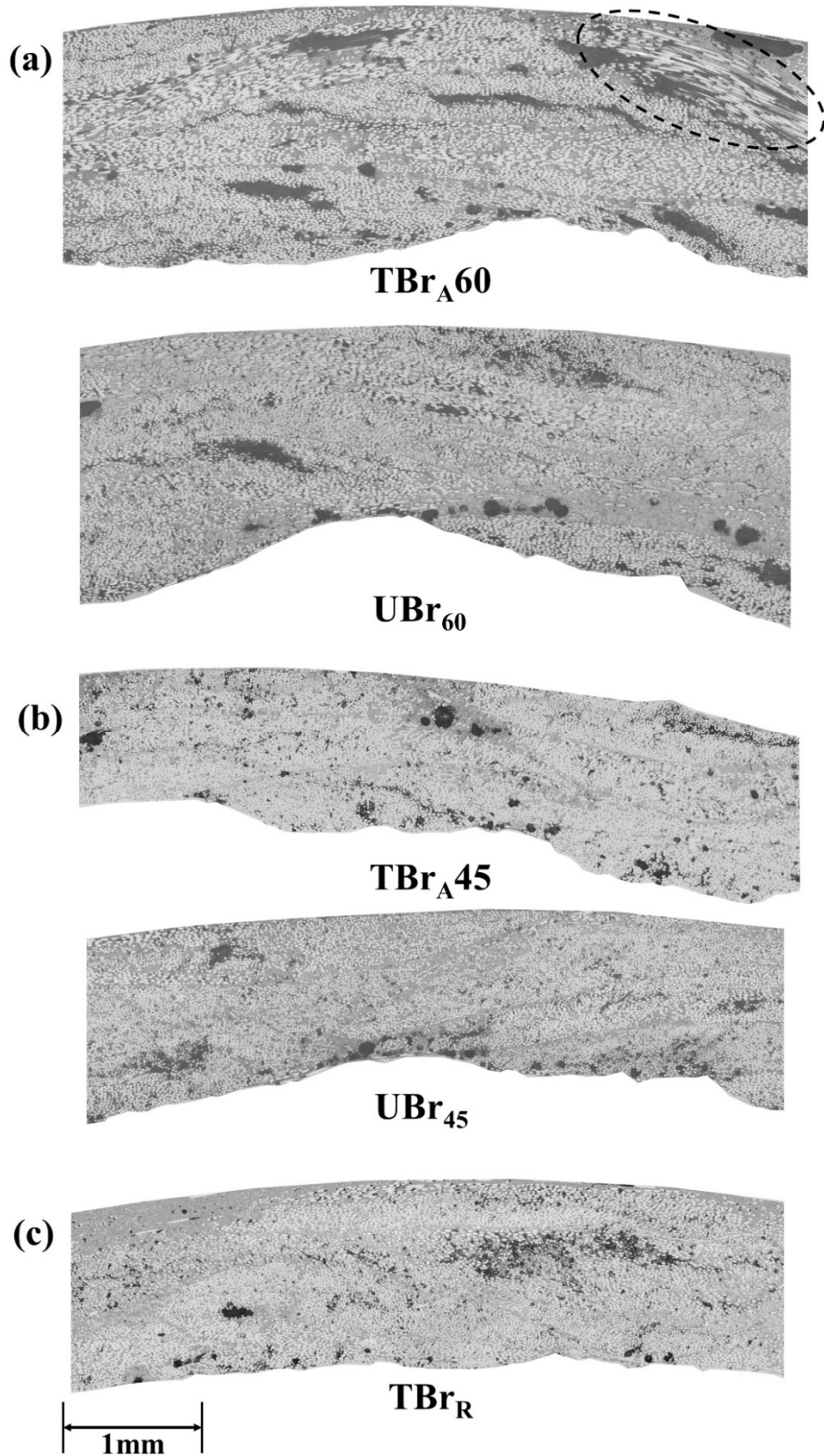
Figure 6.9 Micrographs of braided beam sections corresponding to (a) 60° region of $TBr_A$ beam with highlighted fibre waviness, (b) 45° region of $TBr_A$ beam and (c) $TBr_R$ beam. Note: Micrographs of $UBr_{45}$ and $UBr_{60}$ beam sections are also shown for comparison.

## 6.4    Three-point flexure performance of tailor-braided beams

Figure 6.10(a) shows the three-point flexure load-displacement curves corresponding to the tested tailor-braided beams.
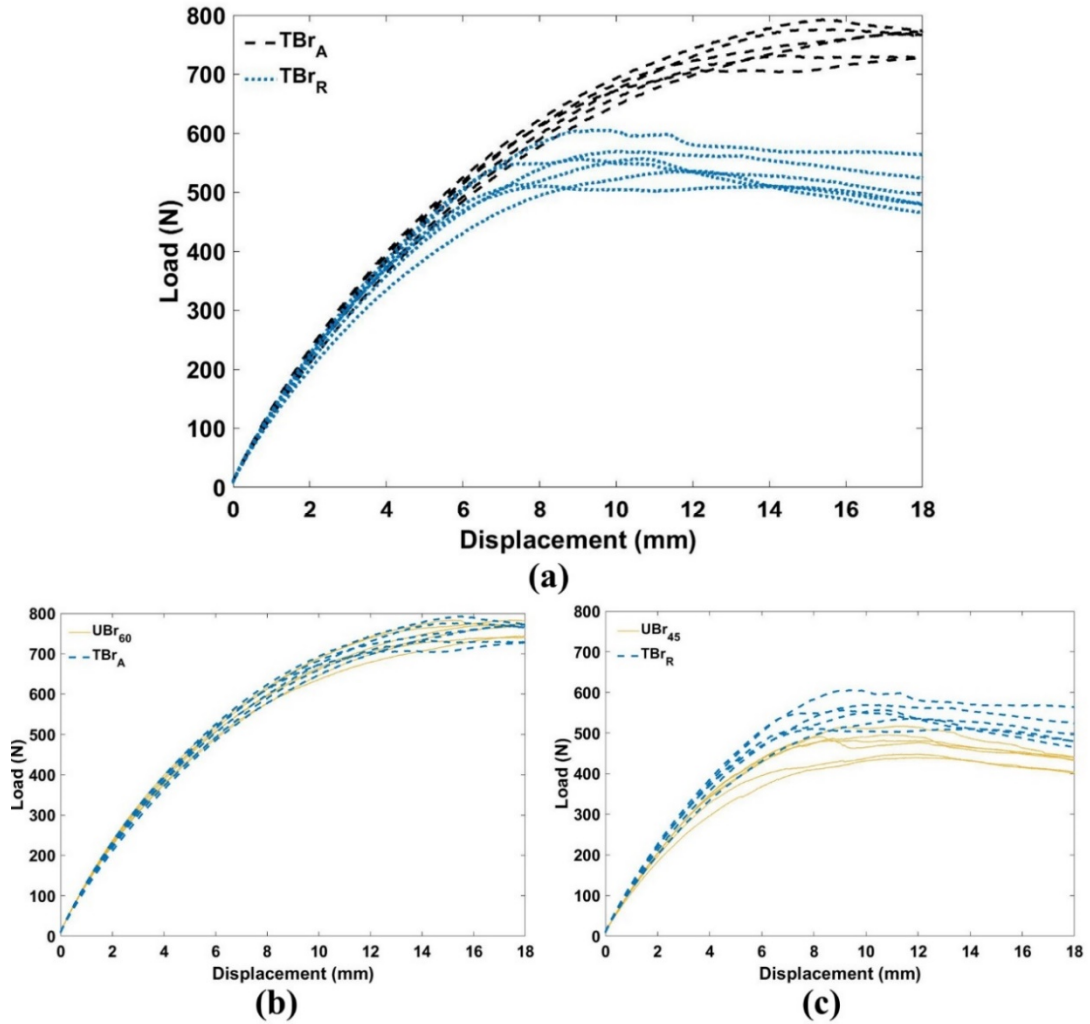


Figure 6.10 Load-displacement data from three-point flexure experiments of (a) all tailor-braided beams, (b) $TBr_A$ and $UBr_{60}$ beams and (c) $TBr_R$ and $UBr_{45}$ beams.

The behaviour of the $TBr_A$ and $TBr_R$ beams was similar up to a crosshead deflection of approximately 5 mm. Upon further deformation, the load borne by the $TBr_R$ beams plateaued with frequent undulations. On the other hand, the response corresponding to the $TBr_A$ beams showed a generally consistent increase throughout the deformation with minor inconsistency between the repeats within the last four millimetres of deflection. For comparison, the load-displacement data of the $TBr_A$ and $TBr_R$ beams are shown along with the response recorded for $UBr_{60}$ and $UBr_{45}$ beams in Figures

6.10(b) and (c) respectively. The $TBr_A$ and $UBr_{60}$ beams showed very similar load-displacement behaviour. The plateauing load trends observed for the $TBr_R$ beams was analogous to the $UBr_{45}$ beams, however, the magnitude of the load was greater for the $TBr_R$ beams. As noted for the uni-braided beams, visible cracks were present in the loading area for both the tailor-braided beams, while no damage was visible in the section of the beams opposite to the loading point.

### 6.4.1  Analysis of lightweighting benefits of tailor-braiding

Figure 6.11 shows the S, $P_{max}$ and $E_{abs}$ as well as the mass-specific values (S', $P'_{max}$ and $E'_{abs}$) for all of the tested beam types.
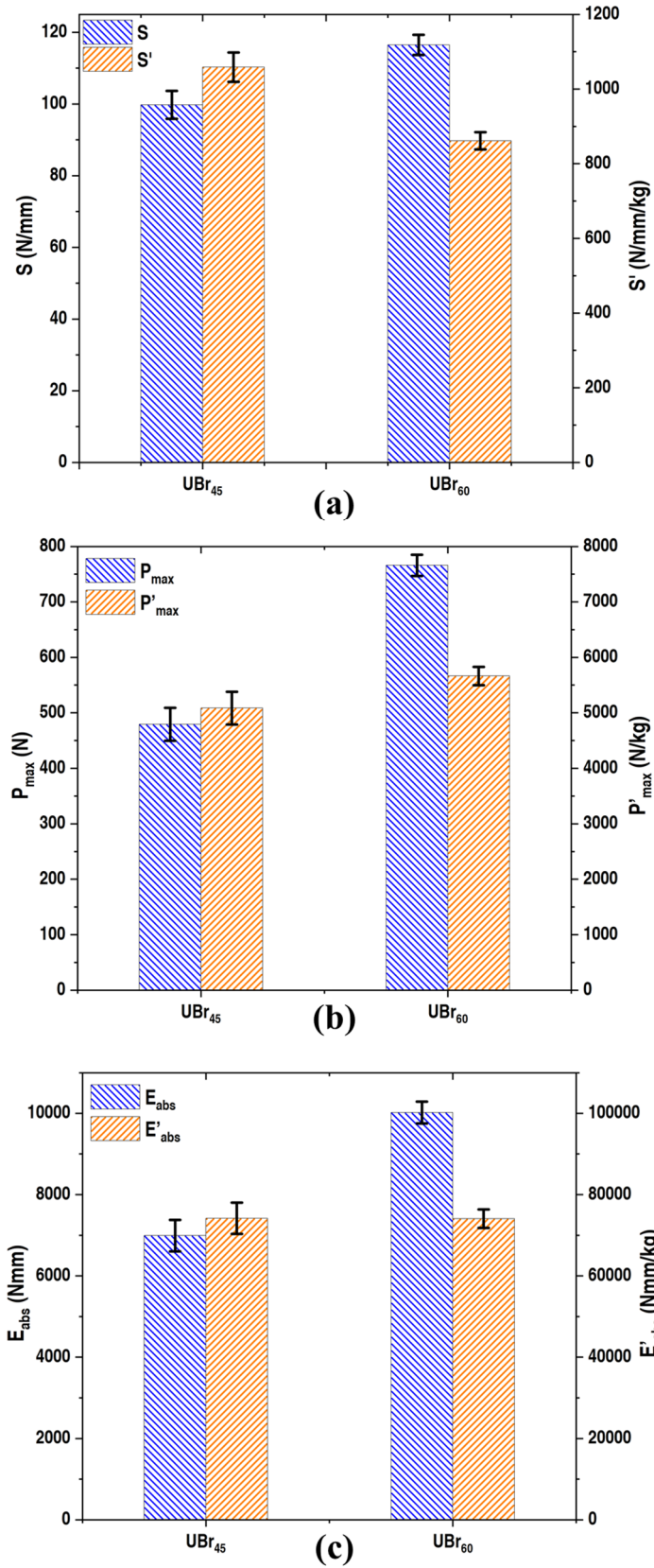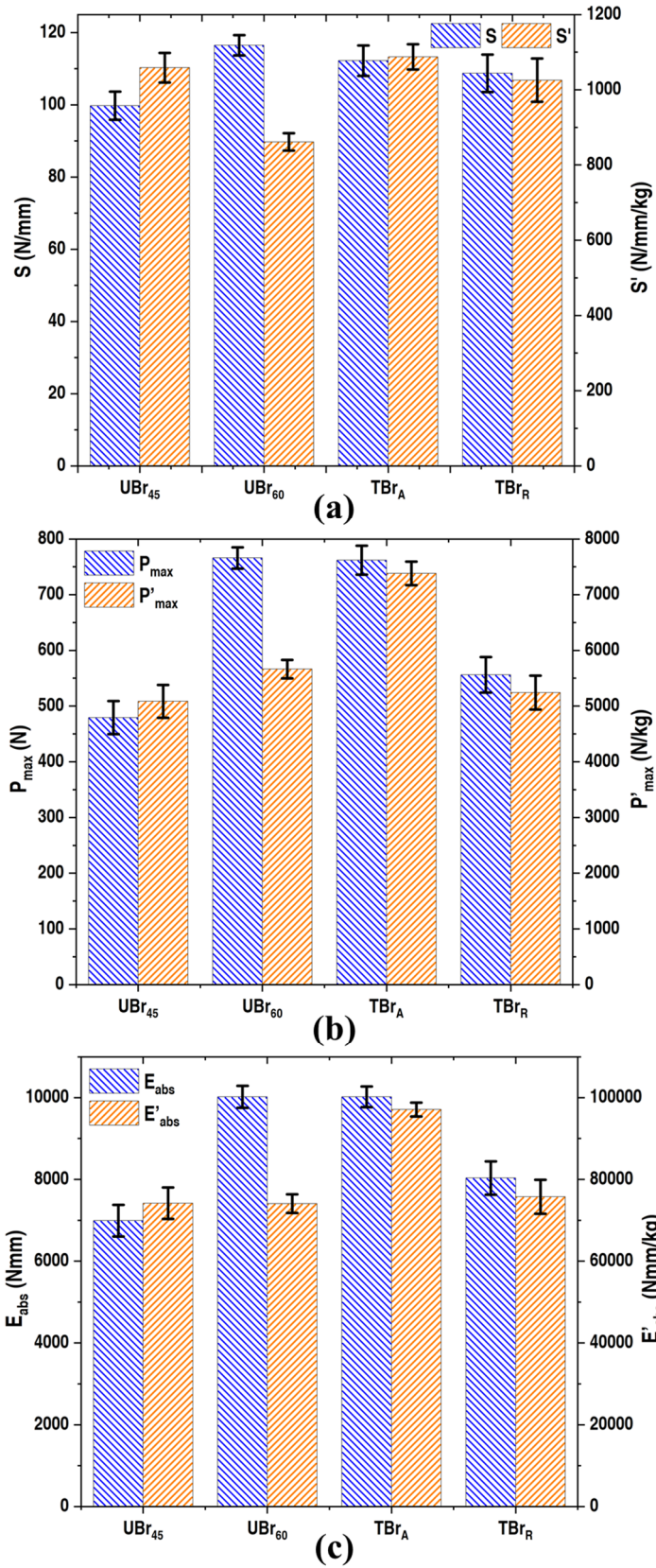
Figure 6.11 Measured values of (a) S and S', (b) $P_{max}$ and $P'_{max}$ and (c) $E_{abs}$ and $E'_{abs}$ of the uni-braided and tailor-braided beams. Note: bars represent mean values from all repeats and errors represent one standard deviation.

As expected from the load-displacement responses, the absolute values (S, $P_{max}$ and $E_{abs}$) of each index were indistinguishable between $UBr_{60}$ and $TBr_A$ beams. Single-factor ANOVA was performed for each mass-specific property. The resulting p-values for each comparison are listed in Table 6.2. All the values being less than 0.05 indicate that across the four types of beams being compared, the differences between all the mass-specific properties were statistically significant.

Table 6.2 p-values obtained from ANOVA performed for comparing the mass-normalised performance indices of tailor-braided and uni-braided beams.

| Property | p-value |
|---|---|
| **Specific Stiffness** | 1.93E-08 |
| **Specific Peak Load** | 1.81E-12 |
| **Specific Energy Absorption** | 4.33E-11 |

In order to further explore these differences, a post-hoc analysis was performed using the Tukey-Kramer method [180]. The Studentised range statistic q (from Equation 5.1) corresponding to every pair-wise comparison is listed in Table 6.3 with the critical q-values.

Table 6.3 q-values obtained from Tukey-Kramer post-hoc analysis performed for the mass-normalised performance indices corresponding to tailor-braided and uni-braided beams. Note: values indicating a statistically significant difference are underlined.

| Pair | $q(S')$ | $q(P'_{max})$ | $q(E'_{abs})$ | $q_{critical}$ |
|---|---|---|---|---|
| $UBr_{45}$-$UBr_{60}$ | <u>12.01</u> | <u>5.66</u> | 0.07 | 4.00 |
| $TBr_A$-$TBr_R$ | 3.76 | <u>20.94</u> | <u>16.52</u> | 4.00 |
| $UBr_{45}$-$TBr_A$ | 1.74 | <u>22.48</u> | <u>17.74</u> | 4.00 |
| $UBr_{45}$-$TBr_R$ | 2.02 | 1.54 | 1.22 | 4.00 |
| $UBr_{60}$-$TBr_A$ | <u>13.76</u> | <u>16.82</u> | <u>17.81</u> | 4.00 |
| $UBr_{60}$-$TBr_R$ | <u>10.00</u> | <u>4.12</u> | 1.29 | 4.00 |

Referring to the table yields the following observations regarding mass-normalised performance:

(i) **$TBr_A$ versus $TBr_R$:** The comparison of the two tailored beam configurations showed no significant difference in S'. However, the $P'_{max}$ and $E'_{abs}$ were greater for $TBr_A$ beams, the mean values being greater by 41% and 28% respectively.

(ii) **TBr$_A$ versus UBr$_{45}$ and UBr$_{60}$:** There were no statistically significant differences measured between the TBr$_A$ beams and UBr$_{45}$ beams with respect to S'. However, P'$_{max}$ and E'$_{abs}$ were both greater for the TBr$_A$ beams with the mean values being 45% and 31% higher. On the other hand, comparisons with the UBr$_{60}$ beams showed that all the performance indices were greater for the TBr$_A$ beams, showing substantial increases in S', P'$_{max}$ and E'$_{abs}$ of 26%, 30% and 31% respectively. Therefore, the local axial tailoring (TBr$_A$) delivered improvements against most of the benchmark (uni-braided) performance indices.

(iii) **TBr$_R$ versus UBr$_{45}$ and UBr$_{60}$:** There were no significant differences measured between the TBr$_R$ and UBr$_{45}$ beams across all three performance indices. Similarly, comparing TBr$_R$ beam performance against that of the UBr$_{60}$ beams, E'$_{abs}$ was found to be comparable. The S' of TBr$_R$ exceeded that of UBr$_{60}$ beams by 19%, while the P'$_{max}$ of UBr$_{60}$ beams was greater by 8%. Overall, braiding the outer layer at a higher braid angle did not yield significant improvements over any of the three benchmark uni-braided performance indices.

## 6.4.2  Analysis and comparison of beam deformation

Figure 6.12 shows the measured localised crushing against crosshead displacement for the tested beams. The TBr$_A$ and UBr$_{60}$ beams showed matching trends, with the localised crushing accounting for approximately 17% and 19% of the total crosshead displacement for TBr$_A$ and UBr$_{60}$ beams respectively. The TBr$_R$ beam showed a reduction in localised crush compared to the UBr$_{45}$ beams, with an overall localised crushing of 35% compared to 45% for the latter. However, the transitions in slope of the curves occurred at identical crosshead displacement values for both beams. Similar to the observations corresponding to the uni-braided beams discussed in Chapter 5, localised crushing was inversely correlated with mechanical performance for the two tested tailor-braided beams. The greater thickness of the TBr$_A$ beams compared to TBr$_R$ beams imparted a greater resistance to localised crushing and therefore resulted in their superior mechanical performance.
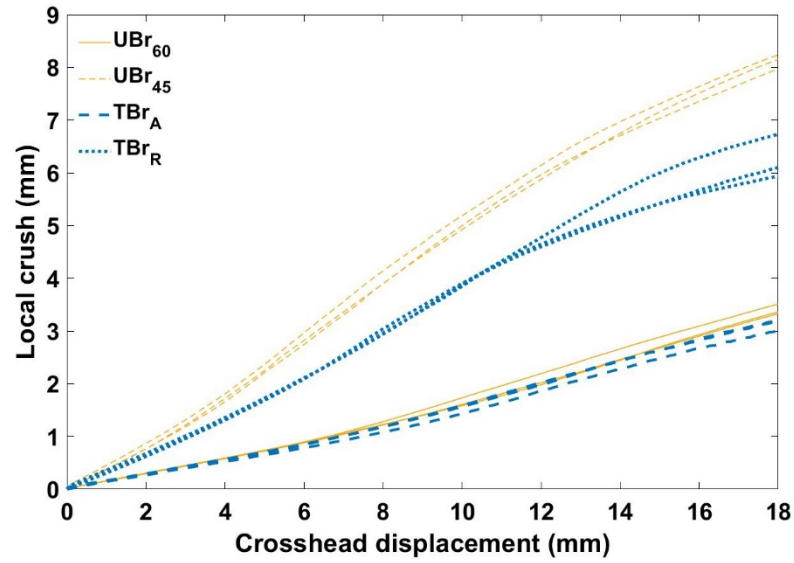
Figure 6.12 Progression of localised crushing during three-point flexure.

In order to compare the surface strain profiles of the tailor-braided beams against the uni-braided beams, 3D DIC was used during the testing of one specimen for each tailor-braided beam type. The estimated accuracy of the measurement system is shown in Table 6.4 through the evaluated bias and precision of the recorded measurements.

Table 6.4 Mean bias and precision of DIC measurements estimated from static images.

| Mean bias [$\varepsilon_x$ (%)] | Mean precision [$\varepsilon_x$ (%)] | Mean bias [dx (mm)] | Mean precision [dx (mm)] | Mean bias [dy (mm)] | Mean precision [dy (mm)] |
|---|---|---|---|---|---|
| -0.0004 | 0.0175 | 0.0023 | 0.0004 | -0.0001 | 0.0005 |

The optically measured axial strain maps are shown for the tested beams in Figure 6.13. Optical strain analysis for the uni-braided beams, presented in Chapter 5, had revealed that greater localised crush resulted in a reduction in applied strains on the bottom (tensile) surface of the beam – the predominant deformation mode was local crush, thus reducing global flexure. A similar correlation between localised crush and lower surface strains is also observed in the tailor-braided beams. Similar to observations from the UBr$_{60}$ beam, during the final millimetres of the applied deflection, a region showing surface strains of >1.5% developed on the lower (tensile) surface of the TBr$_A$ beam at peak deformation, with clear regions of strain concentration corresponding to the

117

macrostructure of the composite (braid). In contrast, such surface strains were less prominent for the $TBr_R$ beams in terms of magnitude and uniformity over the region but were greater as compared to the $UBr_{45}$ beam. Differences in the measured surface strains between $TBr_R$ and $UBr_{45}$ beams correlated inversely with increased prevalence of localised crush under the loading roller.
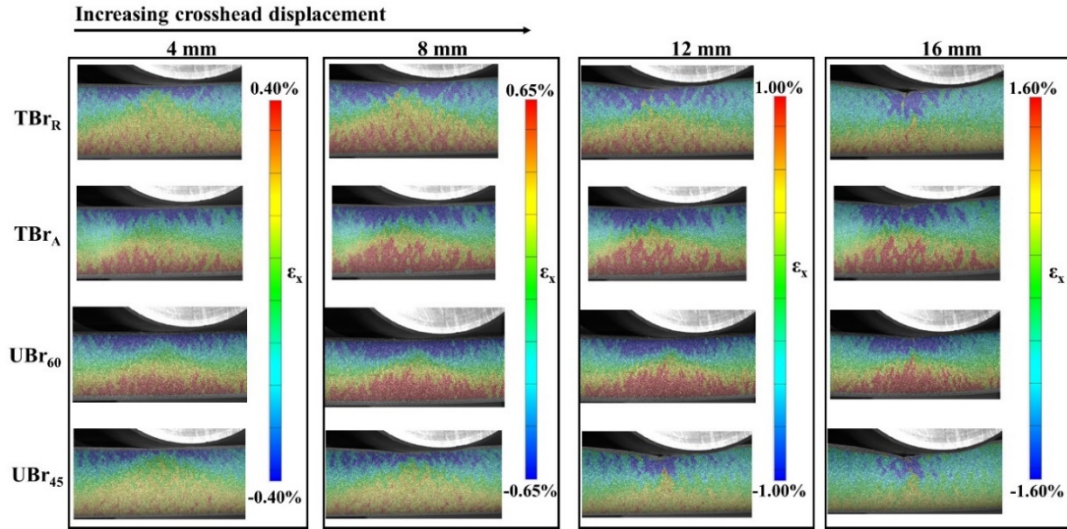


Figure 6.13 Progression of axial surface strain from 3D DIC data with crosshead displacement during three-point flexure.

As presented for the uni-braided beams in section 5.2.1 of Chapter 5, flexural strains recorded along three sections constructed in different regions of the beam surface are shown in Figure 6.14. Compressive and tensile strains of increasing magnitude were observed in the top (strain 1) and bottom (strain 3) regions respectively for all the beams. $TBr_A$ and $UBr_{60}$ beams showed approximately overlapping responses for each strain. Following the onset of localised crushing in the $TBr_R$ and $UBr_{45}$ beams, strain 1 measurements were unavailable due to the propagation of cracks into the RoI. This localised failure occurred earlier for the $UBr_{45}$ beam, showing a tendency towards localised crushing as compared to $TBr_R$ beam. Similarly, curves corresponding to strain 2 and strain 3 also showed visible differences in magnitude but followed the same trend. As observed in Figure 6.13, strain-3, i.e. lower (tensile) region strains for the $UBr_{45}$ and $TBr_R$ beams were greatly reduced as compared to the $TBr_A$ and $UBr_{60}$ beams, again illustrating the tendency of the former ($UBr_{45}$ and $TBr_R$ beams) towards localised crush failure rather than the global flexure deformation modes seen in the latter ($TBr_A$ and $UBr_{60}$ beams).
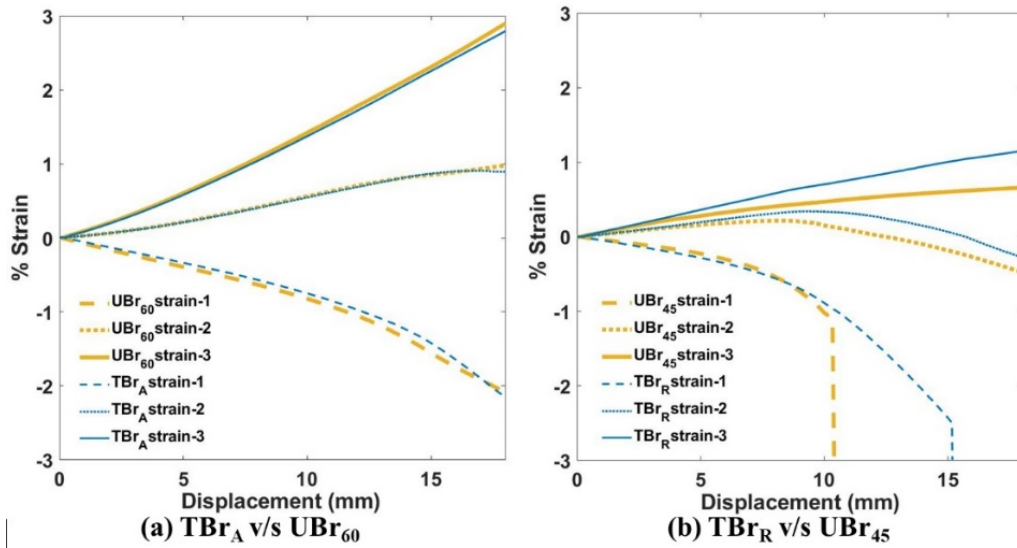
Figure 6.14 Comparison of region-wise flexural strain evolution between (a) TBr$_A$ and UBr$_{60}$ and (b) TBr$_R$ and UBr$_{45}$ beams.

Figure 6.15 shows the progression of section-wise y-displacements y1, y2 and y3 with increasing crosshead displacement, analogous to the results shown for uni-braided beams in Chapter 5.
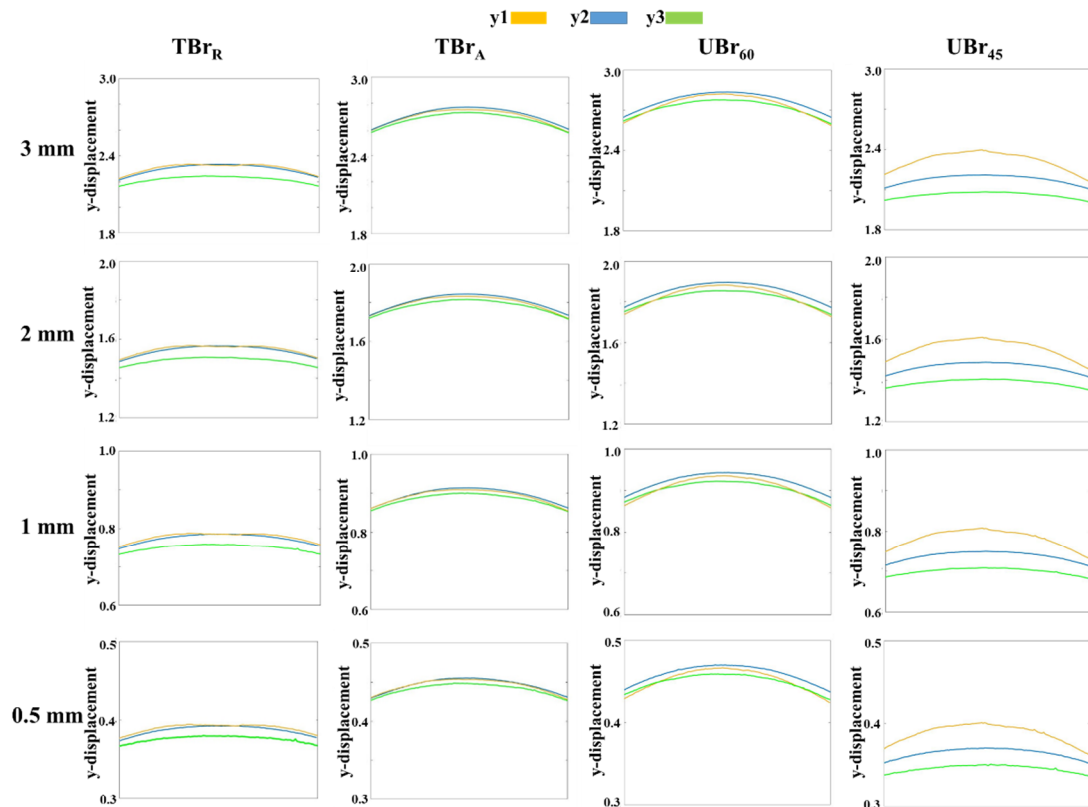


Figure 6.15 Evolution of downward y-displacement y1, y2 and y3 for tailor-braided and uni-braided beams with increasing crosshead displacement (bottom to top) during three-point flexure.

119

Results for uni-braided beams had indicated that differences arising between the three discrete section-wise displacement analyses were positively correlated with localised crush. In order to quantify the disparity in region-wise displacements, the root mean square (RMS) difference between the mid and bottom region y-displacements was evaluated as per Equation 6.2. In this equation, $RMS_{23}$ (mm) is root mean square difference between y2 (mm) and y3 (mm) and n is number of points on the sections.

$$RMS_{23} = \sqrt{\frac{\Sigma(y_2 - y_3)^2}{n}}$$
<div align="right">Equation (6.2)</div>

The evolution of $RMS_{23}$ with increasing crosshead displacement is shown in Figure 6.16. The data shown replicates the order observed for localised crush, thus showing a positive correlation between the two quantities.
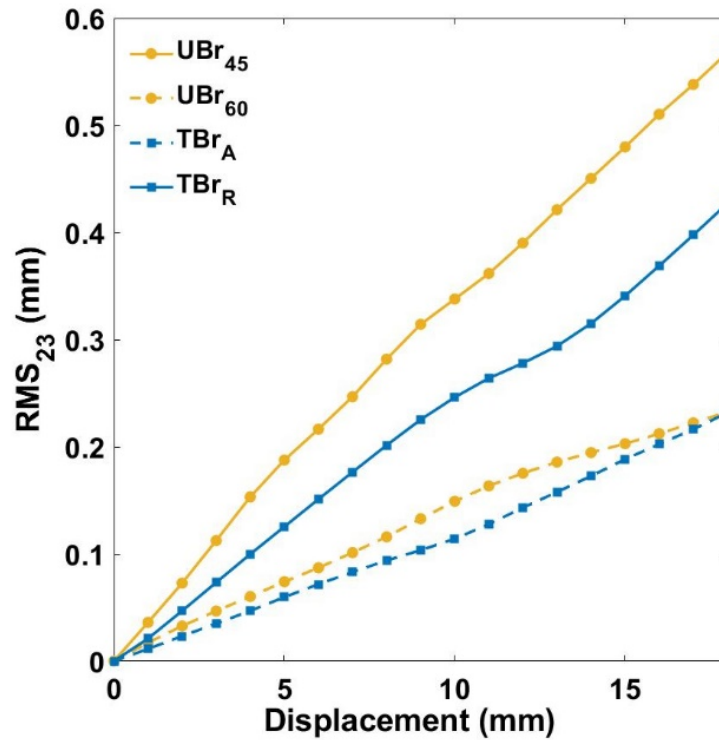


Figure 6.16 Evolution of RMS difference between mid-region and bottom-region y-displacements during three-point flexure.

The deformation analysis performed using both contact and optical strain measurement techniques revealed that the $TBr_A$ beams experienced a very similar deformation behaviour to that observed for the $UBr_{60}$ beams. On the other hand, the $TBr_R$ beams

showed greater localised crushing compared to $TBr_A$ beams, but the $TBr_R$ beam deformation was more inclined towards global flexure as compared to $UBr_{45}$ beams. The superior performance of $TBr_A$ beams over $TBr_R$ beams shows the effectiveness of locally tailoring the fibre architecture across the entire thickness of the beam as compared to making an outer-layer modification globally along the beam.

The deformation results indicate that by exploiting the dependence of performance on resistance to localised crushing through a specifically designed tailor-braiding strategy, an improvement in structural efficiency was achieved in the considered three-point flexure scenario. Hence, the findings encourage the development of bespoke tailor-braiding approaches based on the specific performance dictating characteristics in any given load case to potentially improve performance.

## 6.5 Summary

In this chapter, the three-point flexural performance of tailor-braided beams with axial ($TBr_A$) and radial ($TBr_R$) braid angle variation was presented. Based on the previously obtained flexure test results from uni-braided beams with angles of 45° and 60° ($UBr_{45}$ and $UBr_{60}$), tailored beams with a step-wise 45°/60°/45° axial braid angle configuration were manufactured using a start-stop braiding method due to scale limitations. Moreover, beams with a radial [±60°/±45°/±45°] variation ($TBr_R$) were also manufactured. The quality of the manufactured tailor-braided beams was evaluated through visual surface inspection, microscopy as well as braid angle and thickness measurements. The outer surfaces of the $TBr_A$ beams showed tow distortion (waviness), particularly in the braid angle transition zone. This waviness was also evident in the micrograph of the $TBr_A$ beams. It was proposed that a continuous braid angle transition (instead of step-wise) adopted via advanced process control would minimise/eliminate the fibre waviness observed in this work that arose due to the step-transition in braid angle and start-stop nature of the manufacturing process. Apart from the waviness in the $TBr_A$ beams, braid angle and thickness measurements in different regions of both $TBr_A$ and $TBr_R$ beams were in good agreement with the corresponding measurements from uni-braided beams. Both types of tailor-braided beams were approximately 10% heavier than the $UBr_{45}$ beams, but 24% lighter than $UBr_{60}$ beams.

The tailor-braided (TBr$_A$, TBr$_R$) beams were tested in a static three-point flexure test and their mechanical performance and deformation behaviour were compared with uni-braided beams. Analysis of the load-displacement data from the three-point flexure tests revealed that despite being 24% lighter, the TBr$_A$ beams showed statistically equivalent or greater performance indices compared to the UBr$_{60}$ beams, which had the highest absolute mechanical performance amongst the uni-braided beams. In addition, their mass-normalised performance indices were higher than both the uni-braided beams. Therefore, the axial tailor-braiding resulted in an improvement in the structural efficiency of the braided beams in three-point flexure loading. The superior performance of the TBr$_A$ beams despite the fibre waviness highlighted the potential for further improvement through elimination of the defect. On the other hand, the TBr$_R$ beams showed lower mass-specific properties compared to the TBr$_A$ beams. Moreover, their mass-specific properties did not surpass those of the uni-braided beams. Therefore, despite having the same mass as the TBr$_A$ beams, the TBr$_R$ beams did not offer any lightweighting benefit in this particular load case.

The bottom surface displacements recorded using the deflectometer revealed that localised crushing accounted for 17% and 33% of the total applied displacement respectively for the TBr$_A$ and TBr$_R$ beams compared to 19% and 45% for the UBr$_{60}$ and UBr$_{45}$ beams. Moreover, surface strain and displacement data available from the DIC measurements showed similar values for TBr$_A$ and UBr$_{60}$ beams, whilst the surface strains of the TBr$_R$ beams were intermediate between UBr$_{45}$ and UBr$_{60}$ beams. Therefore, both the deformation analysis techniques showed that changing the braid angle in the loading region to 60° resulted in a replication of the deformation behaviour of UBr$_{60}$ beams, while braiding the outer layer at 60° did not produce an equivalent change.

# 7 Conclusions and future work

This chapter summarises the performed research and lists the major conclusions arising from the obtained results. Moreover, the identified contributions to knowledge in each section are stated. This is followed by a discussion of the identified limitations of the work as well as recommendations for future research to address these limitations. Finally, the findings of the work are discussed from a broader perspective and the potential avenues for impact beyond the academic domain are shown through three industrial applications where the concepts developed and results demonstrated in this thesis can be utilised.

## 7.1 Summary and academic contributions

### 7.1.1 Development of manufacturing process for braided thermoplastic beams

<u>**Summary and key findings**</u>

- A conventional Bladder Inflation Moulding (BIM) process was developed to produce hollow circular braided composite beams with an outer diameter of 35 mm. The part cycle time, i.e. total time for manufacturing a single braided beam, was approximately 4 hours, which does not meet high volume manufacturing requirements. Moreover, the thermal control of the process was found inappropriate for the consistent manufacturing of beams.
- A novel process called Rapid Variothermal Moulding (RVM) was developed to address the limitations of the BIM approach. The manufacturing setup used an agile tooling concept with heating/cooling rates up to 40 °C/min and had a pixelated thermal control configuration, thus allowing for independent dynamic process control in different zones of the part being moulded.
- Implementation of variable process control during the moulding of beams in the RVM setup resulted in precise thermal profile across the entire tool, thus ensuring consistent part manufacturing. Owing to the rapid heating/cooling rates, the RVM process had a total part cycle time of 18 minutes compared to 4 hours for the benchmark process for a 10 minute consolidation cycle, thus showing a 97%

reduction in the time taken during the heat-up and cool-down phases of the process. Therefore, the novel process resulted in combined benefits of improved process control as well as rapid part production.

- Beams with three different braid angles, i.e. 25°, 45° and 60°, were manufactured using a 2×2 regular braid pattern. The braid angle and beam mass measurements taken for the manufactured beams showed significant offset as compared to the theoretically predicted values. Therefore, the 2×2 braid was replaced with a 1×1 diamond braid architecture.

- For the diamond braid, braid angles of 30°, 45° and 60° were selected. A set of modifications were introduced in the braiding as well as the moulding process to minimise defects in the manufactured beams. The finally developed high quality part moulding process had a total press cycle of 37 minutes and was used to produce all the beams subsequently used in the mechanical testing performed in this work. Although the process was optimised under the constraints of the manufacturing environment, some defects such as surface discolouration, fibre waviness and dry fibres could not be eliminated, which indicated that there remains scope for improving the manufacturing process. Nevertheless, the mass and braid angle measurements taken on the produced 1×1 braided beams showed consistency across all repeats and therefore, the beams were considered suitable for the mechanical test program.

## Specific contributions to knowledge

- A novel manufacturing process was developed by integrating a conventional BIM process with a responsive variothermal tooling concept and a hydraulic press.

- The developed RVM process was demonstrated to significantly reduce the cycle time for part production with accurate and repeatable process control and significantly improved part quality.

### 7.1.2 The effect of braid angle on three-point flexural performance of braided beams

**<u>Summary and key findings</u>**

- Hollow circular braided beams with uniform braid angles of 30°, 45° and 60° manufactured via RVM were tested in static three-point flexure. During the tests, a linear deflectometer as well as three-dimensional Digital Image Correlation (DIC) were used to record the deformation characteristics of the beams.

- The load-displacement data obtained from the flexure tests indicated that increasing the braid angle resulted in superior mechanical performance, with significant increase observed in stiffness as well as peak load.

- Two principal deformation modes were observed during the three-point flexure of the braided beams: localised crushing and global flexure. Based on the deflectometer readings, localised crushing was found to account for 63%, 45% and 19% of the total deflection for the 30°, 45° and 60° beams respectively at the point of maximum crosshead deflection.

- The DIC software was used to extract flexural strain as well as the transverse displacement evolution during the flexural deformation. Both the data sets showed that the bottom region underwent significant tensile deformation for the 60° beam. In contrast, the localised crush-dominant deformation in the 30° and 45° beams led to minimal straining in the bottom region. Consequently, the 30° and 45° beams returned to their original shape after unloading while the 60° beams underwent permanent deformation.

- The observed difference in the three-point flexural behaviour between the beams with different braid angles was likely due to the combined effect of three braid angle dependent characteristics, i.e. thickness, material moduli and surface fibre coverage. Based on the trends and independent influence of these features on flexural performance, resistance to localised crushing proved to be the critical factor governing the mechanical response of the braided beams tested in this work.

- Untested specimens were used for performing detailed analysis and comparison of voidage in the braided beams via microscopy and resin-burn off experiments

125

revealed a statistically significant difference in void content. However, the voidage was more severe for the 60° beams, which showed the highest performance indices among the tested braided beams. Therefore, based on the test results, it was reasonably assumed that the differences in void content did not affect mechanical performance as strongly as braid angle.

**Specific contributions to knowledge**

- The effect of braid angle on the performance and deformation characteristics of component-scale braided beams under three-point flexure was investigated for the first time.

- It was shown that the dominant deformation mode was dictated by a combination of multiple characteristics that depend on braid angle. This indirect dependence of deformation on braid angle affected the mechanical performance, with peak load as well as stiffness increasing with braid angle for the beams tested in this work.

### 7.1.3   Three-point flexural performance of tailor-braided composite beams

**Summary and key findings**

- Based on the mass-normalised flexure test results reported for uni-braided beams with braid angles of 45° and 60° ($UBr_{45}$ and $UBr_{60}$) it was hypothesised that tailor-braided beams with a 45°/ 60°/ 45° axial braid angle configuration ($TBr_A$), with 60° region directly under the loading roller would result in improved structural efficiency. For comparison, beams with a globally applied radial [±60°/±45°/±45°] variation ($TBr_R$) were also considered.

- $TBr_A$ preforms were braided using a start-stop braiding method, which resulted in a step transition in the braid angle. On the other hand, braiding the $TBr_R$ beams was relatively straightforward, with a 60° layer braided over two overbraided 45° layers. The $TBr_A$ and $TBr_R$ preforms were moulded using the previously developed RVM process.

- Both the tailor-braided beams were 24% lighter compared to the $UBr_{60}$ beams. The $TBr_A$ beams showed notable fibre waviness at the braid angle transition zone, which

continued into the central 60° region and was attributed to the step-transition in braid angle was responsible for the observed fibre waviness. Apart from the waviness, braid angle and thickness measurements in different regions of the $TBr_A$ beams were in good agreement with the corresponding measurements from uni-braided beams.

- The tailor-braided beams were tested in static three-point flexure under identical test parameters as the uni-braided beams. The obtained mass-normalised performance indices for the $TBr_A$ beams were higher than both the uni-braided beams. Particularly interesting was the observation that despite being 24% lighter, the $TBr_A$ beams showed identical performance to the $UBr_{60}$, which had superior mechanical performance amongst the uni-braided beams.

- In contrast, the $TBr_R$ beams showed lower mass-specific properties compared to the $TBr_A$ beams. Moreover, their mass-specific properties did not surpass those of the uni-braided beams. Therefore, despite weighing the same as the $TBr_A$ beams, the $TBr_R$ beams did not offer a lightweighting benefit in this particular load case.

- Deformation analysis showed that the localised crushing accounted for 17% and 19% of the total applied displacement respectively for the $TBr_A$ and $UBr_{60}$ beams versus 33% and 45% for the $TBr_R$ and $UBr_{45}$ beams. The optical strains measured on the beams' surfaces also showed similar values for $TBr_A$ and $UBr_{60}$ beams, whilst the $TBr_R$ beams' surface strains were intermediate between $UBr_{45}$ and $UBr_{60}$ beams.

- Mechanical performance results and deformation analyses indicated that changing the braid angle in the loading region to 60° resulted in a replication of the deformation behaviour of $UBr_{60}$ beams, while braiding the entire outer layer at 60° did not produce an equivalent change.

**Specific contribution to knowledge**

- The effect of the proposed *tailor-braiding* method on the structural performance of component-scale braided composite beams was investigated for the first time. Considering three-point flexure as a load case, it was shown that suitably planned tailor-braiding strategy could result in an improvement in structural efficiency.

## 7.2 Limitations of the research and recommendations for further work

The research presented in this thesis established the viability of tailor-braided beam structures for improved structural efficiency via three-point flexure tests. This section describes the limitations of the research as well as the opportunities to perform extensional research work in the context of this thesis.

### 7.2.1 Defects

Throughout Chapters 4-6, the quality of the manufactured and tested braided beams were monitored. Quality inspection was conducted via techniques of microscopic inspection and resin burn-offs. For all the beams, persistent defects were observed. Given the comparative nature of the performed work, as well as several dedicated analyses presented throughout the thesis, the effects of these defects were considered inconsequential. The defects are summarised below with recommendations to eliminate them in extensional research work and are expected to produce interesting results:

- **Discolouration:** The manufactured braided beams showed significant discolouration on the outer as well as inner surfaces. Through a dedicated experiment as well as a review of relevant literature, it was shown that the discolouration was a result of thermo-oxidative chemical reaction of the PA6 and was aggravated upon increased exposure to ambient air. Two remedies are proposed for the discolouration: (i) addition of thermal stabilisers during the manufacture of the commingled material and (ii) use of vacuum or an inert gas atmosphere during the moulding process to isolate the braided parts from ambient atmosphere while the PA6 is above its melting temperature.
- **Voids:** The microstructural inspection as well as the resin burn-off test results discussed in Chapters 5 and 6 showed a consistent presence of voids in all the manufactures specimens. Upon performing detailed comparisons of void content, a statistically significant difference was found between the specimens with different braid angles. However, as the beams with the highest void content showed significantly higher mechanical performance, their effect on the comparative mechanical performance was deemed insignificant. The literature shows few but

promising investigations suggesting that thermoplastic composites are relatively more resistant to voids as compared to thermosets [186]. Therefore, further experimental research aimed at quantification of the knockdown in mechanical performance of thermoplastic composites due to voidage is recommended, with a specific focus on the three-point flexural response of braided composite beams. Moreover, void characteristics such as size, shape and location, which are also known to affect performance, must be considered in these analyses.

- **Fibre waviness:** In Chapter 4, the braided beams manufactured during the initial trials of the RVM process showed significant fibre waviness on their outer surfaces. This defect was addressed to a considerable extent by reducing the diameter of the braiding mandrel. However, the subsequently manufactured beams showed regions with marginal but persistent waviness. Particularly in the $TBr_A$ beams, there was significant waviness at the braid angle transition points, which was a likely consequence of the start-stop braiding approach. As fibre orientation is a significant factor in dictating the performance of composites, eradicating this defect would likely improve the performance of all the tested beams. To eliminate the waviness observed in tailor-braided beams, a continuous variation in braid angle is recommended, which is potentially achievable with advanced computer control of the braiding operation. However, the subject requires detailed investigation with specimens of multiple scales as well as different fibre types for definite results.

### 7.2.2 Damage analysis

The analysis of the three-point flexural response in this thesis was limited to performance based metrics based on the load-displacement data. Expanding the analysis to include the study of damage initiation and propagation in the beams would provide further insights into the effect of braid angle on the mechanical performance and potentially result in greater exploitation of the presented tailor-braiding concept. This is possible through the implementation of in-situ as well as ex-situ inspection techniques such as acoustic emission (AE), micro-computed tomography (CT) etc. The results so generated can be correlated with the existing results in the vast body of literature related to damage mechanisms in braided composites and therefore will be meaningful contributions in the field.

129

### 7.2.3 Material

The research was performed for a specific thermoplastic braided composite material. The following material considerations are considered important to extend the research presented in this thesis:

- **Thermoset composites:** The current work tested braided composite beams with a thermoplastic matrix. Given the differences between the mechanical properties of thermoplastics and thermosets, repeating the performed research using braided thermoset composites will indicate if the demonstrated benefits of tailor-braiding are matrix agnostic.

- **Braid-dependent parameters:** Several characteristics that can be varied during the braiding process are known to influence mechanical properties. Therefore, extending the research of the thesis to encompass these characteristics will improve the understanding of braided composite flexural performance. These characteristics are listed below:
  - Cover factor
  - Braid pattern
  - A wider range of braid angles
  - Continuous braid angle transition in tailor-braided beams

- **Triaxial braids:** The research presented in this thesis is based on biaxial braids. However, triaxial braids are more applicable in load-bearing structures because of the additional mechanical performance due to the inclusion of axial tows. The additional stiffness and strength are particularly relevant for axial and flexural loads considered in this thesis. As discussed in Chapter 2, triaxial braids have been reported to show significantly different mechanical response compared to biaxial braids. Therefore, the transferability of the reported improvement in performance achieved via tailor-braiding to triaxial braids requires experimental verification. Moreover, from a manufacturing perspective, moulding triaxial braids via internal bladder inflation would require modifications at different stages of the process. For instance, the permeability of triaxial braids differs from biaxial braids due to a disparity in fibre packing fraction [187]. Hence, a different set of consolidation parameters is required to achieve suitable consolidation. In addition, the presence of

stiff axial fibres could result in additional resistance to the shearing/scissoring action of the dry braided fibres. Since the scissoring is crucial to enable preform expansion during bladder inflation, successful part manufacturing would require the determination of a maximum usable expansion ratio during process design. Therefore, extending the manufacturing and mechanical testing aspects of the presented research to triaxial braids will result in important findings relevant for the industrial application of tailor-braiding, but requires a systematic research program that suitably considers the various factors discussed above.

- **Specimen scale:** An important observation that was reinforced by the results of this work is the effect of the selected specimen scale for the evaluation of mechanical performance. Therefore, in order to completely understand the effect of braid angle variations on flexural performance and also prove the scalability of the benefits of tailor-braiding, it is recommended to test braided structures of different scales.

- **Load-specific tailor-braiding:** The results of this thesis highlighted the potential of the novel manufacturing approach of tailor-braiding for beams subjected to three-point flexure. However, the proposed tailor-braiding strategy that resulted in an improvement in structural efficiency of braided beams was developed specifically to exploit the dependence of performance on localised crushing. In order to implement the concept of tailor-braiding in structural applications, a holistic approach is required that considers all the load cases relevant to a particular structural component. Therefore, confirming the transferability of the reported benefits of tailor-braiding to actual load-bearing structures would require future work aimed at devising bespoke tailor-braiding strategies according to the real-life load cases specific to each component.

It is noteworthy that covering all the above factors in future work would indicate the specific reasons for the disparities between the observed trends of flexural performance and previously reported results, as the current speculations involve multiple factors including matrix type, specimen scale, specimen geometry etc.

### 7.2.4   Numerical modelling of mechanical performance

The current work does not include a simulation based analysis of the performance of

braided composite beam structures. With the rapid progress of Finite Element (FE) modelling, the reliance of composite engineers on simulation models has been on the rise. Accurate modelling capabilities enable the evaluation of the mechanical performance of structures in a multitude of loading scenarios, thus saving resources utilised in performing physical testing. From the perspective of this work, simulation could be used to optimise the braid angle configuration in the tailor-braided beams as per three-point flexural performance. Moreover, a validated model could be used to analyse the scalability and transferability of the proposed tailor-braiding concept in multiple load-cases. However, in order to accurately predict the performance of composite materials, FE software packages require accurate material properties. Given the non-standard nature of the beams tested in this work, i.e. circular tubes instead of flat plates, acquiring the wide range of material properties requires the extensive use of non-standard mechanical characterisation, which is not in the scope of this work. Therefore, a material characterisation program is also recommended as a part of future research. The results of such fundamental characterisation would also provide further insight into the local beam deformation results discussed in Chapters 5 and 6.

## 7.3 Publications arising from the work

Three papers have been accepted for publication in peer-reviewed journals from the work in this thesis:

1. Singh A, Reynolds N, Carnegie CR, Micallef C, Keating EM, Winnett J, Barnett A, Barbour S, Hughes DJ. A novel route for volume manufacturing of hollow braided composite beam structures. Advanced Manufacturing: Polymer & Composites Science. 2019:1–6.
2. Singh A, Reynolds N, Keating EM, Barnett A, Barbour S, Hughes DJ. The effect of braid angle on the flexural performance of structural braided thermoplastic composite beams. Composite Structures. Accepted for publication.
3. Singh A, Reynolds N, Keating EM, Barnett A, Barbour S, Hughes DJ. Three-point flexural performance of tailor-braided thermoplastic composite beam structures. Composite Structures. Accepted for publication.
   The three papers are attached in Appendices E-G.

## 7.4 Wider implications of the research

The work presented in this thesis provides experimental evidence supporting the lightweighting benefits possible through strategically manufactured tailor-braided composite beam structures. Although the objectives of the thesis were not aimed at a direct industrial application, the results presented can be translated beyond the boundaries of academic research and applied in multiple industrial scenarios. In this section, three examples are discussed for potential applications of tailor-braiding:

(i)     Tailor-braiding can be utilised for achieving optimal structural design. This is demonstrated here with the example of an aircraft wing structure, a component that is already manufactured using braided composites [39]. Similar to any composite structural design exercise, the design of composite wing structure involves extensive work packages aimed at optimising the thickness and fibre orientation of the composite to achieve satisfactory mechanical performance at minimum weight. Figure 7.1 shows the thickness profile of a wing structure from an optimisation study performed by Guo *et al.* [188]. As shown in the figure, the study considered different regions of a wing structure and iteratively optimised the thickness as well as fibre lay-up for each region.
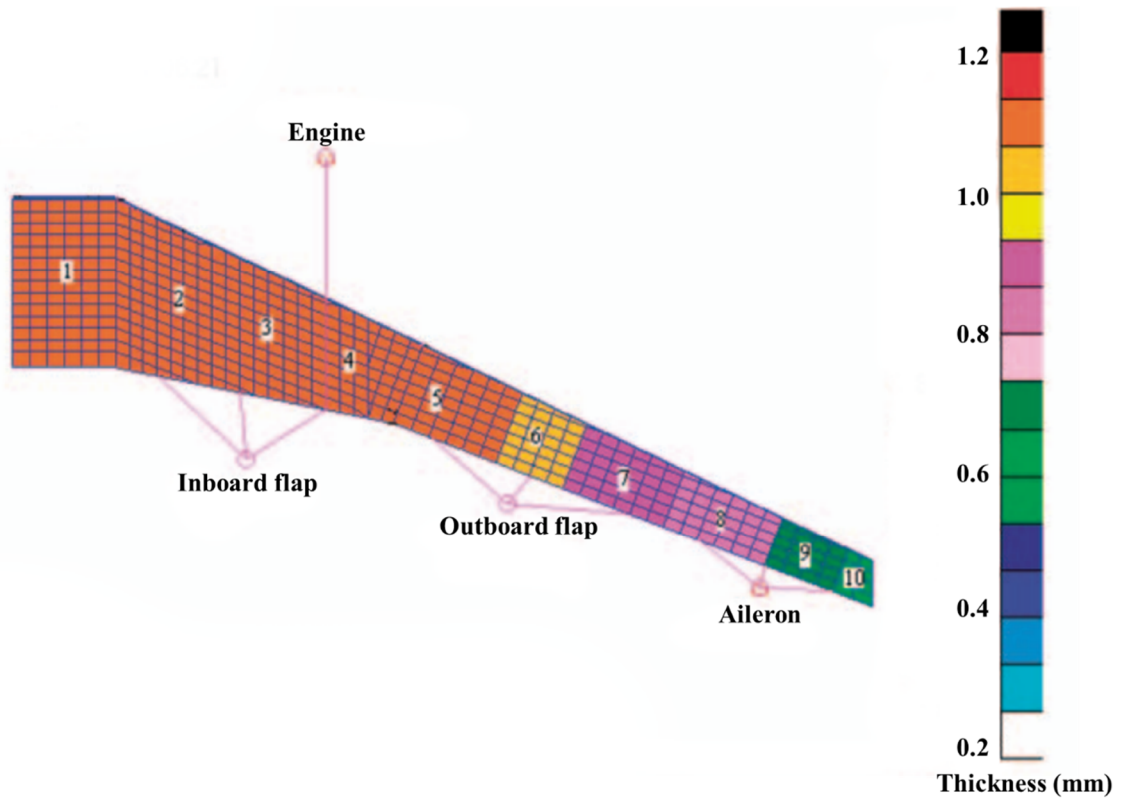
Figure 7.1 Thickness profile of a composite wing structure (Taken from [188]).

As demonstrated for a three-point flexural load case in this thesis, a braided composite wing structure can be designed with variable braid angle for the relevant external loading conditions. Through design iterations, the braid angle profile can be optimised to impart the required part performance while minimising the mass of the wing structure.

(ii)     Tailor-braiding can be advantageous in the manufacturing of complex shaped components designed with a constant braid angle. Knowing the geometry of the final component beforehand, dry preforms can be tailor-braided on constant diameter mandrels such that the preforms result in a constant braid angle upon conforming to the final part geometry. This approach would be advantageous in the Composite Multispar Flap (CMF) project by Airbus Bremen, aimed to replace the outboard flap on the A320 with braided box sections manufactured from braided preforms received from an external supplier [189]. The wing had a tapered structure with variable circumference, as shown in Figure 7.2. However, the received braided preforms were uniformly braided at a particular braid angle on a mandrel with a constant outer diameter. This would result in suboptimal fibre orientation as the braid conformed to the variable

134

geometry of the part. Therefore, the unwanted variation in braid angle was found to result in a significant decrease in mechanical performance. Ultimately, the consortium decided to drop the use of braided preforms. Using tailor-braiding proposed within this thesis, the initial design and manufacturing concepts could be preserved and save significant time and resources.
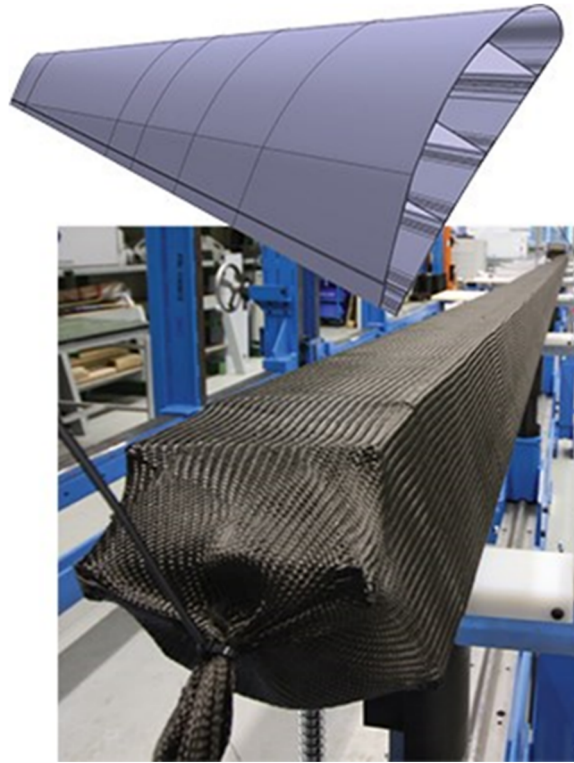


Figure 7.2 Original CMF design with multiple braided boxes (top) and received braided fabric with constant braid angle (bottom) (Taken from [189]).

(iii)    Tailor-braiding presents an opportunity to enhance the mechanical performance of adhesive joints. Adhesive bonding provides several advantages over mechanical fastening and is particularly useful for composite-to-composite as well as composite-to-metal joints. Further improvement in the fatigue life of a joint is possible by achieving a uniform stress distribution in the adhesive [190]. As demonstrated by Ganesh *et al.* [152] through their numerical analysis, a controlled braid angle gradient in the adherents, as shown for a braided preform in Figure 7.3, is suitable for imparting a uniform stress distribution across a joint, thus eliminating the stress concentration. Although this application of tailor-braiding presents promising prospects, demonstration in structural components under real-life load cases is required to prove its overall feasibility.

Figure 7.3 Braided preform with graded braid angle transition (Taken from [152]).

The abovementioned applications are a few examples of the potential of the tailor-braiding concept for manufacturing as well as performance benefits. The discussed applications can be readily transferred to other sectors relying on composites for structural applications. As such, the results presented in this thesis are expected to inspire further work within this sub-topic of research in the domain of structural composite manufacturin

# References

[1]     European Parliament. CO₂ emissions from cars: facts and figures (infographics). 2019. Available from: https://www.europarl.europa.eu/news/en/headlines/society/20190313STO31218/co2-emissions-from-cars-facts-and-figures-infographics. Date accessed: 28th April, 2020.

[2]     International Energy Agency (IEA). CO₂ emissions from fuel combustion highlights. 2018. Available from: https://webstore.iea.org/co2-emissions-from-fuel-combustion-2018-highlights. Date accessed: 28th April, 2020.

[3]     International Energy Agency (IEA). Tracking Transport. 2019. Available from: https://www.iea.org/reports/tracking-transport-2019. Date accessed: 28th April, 2020.

[4]     European Environment Agency. Greenhouse gas emissions from transport in Europe. 2019. Available from: https://www.eea.europa.eu/data-and-maps/indicators/transport-emissions-of-greenhouse-gases/transport-emissions-of-greenhouse-gases-12. Date accessed: 28th April, 2020.

[5]     Directive EU. 53/EC of the European Parliament and of the Council of 18 September 2000 on end-of life vehicles. Off J Eur Union, L Ser 2000;21:34–42.

[6]     Mock P. CO₂ emission standards for passenger cars and light-commercial vehicles in the european union. International Council on Clean Transportation. 2019. Available from: https://theicct.org/publications/ldv-co2-stds-eu-2030-update-jan2019. Date accessed: 28th April, 2020.

[7]     Tietge U, Mock P, Dornoff J. CO₂ Emissions from New Passenger Cars in the European Union: Car Manufacturers' Performance in 2018. International Council on Clean Transportation. 2019. Available from: https://theicct.org/publications/CO2-emissions-PVs-Europe-2018. Date accessed: 28th April, 2020.

[8]     Isenstadt A, German J, Bubna P, Wiseman M, Venkatakrishnan U, Abbasov L, Guillen P, Moroz N, Richman D, Kolwich G. Lightweighting technology development and trends in US passenger vehicles. International Council on Clean Transportation. 2016. Available from: https://theicct.org/publications/lightweighting-technology-development-and-trends-us-passenger-vehicles. Date accessed: 28th April, 2020.

[9]     Hofer J, Wilhelm E, Schenler W. Optimal lightweighting in battery electric vehicles. World Electr Veh J 2012;5:751–62.

[10] Kahl M. Special report : Vehicle lightweighting. Automotive World. 2016. Available from: https://www.automotiveworld.com/articles/special-report-vehicle-lightweighting/. Date accessed: 28th April, 2020.

[11] CES EduPack 2019, ANSYS Granta © 2020 Granta Design.
Available from: https://grantadesign.com/education/students/charts/. Date accessed: 28th April, 2020.

[12] Guide to Composites. Gurit Holding. 2004. Available form: https://www.gurit.com/Our-Business/Composite-Materials. Date accessed: 28th April, 2020.

[13] Gibson RF. Principles of composite material mechanics. CRC press. 2016.

[14] Strong AB. Fundamentals of composites manufacturing: materials, methods and applications. Society of Manufacturing Engineers. 2008.

[15] Howstuffworks.1953 Corvette.
Available from: https://auto.howstuffworks.com/1953-corvette1.htm. Date accessed: 28th April, 2020.

[16] Savage G. Composite Materials Technology in Formula 1 Motor Racing. Honda Racing F1 Team. 2008. Available from: http://www.formula1-dictionary.net/Big/. Date accessed: 28th April, 2020.

[17] Androit Market Research. Global Carbon Fiber Market Trends 2018, by Product (Regular tow carbon fiber, Large tow carbon fiber), by Application (Automotive, Aerospace & defence, Wind turbines, Sports equipment, Industrial materials, others), By Region, and Forecast 2019 to 2025. 2019. Available from: https://www.adroitmarketresearch.com/industry-reports/carbon-fiber-market.
Date accessed: 28th April, 2020.

[18] Koumoulos EP, Trompeta AF, Santos RM, Martins M, Santos CM, Iglesias V, Böhm R, Gong G, Chiminelli A, Verpoest I, Kiekens P. Research and Development in Carbon Fibers and Advanced High-Performance Composites Supply Chain in Europe: A Roadmap for Challenges and the Industrial Uptake. J Compos Sci 2019;3:86.

[19] Heuss R, Müller N, Sintern Wv SA, Tschiesner A. Lightweight, heavy impact. McKinsey & Company. 2012. Available from:
https://www.mckinsey.com/~/media/mckinsey/dotcom/client_service/automotive.
Date accessed: 28th April, 2020.

[20] Malnati P, Sloan J. Fast and Faster: Rapid-cure resins drive down cycle times. CompositesWorld. 2018.
Available from: https://www.compositesworld.com/articles/fast-and-faster-rapid-cure-epoxies-drive-down-cycle-times. Date accessed: 28th April, 2020.

[21] Malnati P. Carbon fiber/epoxy for automotive mass reduction, mass production. CompositesWorld 2019.
Available from: https://www.compositesworld.com/blog/post/carbon-fiberepoxy-for-automotive-mass-reduction-mass-production. Date accessed: 28th April, 2020.

[22] Sloan J. The making of the BMW i3. CompositesWorld. 2014.
Available from: https://www.compositesworld.com/blog/post/the-making-of-the-bmw-i3. Date accessed: 28th April, 2020.

[23] BMW i3 - First Mass Produced Car Made With Composites. CompositesLab. 2016.
Available from: http://compositeslab.com/bmw-i3-first-mass-produced-car-made-largely-with-composites/. Date accessed: 28th April, 2020.

[24] Institute for Advanced Composites Manufacturing Innovation – IACMI.
Available from: https://iacmi.org/. Date accessed: 28th April, 2020.

[25] The EPSRC Future Composites Manufacturing Research Hub. CIMComp.
Available from: https://cimcomp.ac.uk/. Date accessed: 28th April, 2020.

[26] Center for Composite Materials- University of Delaware.
Available from: https://www.ccm.udel.edu/. Date accessed: 28th April, 2020.

[27] National Composites Centre.
Available from: https://www.nccuk.com/. Date accessed: 28th April, 2020.

[28] FIDAMC (The Composites Research, Development and Application Centre).
Available from: https://fidamc.es/home. Date accessed: 28th April, 2020.

[29] Carey JP. Introduction to braided composites. In: Handbook of Advances in Braided Composite Materials. Woodhead Publishing; 2017, p. 1–21.

[30] Kelkar AD, Whitcomb JD. Characterization and structural behavior of braided composites. U.S. Department of Transportation Federal Aviation Administration. 2009.
Available from: https://trid.trb.org/view/892117. Date accessed: 28th April, 2020.

[31] MAN Truck and Bus. 2015.
Available from: https://press.mantruckandbus.com/en/carbon-carrier-for-buses-receives-innovation-award/. Date accessed: 28th April, 2020.

[32] Wilden KS, Harris CG, Flynn BW, Gessel MG, Scholz DB, Stawski S, Winston V. Advanced technology composite fuselage-Manufacturing. National Aeronautics and Space Administration. 1997.
Available from: https://ntrs.nasa.gov/citations/19970016010. Date accessed: 28th April, 2020.

[33] Villaluz K. Porsche Uses the World's Largest Radial Braiding Machine to Create Carbon Fiber Wheels. Interesting Engineering. 2018.
Available from: https://interestingengineering.com/porsche-the-worlds-largest-radial-braiding-machine-create-carbon-fiber-wheels. Date accessed: 28th April, 2020.

[34] Schmitt B. The Making Of The Lexus LFA Supercar. An Inside Report, Chapter 2: In The Clean Room. - The Truth About Cars. Truth about Cars 2012.
Available from: http://www.thetruthaboutcars.com/2012/07/the-making-of-the-lexus-lfa-supercar-an-inside-report-chapter-2-in-the-clean-room/. Date accessed: 28th April, 2020.

[35] Robotic braider open for business. Advanced Manufacturng Research Centre. 2018.
Available from: https://www.amrc.co.uk/news/robotic-braider-open-for-business. Date accessed: 28th April, 2020.

[36] Braiding. National Composites Research Centre.
Availabel from: https://www.nccuk.com/why-ncc/technologies/braiding/. Date accessed: 28th April, 2020.

[37] A&P Technology. GEnx$^{TM}$ Engine 2014.
Available from: http://www.braider.com/Case-Studies/GEnx-Engine.aspx. Date accessed: 28th April, 2020.

[38] A&P Technology. Honeywell Jet Engine Stator Vane 2014.
Available from: http://www.braider.com/Case-Studies/Jet-Engine-Stator-Vane.aspx. Date accessed: 28th April, 2020.

[39] A&P Technology. Bombardier Wing Flap 2014.
Available from: http://www.braider.com/Case-Studies/Bombardier-Wing-Flap.aspx. Date accessed: 28th April, 2020.

[40] Gardiner G. Airbus A350 Update: BRaF & FPP. CompositesWorld. 2012.
Available from: https://www.compositesworld.com/articles/airbus-a350-update-braf-fpp. Date accessed: 28th April, 2020.

[41] Gardiner G. BMW 7 Series CFRP: corrections and missing details. CompositesWorld. 2016.
Available from: https://www.compositesworld.com/blog/post/bmw-7-series-cfrp-corrections-and-missing-details. Date accessed: 28th April, 2020.

[42] Kyosev Y. Advances in braiding technology: Specialized techniques and applications. Woodhead Publishing; 2016.

[43] Gardiner G. Sixth Element: Lamborghini accelerates CFRP. CompositesWorld. 2012.
Available from: https://www.compositesworld.com/articles/sixth-element-lamborghini-accelerates-cfrp. Date accessed: 28th April, 2020.

[44]    Eurocarbon.
        Available from: http://www.eurocarbon.com/. Date accessed: 28th April, 2020.

[45]    Sloan J. Porsche and the braided carbon fiber wheel. CompositesWorld. 2017.
        Available from: https://www.compositesworld.com/blog/post/porsche-and-the-
        braided-carbon-fiber-wheel. Date accessed: 28th April, 2020.

[46]    Brosius D. Composites in sporting goods: Been there, done that? CompositesWorld.
        2015.
        Available from: https://www.compositesworld.com/articles/composites-in-sporting-
        goods-been-there-done-that. Date accessed: 28th April, 2020.

[47]    Gardiner G. Disruptive composite tubing manufacturing. CompositesWorld. 2019.
        Available from: https://www.compositesworld.com/blog/post/disruptive-composite-
        tubing-manufacturing. Date accessed: 28th April, 2020.

[48]    TE Connectivity. Braided & Coiled Catheter Shafts 2018.
        Available from: http://www.te.com/usa-en/industries/medical-healthcare/our-
        focus/interventional/braided-coiled-catheter-shafts.html. Date accessed: 28th April,
        2020.

[49]    Carbon and Aramid (Kevlar) All Braid.
        Available from: https://www.rockwestcomposites.com/shop/shaped-
        tubing/rectangular-tubing/carbon-aramid-braided/25501-cya. Date accessed: 28th
        April, 2020.

[50]    Sturm R, Heieck F. Energy absorption capacity of braided frames under bending loads.
        Compos Struct 2015;134:957–65.

[51]    Carey J, Fahim A, Munro M. Design of braided composite cardiovascular catheters
        based on required axial, flexural, and torsional rigidities. J Biomed Mater Res Part B
        Appl Biomater An Off J Soc Biomater Japanese Soc Biomater Aust Soc Biomater
        Korean Soc Biomater 2004;70:73–81.

[52]    Boss JN, Ganesh VK. Fabrication and properties of graded composite rods for
        biomedical applications. Compos Struct 2006;74:289–93.

[53]    Stanier D, Gent I, Roy SS, Hamerton I, Potluri P, Ivanov DS. Mechanical behaviour of
        patterned multi-matrix composites with gradient properties. In: ECCM 2016:
        Proceedings of the 17th European Conference on Composite Materials, Munich, June
        2016.

[54]    Huang Z-M, Wang Q, Ramakrishna S. Tensile behaviour of functionally graded braided
        carbon fibre/epoxy composite material. Polym Polym Compos 2002;10:307–14.

[55]    Fujihara K, Teo K, Gopal R, Loh PL, Ganesh VK, Ramakrishna S, Foong KW, Chew
        CL. Fibrous composite materials in dentistry and orthopaedics: review and applications.
        Compos Sci Technol 2004;64:775–88.

[56] Slange TK. Rapid Manufacturing of Tailored Thermoplastic Composites by Automated Lay-up and Stamp Forming. PhD Thesis, University of Twente. 2019.

[57] High Performance Computing Studies: DOT HS 812 404. Department of Transportation. 2017. Available from: https://www.nhtsa.gov/document/high-performance-computing-studies-dot-hs-812-404. Date accessed: 28th April, 2020.

[58] Gardiner G. BMW 7 Series Plant: Dingolfing, Germany. CompositesWorld. 2016. Available from: https://www.compositesworld.com/articles/bmw-7-series-plant-dingolfing-germany. Date accessed: 28th April, 2020.

[59] Fiber Patch Placement. Cevotec. Available from: https://www.cevotec.com/en/fpp-technology/. Date accessed: 28th April, 2020.

[60] Gardiner G. Tailored Fiber Placement: Besting metal in volume production. CompositesWorld. 2013. Available from: https://www.compositesworld.com/articles/tailored-fiber-placement-besting-metal-in-volume-production. Date accessed: 28th April, 2020.

[61] Kim T, Schmidt K, Deemie C, Wycech J, Liang H, Giszter SF. Highly flexible precisely braided multielectrode probes and combinatorics for future neuroprostheses. Front Neurosci 2019;13.

[62] Ogale V, Alagirusamy R. Textile preforms for advanced composites. Indian J Fibre Text R 2004; 29(3):366-375.

[63] Potluri P, Rawal A, Rivaldi M, Porat I. Geometrical modelling and control of a triaxial braiding machine for producing 3D preforms. Compos Part A Appl Sci Manuf 2003;34:481–92.

[64] Berthelot J-M, Ling FF. Composite materials: mechanical behavior and structural analysis. Springer, 1999.

[65] Gardiner G. Recycled thermoplastic composites for production. CompositesWorld. 2019. Available from: https://www.compositesworld.com/articles/recycled-thermoplastic-composites-for-production. Date accessed: 28th April, 2020.

[66] Stavrov D, Bersee HEN. Resistance welding of thermoplastic composites-an overview. Compos Part A Appl Sci Manuf 2005;36:39–54.

[67] Ahmed TJ, Stavrov D, Bersee HEN, Beukers A. Induction welding of thermoplastic composites—an overview. Compos Part A Appl Sci Manuf 2006;37:1638–51.

[68]    Gardiner G. New horizons in welding thermoplastic composites. CompositesWorld. 2018.
Available from: https://www.compositesworld.com/blog/post/new-horizons-in-welding-thermoplastic-composites. Date accessed: 28th April, 2020.

[69]    Lafarie-Frenot MC, Touchard F. Comparative in-plane shear behaviour of long-carbon-fibre composites with thermoset or thermoplastic matrix. Compos Sci Technol 1994;52:417–25.

[70]    Mehdikhani M, Gorbatikh L, Verpoest I, Lomov SV. Voids in fiber-reinforced polymer composites: A review on their formation, characteristics, and effects on mechanical performance. J Compos Mater 2019;53:1579–669.

[71]    Sloan J. OOA: Thermoplastic alternative targets performance spec. CompositesWorld. 2016.
Available from: https://www.compositesworld.com/articles/ooa-thermoplastic-alternative-targets-performance-spec. Date accessed: 28th April, 2020.

[72]    Francis S. Thermoplastic composites: Poised to step forward. CompositesWorld. 2019.
Available from: https://www.compositesworld.com/blog/post/thermoplastic-composites-poised-to-step-forward. Date accessed: 28th April, 2020.

[73]    Gardiner G. Thermoplastic composites: Primary structure? CompositesWorld. 2011.
Available from: https://www.compositesworld.com/articles/thermoplastic-composites-primary-structure. Date accessed: 28th April, 2020.

[74]    Black S. Reinforced thermoplastics in aircraft primary structure. CompositesWorld. 2011.
Available from: https://www.compositesworld.com/articles/reinforced-thermoplastics-in-aircraft-primary-structure. Date accessed: 28th April, 2020.

[75]    Black S. Thermoplastic composites save weight in rotorcraft aerostructure. CompositesWorld. 2014.
Available from: https://www.compositesworld.com/articles/thermoplastic-composites-save-weight-in-rotorcraft-aerostructure. Date accessed: 28th April, 2020.

[76]    Gardiner G. Accelerating thermoplastic composites in aerospace. CompositesWorld. 2019.
Available from: https://www.compositesworld.com/blog/post/accelerating-thermoplastic-composites-in-aerospace. Date accessed: 28th April, 2020.

[77]    Reynolds N, Ramamohan AB. High-volume thermoplastic composite technology for automotive structures. In: Advanced composite materials for automotive application. Joh Wiley & Sons; 2013, p. 29–50.

[78]    Black S. Thermoplastic door a first for automotive composites. CompositesWorld. 2019.
        Available from: https://www.compositesworld.com/blog/post/thermoplastic-door-a-first-for-automotive-composites. Date accessed: 28th April, 2020.

[79]    Sloan J. Thermoplastic composite B-pillar? CompositesWorld. 2016.
        Available from: https://www.compositesworld.com/blog/post/thermoplastic-composite-b-pillar. Date accessed: 28th April, 2020.

[80]    Ishikawa T, Amaoka K, Masubuchi Y, Yamamoto T, Yamanaka A, Arai M, Takahashi J. Overview of automotive structural composites technology developments in Japan. Compos Sci Technol 2018;155:221–46.

[81]    Sloan J. Thermoplastics riding into automotive, aerospace. CompositesWorld. 2016.
        Available from: https://www.compositesworld.com/articles/thermoplastics-riding-into-automotive-aerospace. Date accessed: 28th April, 2020.

[82]    Headley M. Auto Industry Explores Thermoplastics. Composite Manufacturing Magazine. 2016.
        Available from:
        http://compositesmanufacturingmagazine.com/2016/09/thermoplastic-composites-draw-automotive-industry-interest/. Date accessed: 28th April, 2020.

[83]    Sloan J. Auto composites quest: One-minute cycle time? CompositesWorld. 2012.
        Available from: https://www.compositesworld.com/articles/auto-composites-quest-one-minute-cycle-time. Date accessed: 28th April, 2020.

[84]    Trudel-Boucher D, Fisa B, Denault J, Gagnon P. Experimental investigation of stamp forming of unconsolidated commingled E-glass/polypropylene fabrics. Compos Sci Technol 2006;66:555–70.

[85]    Thomann UI, Sauter M, Ermanni P. A combined impregnation and heat transfer model for stamp forming of unconsolidated commingled yarn preforms. Compos Sci Technol 2004;64:1637–51.

[86]    Slange TK, Warnet LL, Grouve WJB, Akkerman R. Deconsolidation of C/PEEK blanks: on the role of prepreg, blank manufacturing method and conditioning. Compos Part A Appl Sci Manuf 2018;113:189–99.

[87]    Svensson N, Shishoo R, Gilchrist M. Manufacturing of thermoplastic composites from commingled yarns-A review. J Thermoplast Compos Mater 1998;11:22–56.

[88]     Schneeberger C, Wong JCH, Ermanni P. Hybrid bicomponent fibres for thermoplastic composite preforms. Compos Part A Appl Sci Manuf 2017;103:69–73.

[89]     Reynolds N, Awang-Ngah S, Williams G, Hughes DJ. Direct processing of structural thermoplastic composites using rapid isothermal stamp forming. Appl Compos Mater 2020:1–9.

[90]     Ramasamy A, Wang Y, Muzzy J. Braided thermoplastic composites from powder-coated towpregs. Part I: Towpreg characterization. Polym Compos 1996;17:497–504.

[91]     Ramasamy A, Wang Y, Muzzy J. Braided thermoplastic composites from powder-coated towpregs. Part II: Braiding characteristics of towpregs. Polym Compos 1996;17:505–14.

[92]     Alagirusamy R, Fangueiro R, Ogale V, Padaki N. Hybrid yarns and textile preforming for thermoplastic composites. Text Prog 2006;38:1–71.

[93]     Laberge-Lebel L, Van Hoa S. Manufacturing of braided thermoplastic composites with carbon/nylon commingled fibers. J Compos Mater 2007;41:1101–21.

[94]     Lebel LL, Nakai A. Design and manufacturing of an L-shaped thermoplastic composite beam by braid-trusion. Compos Part A Appl Sci Manuf 2012;43:1717–29.

[95]     Risicato JV, Kelly F, Soulat D, Legrand X, Trümper W, Cochrane C, Koncar V. A complex shaped reinforced thermoplastic composite part made of commingled yarns with integrated sensor. Appl Compos Mater 2015;22:81–98.

[96]     Jacquot P-B, Wang P, Soulat D, Legrand X. Analysis of the preforming behaviour of the braided and woven flax/polyamide fabrics. J Ind Text 2016;46:698–718.

[97]     Bernet N, Wakeman MD, Bourban P-E, Månson J-A. An integrated cost and consolidation model for commingled yarn based composites. Compos Part A Appl Sci Manuf 2002;33:495–506.

[98]     Drzal LT, Madhukar M. Fibre-matrix adhesion and its relationship to composite mechanical properties. J Mater Sci 1993;28:569–610.

[99]     Han SH, Oh HJ, Kim SS. Evaluation of fiber surface treatment on the interfacial behavior of carbon fiber-reinforced polypropylene composites. Compos Part B Eng 2014;60:98–105.

[100]    Anderson J. Manufacturing and microstructural modeling of geometrically complex composite components produced by bladder assisted composite manufacturing (BACM). PhD Thesis, University of Oklahoma, 2013.

[101]    Davis SJ. Long fiber reinforced thermoplastic frame especially for a tennis racquet. U.S. Patent 1993;5,176,868.

[102]    Olson SH, Busby JS, Needle SA. Composite bicycle frame and method of manufacturing. U.S. Patent 1998;5,803,476..

[103]    Bernet N, Bourban P-E, Månson J-AE. Cost-effective manufacturing of hollow composite structures by bladder inflation moulding. In: ICCM 1999: Proceedings of the 12th International Conference on Composite Materials, Paris, July 1999.

[104]    Bernet N, Michaud V, Bourban P-E, Månson J-A. Commingled yarn composites for rapid processing of complex shapes. Compos Part A Appl Sci Manuf 2001;32:1613–26.

[105]    Arold B, Gessler A, Metzner C, Birkefeld K. Braiding processes for composites manufacture. In: Advances in Composites Manufacturing and Process Design. Woodhead Publishing; 2015, p. 3-26.

[106]    Gorbatikh L, Lomov SV. Damage accumulation in textile composites. In: Modeling Damage, Fatigue and Failure of Composite Materials. Woodhead Publishing; 2016, p. 41-59.

[107]    Bibo GA, Hogg PJ. The role of reinforcement architecture on impact damage mechanisms and post-impact compression behaviour. J Mater Sci 1996;31:1115–37.

[108]    Fouinneteau M. Damage and failure modelling of carbon and glass 2D braided composites. PhD Thesis, Cranfield University. 2006.

[109]    Littell J. The experimental and analytical characterization of the macromechanical response for triaxial braided composite materials. PhD Thesis, University of Akron, 2008.

[110]    Falzon PJ, Herszberg I. Mechanical performance of 2-D braided carbon/epoxy composites. Compos Sci Technol 1998;58:253–65.

[111]    Harte A-M, Fleck NA. On the mechanics of braided composites in tension. Eur J Mech 2000;19:259–75.

X

[112] Wehrkamp-Richter T, Hinterhölzl R, Pinho ST. Damage and failure of triaxial braided composites under multi-axial stress states. Compos Sci Technol 2017;150:32–44.

[113] Ivanov D, Lomov SV, Verpoest I, Baudry F, Xie H. Damage initiation and development in triaxial braid and fine structure of damage. In: ECCM 2006: Proceedings of the 12th European Conference on Composite Materials, Biarritz, June 2006.

[114] Naik RA, Ifju PG, Masters JE. Effect of fiber architecture parameters on deformation fields and elastic moduli of 2-D braided composites. J Compos Mater 1994;28:656–81.

[115] Masters JE, Ifju PG. A phenomenological study of triaxially braided textile composites loaded in tension. Compos Sci Technol 1996;56:347–58.

[116] Du GW, Popper P. Analysis of a Circular Braiding Process for Complex Shapes. J Text Inst 1994;85:316–37.

[117] Melenka GW, Carey JP. Development of a generalized analytical model for tubular braided-architecture composites. J Compos Mater 2017;51:3861–75.

[118] Chai Y, Wang Y, Yousaf Z, Storm M, Vo NT, Wanelik K, Burnett TL, Potluri P, Withers PJ. Following the effect of braid architecture on performance and damage of carbon fibre/epoxy composite tubes during torsional straining. Compos Sci Technol 2020;200:108451.

[119] Priem C, Othman R, Rozycki P, Guillon D. Experimental investigation of the crash energy absorption of 2.5 D-braided thermoplastic composite tubes. Compos Struct 2014;116:814–26.

[120] Beard SJ, Chang FK. Energy absorption of braided composite tubes. Int J Crashworthiness 2002;7:191–206.

[121] Chiu CH, Tsai K-H, Huang WJ. Crush-failure modes of 2D triaxially braided hybrid composite tubes. Compos Sci Technol 1999;59:1713–23.

[122] Gautam M, Potluri P, Ogin S, Jain P. Necking behaviour of flattened tubular braided composites. In: ICCM 2015: Proceedings of the 20th International Conference on Composite Materials, Copenhagen, July 2015.

[123] Kyosev Y. Recent developments in braiding and narrow weaving. Berlin: Springer International Publishing; 2016.

[124] Potluri P, Manan A, Francke M, Day RJ. Flexural and torsional behaviour of biaxial and triaxial braided composite structures. Compos Struct 2006;75:377–86.

[125] Carlsson LA, Adams DF, Pipes RB. Experimental characterization of advanced composite materials. CRC press. 2014.

[126] Tolf G, Clarin P. Comparison between flexural and tensile modulus of fibre composites. Fibre Sci Technol 1984;21:319–26.

[127] Cheon SS, Lee DG, Jeong KS. Composite side-door impact beams for passenger cars. Compos Struct 1997;38:229–39.

[128] Basavaraju DH. Design and analysis of a composite beam for side impact protection of a sedan. MSc Thesis, Wichita State University, 2005.

[129] Rebelo P. Design study of a side intrusion beam for automotive safety. MSc Thesis, Instituto Superior Técnico, 2016.

[130] Wilson G. Crashworthiness of side impact beams. PhD Thesis, University of Strathclyde, 2002.

[131] Calonghi A. Alternative design of front door side impact beam for Nissan Navara. MSc Thesis, Cranfield University, 2006.

[132] Belingardi G, Mehdipour H, Mangino E, Martorana B. Progressive damage analysis of a rate-dependent hybrid composite beam. Compos Struct 2016;154:433–42.

[133] Bilston D, Rathnaweera G, Ruan D, Hajj M, Durandet Y. Parametric study of the bending properties of lightweight tubular metal/polymer foam hybrid structures. Compos Part B Eng 2016;105:101–10.

[134] Gardner L, Nethercot DA. Experiments on stainless steel hollow sections—Part 2: Member behaviour of columns and beams. J Constr Steel Res 2004;60:1319–32.

[135] Tang T, Zhang W, Yin H, Wang H. Crushing analysis of thin-walled beams with various section geometries under lateral impact. Thin-Walled Struct 2016;102:43–57.

[136] Kecman D. Bending collapse of rectangular and square section tubes. Int J Mech Sci 1983;25:623–36.

[137] Guo L, Yang S, Jiao H. Behavior of thin-walled circular hollow section tubes subjected to bending. Thin-Walled Struct 2013;73:281–9.

[138] Poonaya S, Teeboonma U, Thinvongpituk C. Plastic collapse analysis of thin-walled circular tubes subjected to bending. Thin-Walled Struct 2009;47:637–45.

[139] Charoenphan S, Bank LC, Plesha ME. Progressive tearing failure in pultruded composite material tubes. Compos Struct 2004;63:45–52.

[140] Shin KC, Lee JJ, Kim KH, Song MC, Huh JS. Axial crush and bending collapse of an aluminum/GFRP hybrid square tube and its energy absorption capability. Compos Struct 2002;57:279–87.

[141] Zhang X, Zhang H, Wang Z. Bending collapse of square tubes with variable thickness. Int J Mech Sci 2016;106:107–16.

[142] Duan L, Xiao N, Li G, Xu F, Chen T, Cheng A. Bending analysis and design optimisation of tailor-rolled blank thin-walled structures with top-hat sections. Int J Crashworthiness 2017;22:227–42.

[143] Sun G, Pang T, Zheng G, Song J, Li Q. On energy absorption of functionally graded tubes under transverse loading. Int J Mech Sci 2016;115–116:465–80.

[144] Liu Q, Xing H, Ju Y, Ou Z, Li Q. Quasi-static axial crushing and transverse bending of double hat shaped CFRP tubes. Compos Struct 2014;117:1–11.

[145] Fujihara K, Yoshida E, Nakai A, Ramakrishna S, Hamada H. Influence of micro-structures on bending properties of braided laminated composites. Compos Sci Technol 2007;67:2191–8.

[146] Tate JS, Kelkar AD. Flexural behavior of biaxial braided composites. In: Proceedings of ASME International Mechanical Engineering Congress and Exposition, Orlando, November 2005.

[147] Wu Z, Shen Y, Pan Z, Hu X. Three-point Bending Behavior and Energy Absorption Capacity of Composite Tube Reinforced by Gradient Braided Structure in Radial Direction. Fibers Polym 2019;20:1455–66.

[148] Kim HC, Shin DK, Lee JJ. Characteristics of aluminum/CFRP short square hollow section beam under transverse quasi-static loading. Compos Part B Eng 2013;51:345–58.

[149] Keating EM. Lightweighting of Stiffness Critical Advanced High Strength Steel Structures using Fibre Reinforced Plastics. PhD Thesis, University of Warwick, 2016.

[150] Sun G, Yu H, Wang Z, Xiao Z, Li Q. Energy absorption mechanics and design optimization of CFRP/aluminium hybrid structures for transverse loading. Int J Mech Sci 2019;150:767–83.

[151] Nishimoto H, Ohtani A, Nakai A, Hamada H. Prediction Method for Temporal Change in Fiber Orientation on Cylindrical Braided Preforms. Text Res J 2010;80:814–21.

[152] Ganesh VK, Choo TS. Modulus graded composite adherends for single-lap bonded joints. J Compos Mater 2002;36:1757–67.

[153] Stanier D, Radhakrishnan A, Gent I, Roy SS, Hamerton I, Potluri P, Scarpa F, Shaffer M, Ivanov DS. Matrix-graded and fibre-steered composites to tackle stress concentrations. Compos Struct 2019;207:72–80.

[154] Coats Performance Materials. Coats Synergex.
Available from: https://www.coats.com/en/Guidance/CoatsSynergex#Commingling.
Date accessed: accessed 27th March, 2020.

[155] Coats Performance Materials. Advanced Composite Fibres Brochure. 2019.
Available from: https://www.coats.com/en/Guidance/CoatsSynergex#Commingling.
Date accessed: accessed 27th March, 2020.

[156] Suzuki T, Takao H, Fujimura S, Dahmani C, Ishibashi T, Mamori H, Fukushima N, Murayama Y, Yamamoto M. Relationships between geometrical parameters and mechanical properties for a helical braided flow diverter stent. Technol Heal Care 2017;25:611–23.

[157] Kyosev Y, Cordes A. Geometrical modelling of tubular and flat braids within the jamming limits—verification and limitations. In: Recent Developments in Braiding and Narrow Weaving. Springer, Cham. 2016, p. 23-31.

[158] Olivier P, Cottu JP, Ferret B. Effects of cure cycle pressure and voids on some mechanical properties of carbon/epoxy laminates. Composites 1995;26:509–15.

[159] BS ISO 1183-1. Plastics. Methods for determining the density of non-cellular plastics—Part 1: Immersion method, liquid pycnometer method and titration method. BSI 2019.

[160] Gupta J, Reynolds N, Chiciudean T, Kendall K. A comparative study between epoxy and vinyl ester CF-SMC for high volume automotive composite crash structures. Compos Struct 2020;244:112299.

[161] BS ISO 14127:2008. Carbon-fibre-reinforced composites. Determination of the resin, fibre and void contents. BSI 2008.

[162] Personal communication. Coats Performance Materials. Date: 13th May, 2019.

[163] ASTM D790-17. Standard test methods for flexural properties of un-reinforced and reinforced plastics and electrical insulating materials. ASTM. 2017.

[164] BS ISO 14125:1998. Fibre-reinforced Plastic Composites: Determination of Flexural Properties. BSI 1998.

[165] Unlusoy C, Melenka GW. Flexural testing of cellulose fiber braided composites using three dimensional digital image correlation. Compos Struct 2019;230:111538.

[166] Makeev A, Ignatius C, He Y, Shonkwiler B. A Test Method for Assessment of Shear Properties of Thick Composites. J Compos Mater 2009;43:3091–105.

[167] GOM. GOM ARAMIS.
Available from: https://www.gom.com/metrology-systems/aramis. Date accessed: 27th March, 2020.

[168]  GOM. ARAMIS: Sensor Configuration Examples. 2008.

[169] Powe RAW. Towards the characterisation of automotive specific woven composite laminates at intermediate strain rates. PhD Thesis, University of Warwick. 2018.

[170] GOM. GOM Correlate Professional.
Available from: https://www.gom.com/3d-software/gom-correlate-professional.html. Date accessed: 27th March, 2020.

[171] Altair Inspire$^{TM}$. solidThinking.
https://solidthinking.com/product/inspire/. Date accessed: 21st June, 2019.

[172] Micallef C. Lightweighting of double-decker buses. EngD Thesis, University of Warwick, 2018.

[173] Surface Generation Limited. About Surface Generation and our unique PtFS technology.
Available from: https://www.surface-generation.com/about-us/. Date accessed: 21st June, 2019.

[174] Froemder C, Kirwan K, Reynolds N, Wilson PR, Fernandes FC, Coles SR. Investigation of the processability of hybrid thermoplastic nonwoven including recycled carbon fibre through fast stamping. In: Proceedings of SAMPE Europe Conference, Southamphon, September 2018.

[175] Grigg MN. Thermo-oxidative degradation of polyamide 6. PhD Thesis, Queensland University of Technology, 2006.

[176] Tung JF. Synthesis and characterisation of polyamide 6 blends made by reactive extrusion. PhD Thesis, Brunel University, 1993.

[177] Levchik SV, Weil ED, Lewin M. Thermal decomposition of aliphatic nylons. Polym Int 1999;48:532–57.

[178] Parlevliet PP, Bersee HEN, Beukers A. Residual stresses in thermoplastic composites— A study of the literature—Part I: Formation of residual stresses. Compos Part A Appl Sci Manuf 2006;37:1847–57.

[179] Carey JP, Melenka GW, Hunt AJ, Ayranci C. Introduction to braided composite material behavior. In: Handbook of Advances in Braided Composite Materials. Woodhead Publishing; 2017, p. 207–37.

[180] Tukey JW. The collected works of John W. Tukey. vol. 1. Taylor & Francis; 1984.

[181] Potluri P, Manan A. Mechanics of non-orthogonally interlaced textile composites. Compos Part A Appl Sci Manuf 2007;38:1216–26.

[182] Melenka, G.W., Hunt, A.J., van Ravenhorst, J.H., Akkerman, R., Pastore, C.M., Ko, F.K., Munro, M., Carey, J.P. Manufacturing processes for braided composite materials. In: Handbook of Advances in Braided Composite Materials. Woodhead Publishing; 2017, p. 47–153.

[183] Lambert J, Chambers AR, Sinclair I, Spearing SM. 3D damage characterisation and the role of voids in the fatigue of wind turbine blade materials. Compos Sci Technol 2012;72:337–43.

[184] Patou J, Bonnaire R, De Luycker E, Bernhart G. Influence of consolidation process on voids and mechanical properties of powdered and commingled carbon/PPS laminates. Compos Part A Appl Sci Manuf 2019;117:260–75.

[185] 3DEXPERIENCE R2017x for Academia on the cloud. Composite Braiding Designer. Dassault Systèmes Catia.
Available from: https://cloud.academy.3ds.com/r2017x/role_cba.html. Date accessed: 2nd May, 2021.

[186] Saenz-Castillo D, Martin MI, Calvo S, Rodriguez-Lence F, Güemes A. Effect of processing parameters and void content on mechanical properties and NDI of thermoplastic composites. Compos Part A Appl Sci Manuf 2019;121:308–20.

[187] Endruweit A, Long AC. A model for the in-plane permeability of triaxially braided reinforcements. Compos Part A Appl Sci Manuf 2011;42:165–72.

[188] Guo S, Li D, Liu Y. Multi-objective optimization of a composite wing subject to strength and aeroelastic constraints. Proc Inst Mech Eng Part G J Aerosp Eng 2012;226:1095–106.

[189]  Gardiner G. Reducing manufacturing cost via RTM. Compositesworld. Available from: https://www.compositesworld.com/articles/reducing-manufacturing-cost-via-rtm. Date accessed: 26th August, 2020.

[190]  Curley AJ, Hadavinia H, Kinloch AJ, Taylor AC. Predicting the service-life of adhesively-bonded joints. Int J Fract 2000;103:41–69.

# Appendix A: Load cell calibration

**CERTIFICATE OF CALIBRATION**
ISSUED BY:
SERCAL MATERIALS TESTING MACHINES SERVICES LTD
UKAS ACCREDITED CALIBRATION LABORATORY
CERTIFICATE NUMBER: 55372
DATE OF ISSUE:    03 August 2020

## SERCAL MTMS LTD.

Page 1 of 3 Pages

Sercal Materials Testing Machines Services Ltd.
Southern Avenue, Leominster,
Herefordshire, HR6 0QH.
Tel: +44 (0) 1527 514015   Fax: +44 (0) 1527 514016
E-mail: enquiries@sercalcalibrations.co.uk

Approved Signatories
J. Swann
Dr N. Wrigley
Andrew Duggan

| | |
|---|---|
| **Issued To:** | **Zwick Roell Ltd (For & On Behalf of University of Warwick)** |
| **Address:** | **MEC Materials Testing Laboratory, University of Warwick Campus, CV4 7AL** |

| | | | |
|---|---|---|---|
| **Machine Description:** | Universal Testing Machine | **Serial Number:** | J6911 |
| **Manufacturer / Type:** | Instron 5800R | **Force Capacity:** | 100kN |
| **Display System:** | Single Range Computer Display | **Software:** Bluehill 2 Version 2.35.917 | |
| **Associated Equipment:** | HP Computer System | **Serial Number:** | CZC50312DN |

| | | | |
|---|---|---|---|
| **Date of Calibration:** | 28 July 2020 | **Ambient Temperature:** 24.5°C | |
| **Sercal Quote Reference:** | Q200208N-1 | **Location:** MEC Materials Testing Laboratory | |
| Previous certificate number: | N/a | | |

**Method:**
The testing machine identified above has been calibrated in accordance with the requirements of **BS EN ISO 7500-1:2018** over the ranges given below for increasing forces only. The calibration was performed using force proving devices and / or masses which meet the requirements of BS EN ISO 7500-1 and equipment which is calibrated in accordance with BS EN ISO 376:2011
The machine complied with the requirements of the standard for the following ranges and classifications with regard to the relative error, repeatability, resolution and zero return to which table 2 of the standard refers:

| Range | Mode | Status | Classification of range(s) to minimum force |
|---|---|---|---|
| 100kN | Tension | As found | 100kN Class 0.5 down to 2kN |
| 100kN | Compression | As found | 100kN Class 0.5 down to 2kN |
| 10kN | Tension | As found | 10kN Class 0.5 down to 0.2kN |
| 10kN | Compression | As found | 10kN Class 0.5 down to 0.2kN |
| 500N | Tension | As found | 500N Class 0.5 down to 10N |
| 500N | Compression | As found | 500N Class 0.5 down to 10N |

Detailed tabulated results are shown on the following pages.

Calibrated by:   Lee Smith

Certified by:

# CERTIFICATE OF CALIBRATION

**ISSUED BY: SERCAL MATERIALS TESTING MACHINES SERVICES LTD**
**UKAS ACCREDITED CALIBRATION LABORATORY 0375**
**CERTIFICATE NUMBER: 55372**
**DATE OF ISSUE:     03 August 2020**

The following traceable force proving equipment was used for the calibration:

| Description | Capacity | Class | Serial Number | Certificate Number | Date Calibrated |
|---|---|---|---|---|---|
| Nobel DC Ratio meter | - | - | 97-6548 | 2019110129-1 | 16 December 2019 |
| Load Cell | 200N | 0.5 | T3Z2528 | 2004011 | 08 April 2020 |
| Load Cell | 1kN | 0.5 | 9561355 | 0157/1902022 | 12 February 2019 |
| Load Cell | 10kN | 0.5 | 020007S | 0157/1907022 | 27 July 2019 |
| Load Cell | 100kN | 0.5 | 020034S | 0157/1907024 | 24 July 2019 |

With reference to clause 6 of BS EN ISO 7500-1 the proving equipment used has been calibrated to BS EN ISO 376 and the class of the proving device(s) was equal to or exceeded the class to which the machine has been verified.

The expiry date of the certificates of calibration for the elastic proving devices used is 26 months and for masses 5 years from the dates given above.

Where masses are used, the value for gravity (g) used to calculate the forces exerted by the masses was $9.815 m/s^2$

When using elastic proving devices the constant indicated force method was used to effect the verification. When masses are used the constant true force method was used to effect the verification. Three verification runs were made on each range

The Sercal Calibration Laboratory is accredited by UKAS to BS EN ISO 17025 (General requirements for the competence of testing and calibration laboratories ) to perform the calibration which is reported on this certificate.

Prior to verification the machine was inspected for good working order and was found to satisfy the guidelines given in section 5 of BS EN ISO 7500-1

The calculation of the accuracy and repeatability errors and the classification of the testing machines performance was made in accordance with the method specified in BS EN ISO 7500-1:2018

In the result tables which follow a negative relative error indicates that the machine indicator lags the true applied force.
Where there are adjacent results at the same force increment, these are at the overlap point from the two proving devices used.

The following results only relate to the machine described on page 1 of this certificate.

The decision rule of the classification does not take into account the uncertainty as described in section 7 of BS EN ISO 7500-1.

The reported expanded uncertainty is based on a standard uncertainty multiplied by a coverage factor k=2, providing a coverage probability of approximately 95%. The uncertainty evaluation has been carried out in accordance with UKAS requirements.
The uncertainty stated above refer to values obtained during calibration and make no allowances for factors such as long term drift, temperature and alignment effects, the influences of these factors should be taken into account by the user.

XIX

# CERTIFICATE OF CALIBRATION

**ISSUED BY:  SERCAL MATERIALS TESTING MACHINES SERVICES LIMITED**
**UKAS ACCREDITED CALIBRATION LABORATORY 0375**
**CERTIFICATE NUMBER:  55372**
**DATE OF ISSUE:    03 August 2020**

**Results:**

**100kN Instron Load Cell  Serial Number 30785**

| Range 1  100kN Tension | | | Range 2  100kN Compression | | |
|---|---|---|---|---|---|
| These results are: | As found - no adjustments were made | | These results are: | As found - no adjustments were made | |
| Nominal Force | Relative Error | Expanded Uncertainty | Nominal Force | Relative Error | Expanded Uncertainty |
| kN | % | % | kN | % | % |
| 2.0000 | 0.27 | 0.27 | 2.0000 | 0.03 | 0.27 |
| 4.0000 | 0.33 | 0.28 | 4.0000 | 0.04 | 0.27 |
| 7.0000 | 0.28 | 0.27 | 7.0000 | 0.17 | 0.27 |
| 10.000 | 0.24 | 0.27 | 10.000 | 0.15 | 0.27 |
| 20.000 | 0.29 | 0.27 | 20.000 | 0.15 | 0.27 |
| 40.000 | 0.30 | 0.27 | 40.000 | 0.17 | 0.27 |
| 60.000 | 0.34 | 0.27 | 60.000 | 0.21 | 0.27 |
| 80.00 | 0.41 | 0.27 | 80.00 | 0.18 | 0.27 |
| 100.00 | 0.43 | 0.27 | 100.00 | 0.13 | 0.27 |

**10kN Instron Load Cell  Serial Number 139957**

| Range 3  10kN Tension | | | Range 4  10kN Compression | | |
|---|---|---|---|---|---|
| These results are: | As found - no adjustments were made | | These results are: | As found - no adjustments were made | |
| Nominal Force | Relative Error | Expanded Uncertainty | Nominal Force | Relative Error | Expanded Uncertainty |
| kN | % | % | kN | % | % |
| 0.2000 | -0.06 | 0.27 | 0.2000 | -0.01 | 0.27 |
| 0.4000 | -0.11 | 0.27 | 0.4000 | -0.01 | 0.27 |
| 0.7000 | -0.09 | 0.27 | 0.7000 | -0.02 | 0.27 |
| 0.7000 | -0.08 | 0.27 | 0.7000 | 0.05 | 0.27 |
| 1.000 | -0.10 | 0.27 | 1.000 | 0.05 | 0.27 |
| 2.000 | -0.10 | 0.27 | 2.000 | 0.04 | 0.27 |
| 4.000 | -0.05 | 0.27 | 4.000 | 0.05 | 0.27 |
| 6.000 | -0.02 | 0.27 | 6.000 | 0.02 | 0.27 |
| 8.000 | -0.03 | 0.27 | 8.000 | 0.05 | 0.27 |
| 10.000 | 0.01 | 0.27 | 10.000 | 0.04 | 0.27 |

**500N Instron Load Cell  Serial Number 44102**

| Range 5  500N Tension | | | Range 6  500N Compression | | |
|---|---|---|---|---|---|
| These results are: | As found - no adjustments were made | | These results are: | As found - no adjustments were made | |
| Nominal Force | Relative Error | Expanded Uncertainty | Nominal Force | Relative Error | Expanded Uncertainty |
| N | % | % | N | % | % |
| 10.00 | 0.11 | 0.29 | 10.00 | 0.15 | 0.27 |
| 20.00 | 0.16 | 0.27 | 20.00 | 0.14 | 0.27 |
| 20.00 | 0.16 | 0.31 | 20.00 | 0.26 | 0.27 |
| 35.00 | 0.19 | 0.28 | 35.00 | 0.20 | 0.27 |
| 50.00 | 0.18 | 0.28 | 50.00 | 0.23 | 0.27 |
| 100.0 | 0.17 | 0.28 | 100.0 | 0.22 | 0.27 |
| 200.0 | 0.22 | 0.27 | 200.0 | 0.25 | 0.27 |
| 300.0 | 0.23 | 0.27 | 300.0 | 0.21 | 0.27 |
| 400.0 | 0.18 | 0.27 | 400.0 | 0.21 | 0.27 |
| 500.0 | 0.16 | 0.27 | 500.0 | 0.16 | 0.27 |

**End of Certificate**

In the result table(s) above a negative relative error indicates that the machine indicator lags the true applied force.

The reported expanded uncertainty is based on a standard uncertainty multiplied by a coverage factor k=2, providing a coverage probability of approximately 95%. The uncertainty evaluation has been carried out in accordance with UKAS requirements.

The uncertainty stated above refer to values obtained during calibration and make no allowances for factors such as long term drift, temperature and alignment effects, the influences of these factors should be taken into account by the user.

XX

# Appendix B: Extensometer calibration

0375

## SERCAL MTMS LTD.

Page 1 of 5 Pages

Sercal Materials Testing Machines Services Ltd.
Southern Avenue, Leominster,
Herefordshire, HR6 0QH.
Tel: +44 (0) 1527 514015 I Fax: +44 (0) 1527 514016
E-mail: enquiries@sercalcalibrations.co.uk

**Approved Signatories**
J. Swann
Dr N. Wrigley
Andrew Duggan

| | | | |
|---|---|---|---|
| **Issued To:** | Zwick Roell Ltd (For & On Behalf of University of Warwick) | | |
| **Addresss:** | MEC Materials Testing Laboratory, University Of Warwick Campus, CV4 7AL | | |
| **Host Machine:** | 100kN Instron Universal | **Serial Number:** | J6911 |
| **Extensometer Type:** | Axial Clip-on | **Serial Number:** | 125140 |
| **Extensometer Model:** | 2630-112 | **Conditioning:** | Instron Amplifier 5800J6911 |
| **Transducer Type:** | Strain Gauge Bridge | **Serial Number:** | 125140 (Strain Channel 1) |
| **Calibration Orientation:** | Vertical | **Software:** | Version 2.35.917 |
| **Display / Indicator Type:** | Computer Display | **Serial Number:** | CZC50312DN |
| **Date of Calibration:** | 29 July 2020 | **Location:** | Materials Testing Laboratory |
| **Sercal Quotation No:** | Q200208N-1 | | |
| **Previous Certificate No.** | N/a | | |

**Method:**
The constant true displacement method was used to perform the calibration. The extensometer has been calibrated in accordance with the requirements of **BS EN ISO 9513:2012** Two calibration runs were made in the vertical orinentation. Extensions were applied in 10% increments of range. Prior to the second run the extensometer was removed from and then re-mounted onto the calibration apparatus. In addition 4 readings were taken at full range making 6 in all, these readings were used to determine repeatability in order that the uncertainty of measurement could be estimated.

The extensometer complied with the requirements of the standard for the following classification(s):

| System Range | Result | Class | Direction | Calibrated Ranges | Gauge Length |
|---|---|---|---|---|---|
| 50 % Strain | As left | 0.5 | Increasing | 5 % Strain down to 0.5 % Strain | 50 mm |
| 50 % Strain | As left | 0.5 | Increasing | 50 % Strain down to 5 % Strain | 50 mm |
| 50 % Strain | As left | 0.5 | Decreasing | 0.5 % Strain down to 0.05 % Strain | 50 mm |
| 50 % Strain | As left | 0.5 | Decreasing | 5 % Strain down to 0.5 % Strain | 50 mm |

The extensometer complied with the requirements of the standard in respect of the relative error of the gauge length, bias error and resolution (refer to table 2 of the standard).

**Calibrated by: Lee Smith**

**Certified by:**

# CERTIFICATE OF CALIBRATION

**ISSUED BY: SERCAL MATERIALS TESTING MACHINES SERVICES LIMITED**
**UKAS ACCREDITED LABORATORY NUMBER 0375**
**CERTIFICATE NUMBER: 55375**
**DATE OF ISSUE:     03 August 2020**

The following equipment, calibrated to **BS EN ISO 9513** was used to perform the calibration:

| Description | Serial Number | Certificate No. | Calibrated |
|---|---|---|---|
| Direct Micrometer Rig | A5309 | 0478/2017110337-1 | 01 August 2018 |
| Gauge Length Calibrator: | EG04 | 2754950001 / 2754950002 | 02 July 2018 |

The class of the calibration apparatus was equal to or exceeds the class to which the extensometer has been calibrated.

**Range 1**    For Extensometer Range:    50% Strain
**Results:**    Measured Gauge Length:    50.16mm    The uncertainty of measurement is ±0.025mm
             The mean temperature was:  23.85°C during the calibration

**Direction:**    Increasing    **These results are As left following adjustment**

| Actual deflection % Strain | Run 1 Indicated deflection % Strain | Bias error % | Absolute error µm | Run 2 Indicated deflection % Strain | Bias error % | Absolute error µm |
|---|---|---|---|---|---|---|
| 0.5 | 0.5004 | 0.08 | 0.20 | 0.5004 | 0.08 | 0.20 |
| 1 | 1.002 | 0.20 | 1.00 | 1.002 | 0.20 | 1.00 |
| 1.5 | 1.504 | 0.27 | 2.00 | 1.502 | 0.13 | 1.00 |
| 2 | 2.004 | 0.20 | 2.00 | 2.003 | 0.15 | 1.50 |
| 2.5 | 2.507 | 0.28 | 3.50 | 2.506 | 0.24 | 3.00 |
| 3 | 3.007 | 0.23 | 3.50 | 3.006 | 0.20 | 3.00 |
| 3.5 | 3.508 | 0.23 | 4.00 | 3.506 | 0.17 | 3.00 |
| 4 | 4.008 | 0.20 | 4.00 | 4.007 | 0.17 | 3.50 |
| 4.5 | 4.509 | 0.20 | 4.50 | 4.508 | 0.18 | 4.00 |
| 5 | 5.010 | 0.20 | 5.00 | 5.008 | 0.16 | 4.00 |

The uncertainty of measurement is ±0.018% Strain

The reported expanded uncertainty is based on a standard uncertainty multiplied by a coverage factor k=2, providing a coverage probability of approximately 95%. The uncertainty evaluation has been carried out in accordance with UKAS requirements. Note: The uncertainty stated above refer to values obtained during calibration and make no allowances for factors such as long term drift, temperature and alignment effects, the influences of such factors should be taken into account by the user of the extensometer.

**CERTIFICATE OF CALIBRATION**

ISSUED BY: SERCAL MATERIALS TESTING MACHINES SERVICES LIMITED
UKAS ACCREDITED LABORATORY NUMBER 0375
CERTIFICATE NUMBER:  55375
DATE OF ISSUE:     03 August 2020

**Page 3 of 5 Pages**

**Range 2**    For Extensometer Range:    50% Strain
**Results:**    Measured Gauge Length:    50.16mm    The uncertainty of measurement is ±0.025mm
The mean temperature was:  23.88°C during the calibration

**Direction:**    Increasing    **These results are As left following adjustment**

| Actual deflection % Strain | Run 1 Indicated deflection % Strain | Bias error % | Absolute error µm | Run 2 Indicated deflection % Strain | Bias error % | Absolute error µm |
|---|---|---|---|---|---|---|
| 5 | 5.010 | 0.20 | 5.00 | 5.008 | 0.16 | 4.00 |
| 10 | 10.00 | 0.00 | 0.00 | 10.00 | -0.03 | -1.50 |
| 15 | 14.99 | -0.07 | -5.00 | 14.98 | -0.13 | -10.00 |
| 20 | 19.97 | -0.15 | -15.00 | 19.97 | -0.15 | -15.00 |
| 25 | 24.96 | -0.16 | -20.00 | 24.95 | -0.20 | -25.00 |
| 30 | 29.95 | -0.17 | -25.00 | 29.95 | -0.17 | -25.00 |
| 35 | 34.96 | -0.11 | -20.00 | 34.96 | -0.11 | -20.00 |
| 40 | 39.98 | -0.05 | -10.00 | 39.98 | -0.05 | -10.00 |
| 45 | 45.04 | 0.09 | 20.00 | 45.03 | 0.07 | 15.00 |
| 50 | 50.12 | 0.24 | 60.00 | 50.12 | 0.24 | 60.00 |

The uncertainty of measurement is ±0.14% Strain

The reported expanded uncertainty is based on a standard uncertainty multiplied by a coverage factor k=2, providing a coverage probability of approximately 95%. The uncertainty evaluation has been carried out in accordance with UKAS requirements.
Note:
The uncertainty stated above refer to values obtained during calibration and make no allowances for factors such as long term drift, temperature and alignment effects, the influences of such factors should be taken into account by the user of the extensometer.

XXIII

# CERTIFICATE OF CALIBRATION

**ISSUED BY: SERCAL MATERIALS TESTING MACHINES SERVICES LIMITED**
**UKAS ACCREDITED LABORATORY NUMBER 0375**
**CERTIFICATE NUMBER: 55375**
**DATE OF ISSUE:    03 August 2020**

**Page 4 of 5 Pages**

**Range 3**          For Extensometer Range:      50% Strain
**Results:**          Measured Gauge Length:       50.16mm    The uncertainty of measurement is ±0.025mm
                       The mean temperature was:   23.55°C during the calibration

**Direction:**    Decreasing          **These results are As left following adjustment**

| Actual deflection % Strain | Run 1 Indicated deflection % Strain | Bias error % | Absolute error μm | Run 2 Indicated deflection % Strain | Bias error % | Absolute error μm |
|---|---|---|---|---|---|---|
| 0.05 | 0.0503 | 0.60 | 0.15 | 0.0501 | 0.20 | 0.05 |
| 0.1 | 0.1005 | 0.50 | 0.25 | 0.1003 | 0.30 | 0.15 |
| 0.15 | 0.1506 | 0.40 | 0.30 | 0.1506 | 0.40 | 0.30 |
| 0.2 | 0.2014 | 0.70 | 0.70 | 0.2011 | 0.55 | 0.55 |
| 0.25 | 0.2514 | 0.56 | 0.70 | 0.2508 | 0.32 | 0.40 |
| 0.3 | 0.3015 | 0.50 | 0.75 | 0.3009 | 0.30 | 0.45 |
| 0.35 | 0.3520 | 0.57 | 1.00 | 0.3510 | 0.29 | 0.50 |
| 0.4 | 0.4030 | 0.75 | 1.50 | 0.4018 | 0.45 | 0.90 |
| 0.45 | 0.4530 | 0.67 | 1.50 | 0.4519 | 0.42 | 0.95 |
| 0.5 | 0.5028 | 0.56 | 1.40 | 0.5017 | 0.34 | 0.85 |

The uncertainty of measurement is ±0.0061% Strain

The reported expanded uncertainty is based on a standard uncertainty multiplied by a coverage factor k=2, providing a coverage probability of approximately 95%. The uncertainty evaluation has been carried out in accordance with UKAS requirements.

Note:
The uncertainty stated above refer to values obtained during calibration and make no allowances for factors such as long term drift, temperature and alignment effects, the influences of such factors should be taken into account by the user of the extensometer.

## CERTIFICATE OF CALIBRATION

ISSUED BY: SERCAL MATERIALS TESTING MACHINES SERVICES LIMITED
UKAS ACCREDITED LABORATORY NUMBER 0375
CERTIFICATE NUMBER: 55375
DATE OF ISSUE:     03 August 2020

**Page 5 of 5 Pages**

**Range 4**       For Extensometer Range:     50% Strain
**Results:**      Measured Gauge Length:     50.16mm    The uncertainty of measurement is ±0.025mm
                  The mean temperature was:  23.58°C during the calibration

**Direction:**    Decreasing       **These results are As left following adjustment**

| Actual deflection % Strain | Run 1 Indicated deflection % Strain | Bias error % | Absolute error μm | Run 2 Indicated deflection % Strain | Bias error % | Absolute error μm |
|---|---|---|---|---|---|---|
| 0.5 | 0.5028 | 0.56 | 1.40 | 0.5017 | 0.34 | 0.85 |
| 1 | 1.004 | 0.40 | 2.00 | 1.002 | 0.20 | 1.00 |
| 1.5 | 1.507 | 0.47 | 3.50 | 1.507 | 0.47 | 3.50 |
| 2 | 2.009 | 0.45 | 4.50 | 2.008 | 0.40 | 4.00 |
| 2.5 | 2.511 | 0.44 | 5.50 | 2.510 | 0.40 | 5.00 |
| 3 | 3.014 | 0.47 | 7.00 | 3.013 | 0.43 | 6.50 |
| 3.5 | 3.516 | 0.46 | 8.00 | 3.515 | 0.43 | 7.50 |
| 4 | 4.019 | 0.48 | 9.50 | 4.018 | 0.45 | 9.00 |
| 4.5 | 4.522 | 0.49 | 11.00 | 4.521 | 0.47 | 10.50 |
| 5 | 5.025 | 0.50 | 12.50 | 5.025 | 0.50 | 12.50 |

The uncertainty of measurement is ±0.018% Strain
End of Certificate

The reported expanded uncertainty is based on a standard uncertainty multiplied by a coverage factor k=2, providing a coverage probability of approximately 95%. The uncertainty evaluation has been carried out in accordance with UKAS requirements.

Note:
The uncertainty stated above refer to values obtained during calibration and make no allowances for factors such as long term drift, temperature and alignment effects, the influences of such factors should be taken into account by the user of the extensometer.

# Appendix C: Test setup compliance

A non-standard experiment was performed to quantify the compliance of the setup used in the three-point flexural tests. Figures C.1(a) and (b) show a hardened steel Instron test fixture with an approximate thickness of 60 mm. The fixture was placed in the test machine similar to the braided composite beams, as shown in Figure C.1(c), and a compressive load was applied.
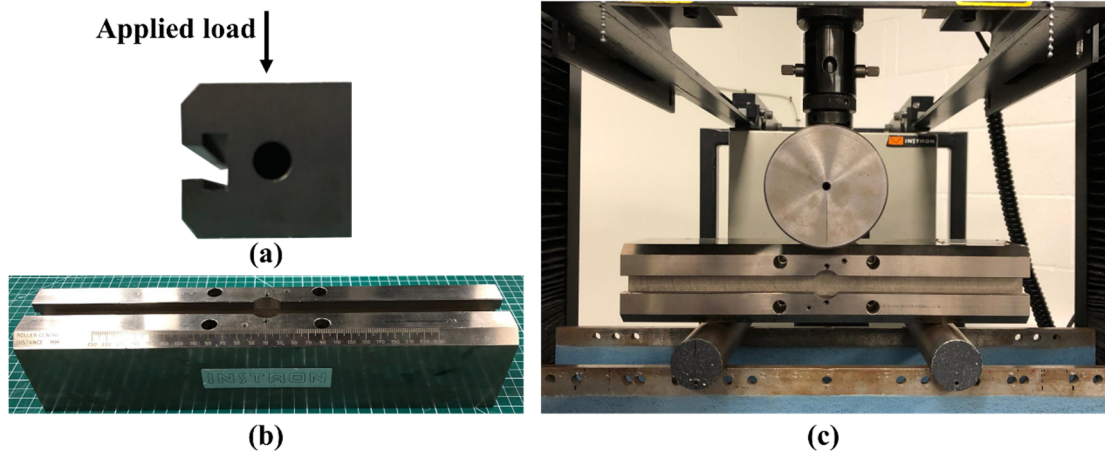


Figure C.1(a) Cross-section and (b) three-dimensional view of steel fixture; (c) Fixture in three-point flexure setup.

Given the rigidity of the steel fixture, it was assumed that the maximum load observed during the testing of the hollow braided beams, i.e. 800 N, would induce negligible deflection. Therefore, any recorded crosshead displacement will arise due to compliance of the test setup. The resulting load-displacement curve is shown in Figure C.2.
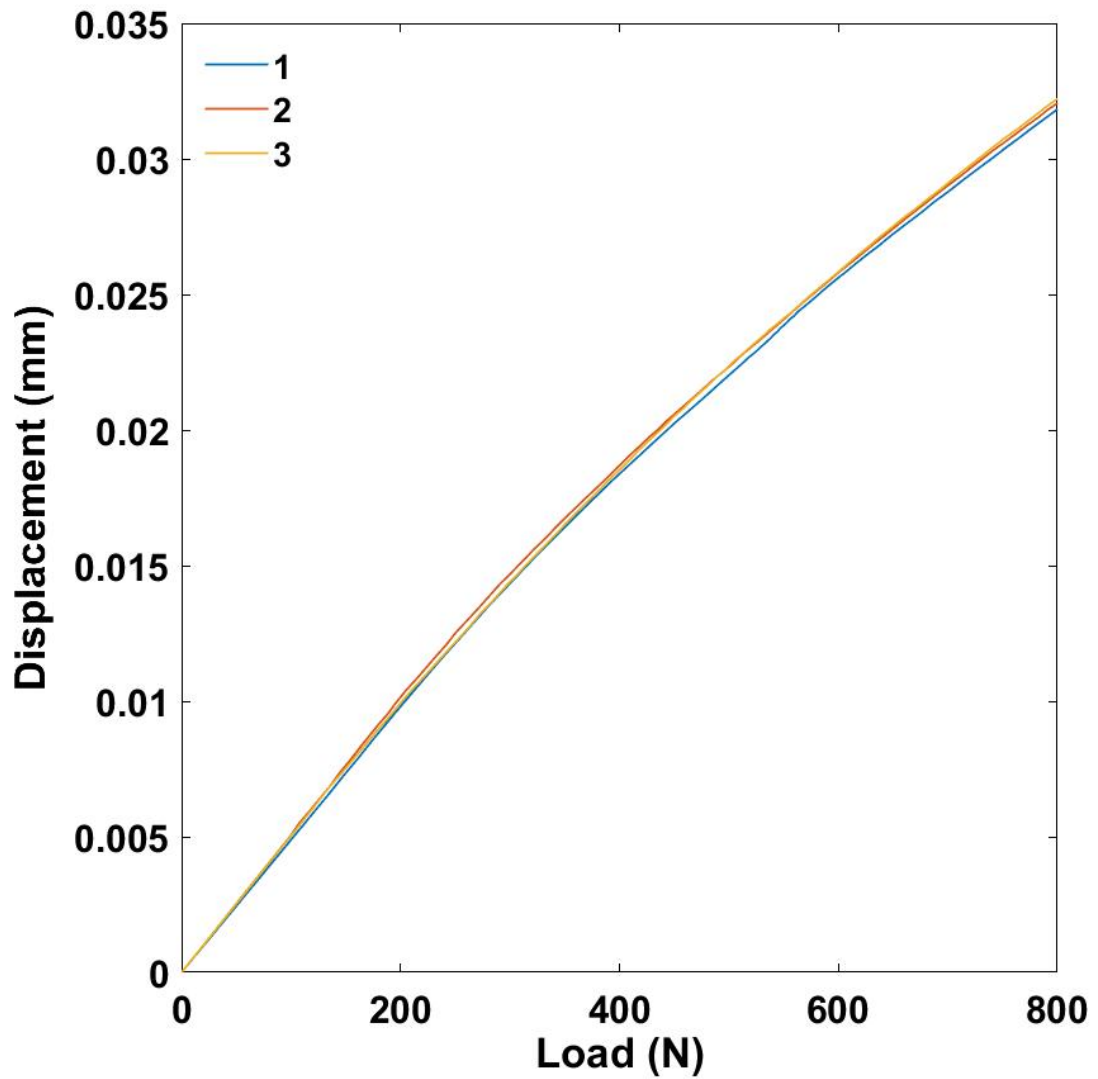
Figure C.2 Evolution of displacement with load representing test setup compliance.

Among the three repeats performed, the maximum displacement recorded at the point of maximum load, i.e. 800 N, was less than 0.035 mm. Therefore, the result indicates that the setup compliance is negligible and the use of crosshead displacement as a measure of beam deflection is valid.

# Appendix D: Load cell precision

The observed loads in the flexural testing of the braided composite beams did not exceed 800 N. However, the load measurements were performed using a 100 kN load cell. As the observed load range is less than 1% of the prescribed capacity of the 100 kN load cell, its precision in compression mode in this range was verified through a dedicated experiment. An Instron 1 kN load cell (Figure D.1(a)) was fixed into the test machine with the 100 kN load cell attached in the overhead slot, as shown in Figure D.1(b). A flexible rubber block was placed between flat rigid surfaces attached to the 1 kN load cell and the machine crosshead, as shown in Figure D.1(c).
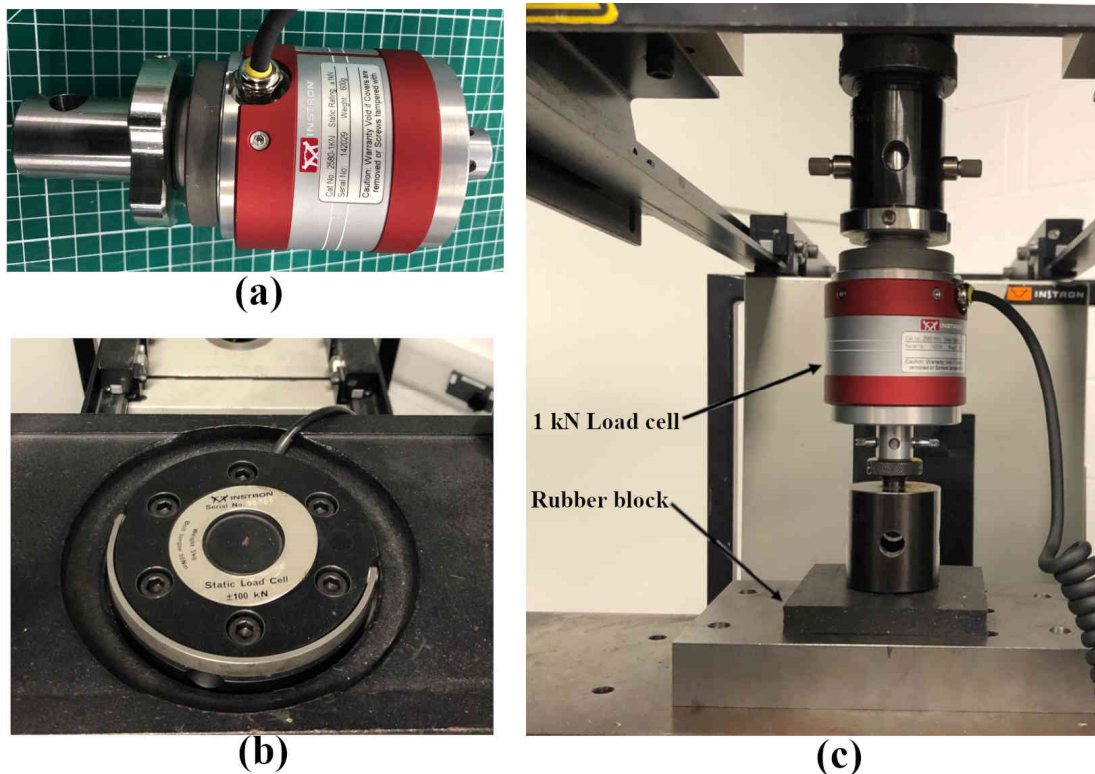


Figure D.1 (a) 1 kN load cell, (b) 100 kN load cell fixed in the overhead machine slot and (c) test setup used for evaluating load cell precision.

The rubber block was compressed at a constant crosshead speed of 10 mm/min and the load was recorded from both the load cells. Figure D.2 shows the error between the two load cells with respect to the measured load. The average error over the three repeats

was approximately 1%, while the average error in the load range corresponding to the beam stiffness calculation, i.e. 30-85N, was less than 2%.
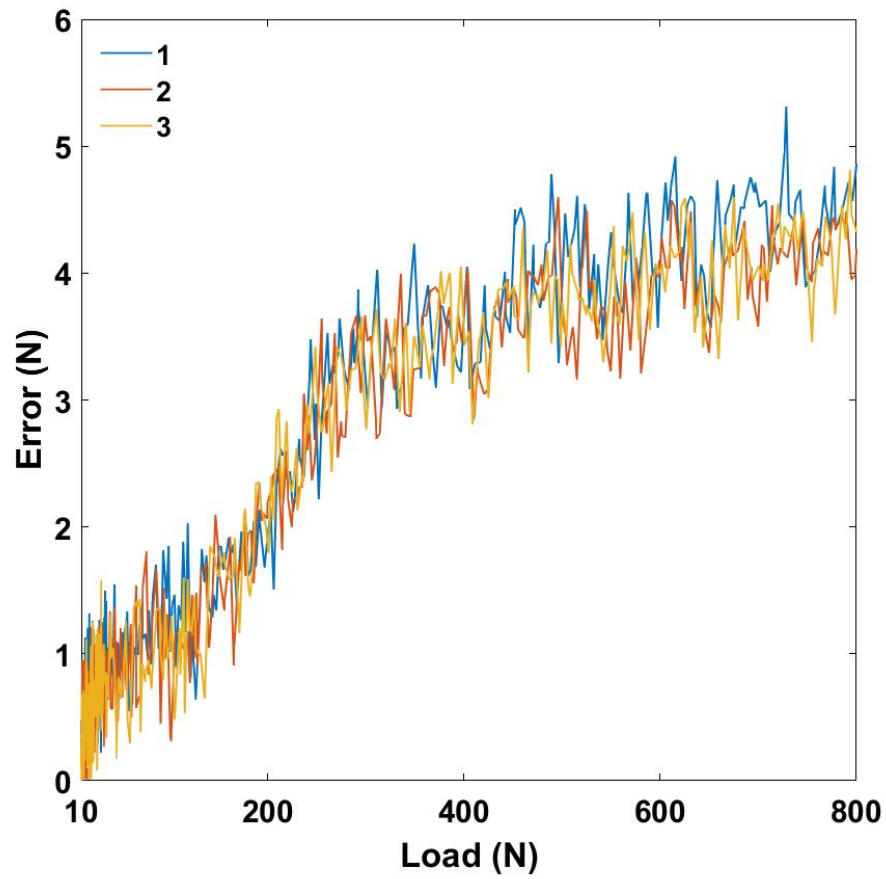


Figure D.2 Error in load cell measurement across the load range 10-800 N.

# Appendix E: Publication 1

## A novel route for volume manufacturing of hollow braided composite beam structures

Anubhav Singh[a],*, Neil Reynolds[a], Craig R Carnegie[a], Christopher Micallef[a], Elspeth M Keating[a], James Winnett[a], Alastair E Barnett[b], Steve K Barbour[b], Darren J Hughes[a]

[a] WMG, University of Warwick, Coventry CV4 7AL, United Kingdom

[b] Composite Braiding Limited, Derby DE24 9FU, United Kingdom

*Corresponding author, E-mail: A.Singh.10@warwick.ac.uk

## Abstract

This work investigates the application of a rapid variothermal moulding process for direct processing of a braided thermoplastic commingled yarn. The process uses locally controllable, responsive tooling which provides opportunities for optimum part quality and significantly reduced cycle times compared with conventional processes. The proposed process was used to directly manufacture hollow beam structures from dry commingled braided preforms. It was demonstrated that the cycle time using the rapid process was reduced by more than 90% as compared to a conventional bladder moulding process, resulting in a total cycle time of 14 minutes. Additionally, initial three point flexure test results indicated an improvement in the mechanical performance of the resultant parts as compared to the benchmark.

**Keywords:** Braiding; Bladder inflation moulding; Commingled Yarn; Thermoplastic; Variothermal tooling; Mechanical testing; High volume

## Introduction

Braiding is an effective method for manufacturing hollow tubular fibre-reinforced composite structures. The method interlaces continuous fibre bundles at a predefined angle resulting in the production of hollow tubular dry fibre preforms, which can then be impregnated with resin. Being an automated low-waste process, braiding finds numerous applications in large scale structural components in the automotive [1–3] and aerospace [4–7] industries as well as in small scale biomedical [8.9] and sports [10] applications. However, a majority of the current applications utilize thermoset matrices, which renders the curing of composites as the cycle-time limiting aspect. Consequently, in spite of the rapid preform production ability of the braiding process, current applications remain limited to the high-value low-volume range. This bottleneck could potentially be overcome by using hybrid fibre-thermoplastic matrix material systems. They are a blend of thermoplastic filaments with

reinforcement fibres, which could be directly processed, thus reducing the time and equipment (plant/tooling requirement) for resin injection. Moreover, their short impregnation paths [11] accelerate fibre wet out and consolidation. Hybrid systems are available in several forms such as commingled, core-spun, co-knit, co-wrapped etc. [12]. Among the available hybrid yarns, commingled thermoplastic yarns are more suitable for braiding because of their easy handleability [13,14] and relatively superior drapeability. Previous literature shows several instances of incorporation of commingled thermoplastic yarns in a braiding process [15–19].

Conventionally, bladder inflation moulding (BIM) has been found feasible for producing hollow composite components [20]. Being a simple and effective technique for consolidation of thermoplastic composites, BIM was also proposed for fabrication of hollow lightweight parts in sports [21,22] industries. The high volume potential of using BIM for processing braided commingled fabric was presented in the past [23,24]. However, there was a lack of manufacturing readiness because of the impractical routes used for pursuing high heating/cooling rates. This paper addresses the need for a high volume production route and presents a rapid variothermal process concept for the first time. The process allows rapid heat up and cool down, thus providing the potential of achieving shorter processing cycles. A conventional BIM process was used as a benchmark for comparison. Findings of this work can help industry in developing more confidence in braided thermoplastic composite manufacturing technologies specifically from the high volume-manufacturing viewpoint.

**Material**

The braided preforms used in this work were produced by braiding three layers of a commingled fabric using a 64-carrier O.M.A. maypole braider [25]. The braiding parameters were set to result in a braid angle of $25^0$ in the final parts. A commingled glass/polyamide 6 yarn from Coats [26] with fibre volume fraction of 55% was used. PA6 was chosen because of its favourable characteristics for high volume applications in the automotive industry [27]. The melting point and recrystallization temperatures of the PA6 used are approximately 221 $^0$C and 185 $^0$C respectively.

**Rapid variothermal moulding**

The proposed novel rapid variothermal moulding (RVM) setup is an integration of three key components:

(i) Elements of the conventional BIM process: The steps involved in a conventional BIM process are explained schematically in Figure 1(a).

(ii) Patented PtFS (Production to Functional Specification) [28] concept by Surface Generation Limited: The PtFS technology enables rapid heating and cooling of customized moulding tools. The reverse faces of the tools are machined into an array of thin-walled channels. Each channel has a dedicated heater below the tool face and a supply of compressed air. Controlling the heat and compressed air supply to each channel separately potentially allows for rapid heat up and cool down as well as precise local control over the temperature in each zone of the part being moulded. A software

XXXI

facilitates real-time monitoring and control of the process cycles across each channel. An existing compression moulding PtFS setup [29,30] at WMG with a total of 32 channels (16 on each tool half) was used with custom-made tool faces. A three dimensional schematic of the tool with the segregated channels is shown in Figure 1(b). As shown in the figure, the tool has two adjacent mould cavities out of which only one was used in this work. Figure 1(b) also shows the top view of the tool with marked thermocouple locations. The end channels of the tool are also highlighted in the figure. Monitoring the temperature of these end channels is critical as they would incur relatively greater heat loss to ambient atmosphere as compared to the other channels.

(iii) Hydraulic press: The application of a press enables rapid opening and closure of the tools, thus reducing the time between cycles. A 100 ton Dassett hydraulic press was used in this work. The customized tool faces were mounted with the PtFS setup on the press as shown in Figure 1(c).

Figure 2(a) shows a step-wise description of the RVM process. The tool was preheated to 150 $^0$C, following which a braided preform with a bladder was placed into the tool cavity and the press was closed. The temperature was increased to 250 $^0$C at a rate of 40 $^0$C/min and then held at 250 $^0$C for 6 minutes. After cooling down to 180 $^0$C, the part was demoulded. The temperature was further reduced to 150 $^0$C and the tooling was prepared for the next cycle. An internal bladder pressure of 0.4 MPa (4 bar) was applied. At the time of the press trials, this was the maximum available pressure due to limitations of the manufacturing environment. A set of preliminary trials were performed to improve the thermal response of the tool. The available electrical heating power was adjusted for each channel on the basis of the monitored temperature. Moreover, during the cooling phase, the channel with the slowest response was designated as the rate-governing channel for the entire tool, which resulted in a slow but uniform cooling rate of approximately 20 $^0$C/min. The implementation of these features resulted in a significant improvement in temperature-time profile, particularly in the consolidation phase, as depicted in Figures 2(b) and (c). The entire part cycle lasted for approximately 14 minutes.

A conventional BIM process in use at Composite Braiding Limited for industrial production of components served as benchmark. A two-part steel tool was designed and used for moulding of the braided fabric, which was heated using an industrial oven. After placing the closed mould into the oven, the temperature was increased to 240 $^0$C and the bladder was internally pressurized to 2 MPa (20 bar). The pressure and temperature were maintained for 10 minutes, following which the tool was cooled and the part was subsequently demoulded at a temperature of approximately 140 $^0$C. The entire process cycle including demoulding and tool separation took 4 hours, which is limiting for high volume production.

**Mechanical testing**

For comparing the beams manufactured using the BIM and RVM processes, a quasi-static three-point flexure test was used. The test was performed at a rate of 10 mm/min using an Instron 5800R test machine equipped with a 100 kN load cell. The test setup is shown in Figure 3(a) with the details of the test specimens. Three RVM beam specimens were tested, however, only one industrially produced

BIM beam specimen was available. The load-displacement curves are depicted in Figure 3(b). The average stiffness and peak load of three RVM beam specimens were higher by 12% and 17% as compared to the BIM specimen. It is speculated that internal thermal stresses (generated because of uncontrolled cooling across the part) and matrix degradation (a consequence of the part being above the melting point of PA6 for long duration) played a role behind the relatively poorer performance of the BIM specimen.

## Conclusions

A novel RVM process was developed providing a route for volume production of thermoplastic braided structures. A conventional bladder moulding technique was used as a benchmark. As compared to a cycle time of 4 hours in BIM, RVM parts took 14 minutes to manufacture. The ability to monitor and control the discrete channels of the tool individually resulted in a uniform temperature profile throughout the part. First mechanical test results indicated superior performance for RVM beams as compared to the single BIM specimen. The study suggests promising prospects for braided composites directly manufactured via the RVM process that provides greater control over manufacturing parameters along with 90% cycle time reduction. Further work aimed at establishing correlations between the manufacturing parameters and part quality is ongoing and will be subsequently reported.

## Funding source

## References

[1]     Schmitt B. The Making Of The Lexus LFA Supercar. An Inside Report, Chapter 2: In The Clean Room. Truth about Cars. http://www.thetruthaboutcars.com/2012/07/the-making-of-the-lexus-lfa-supercar-an-inside-report-chapter-2-in-the-clean-room/ (accessed March 23, 2018).
[2]     Gardiner G. BMW 7 Series CFRP: corrections and missing details. CompositesWorld. https://www.compositesworld.com/blog/post/bmw-7-series-cfrp-corrections-and-missing-details (accessed March 23, 2018).
[3]     Gardiner G. Sixth Element: Lamborghini accelerates CFRP. CompositesWorld. https://www.compositesworld.com/articles/sixth-element-lamborghini-accelerates-cfrp (accessed March 23, 2018).
[4]     A&P Technology. GEnxTM Engine. http://www.braider.com/Case-Studies/GEnx-Engine.aspx (accessed March 23, 2018).
[5]     A&P Technology. Honeywell Jet Engine Stator Vane. http://www.braider.com/Case-Studies/Jet-Engine-Stator-Vane.aspx (accessed March 23, 2018).
[6]     A&P Technology. Bombardier Wing Flap. http://www.braider.com/Case-Studies/Bombardier-Wing-Flap.aspx (accessed June 20, 2019).
[7]     Gardiner G. Airbus A350 Update: BRaF & FPP. CompositesWorld. https://www.compositesworld.com/articles/airbus-a350-update-braf-fpp (accessed June 20, 2019).
[8]     Carey J, Fahim A, Munro M. Design of braided composite cardiovascular catheters based on required axial, flexural, and torsional rigidities. J Biomed Mater Res Part B Appl Biomater An Off J Soc Biomater Japanese Soc Biomater Aust Soc Biomater Korean Soc Biomater 2004;70:73–81.
[9]     TE Connectivity. Braided & Coiled Catheter Shafts. http://www.te.com/usa-en/industries/medical-healthcare/our-focus/interventional/braided-coiled-catheter-shafts.html (accessed March 23, 2018).
[10]     Harrison. The Best Way to Make Graphite Shafts. http://www.harrison.com/articledetail/making-golf-shafts (accessed March 23, 2018).
[11]     Svensson N, Shishoo R, Gilchrist M. Manufacturing of thermoplastic composites from

commingled yarns-A review. J Thermoplast Compos Mater 1998;11:22–56.

[12]     Schneeberger C, Wong JCH, Ermanni P. Hybrid bicomponent fibres for thermoplastic composite preforms. Compos Part A Appl Sci Manuf 2017;103:69–73.

[13]     Ramasamy A, Wang Y, Muzzy J. Braided thermoplastic composites from powder-coated towpregs. Part I: Towpreg characterization. Polym Compos 1996;17:497–504.

[14]     Ramasamy A, Wang Y, Muzzy J. Braided thermoplastic composites from powder-coated towpregs. Part II: Braiding characteristics of towpregs. Polym Compos 1996;17:505–14.

[15]     Bechtold G, Kameo K, Langler F, Hamada H, Friedrich K. Pultrusion of Braided Thermoplastic Commingled Yarn-Simulation of the Impregnation Process. 5th Int. Conf. Flow Process Compos. Mater. UK, 1999, p. 257–64.

[16]     Laberge-Lebel L, Van Hoa S. Manufacturing of braided thermoplastic composites with carbon/nylon commingled fibers. J Compos Mater 2007;41:1101–21.

[17]     Lebel LL, Nakai A. Design and manufacturing of an L-shaped thermoplastic composite beam by braid-trusion. Compos Part A Appl Sci Manuf 2012;43:1717–29.

[18]     Risicato J-V, Kelly F, Soulat D, Legrand X, Trümper W, Cochrane C, et al. A complex shaped reinforced thermoplastic composite part made of commingled yarns with integrated sensor. Appl Compos Mater 2015;22:81–98.

[19]     Jacquot P-B, Wang P, Soulat D, Legrand X. Analysis of the preforming behaviour of the braided and woven flax/polyamide fabrics. J Ind Text 2016;46:698–718.

[20]     Anderson J. Manufacturing and Microstructural Modeling of Geometrically Complex Composite Components Produced by Bladder Assisted Composite Manufacturing (BACM). PhD Thesis, University of Oklahoma, 2013.

[21]     Davis SJ. Long fiber reinforced thermoplastic frame especially for a tennis racquet. U.S. Patent 1993;5,176,868.

[22]     Olson SH, Busby JS, Needle SA. Composite bicycle frame and method of manufacturing. U.S. Patent 1998;5,803,476.

[23]     Bernet N, Bourban P-E, Månson J-AE. Cost-effective manufacturing of hollow composite structures by bladder inflation moulding. 12th Int. Conf. Compos. Mater. Paris, 1999.

[24]     Bernet N, Michaud V, Bourban P-E, Månson J-A. Commingled yarn composites for rapid processing of complex shapes. Compos Part A Appl Sci Manuf 2001;32:1613–26.

[25]     O.M.A. High Tech Systems. Horizontal Braiders. http://www.omabraid.it/en/trecciatrici-orizzontali.php (accessed June 20, 2019).

[26]     Coats. Coats Synergex. https://www.coats.com/en/Guidance/Coats-Synergex#Commingling (accessed June 20, 2019).

[27]     Reynolds N, Ramamohan AB. High-volume thermoplastic composite technology for automotive structures. Adv Compos Mater Automot Appl Chichester Wiley 2014:29–50.

[28]     Surface Generation Limited. About Surface Generation and our unique PtFS technology. https://www.surface-generation.com/about-us/ (accessed May 9, 2019).

[29]     Reynolds N, Ngah SA, Williams G, Hughes DJ. Direct processing of structural thermoplastic composites using rapid isothermal stamp forming. In progress.

[30]     Froemder C, Kirwan K, Reynolds N, Wilson PR, Fernandes FC, Coles SR. Investigation of the processability of hybrid thermoplastic nonwoven including recycled carbon fibre through fast stamping. SAMPE Eur. Conf. Southampton, 2018.

[31]     Micallef C. Lightweighting of double-decker buses. EngD Thesis, University of Warwick, 2018.
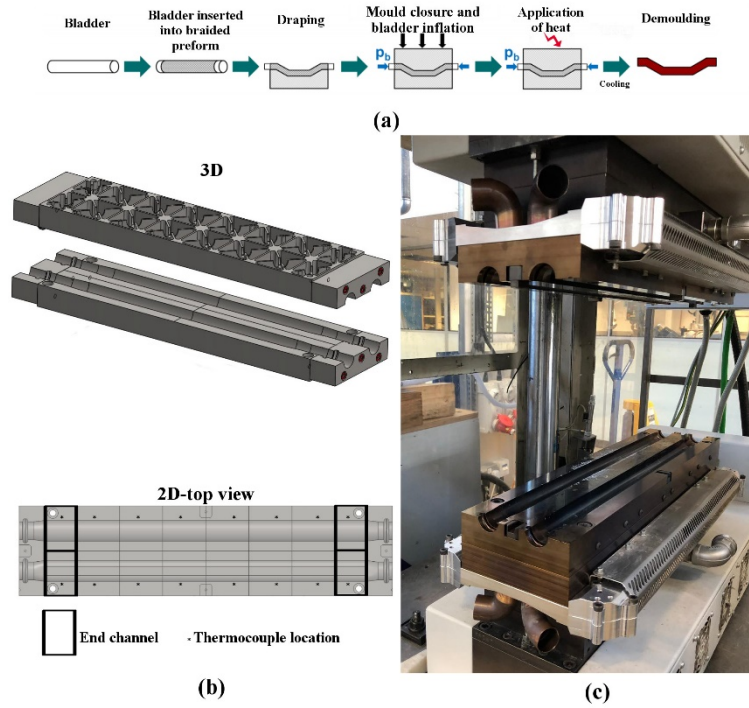
Figure 1. (a) Step-wise illustration of BIM process (Adapted from [31]); (b) Schematic of the RVM tool faces showing segregated channels & (c) Customized tool face with the PtFS setup mounted onto the press
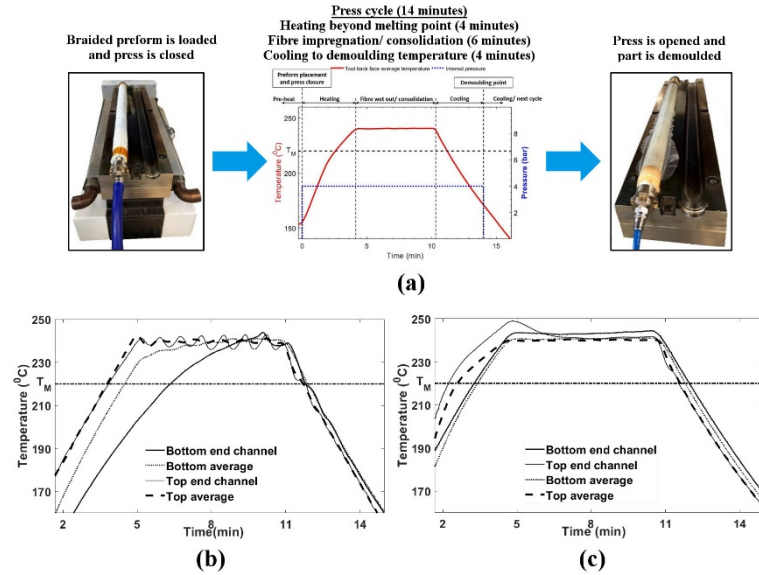


Figure 2. (a) Steps involved in RVM process with pressure and temperature profile during press cycle; Average and end-channel temperature profiles of the top and bottom tool halves (b) before and (c) after employing PtFS control features. Note: the material temperature was approximately 10 $^0$C above the plotted tool back face temperature

XXXV

| | Test span | Thickness | Outer Diameter | Mass |
|---|---|---|---|---|
| | (mm) | (mm) | (mm) | (g) |
| RVM1 | 400 | 1.99 ± 0.19 | 34.85 ± 0.21 | 183.8 |
| RVM2 | 400 | 1.71 ± 0.35 | 34.81 ± 0.17 | 173.1 |
| RVM3 | 400 | 1.97 ± 0.04 | 34.81 ± 0.07 | 178.6 |
| BIM | 400 | 1.92 ± 0.06 | 35.02 ± 0.18 | 170.5 |

**(a)**                                                          **(b)**
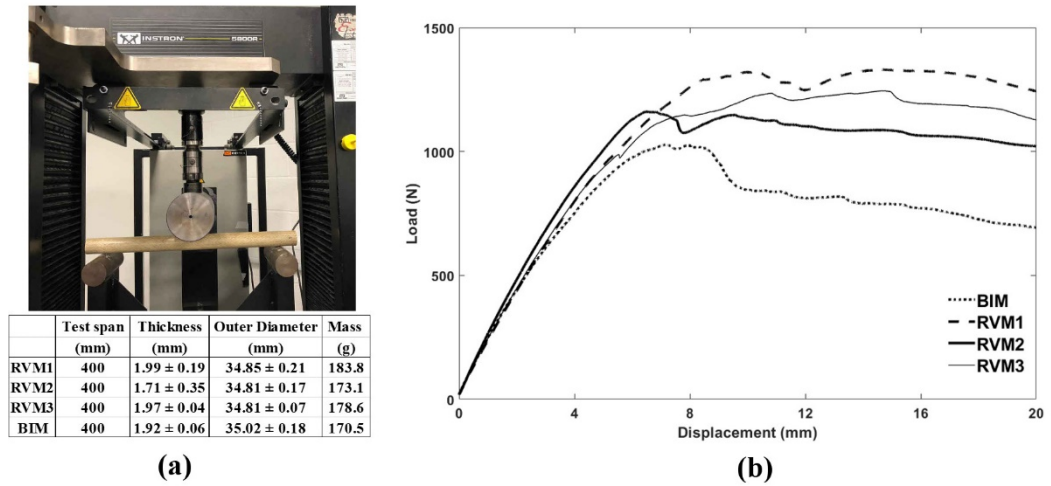
Figure 3. (a) Three-point flexure testing setup with specifications of test specimens; (b) Load-displacement response of the BIM and RVM beams

# Appendix F: Publication 2

## The effect of braid angle on the flexural performance of structural braided thermoplastic composite beams

Anubhav Singh[a],*, Neil Reynolds[a], Elspeth M Keating[a], Alastair E Barnett[b], Steve K Barbour[b], Darren J Hughes[a]

[a] WMG, University of Warwick, Coventry CV4 7AL, United Kingdom
[b] Composite Braiding Limited, Derby DE24 9FU, United Kingdom

*Corresponding author, E-mail: A.Singh.10@warwick.ac.uk

### Abstract

Thermoplastic braided composite tubular beams were manufactured using commingled hybrid yarn with braid angles 30°, 45° and 60° and tested in static three-point flexure. Two principal deformation modes were observed during the flexural loading: global flexure and localised crush. The extent of each mode occurring in the three braid angle variants was measured using a linear deflectometer as well as 3D digital image correlation. Localised crushing was found to decrease significantly with increasing braided angle, accounting for 63%, 45% and 19% of the total applied deflection for the 30°, 45° and 60° beams respectively. Further, surface strain measurements obtained from 3D DIC showed increasing the braid angle led to a global flexure-dominated deformation. In addition, the stiffness and peak load increased with increasing braid angle. The observed differences in deformation modes were due to a combination of multiple braid angle-dependent properties of braided composites such as modulus, thickness etc.

**Keywords**: Braiding; Thermoplastic; Flexure; Localised crush; Digital image correlation

### Introduction

The past three decades have seen braiding rise as a strong candidate among fibre reinforced polymer composite (henceforth referred to as composite) manufacturing techniques. Braiding involves the production of hollow tubular preforms by interlacing reinforcing fibres at an angle with respect to the axis of the preform. This is achieved by using a braiding machine, which enables bobbins loaded with the fibres to be moved in serpentine circular paths while pulling the free end of the fibres at a controlled velocity. During the braiding process, the shape and orientation of the braiding mandrel can be controlled, thus producing near-net shape preforms and minimising the wastes incurred due to trimming operations [1]. From a performance perspective, braided composite structures are known for their greater impact resistance compared to laminated composites with unidirectional fibres in each layer [2,3]. Owing to these advantages, braided composites find a wide range of applications in the automotive and aerospace industry [4].

The angle at which the fibres are interlaced with respect to the local axis of a braid is termed as braid angle. It is related with the braiding machine parameters as per Equation 1.

$$\alpha = \tan^{-1}\left(\frac{\omega_h D}{N_h v}\right) \tag{1}$$

where $\alpha$: braid angle, $\omega_h$: horn gear angular velocity (rpm), D: mandrel diameter (mm), $N_h$: number of horn gears and v: mandrel pull-off velocity (m/s).

Previous work has shown that the braid angle is directly related to the properties of the produced composite. For example, braiding at a higher braid angle leads to an increase in the thickness of the braided tows, therefore increasing the thickness of the braided component [5]. The mechanical properties of braided composites including elastic properties as well as mechanical strength have been shown to depend on braid angle [6–8]. Moreover, the braid angle has been reported to influence the deformation modes in braided composites. Under uniaxial tension, tubular braided specimens with small braid angles (<30°) were observed to show a linear elastic response until failure by Harte et al. [6], while specimens with large braid angles (>50°) showed a non-linear response accompanied with progressive necking, which delayed the ultimate failure. Similarly, Priem et al. [9] reported the failure mode of braided tubes under uniaxial compression to diverge from a splayed failure to a more stable progressive failure with an increase in braid angle.

The flexural response of braided composites has also been shown to depend on braid angle. For instance, Sturm et al. [10] conducted four-point bending tests of 38 mm wide and 400 mm long open section braided beams to assess their energy absorption characteristics for potential fuselage frame applications. It was observed that increasing the braid angle reduced the proclivity to flange buckling, hence improving energy absorption. As demonstrated by Sturm et al. [10], flexure tests performed using component scale specimens with complex geometries provide a direct assessment of structural performance. Unlike coupon level tests aimed at analysis and comparison of material properties, the response is a combination of specimens' material characteristics as well as geometry. Among the conventional flexural tests, three-point flexure is considered to be more relevant for structural applications as it is comparable to real-life load cases such as side impact on an automotive structure [11]. Therefore, three-point flexure has been used in several studies to evaluate the performance of side impact beams [12–14]. Moreover, three-point flexure allows for a combined assessment of resistance to localised crushing failure as well as global flexural deformation [11]. The localised crush in the impacted region manifests in different forms depending on the material and geometry of the specimens [15–20].

As mechanical behaviour of material as well as geometry are both directly related with braid angle, it is intuitive to expect braid angle to show a significant effect on localised crushing however, such a correlation has not been reported in the past. Previously reported studies on three-point flexure test response of braided rectangular coupons showed a decrease in flexural modulus and strength with increasing braid angle [21–23]. Moreover, increasing the braid angle was observed to delay the failure.

Potluri et al. [24] conducted three-point flexure tests of tubular braided composites and reported similar trends of flexural modulus and strength as the results corresponding to rectangular coupons. These coupon-level studies showed a strong correlation between the flexural performance and braid angle. However, due to the coupons' geometry and scale, no localised deformations were reported. In contrast, the investigation conducted by Wu et al. [25] showed severe localised crushing during three-point flexure tests. However, the size of the loading roller and span to diameter ratio of the tested specimens were both inclined to induce localised crush over global flexure irrespective of braid angle. Moreover, the fibre volume fractions of the specimens were below 30%, which is not typical of structural composites. Thus, current literature lacks studies on three-point flexural response of braided structural composites, in particular investigating potential correlations between braid angle and multiple deformation modes, which dictate structural performance. Furthermore, existing literature focuses mainly on thermoset matrices, with no studies on thermoplastic matrix tubular braided materials.

This paper addresses this need through a systematic experimental study on component scale tubular braided beams. The results improve the current understanding of braided composite properties and their implications from a structural viewpoint. The presented work reports the flexural properties of tubular braided composite structures with a thermoplastic matrix for the first time.

### Experimental methodology

### Materials and manufacturing

A commingled E-glass/polyamide 6 (PA6) yarn from Coats [26] was used for braiding. The material characteristics of the commingled tows are listed in Table 1.

A 64-carrier braiding machine at Composite Braiding Limited was used to braid the commingled tows. Figure 1(a) shows the braiding process. The machine was used at half-capacity, i.e. 32 carriers, to produce a 1×1 diamond braid. Three braid angles were considered: 30°, 45° and 60°. For each braid angle, three layers of the commingled fabric were braided over 25 mm diameter mandrels to produce multi-layer braided preforms. Figure 1(b) shows flattened pieces cut from the braided preforms with different braid angles.

A bladder moulding process previously developed by the authors, called rapid variothermal moulding (RVM) [27], was used to produce tubular beams from braided commingled preforms. Figure 2(a) shows the steel tool used to mould the braided beams. The tool has a 530 mm long circular cavity with a diameter of 35 mm. The braided preforms were cut to the required length and then carefully removed from the mandrel. Prior to the moulding process, the braided preforms were dried in an industrial dryer at 70 °C for 24 hours to remove absorbed moisture from the fabric. A 1% drop in preform weight was observed after the drying process. A silicone rubber bladder was inserted through the preform and metallic end fittings were fit at both ends as shown in Figure 2(b).

During the RVM process, the tool was preheated to 150 °C and the preform-bladder assembly was placed into the mould cavity (tool). After closing the press, an internal bladder pressure of 4 bar was applied as the tool was heated to a consolidation temperature of 240 °C. This ensured that the braided fabric was in contact with the tool surface. On reaching the consolidation temperature, the pressure was increased to 20 bar. The temperature and pressure were maintained for 15 minutes, following which the tool was cooled to the demoulding temperature. The consolidation pressure and temperature were limited to 20 bar and 240 °C respectively because of the high temperature durability of the silicone rubber bladders. In order to minimise thermal distortion, the demoulding was carried out at a temperature of 50 °C, which is below the glass transition temperature of PA6. The bladder pressure of 20 bar was maintained during the cool-down phase. Figure 3 shows the temporal characteristics of the temperature and bladder pressure during RVM.

The outer and inner surfaces of the consolidated 30°, 45° and 60° braided beams produced using the RVM process are shown in Figures 4 (a), (b) and (c). The beams had smooth outer surfaces (due to contact with the tool), while the inner surfaces had the undulating texture of the braided fabric (due to contact with the flexible silicone rubber bladder). Similar to the flattened braids shown in Figure 1(b), an increase in the surface area covered by the fibres was observed with increasing braid angle. This was in agreement with previous studies [4]. Brownish discolouration was observed on the surfaces of the beams. On the outer surface, the degree of discolouration appeared to decrease with increasing braid angle, however, all the beams showed similar levels of discolouration on the inner surfaces. Previous literature has linked this discolouration with thermo-oxidative chemical reactions of the PA6 [28,29]. A test was conducted where 5 cm long commingled tows extracted from the braided fabric were heated in ambient atmosphere and argon separately. The fabric retrieved after the thermal experiments are shown in Figures 4 (d) and (e). The fabric heated in the presence of argon displayed no discolouration, which confirmed that the interaction of ambient air with the PA6 at high temperature was responsible for the discolouration. Patches of dry fibres and intermittent fibre waviness were also observed on the outer surfaces of the consolidated beams.

A total of seven beams were manufactured for the braid angles of 30°, 45° and 60° and cut to a length of 420 mm. For six of the braided beams of each type, the braid angle was measured at 20 random locations on the outer surface and averaged. The measured braid angle values are shown for all the beams in Figure 5.

**Part quality evaluation**
In order to enable a comparison of the quality of consolidation in the braided beams, destructive (sectioning) evaluation was performed on one beam of each braid angle. The microstructure was analysed using optical microscopy to compare the defects between different beams. Moreover, the fractional composition of the beams was determined using resin burn-off tests.

The cross-section perpendicular to the beams' axes was selected for microstructural analysis. Approximately 10 mm-long cylindrical specimens were extracted by slicing the beams at two different

locations using an abrasive wheel cutter. After slicing, the specimens were cold mounted in epoxy resin.  The samples were polished using a Buehler EcoMet™ 300 automatic grinder-polisher to a 3 µm finish. Following the polishing operation, the samples were imaged using an automated stage ZEISS Axio Imager 2 microscope fitted with a 5 megapixel Axiocam 305 digital camera. A magnification of 5x was used. ZEISS ZEN 2 Core imaging software was used to perform stitching and generate images covering a wide area of the sample cross-section. Thickness variations within the braided beams were also measured from the polished samples using a macro zoom camera. The thickness was measured at a minimum of 350 locations taken from the two polished samples prepared for each braid angle. This was essential for capturing the non-uniform thickness distribution in the beams resulting from the undulating inner surfaces.

The resin burn-off experiments were conducted using the method introduced by Gupta et al. [30]. Six 20 mm long semi-circular specimens were cut from the braided beams, each weighing >500 mg. The density of each specimen was determined using the Archimedes principle as per BS EN ISO 1183-1 [31]. The thermal degradation of the resin was performed by heating the specimens to 500 °C using an 1800 Watt Milestone ETHOS UP High Performance Microwave heating system with ceramic furnace accessory. The fibre volume fractions ($F_{vf}$) and void volume fractions ($V_{vf}$) were subsequently determined as per BS EN ISO 14127 [32].

**Quasi-static three-point flexure tests**

An Instron 5800R test machine equipped with a 100 kN load cell was used to perform quasi-static three-point flexure experiments. The test setup is shown in Figure 6(a). Test control and data collection were performed using the Instron material testing software Bluehill version 2. During the test, the beams were supported over a test span of 350 mm on rollers having a diameter of 40 mm. A central loading roller of 100 mm diameter was used. The effect of through-thickness beam shear during the flexural deformation was analytically determined using the approach presented by Tolf et al. [33]. The induced deviation from pure flexure is less than 10% for the span-to-depth ratio corresponding to the beams and test geometry used in this study.

In order to measure the flexural displacement at the bottom surface of the beams, an Instron 2630-112 extensometer was used in deflectometer mode. The extensometer was attached to a spring-loaded plunger, thus making a linear deflectometer, as shown in Figure 6(b). The deflectometer assembly was rigidly fixed onto the test bed such that the tip of the plunger maintained contact with the lower surface of the beam throughout the flexural deformation. The difference between the measured bottom surface displacement and the applied crosshead displacement was used to evaluate the localised crushing propagating from the top surface. Six repeats of each braid angle were tested in three-point flexure, out of which the bottom surface displacement was recorded for 3 repeats.

Before each test, the beam was preloaded to 10 N to ensure full engagement of the upper loading roller with each beam before starting the test. The test was carried out at a constant crosshead displacement rate of 10 mm/min, which corresponds to a flexural strain rate of less than 2 %/min. The test data (load,

crosshead position and deflection) was recorded at a rate of 10 Hz. Dedicated experiments were performed to evaluate the compliance of the test setup and the precision of the load cell in the load range observed during the flexural testing of the braided beams. Results of these experiments indicated that a maximum displacement of 0.03 mm was induced due to the setup compliance at maximum load, while the maximum error in the load cell measurements was less than 2%.

**Digital image correlation**

In order to measure and compare the surface strains during three-point flexure, a three-dimensional digital image correlation (DIC) system was used during the flexure test for one repeat of each braid angle. As demonstrated in literature [34,35], DIC is useful for recording the multiaxial strains as well as out-of-plane deformations induced during flexural testing.

The DIC measurements in this work were performed on images obtained using a matched pair of GOM 12M digital cameras. The lenses attached to the cameras had a focal length of 100 mm. Commercially available DIC software GOM ARAMIS [36] version 6.1 was used to acquire and analyse the DIC images. As the majority of deformation was observed to occur in the contact region directly under the loading roller, the central segment of the beams was selected as the Region of Interest (RoI). It should be noted that the surface strain measurements were made on the region of the beam surface visible to the cameras. The area undergoing the damage was beneath the central loading roller and therefore could not be captured within the view of the cameras. After mounting the measurement system, both the cameras were focused on a plane tangential to the circular surface of the braided beam closest to the cameras. Twin-LED lights were used to illuminate the RoI during the experiments. A schematic of the three-point flexure setup with the DIC measurement system is shown in Figure 7. The DIC system and software parameters are listed in Table 2.

In order to ensure consistency, DIC calibration and the flexure experiments were performed under precisely the same conditions. Prior to performing three-dimensional calibration of the optical apparatus, the cameras were turned on and allowed to warm up and equilibrate with the entire system for 30 minutes. The obtained calibration deviation was within the GOM ARAMIS recommended threshold of 0.04 pixels, indicating a successful calibration. The RoI of every beam was prepared for the optical strain measurement by applying a stochastic white speckle pattern on a matt black background. Firstly, the beam surfaces were coated with a black coloured base using a Plastikote Black Primer. The black base was allowed to dry fully, following which the white speckle pattern was sprayed onto the RoI using a Badger air brush using generic white emulsion paint diluted to approximately 50% by volume.

The post-processing of the DIC data was conducted using GOM Correlate Professional software [37]. For every beam, the software creates a surface component using the recognised facets. In order to ensure that the measured displacements are aligned correctly with respect to the tested beam, a modified alignment was created using an imported CAD geometry. For every beam, six static images were captured after preloading the beam. These images were analysed to estimate the measurement

accuracy as well as evaluate the fitness of the pattern and the calibration for successful acquisition of DIC data. Figure 8 shows the strain distribution in a static image in the preload condition. The 'false' strain values shown in the figure arise due to sensor noise. The 'false' strain is randomly distributed across the entire image without any localised anomalies, as shown in the figure, indicating that the measurement system is correctly set up. Assuming that the strain measurements in static images are normally distributed, the mean of these falsely determined strains and displacements represent the bias of the measurement, while the standard deviations represent the resolution of the measuring system [38]. These statistical metrics for DIC data are listed in Table 3.

## Results and discussion

### Evaluation of part quality

The $F_{vf}$ and $V_{vf}$ values of the braided beams determined from resin burn-off experiments are listed in Table 4. Single-factor analysis of variance (ANOVA) was performed to statistically compare the $F_{vf}$ and $V_{vf}$ obtained for the three braid angles. A 95% confidence level was used. The corresponding p-values for both the $F_{vf}$ and $V_{vf}$ comparisons are listed in Table 5. The p-value corresponding to $F_{vf}$ is greater than 0.05. Therefore, the ANOVA results indicate that the $F_{vf}$ values did not differ significantly between the braided beams with different braid angles. The lack of correlation between $F_{vf}$ and braid angle was due to the predetermined composition of the commingled preforms used to manufacture the braided beams. Similar observation was reported by Laberge-Lebel [23] for rectangular braided coupons manufactured using a commingled carbon fibre-PA12 system. However, the p-value for $V_{vf}$ is less than 0.05, which indicates that the void content was significantly different between the three beams. In order to analyse the difference in the $V_{vf}$ values, a post hoc analysis was performed using the Tukey-Kramer method [39]. As per the method, the Studentised range statistic q was evaluated for each pair using Equation 2.

$$q_{AB} = \frac{|\mu_A - \mu_B|}{\sqrt{\frac{MS_W}{2}\left(\frac{1}{n_A}+\frac{1}{n_B}\right)}} \tag{2}$$

where $q_{AB}$: q-statistic for the pair A-B; $\mu_A$: mean for sample A; $\mu_B$: mean for sample B; $n_A$: sample size of A; $n_B$: sample size of B and $MS_W$: mean square error within samples.

If the evaluated q value is greater than the critical value of q, determined from the q-table, it implies that the difference between the means corresponding to the respective pair of samples is statistically significant. The obtained q-values corresponding to every comparison are listed in Table 6.

The results indicate that the $V_{vf}$ of the 30° and 45° beams are similar, while the voidage is greater for the 60° beams. As higher void content typically results in reduced mechanical properties of composite structures [40], the three-point flexural response of the 60° beams would be expected to be more severely affected as compared to the 30° and 45° beams.

The measured thickness values were distributed in increasing bands of 0.05 mm between the maximum and minimum values for each braid angle. The resulting distributions are shown in Figure 9 in the form of frequency line plots. The mean, maximum and minimum thickness for each braid angle are listed in

XLIII

Table 7. The histograms show that the thickness increases with braid angle. The mean thickness increased by 18% from the 30° to 45° beam, while the increase from 45° to 60° was 42%.

Braided tow width was measured on the outer surface of the untested braided beam for each braid angle at 25 randomly located points. The measured tow width was used to determine analytically the cover factor, i.e. surface area of the braided composite covered by the braided fibres, as per Equation 3. Further details of the analytical calculations can be found in references [41,42].

$$\text{Cover factor} = 1 - \left(1 - \frac{wN_c}{2\pi D \cos\alpha}\right)^2 \tag{3}$$

where w: tow width (mm) and $N_c$: number of carriers used in braiding.

Table 8 shows the measured tow width and the analytically estimated cover factor for beams with different braid angles. The width of the tows decreased with increasing braid angle, while the cover factor increased, which is in agreement with previously reported results.

Figure 10 shows selected micrographs of the three beams (30°, 45° and 60°). The observed material distribution displaying resin rich pockets between fibre tows is characteristic to braided composites. Three types of voids were identified from the micrographs:

(a) Intra-tow micro voids: Circular voids visible as dark spots between fibre filaments.

(b) Intra-tow macro voids: An agglomeration of multiple micro-voids that lead to the formation of larger voids, often elliptical in shape.

(c) Inter-tow voids: Voids in the resin-rich pockets between fibre-tows.

In addition to void fraction, void characteristics such as location, morphology and distribution also individually influence mechanical performance [43,44]. Therefore, particle analysis was performed using the image processing software ImageJ (release 1.49v) [45] to quantify and compare the size and shape of the voids observed in the micrographs. Figure 11 shows histograms representing the size distribution of voids for 30°, 45° and 60° beams.

The shape of the voids was quantified using the circularity parameter C in ImageJ, shown in Equation 4.

$$C = \frac{4\pi A}{P^2} \tag{4}$$

where A: area ($\mu m^2$) and P: perimeter ($\mu m$).

A circularity value of 1 represents a perfect circle, whilst a value approaching 0 corresponds to a stretched elliptical shape. Figure 12 shows histograms representing the shape distribution of voids for the 30°, 45° and 60° beams.

The size and shape distributions for different braid angles were assessed through ANOVA. The obtained p-values are listed in Table 9. As both p-values are less than 0.05, it was concluded that the difference between the size and shape distributions of the voids is statistically significant between the braided beams with different braid angles. Results of the Tukey-Kramer post-hoc analysis, shown in Table 10, revealed that voids in 60° beam were larger, while those in 30° and 45° beams did not differ significantly. On the other hand, the circularity of the voids was the greatest in the 45° beams followed by 60° and 30° in that order. Previously conducted investigations have shown that effects of the void characteristics on mechanical performance are specific to material as well as load cases [46]; it is therefore proposed that a discrete work package would be required to establish the absolute effect of voidage on the performance of the beams tested in this work, which was considered out of scope of this study.

**Static three-point flexure performance**

Figure 13 shows the load-crosshead displacement curves obtained from the three-point flexure tests. The crosshead displacement was limited to 18 mm for all the beams, as further applied displacements led to visible lateral movement at the beam-support roller interface.

The load-displacement curves corresponding to different braid angles form three discrete populations. This indicates a significant dependence of the mechanical response on braid angle, which directly influences both material properties and beam thickness. Each response showed an initial increase in load. During this load rise, audible cracking was noted for all the beams. For the 60° beams, the load generally increased throughout the deformation, with a visible plateauing within the last one millimetre of crosshead displacement. On the other hand, for the 45° and 30° beams, the load increased to a local maximum followed by undulating load profiles with multiple peaks and troughs, ending with an ultimate steady decline.

Figure 14 shows one deformed beam for each braid angle in the test setup before unloading. The visible differences in the cross-sectional depth and bottom surface curvatures between the three beams indicate the correlation between the deformation modes and braid angle. Cracks were observed ex-situ in the loading area for every beam. These cracks originated in the region in direct contact with the loading roller and propagated along the braided fibres. None of the beams had visible damage in the region of the beam opposite the central loading point. A closer view of the unloaded deformed beams revealed that there was a transition from a single-region contact at the start of the test to a double-region contact at the loading roller-beam interface. The contact transitions were more noticeable for the 30° and 45° beams as compared to the 60° beams. Therefore, it is reasonable to assume that the localised contact-dependent damage propagation was responsible for the variable trends observed in the load-displacement curves. After unloading the beams, the 30° and 45° beams returned to their original shape, while the 60° beams had a noticeable permanent curvature.

The extent of localised crushing, recorded using the deflectometer assembly, is plotted against crosshead displacement in Figure 15. The curves show that the localised crushing initiated with the

onset of flexural deflection and progressed with an approximately linear trend. For a crosshead displacement of 18 mm, the localised crushing accounted for approximately 63%, 45% and 19% of the applied crosshead deflection for 30°, 45° and 60° beams respectively. Therefore, localised crush was the dominant deformation mode for the 30° beams, while global flexure was observed to dominate for the 60° beams. The response of the 45° beams was intermediate between the 30° and 60° beams.

The stiffness of the braided beams during the three-point flexure tests was determined using a chord definition represented in Equation 5.

$$S = \frac{\Delta P}{\Delta d} \tag{5}$$

where S: stiffness (N/mm); P: load (N) and d: displacement (mm).

The displacement range between 0.2 mm and 1 mm was considered for the stiffness calculations. In this range, the per cent localised crushing was 62%, 38% and 15% for the 30°, 45° and 60° beams respectively. The 60° beams showed the highest stiffness and peak load values, which are shown for the three braid angles in Figure 16. It is important to note that stiffness and peak load here are indicators of structural mechanical response, which is a combination of the beams' material characteristics as well as the beam sections' geometric properties. The average stiffness of the 45° and 30° beams were 14% and 36% lower relative to the 60° beams respectively. Similarly, the average peak load values were 37% and 57% lower respectively. This suggests that the effect of the aforementioned observed small disparity in void content is not a dominant factor upon the flexural response and the analysis based on the braid angle of beams remains meaningful. A dedicated experimental program is required to establish the actual effect of void size and shape distributions.

The observed trends of stiffness and peak load are in disagreement with the results reported by Potluri et al. [24] using coupon scale beams. This disagreement was likely due to the localised crushing observed in the present study which was not observed previously. However, the work by Potluri studied thermoset matrix-based composites and did not report the number of test repeats, which made it difficult to perform a conclusive comparison.

**DIC analysis**

The evolution of x-strain ($\varepsilon_x$), i.e. surface strain along the beam axis, is shown for the three braid angles in Figure 17(a). The load-crosshead displacement response of the beams tested with the DIC measurements are also shown in Figure 17(b) for reference. A non-uniform distribution was observed in all the strain profiles. The strain profile corresponding to the 60° beam approximates to pure flexure with distinguishable bands of compressive and tensile strains of similar magnitude in the top and bottom regions of the beam. These strain bands were symmetric about the central load introduction point and maintained their trends with increasing deflection. The effect of localised crushing appeared towards the end of the deformation in the form of minimal observable strain localisation in the upper loading region. Contrary to the 60° beam, the severe localised crushing in the 30° beam resulted in concentrated zones of compressive strain in the top region (around the central roller), while negligible strain was observed in the bottom region. With increasing crosshead displacement, the cracks

XLVI

propagated from the central loading point and appeared in the RoI. This was accompanied by further strain concentration in this loading region. The 45° beam showed emerging compressive and tensile strain bands similar to the 60° beam during the initial phase. However, the magnitude of the bottom region tensile strain was significantly lower. As the localised damage progressed into the RoI, strains became concentrated in the upper loading region similar to the 30° beam.

In order to further explore the differences in strain distribution that arose during loading of the beams, three parallel horizontal sections were constructed on the beam surface using the GOM software, as shown in Figure 18(a). The figure also shows that the three computed sections flex with the increasing deformation. Along each section, the GOM Correlate interface was used to evaluate flexural strain, computed as the average of the axial strains calculated at all integration points along the chosen line section. The evolution of the flexural strains 1, 2 and 3, corresponding to the top, middle and bottom regions respectively, are plotted against crosshead displacement for different braid angles in Figures 18(b), (c) and (d). Irrespective of braid angle, the top and bottom region strains (strain 1 and 3) showed increasing compressive and tensile trends respectively throughout the deformation. Owing to the localised deformation, the top region strain measurements (strain 1) became invalid for the 30° and 45° beams once damage propagated into the uppermost section. Until that point, the top region strains showed comparable magnitudes for all braid angles. On the contrary, the strains in the bottom region (strain 3) calculated for the 30° and 45° beams were low in magnitude in comparison to the 60° beam. Quantitatively, the bottom region strains at test completion (a crosshead displacement of 18 mm) were 77% and 91% lower for 45° and 30° beams respectively as compared to the 60° beam. In the middle region (strain 2), the flexural strains were initially tensile for all the braid angles. However, as the deformation advanced and the 30° and 45° beams collapsed under the loading roller, the recorded strains transitioned into compressive domain, while the obtained strain in the corresponding middle region in the 60° beam remained tensile.

In addition to these flexural strain analyses, three parallel sections were constructed on the beam surface using the GOM software, as shown in Figure 19(a). The downward (y-) displacements were recorded on all the points lying on these sections with respect to the crosshead. Figure 19(b) shows the progression of section-wise y-displacements y1, y2 and y3 with increasing crosshead displacement. The increase in disparity between the three section-wise displacements with decreasing braid angle is a representation of the departure from pure global flexure and into localised crush. Moreover, the increasing curvature of y3 with increasing braid angle further indicates the escalation of tensile deformation in the bottom region. It should be noted that the size of the error metrics presented in Table 3 are very small as compared to the obtained means and observed differences in the optically-measured strains and displacements between the three types of braided beams.

The results are interesting in that the DIC measurements show that with decreasing braid angle, the bottom halves of the braided beams showed decreasing tendency away from flexural deformation. This was due to the localised crushing in the upper half of the beam accommodating most of the applied

crosshead displacement. Moreover, the higher tensile strain measured in the bottom half of the 60° beam explains the plastic deformation (permanent curvature) observed after unloading.

The observed braid-angle dependence of the overall mechanical response is attributed to three braid angle dependent factors:

(iv) Thickness: As per classical beam flexure theory, increasing the section thickness increases its section modulus, hence improving the structure's resistance to flexural deformation. Furthermore, a hollow section's proclivity for localised crushing decreases with increasing wall thickness. Therefore, an increase in wall thickness makes the beam more resistant against both deformation modes and is expected to render an improvement in mechanical response. As observed in previous studies as well as discussed here, the thickness of braided beams increases with braid angle.

(v) Material moduli: Theoretically, axial modulus of a material is positively correlated to the resistance to flexural deformation in a structure via an increase in section modulus. On the other hand, transverse modulus, directed along the hoop direction for a circular beam, would strengthen a beam structure against local crushing. For a braided composite, previously reported experimental data has clearly shown that axial modulus decreases with braid angle, while transverse modulus increases [6-8].

(vi) Surface Coverage: The resin rich pockets present on the surface - as well as in the internal structure - often act as damage initiation sites for braided composites [47,48]. As displayed through analytical estimates presented in Table 8, the surface fibre coverage of the braided beams increased with increasing braid angle. Therefore, the 30° beams, having the least fibre coverage, had relatively larger resin rich pockets on the outer surface, followed sequentially by the 45° and 60° beams. Therefore, it is proposed that the interaction of the central loading roller with the increased level of resin rich regions in the 30° beams contributes to early initiation and propagation of localised damage.

The flexure test results show that increasing the braid angle resulted in enhanced mechanical performance. Moreover, the poorer mechanical performance of the lower braid angles coincided with greater local crushing. Considering the observed trends of the three discussed braid-angle dependent features as well as their expected influence upon deformation behaviour, the flexure test results indicate that resistance to localised crush was the critical performance factor for the beams characterised in this study. It is proposed that localised crush is an important consideration for thermoplastic composites in this particular loading configuration because of the lower stiffness and higher ductility of the matrix compared to thermosetting matrices, and thus explains any disagreement of the results obtained in this study with previously reported results from studies on the latter material type.

## Conclusions

The static three-point flexure response of component scale thermoplastic braided composite beams with braid angles of 30°, 45° and 60° was investigated. The flexural deformation manifested through two principal modes: localised crushing and global flexure. Localised crushing was observed to account for 63%, 45% and 19% of the total deflection for the 30°, 45° and 60° beams respectively at the point of maximum experimental deflection. Surface strain profiles obtained using three-dimensional DIC showed significant variation between the beams with different braid angles, particularly on the lower (tensile) face furthest away from the loading point. Analysis of the flexural strains as well as the transverse displacements showed significant tensile deformation in the bottom region for the 60° beam. On the other hand, the localised crush-dominant deformation led to minimal applied strains in bottom regions of the 30° and 45° beams. Consequently, the 30° and 45° beams returned to their original shape after unloading while the 60° beams underwent permanent (plastic) deformation due to the much higher applied strains. Increasing the braid angle resulted in improvement in mechanical performance, with significant increases observed in stiffness as well as peak load. Three braid angle dependent factors: thickness, material moduli and surface fibre coverage, were identified as the contributing factors to the observed differences in the mechanical performance as well as deformation modes. Based on the trends and independent influence of these features on flexural performance, resistance to localised crushing proved to be the critical factor governing the mechanical response of the braided beams tested in this work. The observed trends of flexural performance disagreed with previously reported flexural results of coupon scale braided beams, which could be attributed to the effect of beams' scale and test geometry as well as the use of relatively ductile lower stiffness thermoplastic matrix as opposed to thermoset matrices as studied previously. As such, the reported results establish a clear correlation between braid angle and deformation modes during the three-point flexural testing of thermoplastic braided beam structures. Detailed analysis and comparison of voidage in the braided beams was conducted using microscopy and resin-burn off experiments. A statistically significant difference in void morphology according to braid angle was observed, but the analysis revealed that these differences in void content/morphology did not affect mechanical performance as strongly as braid angle, and as such effects were not able to be measured. Therefore, a controlled study is required to understand the effects of voids on three-point flexural performance in such braided thermoplastic composite beam structures. Finally, as the current study is limited to thermoplastic braided composites with a biaxial regular braid pattern, the authors consider that a study of trends in flexural performance obtained using thermoset-based braided composites as well as triaxial braid patterns would be useful additions to the body of work in this area.

**Data Availability Statement**

The raw/processed data required to reproduce these findings cannot be shared at this time as the data also forms part of an ongoing study.

**References**

[1]      Kelkar AD, Whitcomb JD. Characterization and structural behavior of braided composites. U.S. Department of Transportation Federal Aviation Administration. 2009.

[2]      Arold B, Gessler A, Metzner C, Birkefeld K. Braiding processes for composites manufacture. In: Advances in Composites Manufacturing and Process Design. Woodhead Publishing; 2015, p. 3-26.

[3]      Verpoest I. Composite preforming techniques. In: Polymer matrix composites. Elsevier Science Limited; 2000, p.623-669.

[4]      Carey JP. Introduction to braided composites. In: Handbook of Advances in Braided Composite Materials. Woodhead Publishing; 2017, p. 1–21.

[5]      Gautam M, Potluri P, Ogin S, Jain P. Necking behaviour of flattened tubular braided composites. In: ICCM 2015: Proceedings of the 20th International Conference on Composite Materials, Copenhagen, July 2015.

[6]      Harte AM, Fleck NA. On the mechanics of braided composites in tension. Eur J Mech A/Solids 2000;19:259–75.

[7]      Melenka GW, Carey JP. Development of a generalized analytical model for tubular braided-architecture composites. J Compos Mater 2017;51:3861–75.

[8]      Falzon PJ, Herszberg I. Mechanical performance of 2-D braided carbon/epoxy composites. Compos Sci Technol 1998;58:253–65.

[9]      Priem C, Othman R, Rozycki P, Guillon D. Experimental investigation of the crash energy absorption of 2.5D-braided thermoplastic composite tubes. Compos Struct 2014;116:814–26.

[10]      Sturm R, Heieck F. Energy absorption capacity of braided frames under bending loads. Compos Struct 2015;134:957–65.

[11]      Reynolds N, Ramamohan AB. High-volume thermoplastic composite technology for automotive structures. In: Advanced composite materials for automotive application. Joh Wiley & Sons; 2013, p. 29–50.

[12]      Cheon SS, Lee DG, Jeong KS. Composite side-door impact beams for passenger cars. Compos Struct 1997;38:229–39.

[13]      Rebelo PM. Design Study of a Side Intrusion Beam for Automotive Safety. MSc Thesis, Instituto Superior Técnico, Lisboa, 2016.

[14]      Calonghi A. Alternative design of front door side impact beam for Nissan Navara. MSc Thesis, Cranfield University, 2006.

[15]      Belingardi G, Mehdipour H, Mangino E, Martorana B. Progressive damage analysis of a rate-dependent hybrid composite beam. Compos Struct 2016;154:433–42.

[16]      Bilston D, Rathnaweera G, Ruan D, Hajj M, Durandet Y. Parametric study of the bending properties of lightweight tubular metal/polymer foam hybrid structures. Compos Part B Eng 2016;105:101–10.

[17]      Gardner L, Nethercot DA. Experiments on stainless steel hollow sections—Part 2: Member behaviour of columns and beams. J Constr Steel Res 2004;60:1319–32.

[18]      Tang T, Zhang W, Yin H, Wang H. Crushing analysis of thin-walled beams with various section geometries under lateral impact. Thin-Walled Struct 2016;102:43–57.

[19]      Kecman D. Bending collapse of rectangular and square section tubes. Int J Mech Sci 1983;25:623–36.

[20]      Liu Q, Xing H, Ju Y, Ou Z, Li Q. Quasi-static axial crushing and transverse bending of double hat shaped CFRP tubes. Compos Struct 2014;117:1–11.

[21]      Fujihara K, Yoshida E, Nakai A, Ramakrishna S, Hamada H. Influence of micro-structures on bending properties of braided laminated composites. Compos Sci Technol 2007;67:2191–8.

[22]      Tate JS, Kelkar AD. Flexural behavior of biaxial braided composites. In: Proceedings of ASME International Mechanical Engineering Congress and Exposition, Orlando, November 2005.

L

[23]     Laberge-Lebel L, Van Hoa S. Manufacturing of braided thermoplastic composites with carbon/nylon commingled fibers. J Compos Mater 2007;41:1101–21.

[24]     Potluri P, Manan A, Francke M, Day RJ. Flexural and torsional behaviour of biaxial and triaxial braided composite structures. Compos Struct 2006;75:377–86.

[25]     Wu Z, Shen Y, Pan Z, Hu X. Three-point Bending Behavior and Energy Absorption Capacity of Composite Tube Reinforced by Gradient Braided Structure in Radial Direction. Fibers Polym 2019;20:1455–66.

[26]     Coats. Coats Synergex. Available from: https://www.coats.com/en/Guidance/CoatsSynergex#Commingling (accessed March 27, 2020).

[27]     Singh A, Reynolds N, Carnegie CR, Micallef C, Keating EM, Winnett J, et al. A novel route for volume manufacturing of hollow braided composite beam structures. Adv Manuf Polym Compos Sci 2019:1–6.

[28]     Grigg MN. Thermo-oxidative degradation of polyamide 6. PhD Thesis, Queensland University of Technology, 2006.

[29]     Tung JF. Synthesis and characterisation of polyamide 6 blends made by reactive extrusion. PhD Thesis, Brunel University, 1993.

[30]     Gupta J, Reynolds N, Chiciudean T, Kendall K. A comparative study between epoxy and vinyl ester CF-SMC for high volume automotive composite crash structures. Compos Struct 2020;244:112299.

[31]     BS EN ISO 1183-1. Plastics. Methods for determining the density of non-cellular plastics—Part 1: Immersion method, liquid pycnometer method and titration method. BSI 2019.

[32]     BS EN ISO 14127:2008. Carbon-fibre-reinforced composites. Determination of the resin, fibre and void contents. BSI 2008.

[33]     Tolf G, Clarin P. Comparison between flexural and tensile modulus of fibre composites. Fibre Sci Technol 1984;21:319–26.

[34]     Unlusoy C, Melenka GW. Flexural testing of cellulose fiber braided composites using three dimensional digital image correlation. Compos Struct 2019;230:111538.

[35]     Makeev A, Ignatius C, He Y, Shonkwiler B. A Test Method for Assessment of Shear Properties of Thick Composites. J Compos Mater 2009;43:3091–105.

 [36]     GOM. GOM ARAMIS. Available from: https://www.gom.com/metrology-systems/aramis. (accessed March 27, 2020).

[37]     GOM. GOM Correlate Professional. Available from: https://www.gom.com/3d-software/gom-correlate-professional.html. (accessed March 27, 2020).

[38]     Powe RAW. Towards the characterisation of automotive specific woven composite laminates at intermediate strain rates. PhD Thesis, University of Warwick. 2018.

[39]     Tukey JW. The collected works of John W. Tukey. vol. 1. Taylor & Francis; 1984.

[40]     Olivier P, Cottu JP, Ferret B. Effects of cure cycle pressure and voids on some mechanical properties of carbon/epoxy laminates. Composites 1995;26:509–15.

[41]     Potluri P, Manan A. Mechanics of non-orthogonally interlaced textile composites. Compos Part A Appl Sci Manuf 2007;38:1216–26.

[42]     Melenka, G.W., Hunt, A.J., van Ravenhorst, J.H., Akkerman, R., Pastore, C.M., Ko, F.K., Munro, M., Carey, J.P. Manufacturing processes for braided composite materials. In: Handbook of Advances in Braided Composite Materials. Woodhead Publishing; 2017, p. 47–153.

[43]     Lambert J, Chambers AR, Sinclair I, Spearing SM. 3D damage characterisation and the role of voids in the fatigue of wind turbine blade materials. Compos Sci Technol 2012;72:337–43.

[44]     Patou J, Bonnaire R, De Luycker E, Bernhart G. Influence of consolidation process on voids and mechanical properties of powdered and commingled carbon/PPS laminates. Compos Part A Appl Sci Manuf 2019;117:260–75.

[45]     Schneider CA, Rasband WS, Eliceiri KW. NIH Image to ImageJ: 25 years of image analysis. Natural Methods 2012;9:671–5.

[46]     Mehdikhani M, Gorbatikh L, Verpoest I, Lomov S V. Voids in fiber-reinforced polymer composites: A review on their formation, characteristics, and effects on mechanical performance. J Compos Mater 2019;53:1579–669.

[47]     Bibo GA, Hogg PJ. The role of reinforcement architecture on impact damage mechanisms and post-impact compression behaviour. J Mater Sci 1996;31:1115–37.

[48]     Fouinneteau M. Damage and failure modelling of carbon and glass 2D braided composites. PhD Thesis, Cranfield University. 2006.
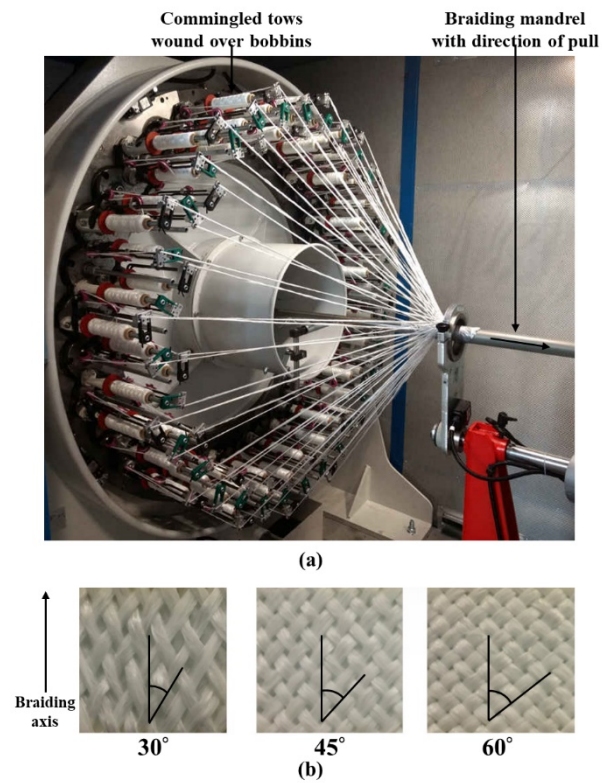
Figure 1 (a) Braiding of commingled tows and (b) flattened 1×1 diamond preforms with braid angle of 30°, 45° and 60°
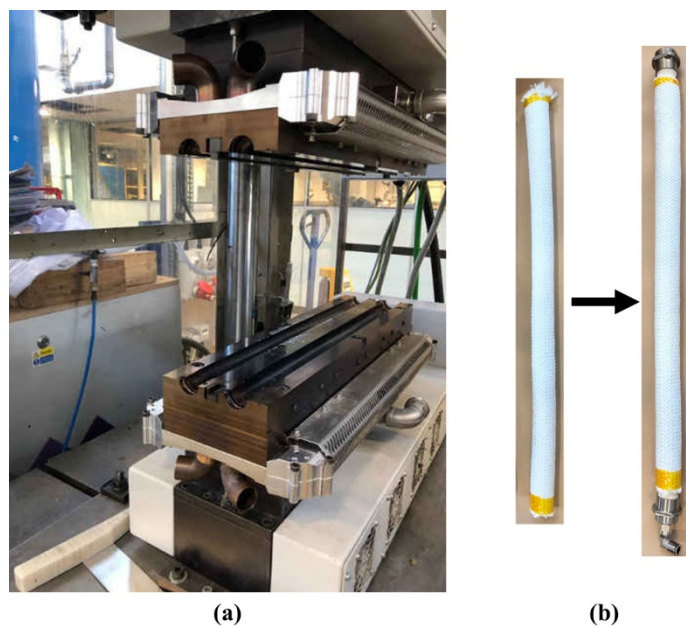


Figure 2 (a) RVM tool used for moulding of braided beams and (b) preparation of bladder-preform assembly from braided fabric
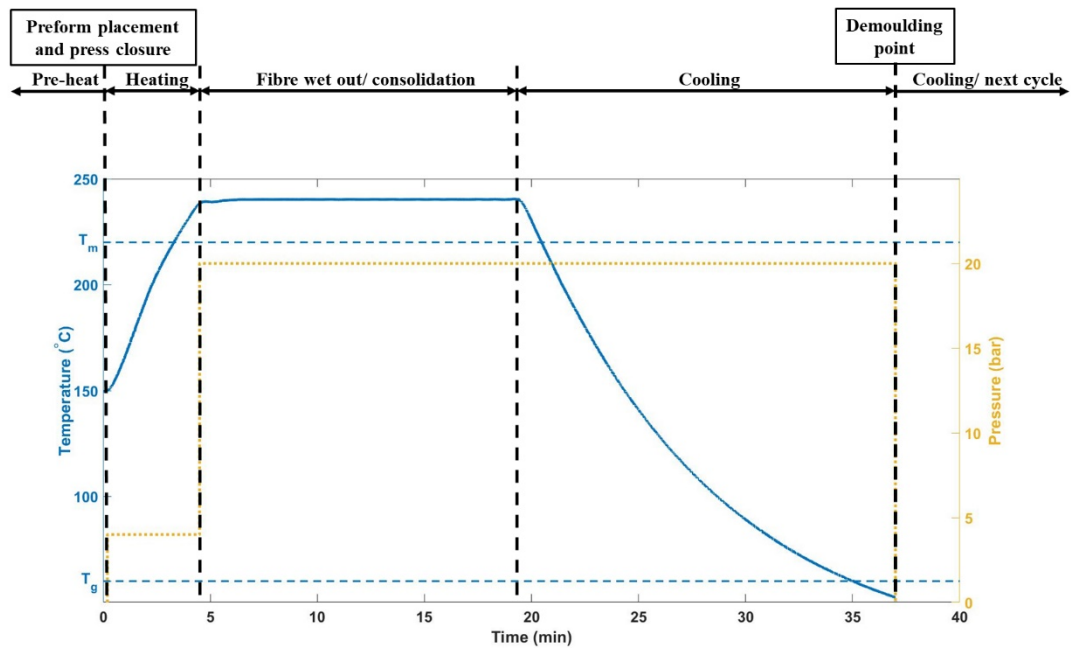
Figure 3 RVM process profile showing temporal characteristics of pressure and temperature during the process cycle. Note: melt temperature ($T_m$) and glass transition temperature ($T_g$) of PA6 are shown for reference
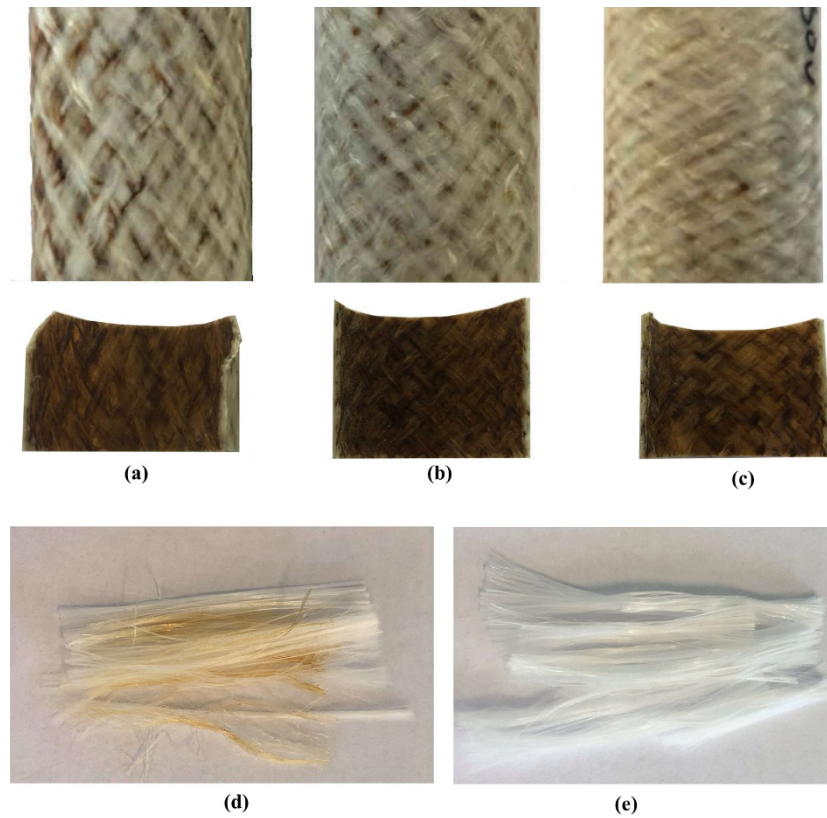


Figure 4 Outer and inner surfaces of (a) 30°; (b) 45° and (c) 60° braided beam; retrieved commingled fabric after heating to 250 °C: (d) visible brownish discolouration upon heating in ambient atmosphere with exposure to air and (e) no discolouration upon heating in an inert argon atmosphere
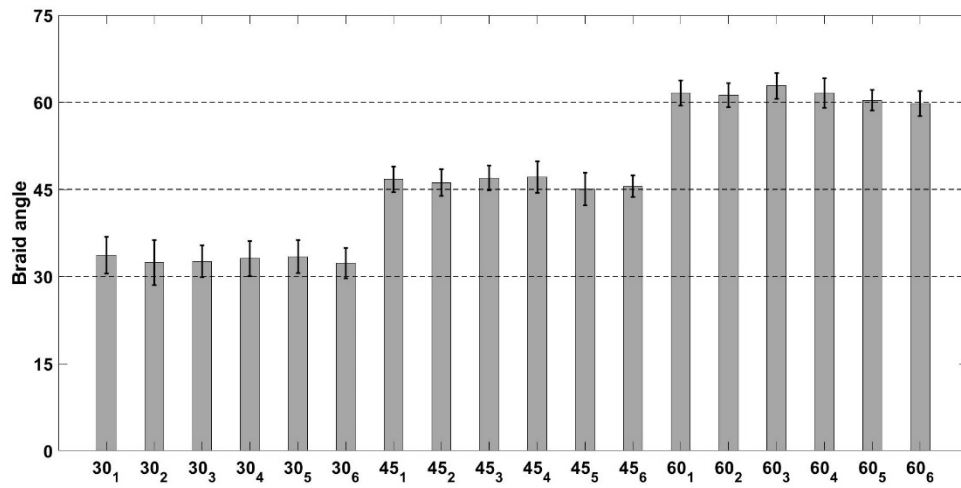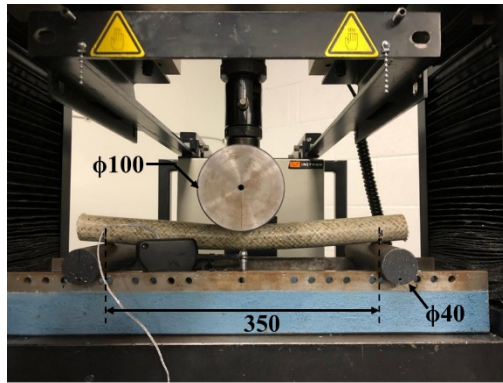
LIII

Figure 5 Measured braid angle for all the braided beams (30°, 45° and 60°). Note: values represent mean ± std. dev.



**(a)**                                    **(b)**

Figure 6 (a) Three-point flexure setup on the test machine frame and (b) deflectometer assembly. Note: all units are in mm
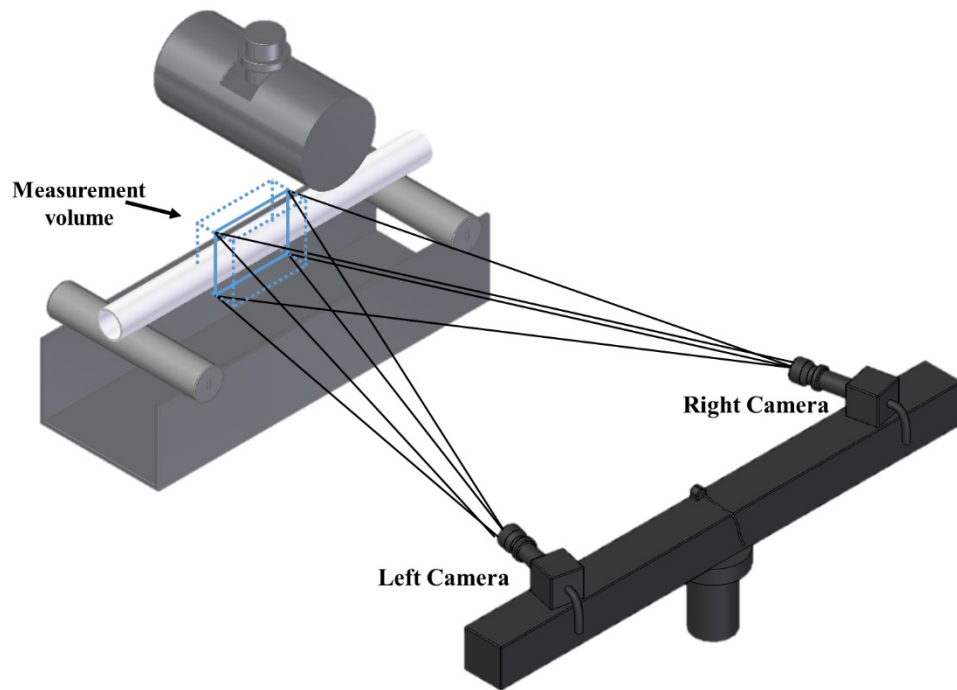
Figure 7 Schematic of DIC measurement during three-point flexure test
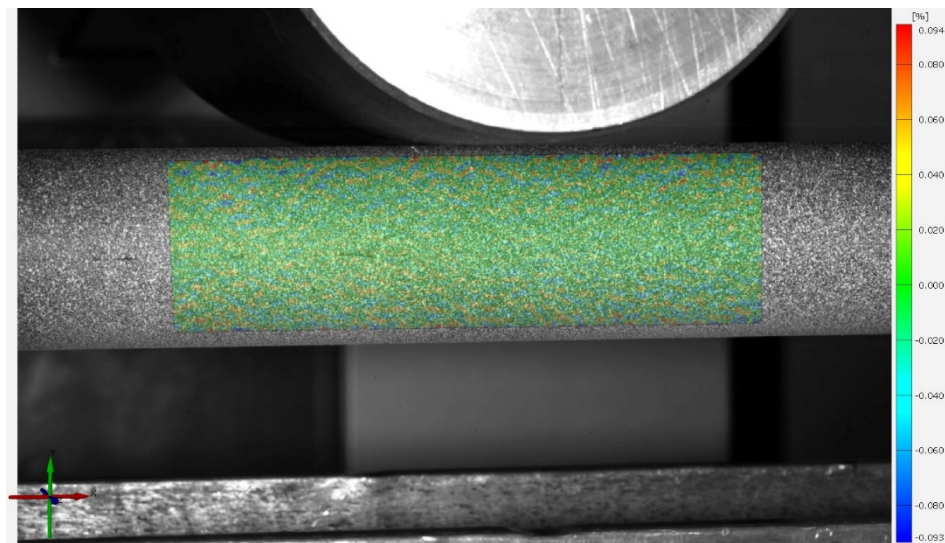


Figure 8 Static image in the preload condition with a distribution of false strain values
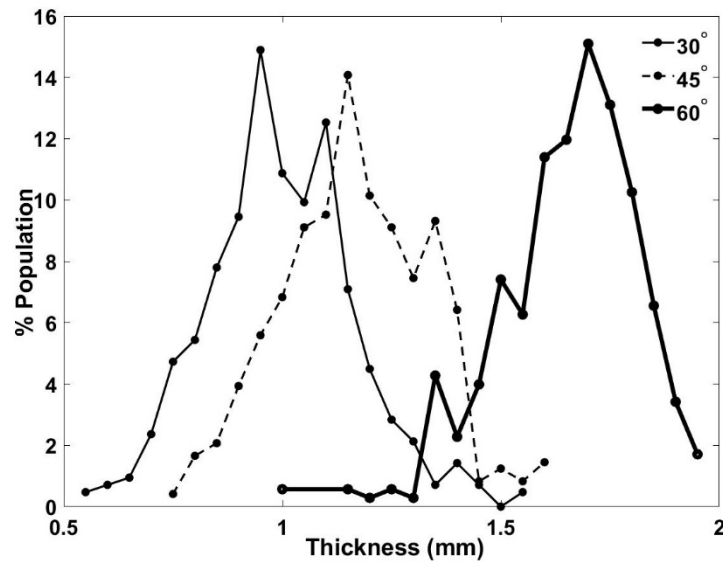
Figure 9 Measured thickness for braided beams with different braid angles
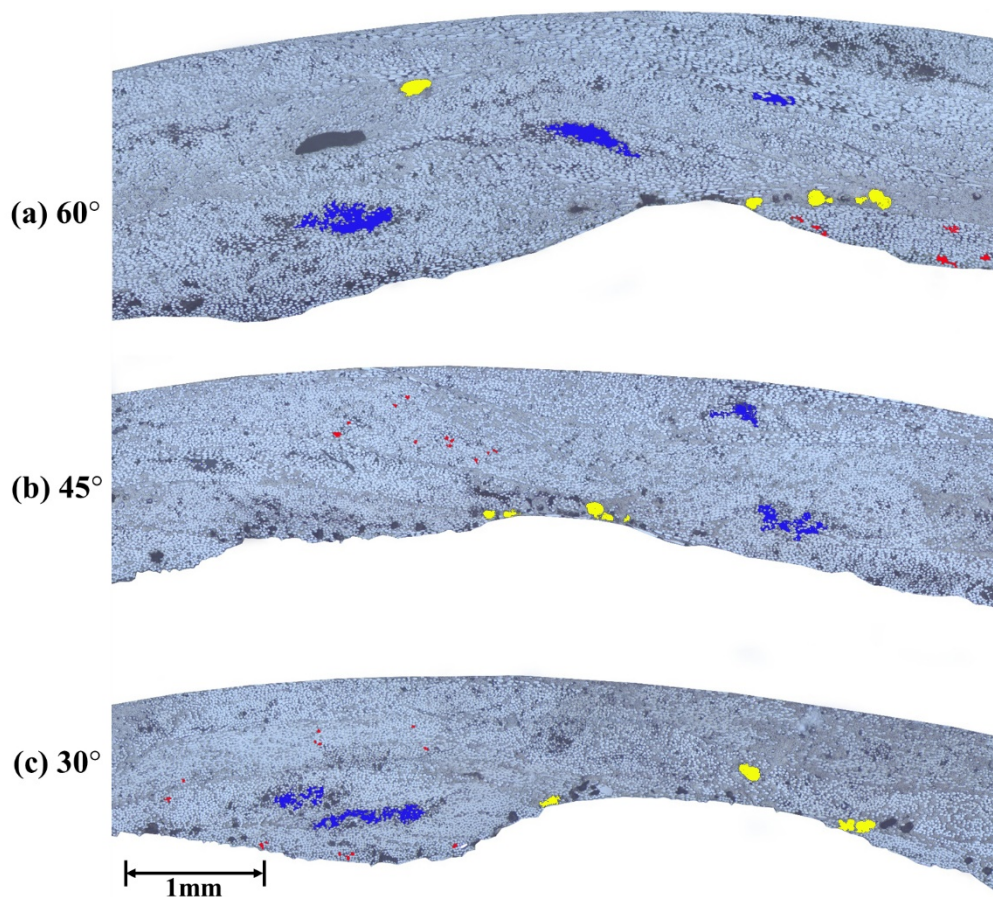


**(a) 60°**

**(b) 45°**

**(c) 30°**

1mm

Figure 10 Micrographs of braided beam sections with braid angles of (a) 60°, (b) 45° and (c) 30°. Note: Coloured regions highlight a representative selection (non-exhaustive) of intra-tow micro (Red), intra-tow macro (Blue) and inter-tow voids (Yellow)
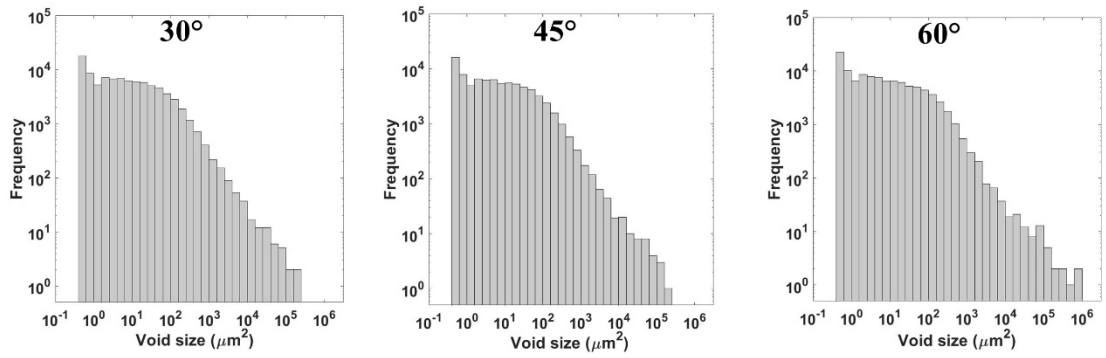
Figure 11 Distribution of void size corresponding to different braid angles
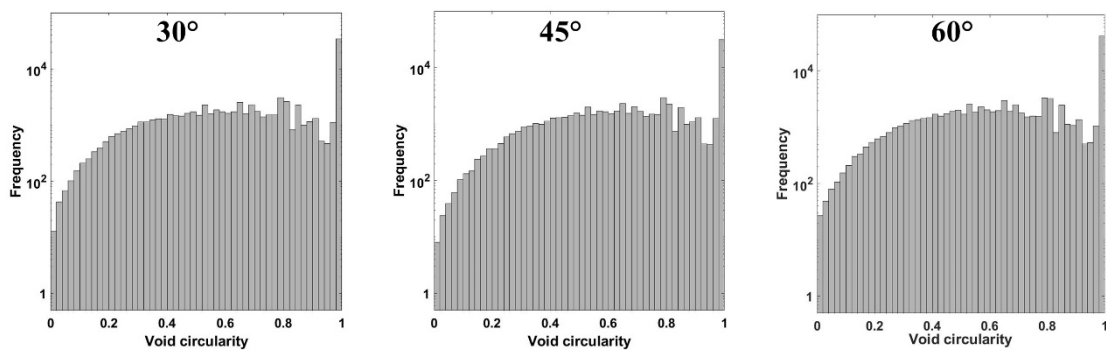


Figure 12 Distribution of void circularity corresponding to different braid angles
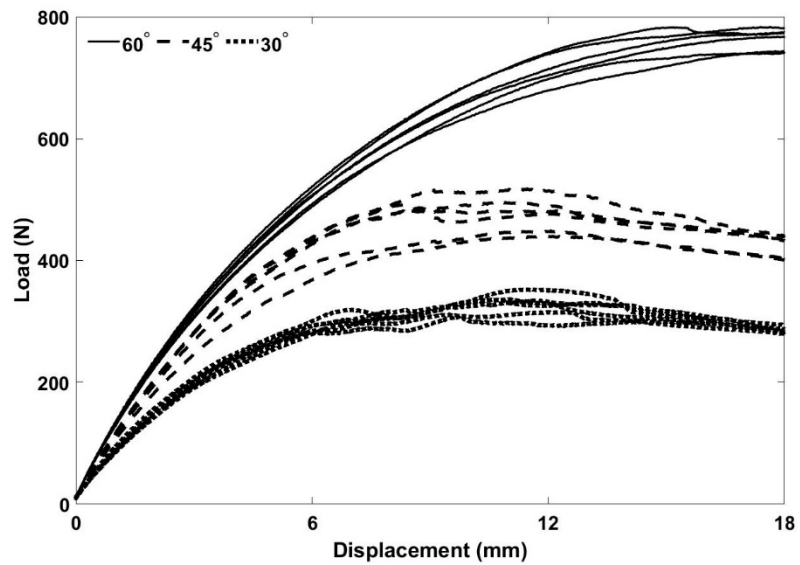


Figure 13 Load-crosshead displacement data from three-point flexure experiments for 6 repeats of each 30°, 45° and 60° beam sets
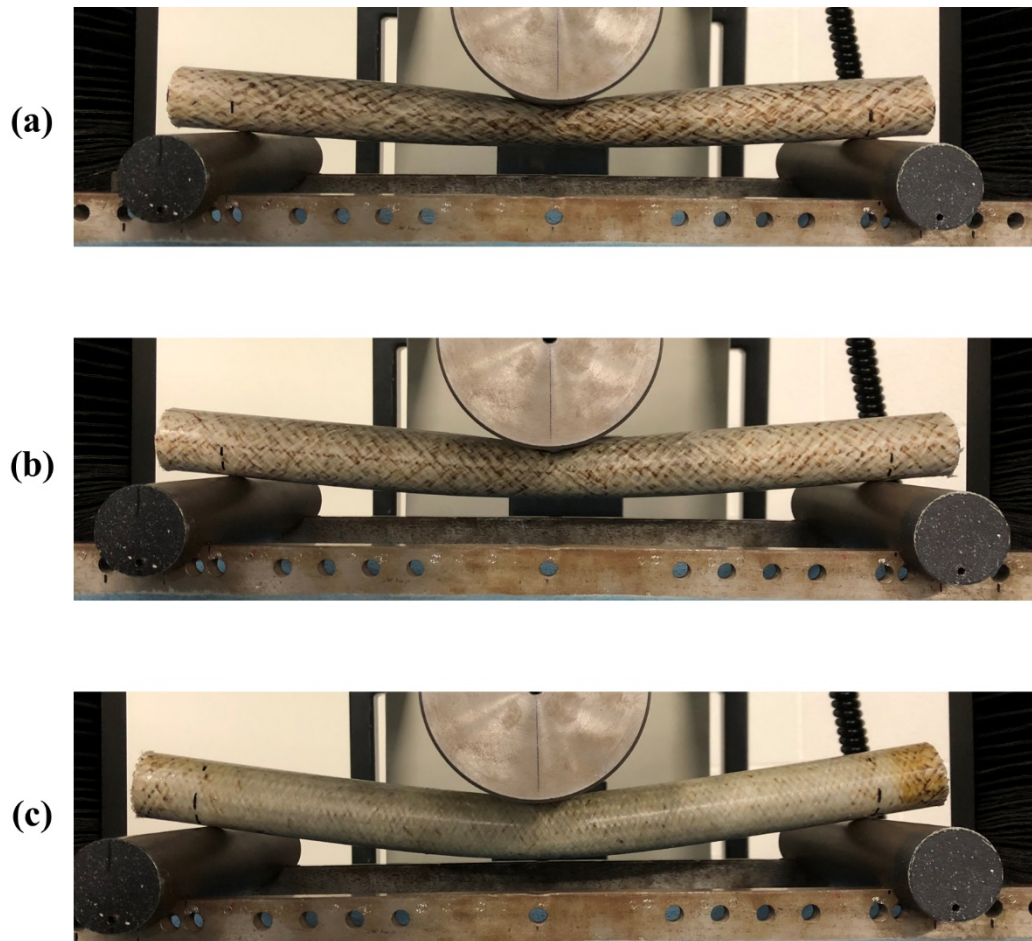
Figure 14 Beams with braid angles of (a) 30°, (b) 45° and (c) 60° in the test fixture after 18 mm of crosshead deflection
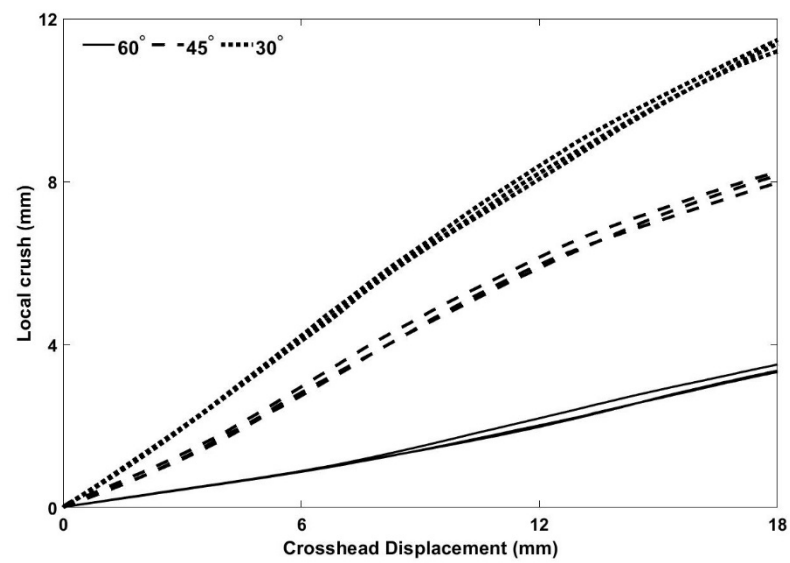


Figure 15 Progression of localised crushing (from the difference between crosshead displacement and the deflectometer displacement) during three-point flexure

LVIII
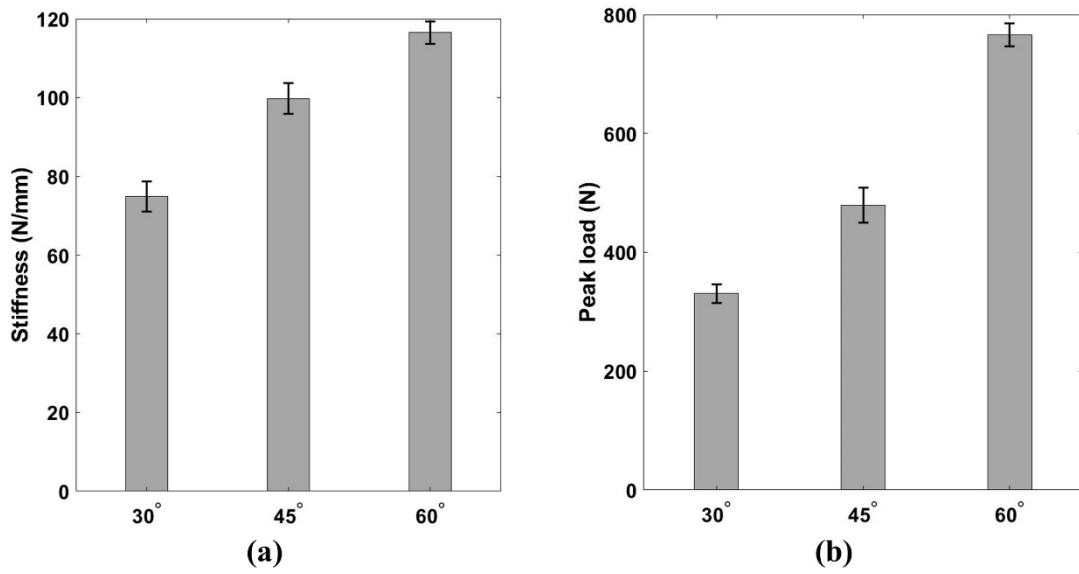
Figure 16 (a) Stiffness and (b) peak load data for different beams. Note: bars represent mean values from 6 repeats and errors represent one standard deviation
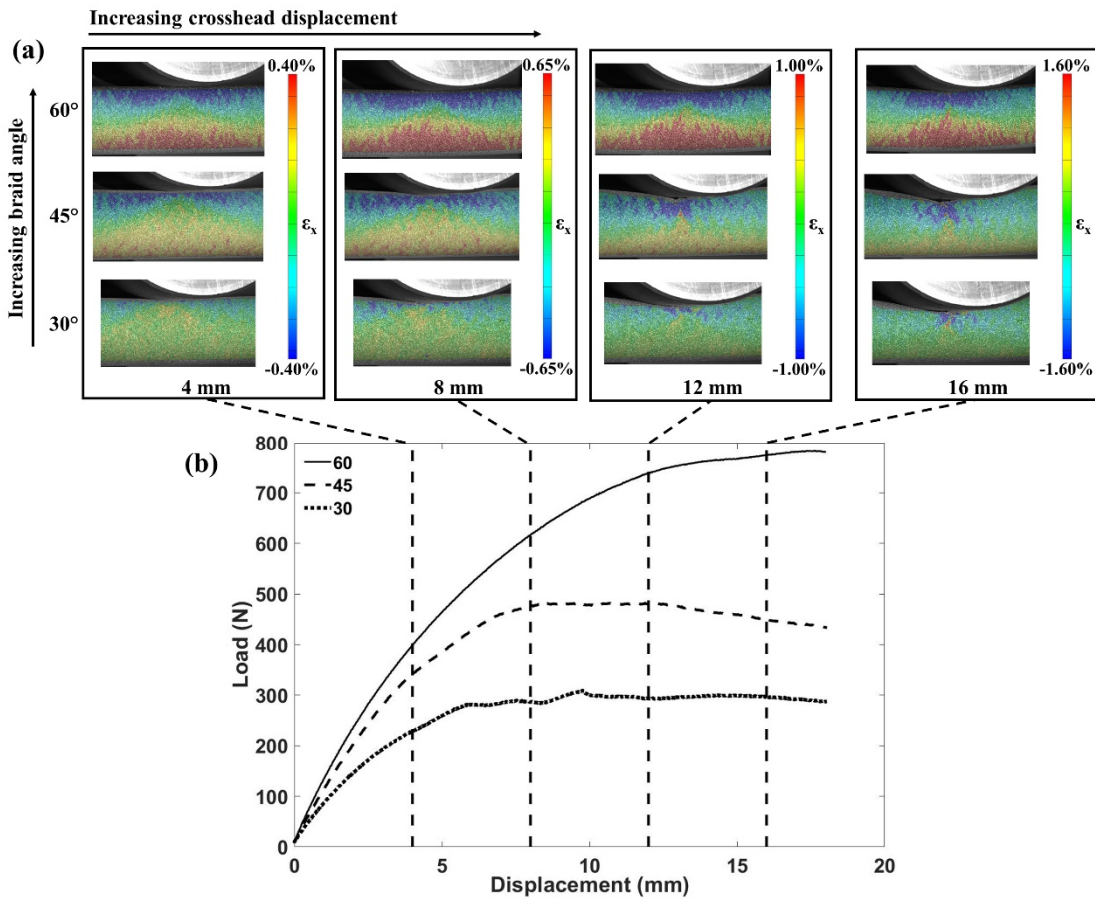


Figure 17 (a) $\varepsilon_x$ progression with crosshead displacement during three-point flexure and (b) load-displacement curves corresponding to the beams tested with DIC measurement

LIX

**(a)**



**(b) 30°**

**(c) 45°**

**(d) 60°**
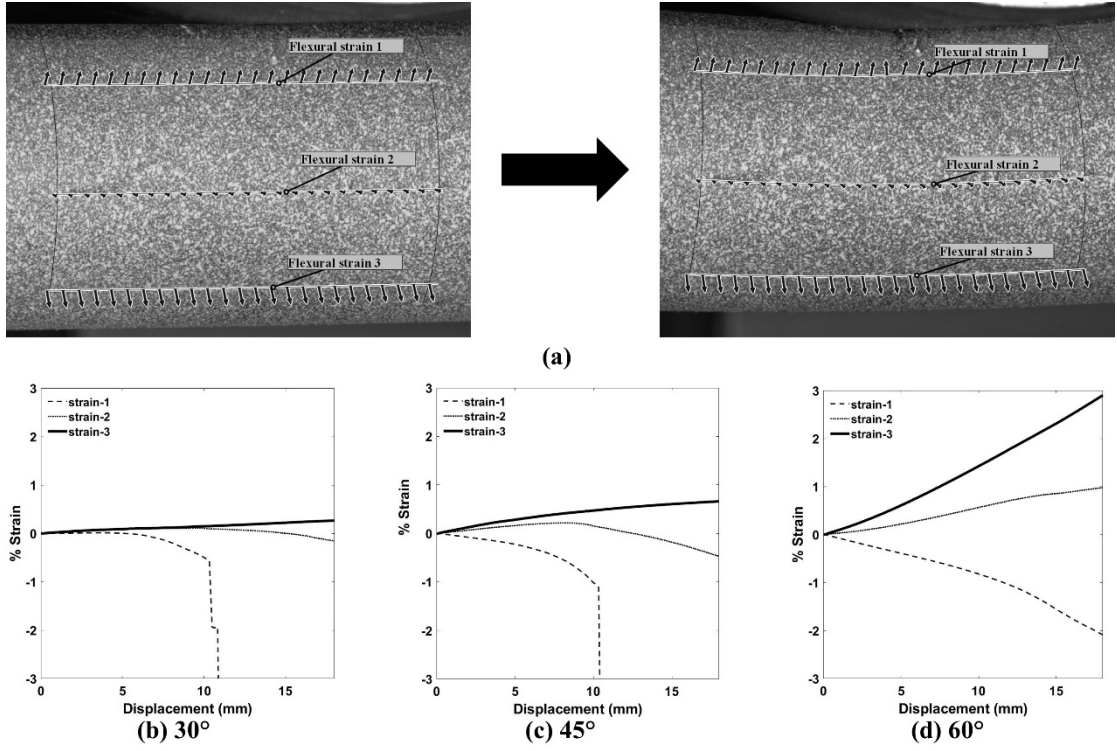
Figure 18 (a) Horizontal sections (strain 1-3) constructed on the surface of a beam showing the initial (preloaded) condition and the condition at increased crosshead displacement. b-d) evolution of flexural strain at 3 locations (strain 1-3) for braided beams during three-point flexure with braid angle of (b) 30°, (c) 45° and (d) 60°
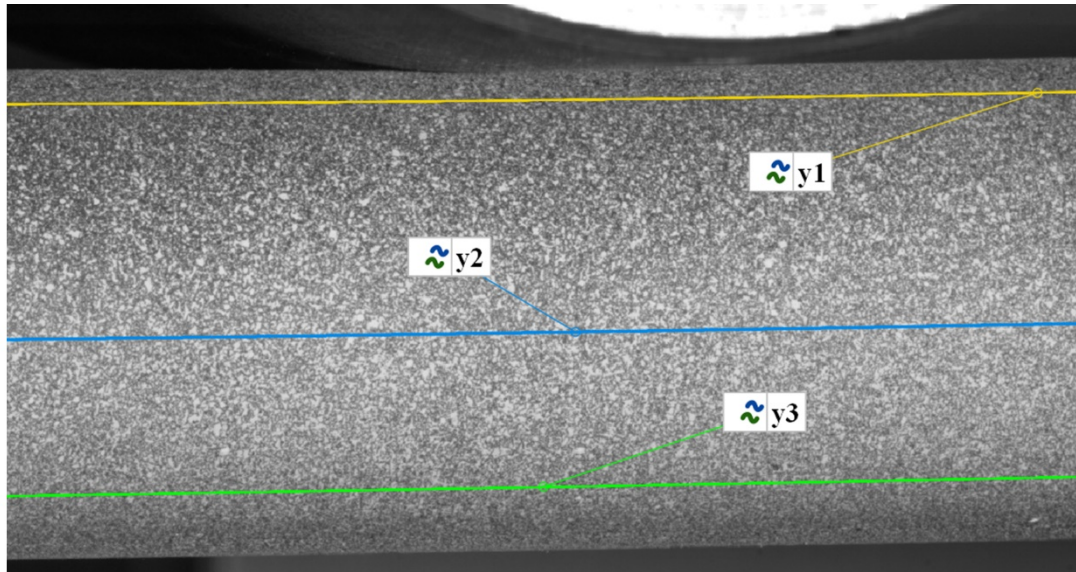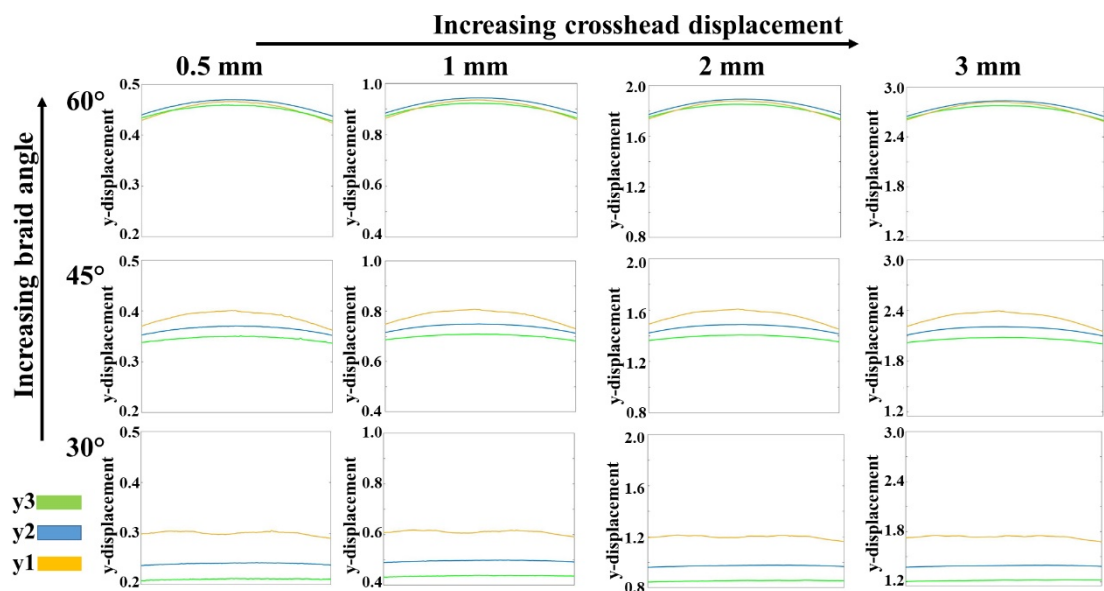
Figure 19 (a) Parallel sections y1-3 for comparing flexural displacements ($y$-, downward in the figure) on the surface of a beam and (b) evolution of downward y-displacement y1, y2 and y3 for beams with different braid angles during three-point flexure (increasing crosshead displacement)

Table 1 Properties of commingled E-glass/PA6 material

| Property | Value |
|---|---|
| Linear weight | 1650 g/km |
| Glass fibre weight fraction | 72% |
| Theoretical fibre volume fraction | 54% |
| E-glass density | 2.54 g/ml |
| PA6 density | 1.15 g/ml |
| PA6 melting point | 221 °C |
| PA6 glass transition temperature | 60 °C |

Table 2 DIC system parameters employed during acquisition and analysis

| Parameter | |
|---|---|
| Sensor/camera | GOM 12M |
| Lens | Titanar 100 mm |
| Image window | 4000 pixel × 3000 pixel |
| Measurement area | 150 mm × 100 mm |
| Calibration plate used | CP20 90 × 72 |
| Facet size | 19 pixels (16 pixels step size) |
| Lens Aperture | f-stop f/16 |
| Depth of field | 39 mm |
| Exposure time | 55 to 60 ms (depending on speckle pattern) |
| Frame rate | 2 Hz |

Table 3 Mean bias and precision of DIC measurements estimated from static images

| Mean bias $[\varepsilon_x (\%)]$ | Mean precision $[\varepsilon_x (\%)]$ | Mean bias $[dx \, (mm)]$ | Mean precision $[dx \, (mm)]$ | Mean bias $[dy \, (mm)]$ | Mean precision $[dy \, (mm)]$ |
|---|---|---|---|---|---|
| 0.0001 | 0.0162 | 0.0029 | 0.0003 | -0.0007 | 0.0004 |

Table 4 $F_{vf}$ and $V_{vf}$ estimated from resin burn-off. Note: values represent mean ± std. dev.

| | $F_{vf}$ | $V_{vf}$ |
|---|---|---|
| **30°** | 48.8 ± 1.1 | 7.8 ± 1.2 |
| **45°** | 49.9 ± 1.1 | 8.5 ± 1.2 |
| **60°** | 49.6 ± 1.1 | 10.5 ± 0.8 |

Table 5 p-values corresponding to $V_{vf}$ and $F_{vf}$ comparisons obtained from ANOVA

|  | p-value |
|---|---|
| $V_{vf}$ | 0.002 |
| $F_{vf}$ | 0.236 |

Table 6 q-values obtained from Tukey-Kramer post-hoc analysis performed for $V_{vf}$. Note: values indicating a statistically significant difference are underlined

| Pair | q ($V_{vf}$) | q$_{critical}$ |
|---|---|---|
| 30°- 45° | 1.70 | 3.67 |
| 45°- 60° | 4.22 | 3.67 |
| 30°- 60° | 5.92 | 3.67 |

Table 7 Mean, maximum and minimum thickness values measured for different braided beams. Note: All values are in mm

| Thickness | 30° | 45° | 60° |
|---|---|---|---|
| Mean | 0.972 | 1.145 | 1.630 |
| Maximum | 1.503 | 1.596 | 1.934 |
| Minimum | 0.526 | 0.747 | 1.118 |

Table 8 Tow geometry parameters corresponding to different braided beams. Note: tow width values represent mean ± std. dev.

|  | 30° | 45° | 60° |
|---|---|---|---|
| Tow width (mm) | 3.18 ± 0.18 | 2.69 ± 0.16 | 2.23 ± 0.14 |
| Estimated cover factor | 78.3% | 80.2% | 87.7% |

Table 9 p-values corresponding to void size and shape comparison obtained from ANOVA

|  | p-value |
|---|---|
| Void size | 0.005 |
| Void shape | <0.001 |

Table 10 q-values obtained from Tukey-Kramer post-hoc analysis performed for void shape and size. Note: values indicating a statistically significant difference are underlined

| Pair | q (void size) | q (void shape) | q$_{critical}$ |
|---|---|---|---|
| 30°- 45° | 0.72 | 15.11 | 3.31 |
| 45°- 60° | 4.20 | 7.97 | 3.31 |
| 30°- 60° | 4.80 | 7.85 | 3.31 |

# Appendix G: Publication 3

## Three-point flexural performance of tailor-braided thermoplastic composite beam structures

Anubhav Singh[a],*, Neil Reynolds[a], Elspeth M Keating[a], Alastair E Barnett[b], Steve K Barbour[b], Darren J Hughes[a]

[a] WMG, University of Warwick, Coventry CV4 7AL, United Kingdom
[b] Composite Braiding Limited, Derby DE24 9FU, United Kingdom

*Corresponding author, E-mail: A.Singh.10@warwick.ac.uk

**Abstract**

This work investigates the potential of improving the mechanical performance of braided composite beams through the introduction of local braid angle variations. Tubular braided beams with a 45°/60°/45° length-wise (axial) braid angle variation were manufactured and tested in quasi-static three-point flexure and their performance was compared with beams having a layer-wise (radial) [±60°/±45°/±45°] variation. Compared to beams having uniform braid angles, axial braid angle tailoring resulted in equivalent flexural performance with a 24% reduction in part weight. In contrast, tailoring in the radial direction did not yield any improvement in mass-specific performance. Deformation analysis of the beams using an extensometer and digital image correlation showed that an axial braid angle variation in each layer resulted in a comprehensive shift in deformation characteristics. Changing the braid angle in the outer layer across the whole beam showed partial change in deformation mode, but did not match the modification observed through axial variation.

**Keywords**: Braiding; Tailoring; Thermoplastic; Flexure; Lightweighting; Digital image correlation

## Introduction

Braiding has emerged as an attractive composite manufacturing technology over the last few decades. The technique uses automated braiding machines to produce multi-layered dry fibre preforms through controlled interlacing of the fibres over the surface of a mandrel. The process is inherently flexible in terms of shape, size and orientation of the mandrels and hence creates near-net shape preforms [1]. Consequently, the preforms require minimal trimming operations and hence reduce material waste. Additionally, the complex fibre interlacements, achieved through the braiding process, impart superior mechanical performance under certain load cases compared to competitor manufacturing processes. These advantages of braided composites have led to their adoption for the production of load-bearing structures in the automotive and aerospace industry [2].

A particular advantage of composite materials is the possibility of modifying them as per the bespoke requirements of a given application. Such modifications are largely embodied in components via judicious variation of fibre orientation and part thickness [3,4]. Braided composites are no exception,

and braiding provides several avenues to modify part performance to a structure's local specific requirements. For instance, the mechanical properties of a braided structure can be enhanced in the length-wise direction by the selective introduction of axial tows [5]. Additionally, the process can readily combine different types of reinforcement without adding significant time or cost. For instance, braiding of carbon and aramid tows was demonstrated to enhance mechanical stiffness as well as energy absorption [5]. A potential technique for modification of braided composites is through the variation of braid angle in different regions of the composite. The braid angle influences the material characteristics as well as the thickness of a braided composite [6–14]. Therefore, local variations in braid angle provide significant potential for improvement in overall structural performance. This inherent capability of the braiding process has been utilised in the past to produce braided components with varying properties. Carey et al. [15] varied the braid angle for achieving variable stiffness along the length of composite catheter shafts with different combinations of fibres and matrices. Similarly, variable stiffness was achieved by Fujihara et al. [16] in dental posts by braiding the fibres with a graded variation in braid angle. Boss et al. [17] fabricated braided rods with a gradual braid angle variation. The flexural and tensile moduli of the rods were found to be an average of the properties corresponding to beams with uniform braid angles, while the overall tensile strength depended on the braid angle region that had the lowest strength. Ganesh et al. [18] used braided preforms with graded braiding angles in single-bond lap joints to gradually reduce the longitudinal modulus from the loaded end to the joint's overlap region. The results showed a more uniform stress distribution in the overlap area. Stanier et al. [19,20] performed open-hole tensile tests on triaxially braided rectangular plates with a controlled braid angle variation and reported an improvement in strength as compared to beams with a constant braid angle. Similar improvement was observed by Huang et al. [21] in the tensile strength of braided tubes with graded braid angle profiles.

The abovementioned studies showed that braid angle variations can result in improved performance. However, the available studies are limited to uniaxial loads. In order to establish the viability of braided composites with variable braid angle, it is important to analyse their performance in other structural load cases. A simple and effective loading scenario for global assessment of structural performance is provided by a three-point flexure test. The localised loading in three-point flexure subjects the test specimen to variable stress states and mixed-mode failure, thus making it ideal for testing beam structures where trade-offs between different characteristics that depend on braid angle can be studied. Moreover, there are several previous studies that present three-point flexure as a means to explore the performance of beam structures with variable properties along the axis. Duan et al. [22] tested what they termed 'tailor-rolled' top hat metallic structures with preferentially greater thickness in the loading zone. Similarly, Sun et al. [23] tested thickness-graded metallic beams under flexure. Both of these approaches were reported to achieve significant weight saving without compromising mechanical performance. In addition to variable property metallic beams, the results reported by Keating [24] and Sun et al. [25] showed lightweighting benefits are also achievable by locally reinforcing metallic beams with composite patches in the loading region of a three-point flexure test.

As the weight of a braided beam is directly related to the braid angle [5], controlled braid angle variations also presents an opportunity for structural lightweighting as reported for metallic and hybrid structures.

Recent work performed by the authors studied the effect of braid angle on three-point flexural performance of uni-braided (UBr) thermoplastic composite beams, i.e. beams with a constant braid angle [26]. Building on this recent work, the authors propose a 'tailor-braiding' approach for a composite braided structure in order to create structurally efficient components offering performance improvement over UBr variants. This current study uses the results obtained from testing UBr beams to devise suitable strategies for length-wise tailoring of braid angle, i.e. axial tailor-braiding (TBr$_A$), followed by manufacturing and testing of the TBr$_A$ beams in static three-point flexure. Results reported by Wu et al. [27] had previously shown that a radial variation can modify the flexural response. Therefore, beams with a layer-wise braid angle variation, i.e. radial tailor-braiding (TBr$_R$) are also manufactured and tested for comparison. Using three-point flexure as a test scenario, the results are presented and analysed against those obtained from the previous UBr beams to determine the potential of the two tailor-braiding (TBr) strategies for achieving performance improvements. Moreover, since most of the previous research on braided structures has focused on thermosetting matrix composites; given the difference in ductility between thermoset and thermoplastic polymer matrices, it is expected that the results obtained in this work will invite further research questions over the influence of the matrix in tailor-braided structures.

**Three-point flexure performance of UBr beams**

Previously, 420 mm-long uni-braided beams with an outer diameter of 35 mm having braid angles of 45° (UBr$_{45}$) and 60° (UBr$_{60}$) were tested in three-point flexure [26]. During the tests, the applied crosshead displacement resulted in two principal deformation modes: global beam flexure and localised crushing. Quantitatively, 45% and 19% of the total deflection in the UBr$_{45}$ and UBr$_{60}$ beams respectively was through local crushing. The stiffness (S) of the tested beams was evaluated in the displacement range between 0.2 mm and 1 mm using Equation 1. The energy absorption (E$_{abs}$) was also determined by evaluating the area under the load-displacement curves, as shown in Equation 2. The beams were deformed up to a crosshead displacement of 18 mm.

$$S = \frac{(P_1 - P_{0.2})}{(0.8)} \qquad (1)$$

$$E_{abs} = \int_0^{18} P \, dx \qquad (2)$$

where S: stiffness (N/mm); P$_1$: load (N) at 1 mm crosshead displacement and P$_{0.2}$: load (N) at 0.2 mm crosshead displacement; E$_{abs}$: energy absorption (Nmm); x: displacement (mm).

The three performance indices: S, peak load (P$_{max}$) and E$_{abs}$ corresponding to the UBr beams during three-point flexure are shown in Figure 1. Compared to the UBr$_{45}$ beams, S, P$_{max}$ and E$_{abs}$ were 17%, 60% and 43% greater respectively for the UBr$_{60}$ beams, clearly demonstrating overall superior

LXVI

mechanical performance. Beam deformation analyses indicated that for the tested UBr beams, resistance to localised crush was the critical governing factor in overall mechanical performance.

In addition to the mechanical performance indices reported in [26], Figure 1 also shows the measured mass values for the two UBr beam types, which are presented for the first time in this work. Comparing the average masses revealed that the relative improvement in mechanical performance of the $UBr_{60}$ beams was accompanied with a 44% increase in mass as compared to the $UBr_{45}$ beams. This data is used to calculate mass-normalised performance indices (S', $P'_{max}$, $E'_{abs}$), and these are also shown in Figure 1. In order to compare the mass-specific properties, a single factor analysis of variance (ANOVA) was performed. A significance level of 0.05 was selected and the resulting p-values are listed in Table 1.

As the p-value for the mass-specific energy absorption ($E'_{abs}$) was greater than 0.05, it could be stated with 95% confidence that the difference in $E'_{abs}$ between the $UBr_{45}$ and $UBr_{60}$ beams was not statistically significant; however differences between beams in specific stiffness (S') and specific peak load ($P'_{max}$) were statistically significant. Specifically, S' was 23% greater for $UBr_{45}$ beams, while $P'_{max}$ was 11% greater for $UBr_{60}$ beams. Therefore, from a structural lightweighting perspective, the $UBr_{60}$ beams did not offer a clear advantage over the $UBr_{45}$ beams under flexural loading.

These mechanical test results as obtained from the UBr beams were used as a baseline for devising a tailor-braiding strategy for the current study. Given the $UBr_{60}$ beams' greater resistance to localised crush and the improved specific (flexural) stiffness of the $UBr_{45}$ beams, it was hypothesised that beams with a braid angle of 60° in the central loading region with adjacent regions of 45° located symmetrically either side would result in overall improved mechanical performance compared to 45° beams, whilst being significantly lighter than $UBr_{60}$ beams. Therefore, as shown in Figure 2, a 45°/60°/45° configuration was selected for the $TBr_A$ beams. For the $TBr_R$ beams, as the outer layer directly interacts with the loading roller, beams with two inner layers of 45° and an outer layer of 60°, i.e. a [±60°/±45°/±45°] braid angle profile, were manufactured for comparison with the $TBr_A$ beams.

## Experimental methodology

### Materials and manufacturing

Commingled E-glass/polyamide 6 (PA6) tows were braided using a 64-carrier machine. The details of the material and braiding process are listed in Table 2.

During the braiding process, the fibre tows originate from the bobbins on the braiding machine. The bobbins are in constant circular motion in a fixed plane adjacent to the braiding machine, called the braiding plane (BP). All the fibre tows converge on the braiding mandrel in a plane known as fall plane (FP). As a consequence of the location of the FP relative to the BP, the angle subtended between a fibre tow and the mandrel is equal to the braid angle. This is schematically depicted in Figure 3.

As shown by Nishimoto et al. [28], an axial braid angle variation necessitates a shift of the FP. This creates a transition region on the resulting braided beam between the FPs of the two target braid angles

that has a continuously varying braid angle. However, during the braiding of the $TBr_A$ preforms, the transition regions were found to be extremely long with respect to the length of the beams produced and tested in this work. Therefore, a step transition was adopted. This was achieved by braiding the tows in a start/stop mode, as depicted in Figure 4(a). After braiding the required length at the FP corresponding to 45°, the process was stopped, the mandrel was moved linearly to align the tow converging point with the FP of 60° and the braiding process was restarted with the corresponding braiding parameters. This adjustment process was repeated to achieve each required length of tailored braid. The FPs for braid angles of 45° and 60° are shown in Figure 4(b). The adjustment process was repeated for each layer of these multi-layer braided preforms. On the other hand, the braiding of $TBr_R$ preforms was conducted by braiding the two inner layers at 45° and the outermost layer with a braid angle of 60°.

Following the braiding process, the preforms having 3 layers of braided fabric were used to produce tubular braided beams with an outer diameter of 35 mm in a bladder moulding process, known as Rapid Variothermal Moulding (RVM). The entire process of preform preparation and moulding is shown step-by-step in Figure 5. For further details regarding the manufacturing process, the readers are referred to [26] and [29].

The produced $TBr_A$ beams had an approximately 80 mm-long region of braid angle of 60° in the centre, with equal-length regions of 45° located at both ends. The outer surfaces of the $TBr_A$ and $TBr_R$ braided beams produced using the RVM process are shown in Figure 6. For the purpose of comparison, surfaces of $UBr_{45}$ and $UBr_{60}$ beams are also shown. The visible discolouration on beam surfaces was due to exposure of the molten PA6 polymer to ambient air during the moulding process [26]. There was an observable difference in the brownish discolouration of the $UBr_{45}$ and $UBr_{60}$ beams, which occurred due to larger air gaps between tows in the $UBr_{45}$ beams. For the $TBr_A$ beams, the difference in discolouration between regions with braid angles of 45° and 60° created an identifiable transition zone between the two regions. As shown in the figure, the fibres in both the regions resemble the outer surface characteristics of the corresponding UBr beams. Fibre waviness was observed at angle transition points as well as the adjacent 60° region in all of the beams. This was likely due to the discrete step-change in braid angle during manufacturing (as opposed to a continuous variation); minimisation of this uncontrolled defect was not within the scope of the present study. On the other hand, the discolouration on the surface of the $TBr_R$ beams was an intermediate between the $UBr_{45}$ and $UBr_{60}$ beams. Unlike the UBr as well as $TBr_A$ beams, the $TBr_R$ beams did not show any dry fibres on the outer surface. This is discussed later in the paper.

The mass of all the beams was measured after cutting them all to a length of 420 mm (Figure 7). The mean mass of the $TBr_A$ beams was 3% lower than the $TBr_R$ beams. Considering the UBr beams, the TBr beams were approximately 10% heavier than the $UBr_{45}$ beams, but 24% lighter than $UBr_{60}$ beams.

Braid angle was physically measured at randomly located points on the outer surface for 4 repeats for both types of TBr beams and are shown in Figure 8. Due to the fibre waviness at the transition points

LXVIII

and shorter span of the 60° region in the $TBr_A$ beams, limited measurements (minimum 6) were possible. The deviation in the measured braid angles were similar to the values previously recorded for the UBr beams.

Specimens of 10 mm length were extracted from one untested repeat each for the $TBr_A$ and $TBr_R$ beams. The extracted specimens were cold-mounted in epoxy resin and polished to a 3 µm finish, following which the cross section perpendicular to the beam axis was analysed using images from a macro zoom camera. The thickness of the beams was measured at a minimum of 400 locations across two polished specimens prepared for the 45° and 60° regions of the $TBr_A$ beam as well as $TBr_R$ beam. The measured thickness distributions are represented through box plots shown in Figure 9. The thickness of the $UBr_{45}$ and $UBr_{60}$ beams, reported in [26] are also shown for comparison. The thickness measurements of the two regions of $TBr_A$ beam are in reasonable agreement with the corresponding UBr beams. However, the 60° region showed greater variance against its UBr counterpart as compared to the 45° region, which could be a result of excessive braid angle distortions, observable as fibre waviness on the outer surface. As expected, the thickness distribution of the $TBr_R$ beams resided between the measured values corresponding to the two UBr beams, with the mean thickness being approximately 19% greater than $UBr_{45}$ but 17% less than $UBr_{60}$.

The polished section specimens were also imaged using a ZEISS Axio Imager 2 microscope fitted with a 5 megapixel Axiocam 305 digital camera at 5x magnification. Figures 10 (a) and (b) shows selected micrographs of the 60° and 45° regions of $TBr_A$ beams respectively. For reference, micrographs of $UBr_{45}$ and $UBr_{60}$ beams are also shown. The $TBr_A$ and corresponding UBr micrographs showed comparable characteristics, with fibre tows separated by resin rich regions. Regions with extensive tow distortion/fibre waviness are highlighted in the micrograph pertaining to the 60° region of $TBr_A$ beams. The waviness could affect the mechanical performance of the beams and highlights scope for improving process control during the tailor-braiding process. A micrograph of a $TBr_R$ beam is shown in Figure 10(c). Notably, a resin-rich region was visible in the outermost layer (60° layer) above the fibre tows, explaining the absence of dry regions on the outer surface. The micrographs of both the TBr beams showed intra- and inter-tow voids similar to the UBr beam sections. However, based on the prior detailed analysis of void content morphology previously conducted [26] in addition to the mechanical test results of the UBr beams, it is proposed that the presence of voids does not prejudice the comparative analysis of mechanical performance as performed here.

**Quasi-static three-point flexure tests**

Quasi-static three-point flexural testing was performed using an Instron 5800R test machine with a 100 kN load cell in compression mode. Figure 11(a) shows the test setup used. The parameters used during the test are listed in Table 3. All parameters are consistent with those used in the previous reference study to test the UBr beams. During the tests, the vertical displacement at the beams' bottom surface was recorded using a linear deflectometer created by combining an Instron 2630-112 extensometer and a spring-loaded plunger, as shown in Figure 11(b). This was used to evaluate the localised crushing in

the central loading region by subtracting the recorded value from the crosshead displacement. Six repeat tests of each beam type were conducted, while the bottom surface displacement was recorded for three repeats each. The tests were stopped at a crosshead displacement of 18 mm as significant lateral movement was observed at the beam-support roller interfaces upon deflections beyond this. Similar to the analysis performed for UBr beams, the mechanical response of the TBr beams were compared using the indices S', $P'_{max}$ and $E'_{abs}$. The mean $P'_{max}$ and $E'_{abs}$ of $UBr_{60}$ beams and mean S' of $UBr_{45}$ beams were selected as the benchmark values (being the highest in each case) against which the performance of the TBr beams would be evaluated.

During the three-point flexure tests, the surface strain distribution was evaluated using a three-dimensional digital image correlation (3D-DIC) system. These optical strain measurements were conducted for one single repeat during testing of both $TBr_A$ and $TBr_R$ beams. The GOM 12M system was used to capture 3D-DIC images, and GOM ARAMIS and GOM Correlate Professional were used for the acquisition and post-processing of the DIC images. For all the conducted measurements, the Region of Interest (RoI) was the region directly under the central loading roller, as deformations were concentrated in this region. The parameters of the DIC system are listed in Table 4. The surface elements created in the software from the recognised facets were realigned in the software to ensure consistent orientation of the measured displacements. In order to estimate the accuracy of the measurement system, six static (undeformed) images were recorded and analysed. The evaluated bias and resolution of the measurements are listed in Table 5.

The acquired optical strain measurements were used to compare the deformation in different regions of the beam. Figure 12(a) shows three separate line sections along which flexural strains 1, 2 and 3 are evaluated - corresponding to the top, middle and bottom regions respectively. For each line section, the flexural strain was calculated as the average of the axial strains at all integration points along the section. Similarly, Figure 12(b) shows the sections used to record the point-wise downward y-displacements y1, y2 and y3 in the top, middle and bottom regions respectively. Analysing the obtained flexural strain and y-displacements in different regions of the beams enabled further comparison of deformation modes between the TBr variants as well as against the UBr beams. For further details of the analysis process, the readers are referred to [26].

## Results and discussion
### Three-point flexure performance of tailor-braided beams
Figure 13(a) shows the three-point flexure load-displacement curves corresponding to the tested TBr beams.

The behaviour of the $TBr_A$ and $TBr_R$ beams was similar up to a crosshead deflection of approximately 5 mm. Upon further deformation, the load borne by the $TBr_R$ beams plateaued with frequent undulations. On the other hand, the response corresponding to the $TBr_A$ beams showed a generally consistent increase throughout the deformation with minor inconsistency between the repeats within the last two millimetres of deflection. For the purpose of comparison, the load-displacement data of the

LXX

TBr$_A$ and TBr$_R$ beams are shown along with the response recorded for UBr beams in Figure 13 (b) and (c) respectively. Despite the significant fibre waviness, the TBr$_A$ and UBr$_{60}$ beams showed very similar load-displacement behaviour. The plateauing load trends observed for the TBr$_R$ beams was analogous to the UBr$_{45}$ beams, however the magnitude of the load was greater for the TBr$_R$ beams.

In order to identify and semi-quantitatively compare the damage in the tested beams, active infrared thermography was employed ex-situ. The beams were held in free space using a retort stand and heated internally using hot air (~150 °C) supplied from a heat gun for approximately 10 seconds whilst an FLIR SC5200 infrared camera was used to acquire thermal images at 25 Hz of the outer surface of the beams in the region of interest. This image acquisition was conducted for the load bearing surface (upper) as well as the opposite (lower) surface for one repeat of each beam type. The acquired images were processed using FLIR Altair thermography software, evaluating the variation in heating detected at the beam surface due to differential conduction by subtracting the reference frame (unheated surface, t = 0 s) from the target frame (t = 3 s). The differential thermal images corresponding to different beam types are shown in Figure 14. Optical images of the same upper and lower surfaces are also shown for context. The different digital levels visible in the thermal images of the beam surface represent difference in heat conduction outward through the beam wall from the inner surface that arise from variabilities in wall thickness, density (local fibre/resin content) as well as localised damage. Damaged regions in the composite such as local cracking and larger-scale delaminations present the most severe impediment to heat conduction (as compared to changes in density and wall thickness) and will therefore be clearly visible at the highest end of the differential scale. The colour scale was automatically adjusted for each image to span the maximum and minimum detected levels and therefore there is not a common scale applied to the images; however, this approach allows semi-quantitative assessment of the differential conductive heating within each discrete image. Damage is visible on the upper loading surfaces of all the tested beams in the thermal images with the lowest surface temperature visible as lightest red within each thermal image, and corresponds to the surface damage seen in the optical images, with identical location and morphology in both image types. The images indicate that the damage initiated under the loading roller followed by propagation along the braided fibres in close proximity. However, neither the optical nor thermal images revealed any damage on the lower surfaces of the beams. Interestingly, this semi-quantitative differential thermal analysis approach also clearly reveals the characteristic trellis braided tow pattern within the beams (blue-black-white, as per differential fibre/resin density), and the inherent wall thickening at the higher 60° braid angle (darker red); this occurs in local patches along the UBr$_{60}$ beam and within the entire 60° mid-section of TBr$_A$ beam.

**Analysis of lightweighting benefits of tailor-braiding**

Figure 15 shows the S, $P_{max}$ and $E_{abs}$ as well as the mass-specific values (S', $P'_{max}$ and $E'_{abs}$) for all of the tested beam types. As expected from the load-displacement responses, the absolute values (S, $P_{max}$ and $E_{abs}$) of each index were indistinguishable between $UBr_{60}$ and $TBr_A$ beams.

Single-factor ANOVA was performed for each mass-specific property. The resulting p-values for each comparison are listed in Table 6. All the values being less than 0.05 indicate that across the four types of beams being compared, the differences between all the mass-specific properties were statistically significant.

In order to further explore these differences, a post-hoc analysis was performed using Tukey-Kramer method [30].The Studentised range statistic q was evaluated for each pair using Equation 3.

$$q_{AB} = \frac{|\mu_A - \mu_B|}{\sqrt{\frac{MS_W}{2}\left(\frac{1}{n_A} + \frac{1}{n_B}\right)}} \tag{3}$$

where $\mu_A$:mean for sample A; $\mu_B$:mean for sample B; $n_A$:sample size of A; $n_B$:sampl size of B and $MS_W$: mean square error within.

As per the method, depending on the number of samples, a critical q-value is determined from a standard q-table. If the evaluated q-value from Equation (3) is greater than the critical q-value, the difference between the means corresponding to the respective pair of samples is statistically significant. The obtained q-values corresponding to every comparison are listed in Table 7 with the critical q-values. Referring to the table yields the following observations regarding mass-normalised performance:

    (iv)    **$TBr_A$ versus $TBr_R$:** The comparison of the two tailored beam configurations showed no significant difference in S'. However, the $P'_{max}$ and $E'_{abs}$ were greater for $TBr_A$ beams, the mean values being greater by 41% and 28% respectively.

    (v)    **$TBr_A$ versus UBr:** There were no statistically significant differences measured between the $TBr_A$ beams and $UBr_{45}$ beams with respect to S'. However, $P'_{max}$ and $E'_{abs}$ were both greater for the $TBr_A$ beams with the mean values being 45% and 31% higher. On the other hand, comparisons with the $UBr_{60}$ beams showed that all the performance indices were greater for the $TBr_A$ beams, showing substantial increases in S', $P'_{max}$ and $E'_{abs}$ of 26%, 30% and 31% respectively. Therefore, the local axial tailoring ($TBr_A$) delivered improvements against most benchmark (UBr) performance indices.

    (vi)    **$TBr_R$ versus UBr:** There were no significant differences measured between the $TBr_R$ and $UBr_{45}$ beams across all three performance indices. Similarly, comparing $TBr_R$ beam performance against that of the $UBr_{60}$ beams, $E'_{abs}$ was found to be comparable. The S' of $TBr_R$ exceeded that of $UBr_{60}$ beams by 19%, while the $P'_{max}$ of $UBr_{60}$ beams was greater by 8%. Overall, braiding the outer layer at a higher braid angle did not yield significant improvements over any of the three benchmark UBr performance indices.

**Analysis and comparison of beam deformation**

LXXII

Figure 16 shows the measured localised crushing against crosshead displacement for the tested beams. The $TBr_A$ and $UBr_{60}$ beams showed matching trends, with the localised crushing accounting for approximately 17% and 19% of the total crosshead displacement for $TBr_A$ and $UBr_{60}$ beams respectively. The $TBr_R$ beam showed a reduction in localised crush with respect to the $UBr_{45}$ beams, with an overall localised crushing of 35% compared to 45% for the latter. However, the transitions in slope of the curves occurred at identical crosshead displacement values for both beams.

The optically-measured axial strain maps are shown for the tested beams in Figure 17. Optical strain analysis for the UBr beams, previously reported in [26], had revealed that greater localised crush resulted in a reduction in applied strains on the bottom (tensile) surface of the beam – the predominant deformation mode was local crush, thus reducing global flexure. A similar correlation between localised crush and lower surface strains is also observed in the TBr beams. Similar to observations from the $UBr_{60}$ beam, during the final millimetres of the applied deflection, a region showing surface strains of >1.5% developed on the lower (tensile) surface of the $TBr_A$ beam at peak deformation, with clear regions of strain concentration corresponding to the macrostructure of the composite (braid). In contrast, such surface strains were less prominent for the $TBr_R$ beams in terms of magnitude and uniformity over the region, but nonetheless were greater as compared to the $UBr_{45}$ beam. As observed for the UBr beams, differences in the measured surface strains between $TBr_R$ and $UBr_{45}$ beams correlated inversely with increased prevalence of localised crush under the loading roller.

The flexural strains recorded on the beam surface are shown in Figure 18. Compressive and tensile strains of increasing magnitude were observed in the top (strain 1) and bottom (strain 3) regions respectively for all the beams. $TBr_A$ and $UBr_{60}$ beams showed approximately overlapping responses for each strain. Following onset of localised crushing in the $TBr_R$ and $UBr_{45}$ beams, strain 1 measurements were unavailable due to the propagation of cracks into the RoI. This localised failure occurred earlier for the $UBr_{45}$ beam, showing a tendency towards localised crushing as compared to $TBr_R$ beam. Similarly, curves corresponding to strain 2 and strain 3 also showed visible differences in magnitude but followed the same trend. As observed in Figure 17, strain-3, i.e. lower (tensile) region strains for the $UBr_{45}$ and $TBr_R$ beams were greatly reduced as compared to the $TBr_A$ and $UBr_{60}$ beams, again illustrating the tendency of the former ($UBr_{45}$ and $TBr_R$ beams) towards localised crush failure rather than the global flexure deformation modes seen in the latter ($TBr_A$ and $UBr_{60}$ beams).

Figure 19 shows the progression of section-wise y-displacements y1, y2 and y3 with increasing crosshead displacement. Results for UBr beams had indicated that differences arising between the three discrete section-wise displacement analyses is positively correlated with localised crush. In order to quantify the disparity in region-wise displacements, the root mean square (RMS) difference between the mid and bottom region y-displacements was evaluated as per Equation 4.

$$RMS_{23} = \sqrt{\frac{\Sigma(y_2 - y_3)^2}{n}} \tag{4}$$

where RMS$_{23}$: root mean square difference between y2 and y3 and n: number of points on the sections.

The evolution of RMS$_{23}$ with increasing crosshead displacement is shown in Figure 20. The data shown replicates the order observed for localised crush, thus showing a positive correlation between the two quantities.

The deformation analysis performed using both contact and optical strain measurement techniques revealed that the TBr$_A$ beams experience a very similar deformation behaviour to that observed for the UBr$_{60}$ beams. On the other hand, the TBr$_R$ beams showed greater localised crushing as compared to TBr$_A$ beams, but the TBr$_R$ beam deformation was more inclined towards global flexure as compared to UBr$_{45}$ beams. The superior performance of TBr$_A$ beams over TBr$_R$ beams shows the effectiveness of locally tailoring the fibre architecture across the entire thickness of the beam as compared to making an outer-layer modification globally along the beam.

## Conclusions

This paper presents 'tailor-braiding' as a novel approach to create composite beams with higher structural efficiency than conventionally uni-braided beams. As such the performance of tailored braided beam structures with axial (TBr$_A$) and radial (TBr$_R$) braid angle variation was investigated in quasi-static three-point flexure. Based on the previously obtained flexure test results from uni-braided beams with angles of 45° and 60° (UBr$_{45}$ and UBr$_{60}$), tailored beams with a step-wise 45°/ 60°/ 45° axial braid angle configuration were manufactured using a start/stop braiding method. Beams with a globally-applied radial [±60°/±45°/±45°] variation (TBr$_R$) were also manufactured. The tailored (TBr$_A$, TBr$_R$) beams were tested in a static three-point flexure test and their mechanical performance and deformation behaviour were compared with UBr beams.

The TBr$_A$ beams showed tow distortion (waviness) at the braid angle transition zone. Apart from the waviness, braid angle and thickness measurements in different regions of the TBr$_A$ beams were in reasonable agreement with the corresponding measurements from UBr beams. It is proposed that a continuous braid angle transition (instead of step-wise) would minimise/eliminate the fibre waviness observed in this work that has arisen due to the step-transition in braid angle and start/stop nature of the manufacturing process. The performance indices of the TBr$_A$ beams were higher than the UBr beams. Particularly interesting was the observation that despite being 24% lighter, the TBr$_A$ beams showed statistically equivalent performance to the UBr$_{60}$, which had highest mechanical performance amongst the UBr beams. This superior performance of the TBr$_A$ beams, despite the presence of fibre waviness, was encouraging and suggests that further improvements in performance might be achieved through elimination of defects. Therefore, changing the braid angle in the loading region to 60° resulted in a replication of the deformation behaviour of UBr$_{60}$ beams, while braiding the outer layer at 60° did not produce an equivalent change.

The results offer  a demonstration of the lightweighting of potential of the proposed axial-wise tailor-braiding (TBr$_A$) approach. It is proposed that future work varying the length of the central 60° region in

TBr$_A$ beams could optimise performance and yield further reduction in the weight of the beams without affecting deformation modes. Additionally, investigating structures produced with continuous braid angle transitions (as opposed to the step-wise discrete transition presented here), and investigating the effect of the same TBr$_A$ approach in thermoset matrix-based composites would be worthwhile additions in this area of study.

## Acknowledgements

## Funding source

## Data Availability Statement

The raw/processed data required to reproduce these findings cannot be shared at this time as the data also forms part of an ongoing study.

## References

[1]       Kyosev Y. Recent developments in braiding and narrow weaving. Berlin: Springer International Publishing; 2016.

[2]       Carey JP. Introduction to braided composites. In: Handbook of Advances in Braided Composite Materials. Woodhead Publishing; 2017, p. 1–21.

[3]       Slange TK. Rapid Manufacturing of Tailored Thermoplastic Composites by Automated Lay-up and Stamp Forming: A Study on the Consolidation Mechanisms. PhD Thesis, University of Twente. 2019.

[4]       High Performance Computing Studies: DOT HS 812 404. Department of Transportation. 2017.

[5]       Sturm R, Heieck F. Energy absorption capacity of braided frames under bending loads. Compos Struct 2015;134:957–65.

[6]       Harte AM, Fleck NA. On the mechanics of braided composites in tension. Eur J Mech A/Solids 2000;19:259–75.

[7]       Melenka GW, Carey JP. Development of a generalized analytical model for tubular braided-architecture composites. J Compos Mater 2017;51:3861–75.

[8]       Falzon PJ, Herszberg I. Mechanical performance of 2-D braided carbon/epoxy composites. Compos Sci Technol 1998;58:253–65.

[9]       Potluri P, Manan A, Francke M, Day RJ. Flexural and torsional behaviour of biaxial and triaxial braided composite structures. Compos Struct 2006;75:377–86.

[10]      Priem C, Othman R, Rozycki P, Guillon D. Experimental investigation of the crash energy absorption of 2.5D-braided thermoplastic composite tubes. Compos Struct 2014;116:814–26.

[11]      Gautam M, Potluri P, Ogin S, Jain P. Necking behaviour of flattened tubular braided composites. In: ICCM 2015: Proceedings of the 20th International Conference on Composite Materials, Copenhagen, July 2015.

[12]      Fujihara K, Yoshida E, Nakai A, Ramakrishna S, Hamada H. Influence of micro-structures on bending properties of braided laminated composites. Compos Sci Technol 2007;67:2191–8.

[13]      Tate JS, Kelkar AD. Flexural behavior of biaxial braided composites. In: Proceedings of ASME International Mechanical Engineering Congress and Exposition, Orlando, November 2005.

[14]      Laberge-Lebel L, Van Hoa S. Manufacturing of braided thermoplastic composites with carbon/nylon commingled fibers. J Compos Mater 2007;41:1101–21.

[15]      Carey J, Fahim A, Munro M. Design of braided composite cardiovascular catheters based on required axial, flexural, and torsional rigidities. J Biomed Mater Res Part B Appl Biomater An Off J Soc Biomater Japanese Soc Biomater Aust Soc Biomater Korean Soc Biomater 2004;70:73–81.

[16]     Fujihara K, Teo K, Gopal R, Loh PL, Ganesh VK, Ramakrishna S, et al. Fibrous composite materials in dentistry and orthopaedics: review and applications. Compos Sci Technol 2004;64:775–88.

[17]     Boss JN, Ganesh VK. Fabrication and properties of graded composite rods for biomedical applications. Compos Struct 2006;74:289–93.

[18]     Ganesh VK, Choo TS. Modulus graded composite adherends for single-lap bonded joints. J Compos Mater 2002;36:1757–67.

[19]     Stanier D, Gent I, Roy SS, Hamerton I, Potluri P, Ivanov DS. Mechanical behaviour of patterned multi-matrix composites with gradient properties. In: ECCM 2016: Proceedings of the 17th European Conference on Composite Materials, Munich, June 2016.

[20]     Stanier D, Radhakrishnan A, Gent I, Roy SS, Hamerton I, Potluri P, et al. Matrix-graded and fibre-steered composites to tackle stress concentrations. Compos Struct 2019;207:72–80.

[21]     Huang Z-M, Wang Q, Ramakrishna S. Tensile behaviour of functionally graded braided carbon fibre/epoxy composite material. Polym Polym Compos 2002;10:307–14.

[22]     Duan L, Xiao N, Li G, Xu F, Chen T, Cheng A. Bending analysis and design optimisation of tailor-rolled blank thin-walled structures with top-hat sections. Int J Crashworthiness 2017;22:227–42.

[23]     Sun G, Pang T, Zheng G, Song J, Li Q. On energy absorption of functionally graded tubes under transverse loading. Int J Mech Sci 2016;115–116:465–80.

[24]     Keating EM. Lightweighting of Stiffness Critical Advanced High Strength Steel Structures using Fibre Reinforced Plastics. PhD Thesis. University of Warwick, 2016.

[25]     Sun G, Yu H, Wang Z, Xiao Z, Li Q. Energy absorption mechanics and design optimization of CFRP/aluminium hybrid structures for transverse loading. Int J Mech Sci 2019;150:767–83.

[26]     Singh A, Reynolds N, Keating E, Barnett A, Barbour S, Hughes DJ. The effect of braid angle on the flexural performance of structural braided thermoplastic composite beams. Composite Structures. Submitted.

[27]     Wu Z, Shen Y, Pan Z, Hu X. Three-point Bending Behavior and Energy Absorption Capacity of Composite Tube Reinforced by Gradient Braided Structure in Radial Direction. Fibers Polym 2019;20:1455–66.

[28]     Nishimoto H, Ohtani A, Nakai A, Hamada H. Prediction Method for Temporal Change in Fiber Orientation on Cylindrical Braided Preforms. Text Res J 2010;80:814–21.

[29]     Singh A, Reynolds N, Carnegie CR, Micallef C, Keating EM, Winnett J, Barnett AE, Barbour SK, Hughes DJ. A novel route for volume manufacturing of hollow braided composite beam structures. Adv Manuf Polym Compos Sci 2019:1–6.

[30]     Tukey JW. The collected works of John W. Tukey. vol. 1. Taylor & Francis; 1984.
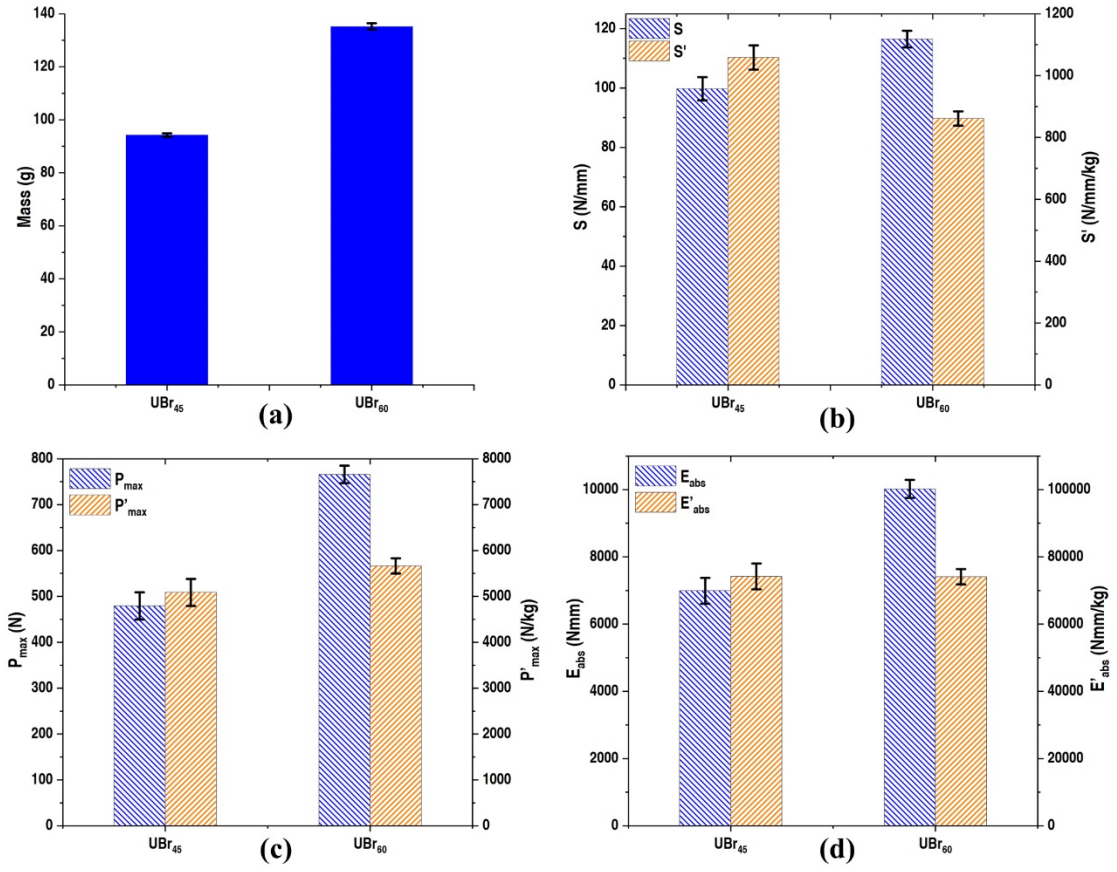
Figure 1 Measured values of (a) mass; (b) S and S'; (c) $P_{max}$ and $P'_{max}$ and (d) $E_{abs}$ and $E'_{abs}$ of the UBr beams. Note: bars represent mean values from 6 repeats and errors represent one standard deviation
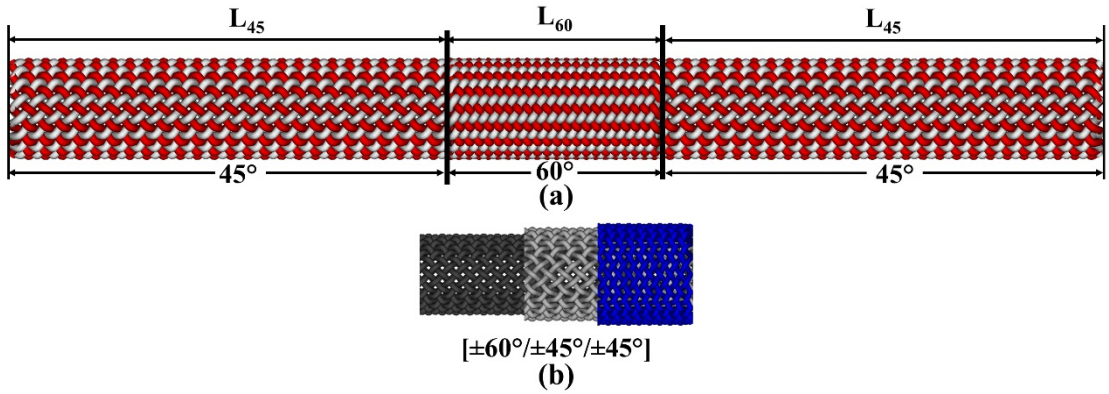


Figure 2 Schematic of axial (a) and radial (b) braid angle variation. Note: $L_{45}$ and $L_{60}$ represent the lengths of 45° and 60° regions respectively
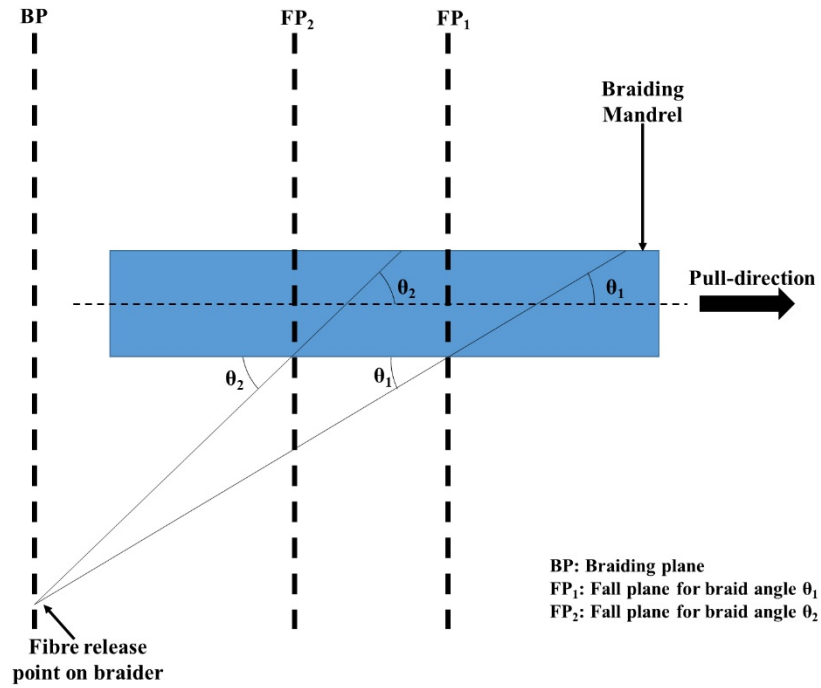
LXXVII

Figure 3 Schematic of the braiding process showing the location of fall planes corresponding to different braid angles



| **(a)** | **(b)** |
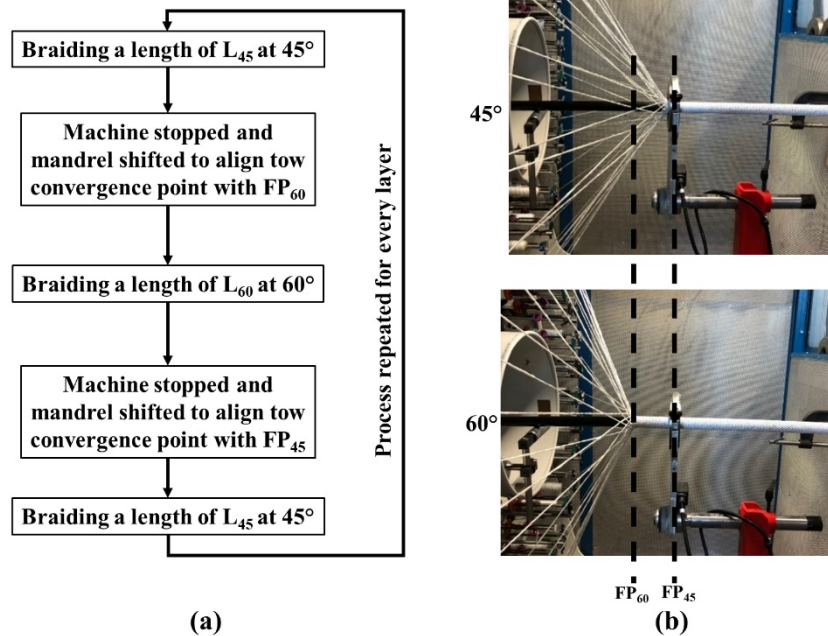
Figure 4 Start-stop braiding: (a) Steps for adjustment in braid angle and (b) Fall planes for 45° and 60° on the braiding mandrel
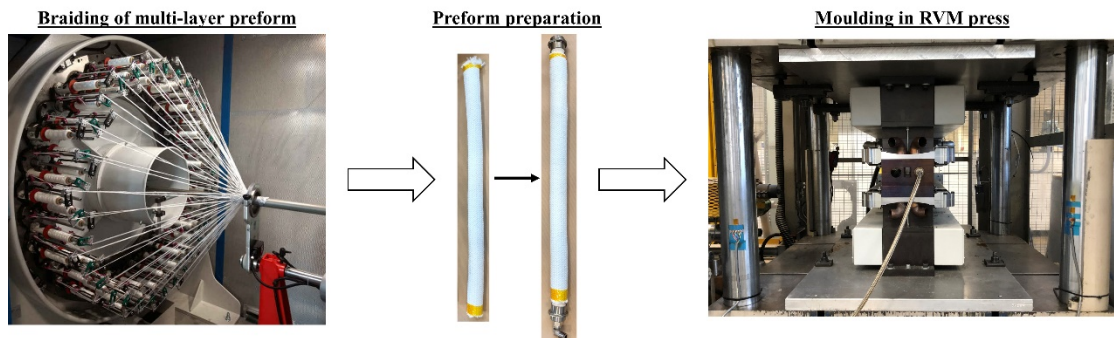
Figure 5 Steps involved in manufacturing of the braided beams (left: Braiding onto mandrel, centre: preform preparation for RVM and right: preform inside closed press with connected pressure line during RVM)



UBr$_{45}$

TBr$_A$

(a)

UBr$_{60}$

TBr$_R$

(b)
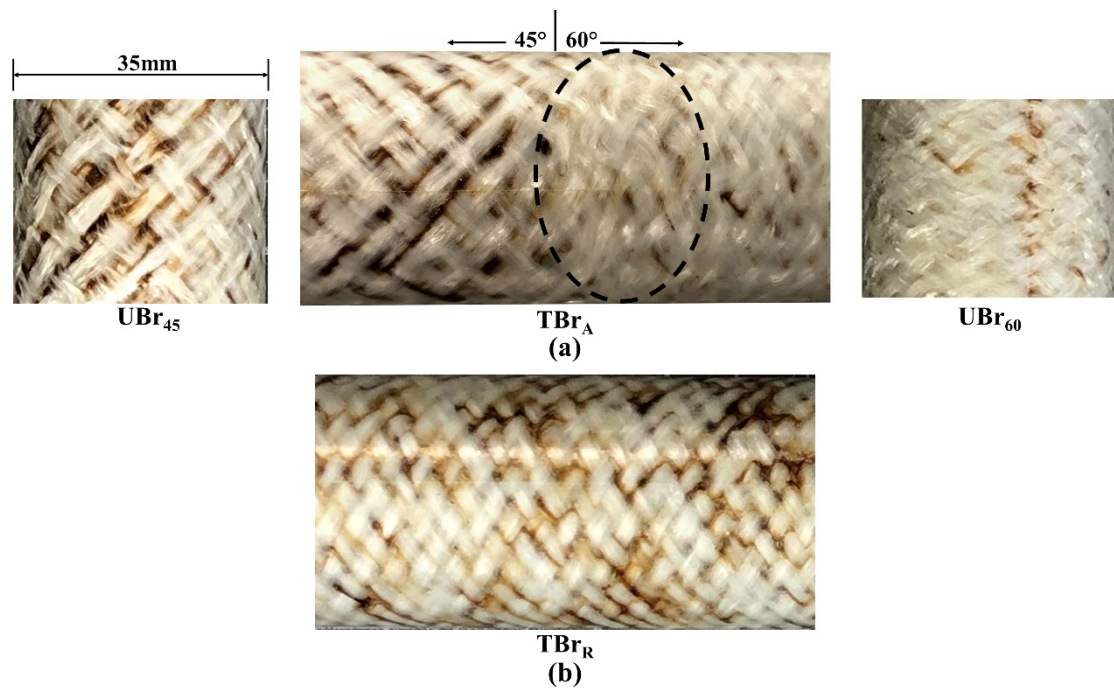
Figure 6 Outer surfaces of (a) TBr$_A$ and UBr beams; (b) TBr$_R$. Note: encircled region shows fibre waviness in TBr$_A$ beams
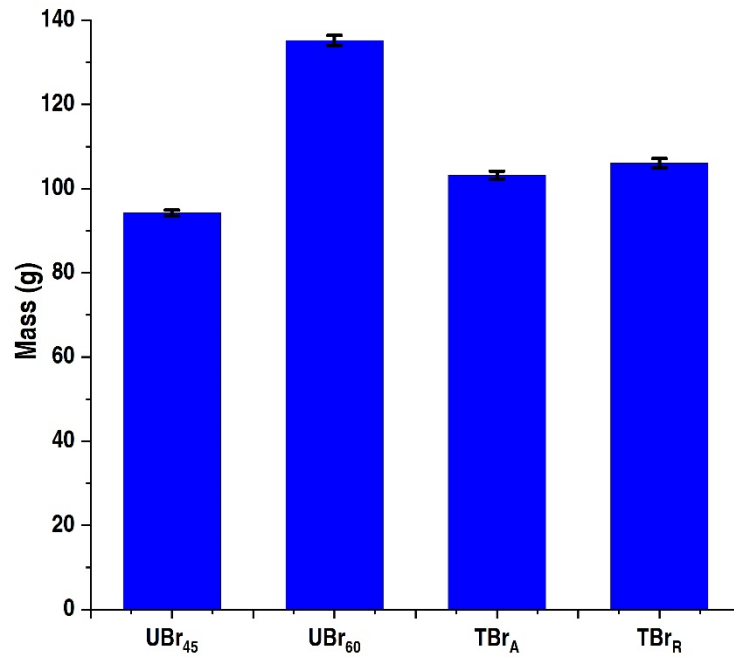
Figure 7 Measured mass of the UBr and TBr beams. Note: bars represent mean values from all repeats and errors represent one standard deviation
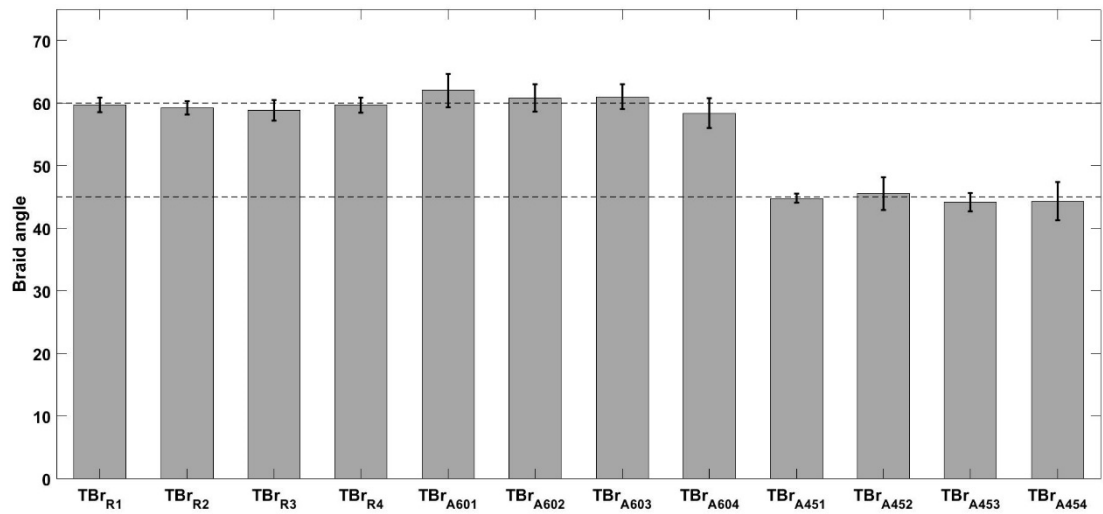


Figure 8 Measured braid angle for TBr beams. Note: bars represent mean values from all repeats and errors represent one standard deviation
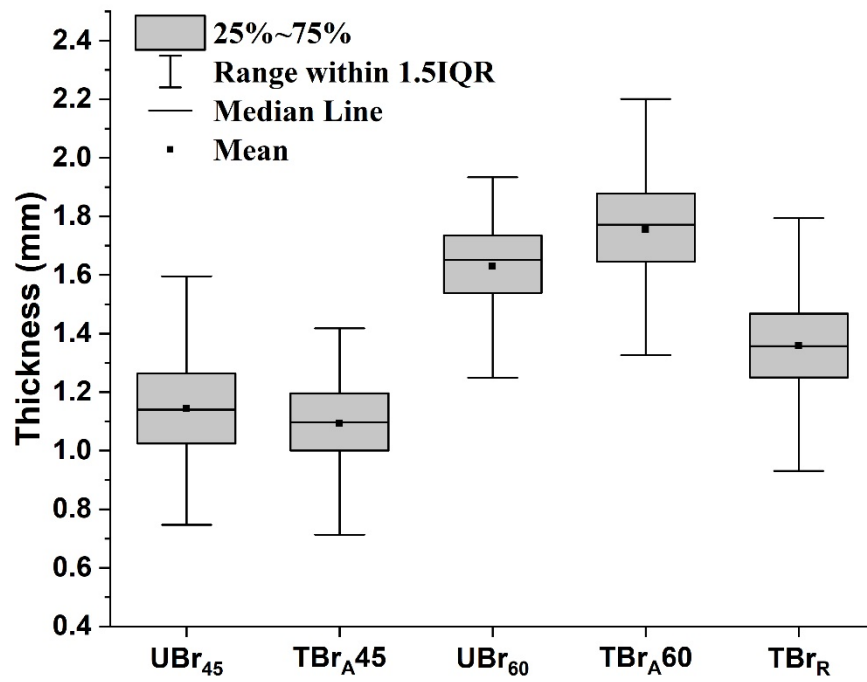
Figure 9 Box plots representing thickness distributions corresponding to TBr beams. Note: thickness distributions of UBr beams are shown for comparison. Note: IQR represents Inter Quartile Range
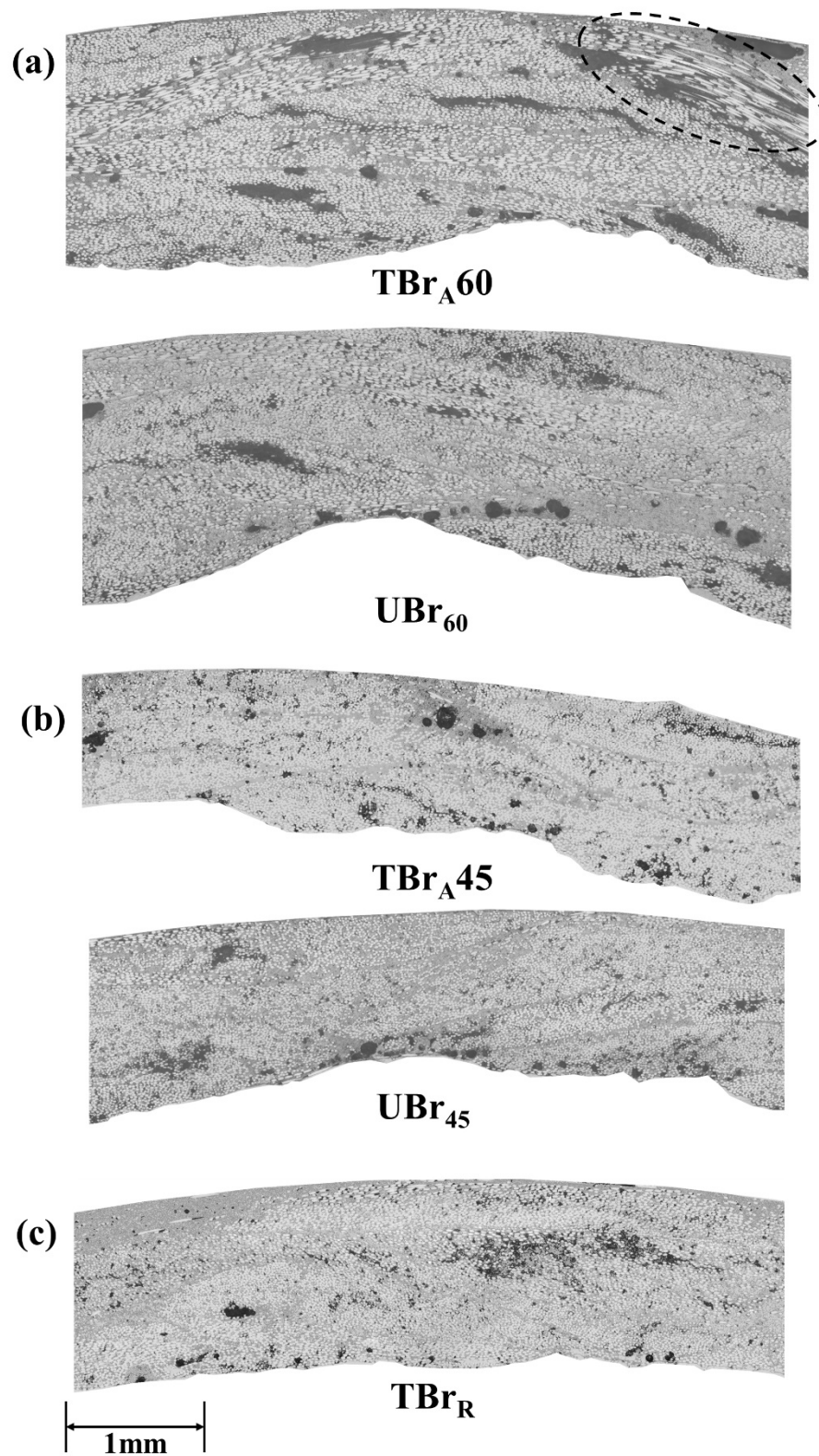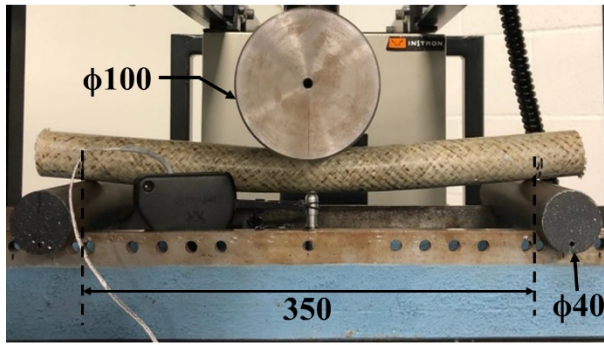
**(a)**

**TBr$_A$60**

**UBr$_{60}$**

**(b)**

**TBr$_A$45**

**UBr$_{45}$**

**(c)**

**TBr$_R$**

**1mm**

Figure 10 Micrographs of braided beam sections corresponding to (a) 60° region of TBr$_A$ beam with highlighted fibre waviness; (b) 45° region of TBr$_A$ beam; (c) TBr$_R$ beam. Note: Micrographs of UBr beam sections are also shown for comparison

LXXXII
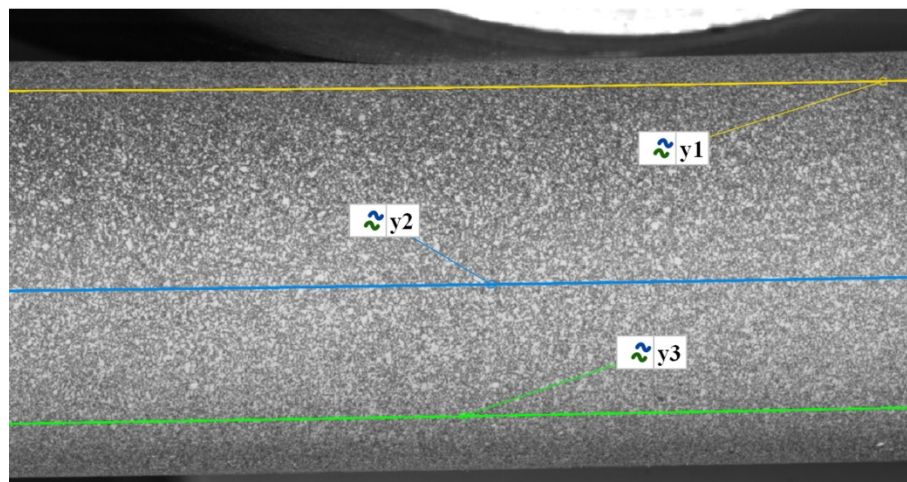
**(a)** **(b)**

Figure 11 (a) Three-point flexure setup on the test machine frame and (b) deflectometer assembly.
Note: all measurements in mm (Taken from [26])
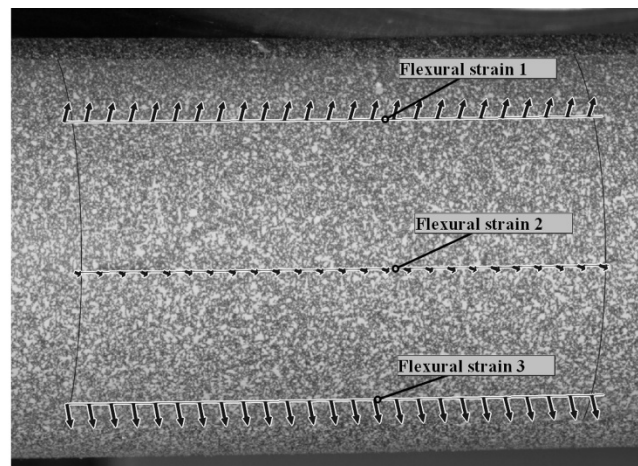


**(a)**



**(b)**

Figure 12 Horizontal sections constructed on the surface of beam in GOM Correlate for evaluating (a)
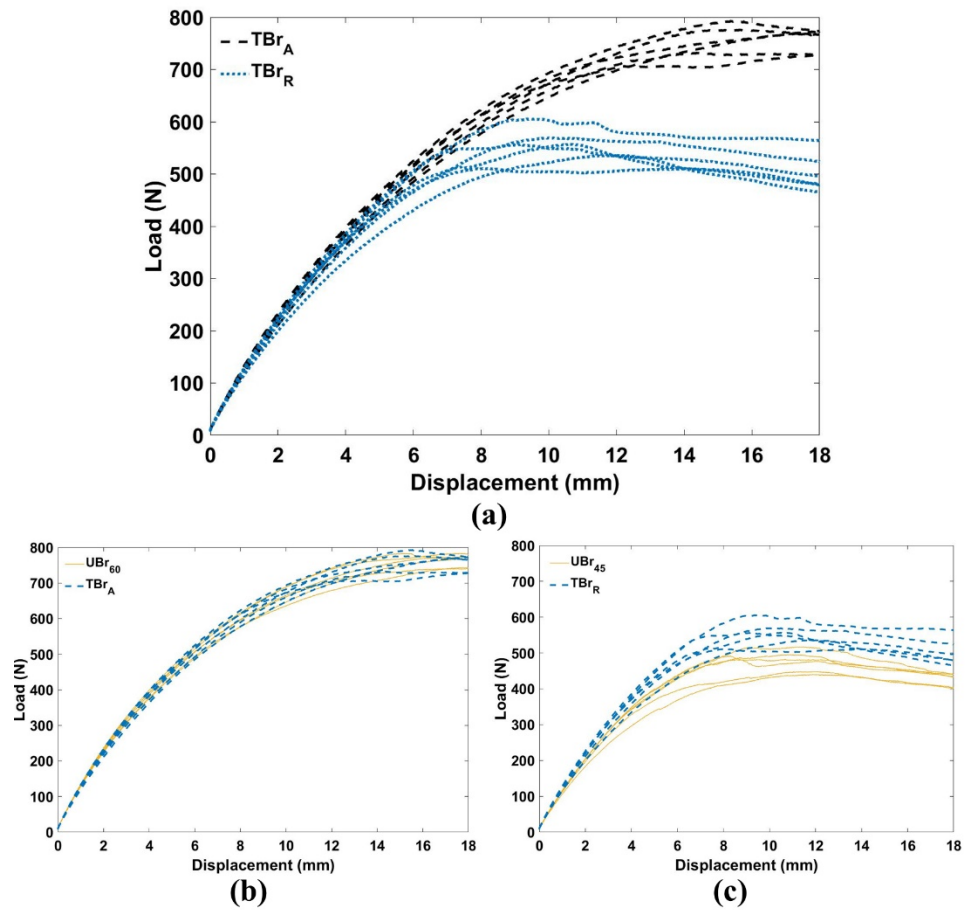flexural strains; (b) vertical displacements

LXXXIII

Figure 13 Load-displacement data from three-point flexure experiments of (a) all tailor-braided beams; (b) $TBr_A$ and $UBr_{60}$ beams; (c) $TBr_R$ and $UBr_{45}$ beams
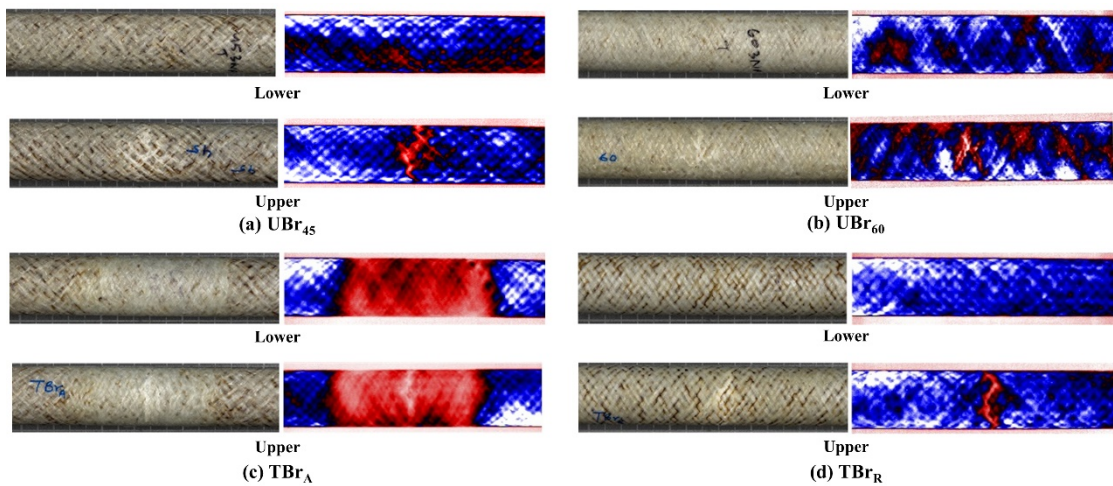


Figure 14 Optical and thermal images corresponding to upper and lower surfaces of (a) $UBr_{45}$, (b) $UBr_{60}$, (c) $TBr_A$ and (d) $TBr_R$ beams. Note: Colour levels individually adjusted for each beam type and do not represent a common temperature scale

LXXXIV

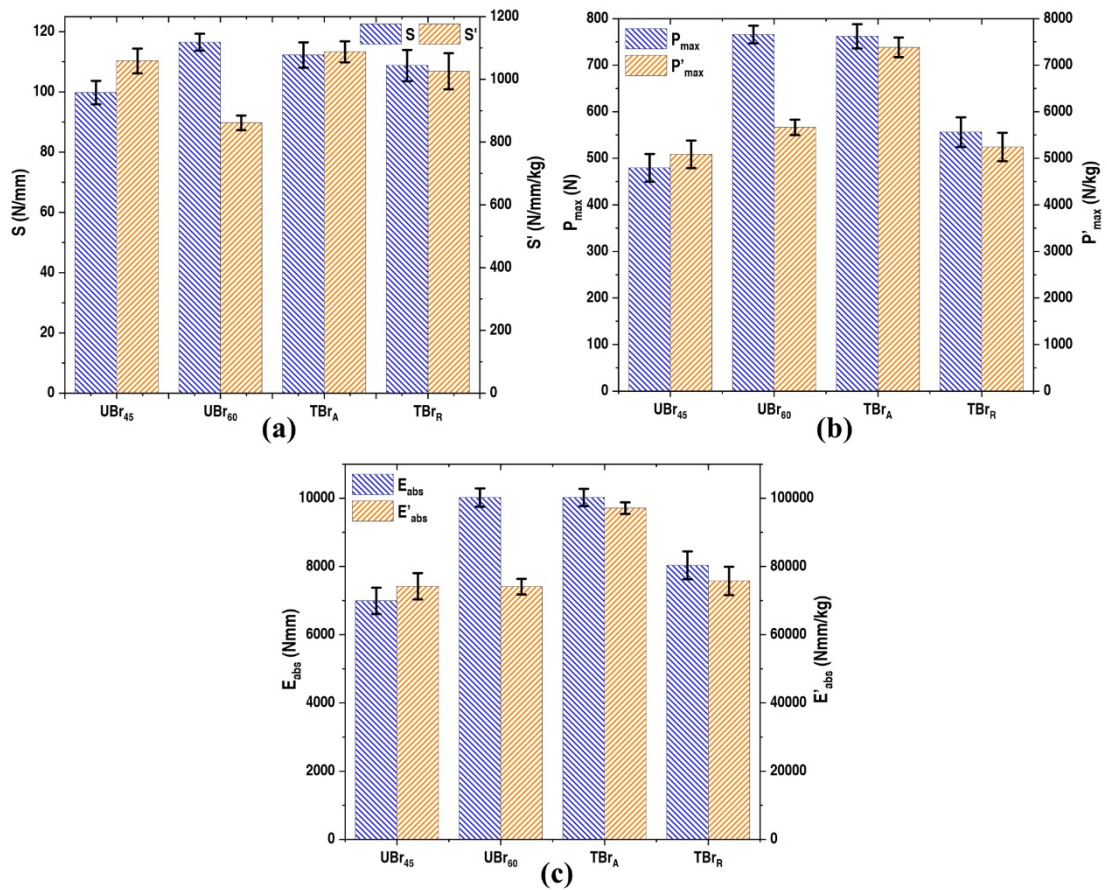Figure 15 Measured mean values of (a) S and S'; (b) $P_{max}$ and $P'_{max}$ and (c) $E_{abs}$ and $E'_{abs}$ of the UBr and TBr beams. Note: bars represent mean values from all repeats and errors represent one standard deviation
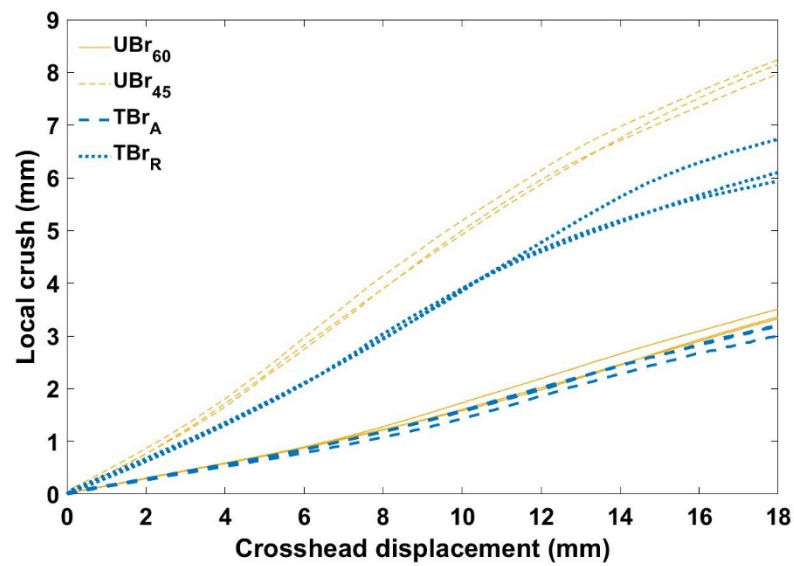


Figure 16 Progression of localised crushing during three-point flexure
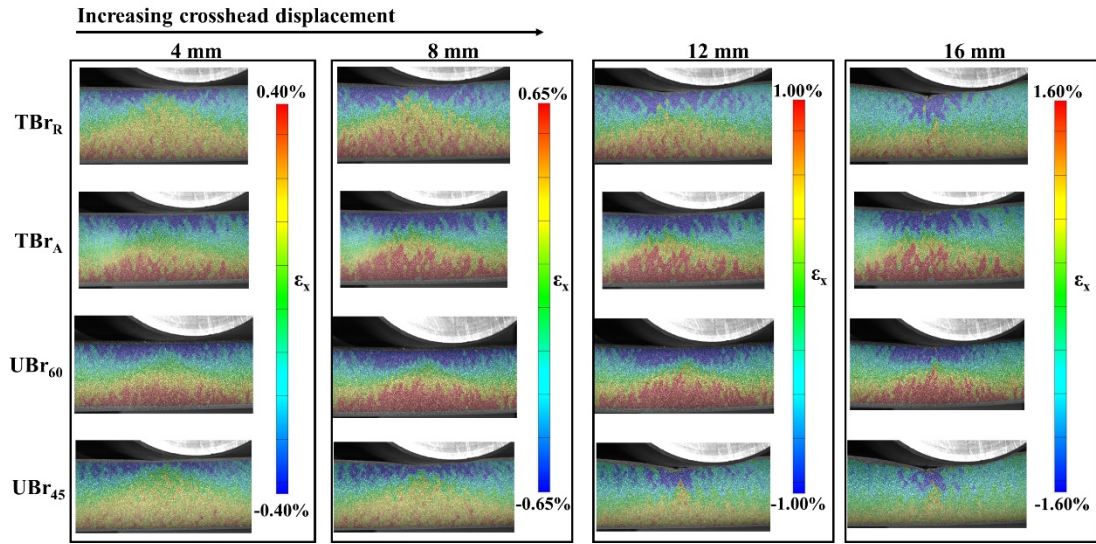
LXXXV

Figure 17 Progression of axial surface strain from 3D DIC data with crosshead displacement during three-point flexure



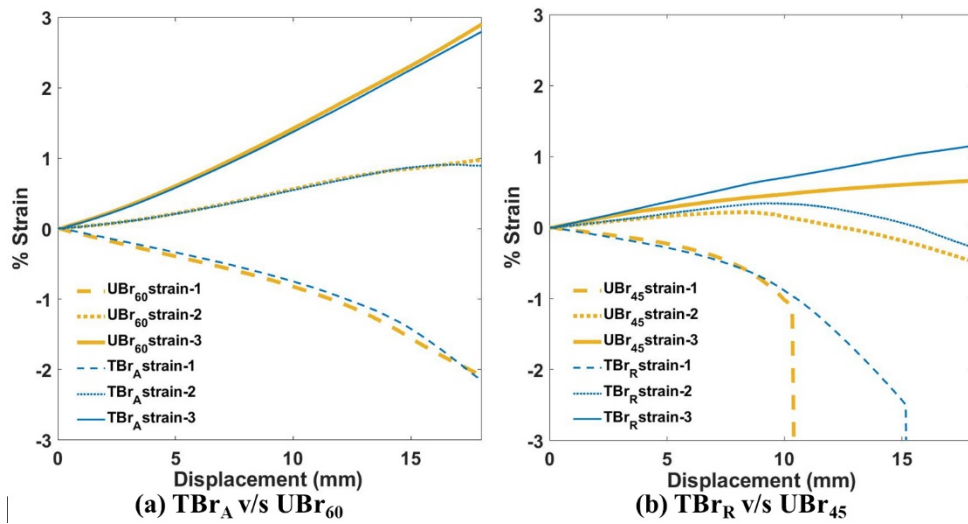**(a) TBr$_A$ v/s UBr$_{60}$**

**(b) TBr$_R$ v/s UBr$_{45}$**

Figure 18 Comparison of region-wise flexural strain evolution between (a) TBr$_A$ and UBr$_{45}$ and (b) TBr$_R$ and UBr$_{45}$ beams

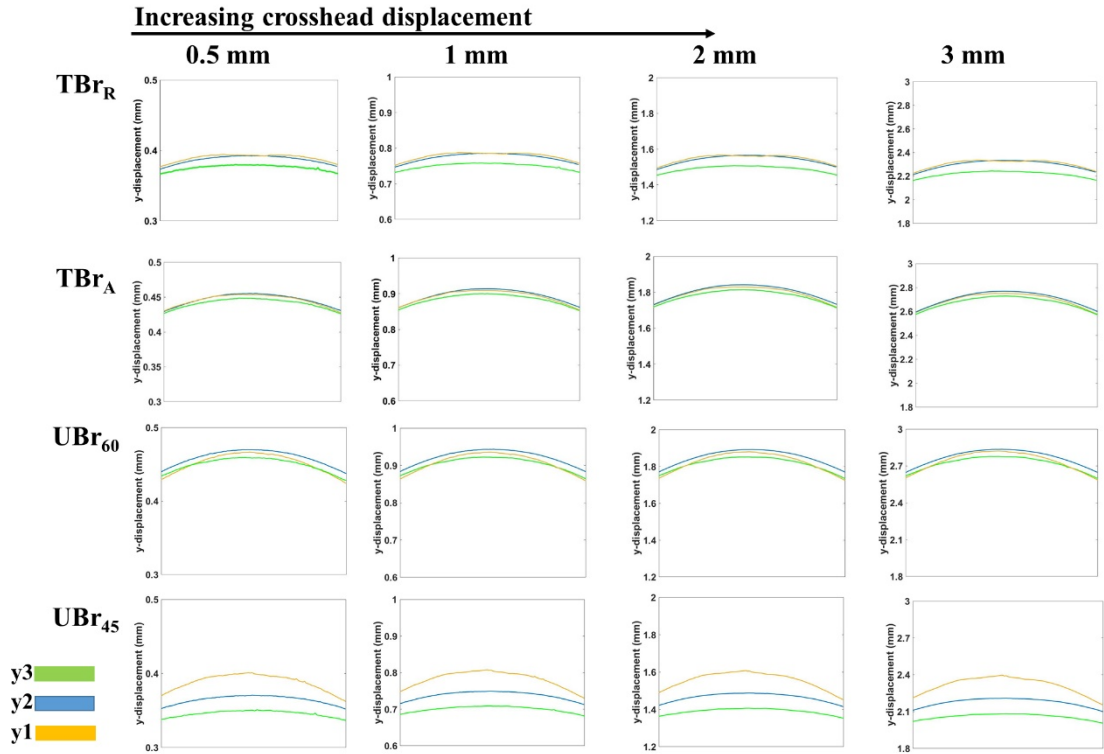Figure 19 Evolution of downward y-displacement y1, y2 and y3 for TBr and UBr beams with increasing crosshead displacement during three-point flexure
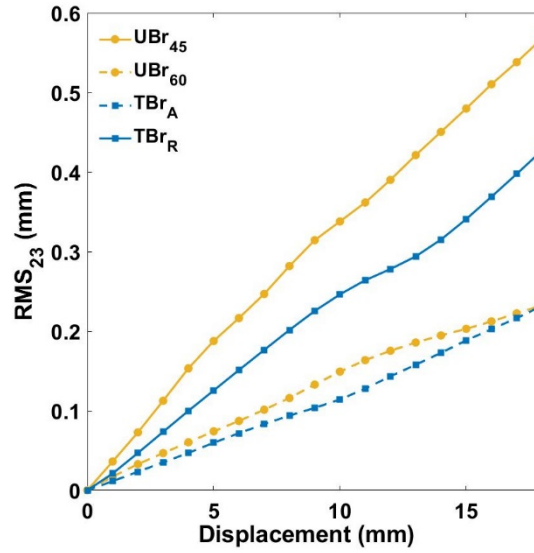


Figure 20 Evolution of RMS difference between mid-region and bottom-region y-displacements during three-point flexure

LXXXVII

Table 1 p-values obtained from ANOVA performed for comparing the mechanical performance of $UBr_{45}$ and $UBr_{60}$ beams

| Property | p-value |
|---|---|
| **Specific Stiffness** | 8.99E-07 |
| **Specific Peak load** | 0.002 |
| **Specific Energy Absorption** | 0.962 |

Table 2 Properties of commingled E-glass/PA6 material and braiding parameters

| Commingled material | | | | Braiding process | |
|---|---|---|---|---|---|
| **Linear weight** | 1650 g/km | **PA6 density** | $1.15 \text{ g/cm}^3$ | **Number of carriers** | 32 |
| **Fibre volume fraction** | 54% | **PA6 melting point** | 221 °C | **Braid architecture** | 1×1 |
| **E-glass density** | $2.54 \text{ g/cm}^3$ | **PA6 glass transition temperature** | 60 °C | **Number of braided layers** | 3 |

Table 3 Three-point flexure testing parameters

| Parameter | |
|---|---|
| Beam length | 420 mm |
| Support span | 350 mm |
| Support roller diameter | 40 mm |
| Loading roller diameter | 100 mm |
| Crosshead displacement rate | 10 mm/min |
| Preload | 10 N |
| Machine compliance induced error | ~0.03mm |
| Load cell error | ~2% |

Table 4 DIC system parameters employed during image acquisition and analysis

| Parameter | |
|---|---|
| Sensor | GOM 12M with Titanar 100 mm lens |
| Image window | 4000 pixel × 3000 pixel |
| Measurement area | 150 mm × 100 mm |
| Calibration plate used | CP20 90 × 72 |
| Facet size | 19 pixels (16 pixels step size) |
| Depth of field | 39 mm |
| Frame rate | 2 Hz |

LXXXVIII

Table 5 Mean bias and precision of DIC measurements estimated from static images

| Mean bias [$\varepsilon_x$ (%)] | Mean precision [$\varepsilon_x$ (%)] | Mean bias [dx (mm)] | Mean precision [dx (mm)] | Mean bias [dy (mm)] | Mean precision [dy (mm)] |
|---|---|---|---|---|---|
| -0.0004 | 0.0175 | 0.0023 | 0.0004 | -0.0001 | 0.0005 |

Table 6 p-values obtained from ANOVA performed for comparing the mechanical performance of TBr and UBr beams

| Property | p-value |
|---|---|
| **Specific Stiffness** | 1.93E-08 |
| **Specific Peak Load** | 1.81E-12 |
| **Specific Energy Absorption** | 4.33E-11 |

Table 7 q-values obtained from Tukey-Kramer post-hoc analysis performed for TBr and UBr beams. Note: values indicating a statistically significant difference are highlighted in **bold**

| Pair | q(S') | q($P'_{max}$) | q($E'_{abs}$) | $q_{critical}$ |
|---|---|---|---|---|
| $UBr_{45}$-$UBr_{60}$ | **12.01** | **5.66** | 0.07 | 4.00 |
| $TBr_A$ -$TBr_R$ | 3.76 | **20.94** | **16.52** | 4.00 |
| $UBr_{45}$- $TBr_A$ | 1.74 | **22.48** | **17.74** | 4.00 |
| $UBr_{45}$-$TBr_R$ | 2.02 | 1.54 | 1.22 | 4.00 |
| $UBr_{60}$- $TBr_A$ | **13.76** | **16.82** | **17.81** | 4.00 |
| $UBr_{60}$-$TBr_R$ | **10.00** | **4.12** | 1.29 | 4.00 |

LXXXIX